Volume 2, Issue 4, December 2022

CHEMICAL SYNTHESIS

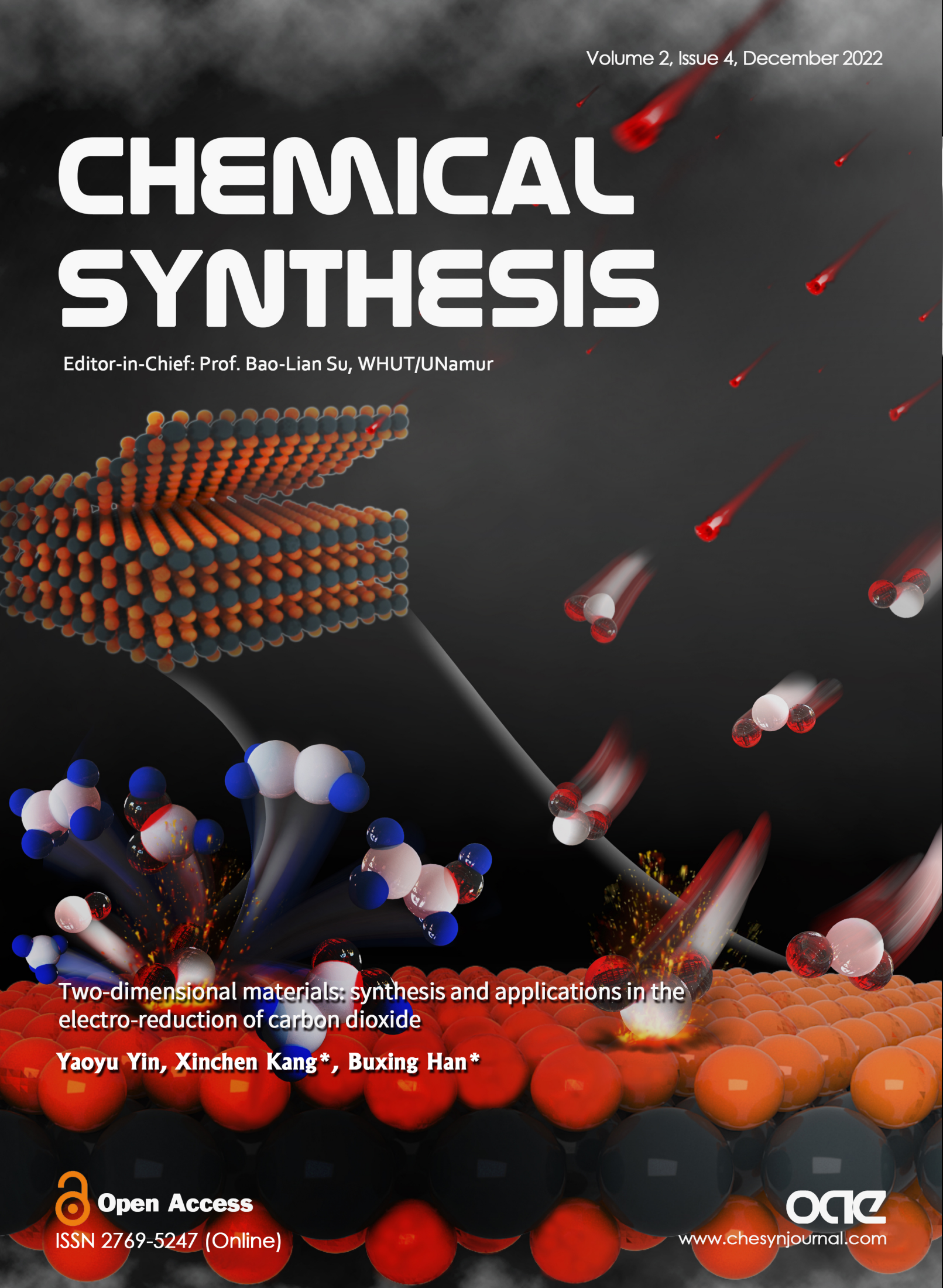

Two-dimensional materials: synthesis and applications in the electro-reduction of carbon dioxide

Yaoyu Yin, Xinchen Kang*, Buxing Han*

Open Access
ISSN 2769-5247 (Online)
www.chesynjournal.com

EDITORIAL BOARD

GENERAL INFORMATION

About the Journal

Chemical Synthesis (*CS*) is an international peer-reviewed, open access, online journal. *Chemical Synthesis* is an open access peer-reviewed journal publishing original research involving all areas of the chemical sciences. The journal aims to be the premier resource of seminal and insightful research and showcases for researchers in both academia and industry, providing a platform of inspiration for the future of chemistry. *Chemical Synthesis* intends to serve as the preeminent international chemistry journal and has the ambition to be among the first choices of chemists for publication of their discoveries.

The scope of the journal focuses on the breadth of the chemical synthetic sciences, covering fields from synthetic methodologies, property studies by theoretical calculations or instrumental approaches at molecular and/or nano levels of the obtained products (materials) to the applications in catalysis, energy conversion and storage, biomedicals, pharmaceuticals, environment protection and remediation, etc.

Information for Authors

Manuscripts should be prepared in accordance with Author Instructions.
Please check www.chesynjournal.com/pages/view/author_instructions for details.
All manuscripts should be submitted online at https://oaemesas.com/login?JournalId=cs.

Copyright

Permissions

For information on how to request permissions to reproduce articles/information from this journal, please visit www.chesynjournal.com.

Disclaimer

The information and opinions presented in the journal reflect the views of the authors and not of the journal or its Editorial Board or the Publisher. Publication does not constitute endorsement by the journal. Neither the *CS* nor its publishers nor anyone else involved in creating, producing or delivering the *CS* or the materials contained therein, assumes any liability or responsibility for the accuracy, completeness, or usefulness of any information provided in the *CS*, nor shall they be liable for any direct, indirect, incidental, special, consequential or punitive damages arising out of the use of the *CS*. The *CS*, nor its publishers, nor any other party involved in the preparation of material contained in the *CS* represents or warrants that the information contained herein is in every respect accurate or complete, and they are not responsible for any errors or omissions or for the results obtained from the use of such material. Readers are encouraged to confirm the information contained herein with other sources.

Publisher

OAE Publishing Inc.
245 E Main Street st112, Alhambra, CA 91801, USA
Website: www.oaepublish.com

Contacts

E-mail: editorialoffice@chesynjournal.com
Website: www.chesynjournal.com

Chemical Synthesis

CONTENTS

Volume 2 / Issue 4 / December 2022

Ji *et al. Chem Synth* 2022;2:17
DOI: 10.20517/cs.2022.27

Chemical Synthesis

Research Article

Open Access

Check for updates

Enantioselective 1,1-diarylation of terminal alkenes catalyzed by palladium with a chiral phosphoric acid

Kai Ji[1,#], Jie Huang[1,#], Xin-Yu Zhang[1], Zhi-Min Chen[1,2,*]

[1]School of Chemistry and Chemical Engineering, Shanghai Key Laboratory for Molecular Engineering of Chiral Drugs, Shanghai Jiao Tong University, Shanghai 200240, China.
[2]State Key Laboratory of Applied Organic Chemistry, Lanzhou University, Lanzhou 730000, Gansu, China.
[#]Authors contributed equally to this work.

Correspondence to: Prof. Zhi-Min Chen, School of Chemistry and Chemical Engineering, Shanghai Key Laboratory for Molecular Engineering of Chiral Drugs, Shanghai Jiao Tong University, No. 800, Dongchuan Road, Minhang District, Shanghai 200240, China. E-mail: chenzhimin221@sjtu.edu.cn

How to cite this article: Ji K, Huang J, Zhang XY, Chen ZM. Enantioselective 1,1-diarylation of terminal alkenes catalyzed by palladium with a chiral phosphoric acid. *Chem Synth* 2022;2:17. https://dx.doi.org/10.20517/cs.2022.27

Received: 13 Sep 2022 **First Decision:** 21 Sep 2022 **Revised:** 28 Sep 2022 **Accepted:** 9 Oct 2022 **Published:** 13 Oct 2022

Academic Editor: Feng Shi **Copy Editor:** Peng-Juan Wen **Production Editor:** Peng-Juan Wen

Abstract

The enantioselective 1,1-diarylation of allyl sulfones and vinyl sulfones is reported for the first time, enabled by a combination of Pd_2dba_3 and a chiral SPINOL-derived phosphoric acid. Various chiral sulfones containing 1,1-diarylalkane motifs were obtained in moderate to good yields with moderate to high enantioselectivities. Control experiments suggested that the sulfone group plays a key role in providing enantioselectivity and reactivity control and might serve as a directing group.

Keywords: Cooperative catalysis, 1, 1-diarylation, allyl sulfone, chiral sulfone, chiral anion phase-transfer catalysis

INTRODUCTION

The chiral 1,1-diarylalkane motif is found in many bioactive natural products and pharmaceuticals [Scheme 1A][1,2]. Accordingly, much effort has been devoted to developing methods for the enantioselective synthesis of such structures[3-7]. Among the methodologies that have been devised, the transition-metal catalyzed asymmetric 1,1-diarylation of commercially available alkenes is one of the most straightforward and adjustable strategies for the synthesis of chiral compounds containing a 1,1-diarylalkane motif and has therefore attracted increasing attention[8,9]. The Sigman group first reported the enantioselective 1,1-

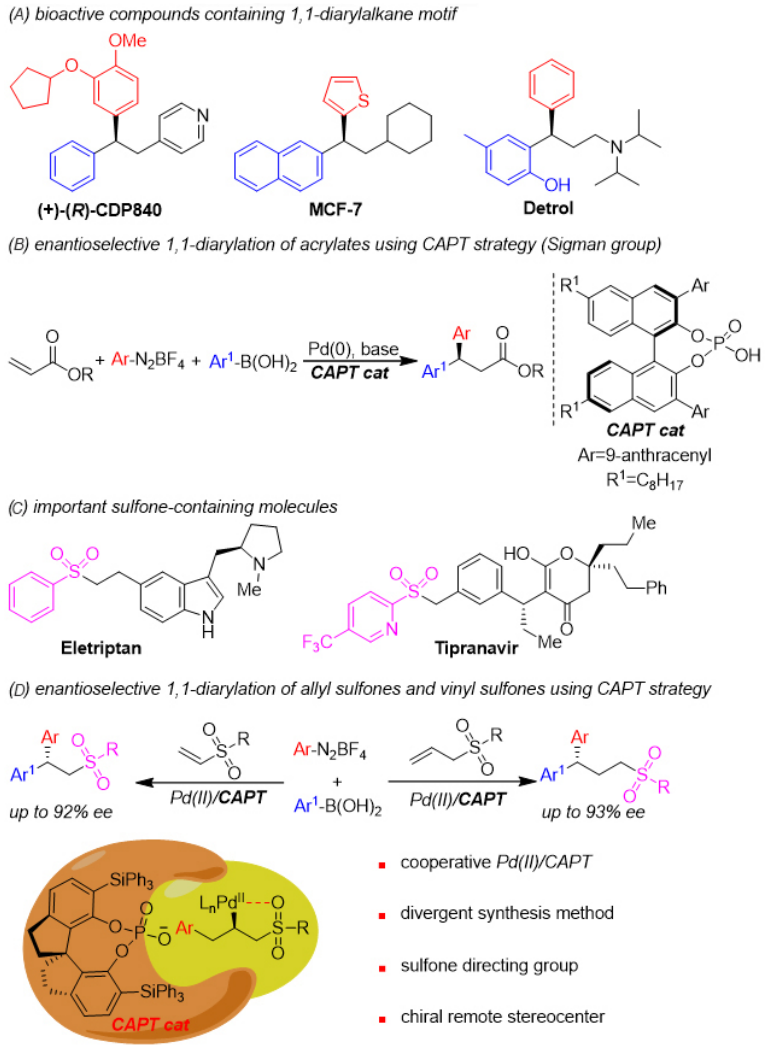

Scheme 1. Design of the enantioselective 1,1-diarylation of allyl sulfones and vinyl sulfones.

diarylation of acrylates based on a combination of palladium catalysis and chiral anion phase-transfer catalysis (*CAPT*) [Scheme 1B][10-14]. However, to the best of our knowledge, there has been no research concerning the catalytic asymmetric 1,1-diarylation of non-conjugated alkenes, which is more challenging because of the lower reactivity of these compounds and the complex requirements for regio- and enantioselectivity[15-17].

Sulfone groups are widely found in biologically active molecules [Scheme 1C][18-21]. Compounds containing these groups are also versatile synthetic intermediates because sulfones are easily transformed into a range of structurally diverse functional groups and can also function as flexible directing groups in various metal-catalyzed reactions to provide site- and enantioselective processes and control reactivity[22-26]. On this basis, we considered that sulfone groups might permit a high level of selectivity during catalytic asymmetric 1,1-diarylation. We aimed to synthesize the highly enantioselective 1,1-diarylation of allyl sulfones. This process involved two main challenges. First, allyl sulfones are less reactive than activated alkenes and so competitive reactions become more important. Examples include the traditional Heck reactions of alkene substrates and aryldiazonium salts[27-30] and the Suzuki reaction of aryldiazonium salts and arylboronic acids[16,31]. Second,

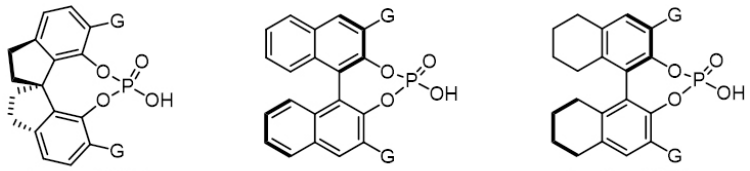

Figure 1. Some different chiral phosphoric acids.

the enantioselectivity control of this novel reaction process was expected to be more difficult. For these reasons, it was thought that a new catalysis system might be required. Herein, we report the highly enantioselective 1,1-diarylation of allylic sulfones using a new co-catalysis system comprising a chiral SPINOL-derived phosphoric acid and Pd_2dba_3. This methodology allows modular and direct access to chiral sulfones that contain a 1,1-diarylalkane motif and a remote stereocenter [Scheme 1D]. This new co-catalysis system was also found to be applicable to vinyl sulfones.

EXPERIMENTAL

In glovebox, **2a** (0.2 mmol), **3a** (0.2 mmol), **4a** (0.1 mmol), Pd_2dba_3 (3.7 mg, 0.004 mmol), (*R*)-**1a** (10.0 mg, 0.012 mmol), Rb_2CO_3 (69.3 mg, 0.3 mmol), anhydrous MTBE (2.0 mL) were added into an oven-dried tube (10 mL) charged with a stir bar, sealed the flask with its septum and then removed from the glovebox. The system was stirred for 48 h at 0 °C. After the reaction was completed (monitored by TLC), the crude reaction mixture was filtered through a short silica column with PE: EA = 1:2, and the solvent was removed in vacuo. An external standard (dibromomethane) was added to the system for determining NMR yields. Product **5a** was obtained by PTLC.

RESULTS AND DISCUSSION

In our initial study, allyl sulfone **2a** was chosen as a model substrate, while 4-methoxybenzene diazonium salt **3a** and phenylboronic acid **4a** were selected as model coupling partners. A series of careful screening trials were performed (see Supplementary Materials for details). As indicated in Scheme 2 and Table 1, entry 1, the desired product **5a** was obtained in 64% yield with 96:4 er when Pd_2dba_3 and chiral SPINOL-derived phosphoric acid (*R*)-**1a** [Figure 1] were used as the catalysts in the presence of Rb_2CO_3 in methyl *tert*-butyl ether (MTBE) at 0 °C. The use of a chiral phosphoric acid was vital to obtaining the desired reactivity and enantioselectivity during this transformation. When (*R*)-**1b** bearing a phenyl substituent was used instead of (*R*)-**1a**, **5a** was obtained in only 11% yield with 71:29 er (entry 2), with the remainder being the traditional Heck product. Replacing (*R*)-**1a** with chiral BINOL-derived phosphoric acid (*R*)-**1c** resulted in a reduction in both the yield and enantioselectivity (entry 3). It was found that the absolute configuration of product **5a** was reversed, which met the opposite axial chirality of (*R*)-BINOL **1c** and (*R*)-SPINOL **1a**. Similar results were obtained using (*R*)-**1e** (entry 5). Both lower yield and reduced enantioselectivity were observed when chiral BINOL-derived phosphoric acid (*R*)-**1d** and H_8-BINOL-derived (*R*)-**1f** were used (entries 4, 6) and the primary result was again the traditional Heck product. A series of different inorganic bases was subsequently examined in place of Rb_2CO_3 (entries 7-9). These trials indicated that the particular base that was used had a significant effect on the yield but only slightly modified the enantioselectivity. Using K_2CO_3 as a base gave similar results as obtained with the standard conditions, while employing Cs_2CO_3 or Na_2CO_3 led to an obvious reduction in yield. Using diethyl ether as the solvent, the enantioselectivity was lowered but not the yield (entry 10). Only a trace amount of **5a** was obtained when toluene was substituted as the solvent (entry 11). Product **5a** was obtained in 21% yield with 88:12 er when this reaction was performed at room temperature (entry 12).

Table 1. Reaction optimization[a]

Entry	Change from the "standard conditions"	Yield (%)[b]	er[c]
1	none	64	96:4
2	(*R*)-**1b** instead of (*R*)-**1a**	11	71:29
3	(*R*)-**1c** instead of (*R*)-**1a**	10	13:87
4	(*R*)-**1d** instead of (*R*)-**1a**	12	65:35
5	(*R*)-**1e** instead of (*R*)-**1a**	24	12:88
6	(*R*)-**1f** instead of (*R*)-**1a**	27	71:29
7	Cs_2CO_3 instead of Rb_2CO_3	51	96:4
8	K_2CO_3 instead of Rb_2CO_3	62	95:5
9	Na_2CO_3 instead of Rb_2CO_3	44	94:6
10	Et_2O instead of MTBE	66	90:10
11	toluene instead of MTBE	trace	-
12	rt instead of 0 ºC	21	88:12

[a]Unless otherwise noted, the reaction was conducted with **2a** (0.2 mmol), **3a** (0.2 mmol), **4a** (0.1 mmol), Rb_2CO_3 (0.3 mmol), (*R*)-**1a** (0.012 mmol) and Pd_2dba_3 (0.004 mmol) in MTBE (2 mL) at 0 ºC for 48 h under Ar. [b]Isolated yields. [c]All er values were determined by SFC.

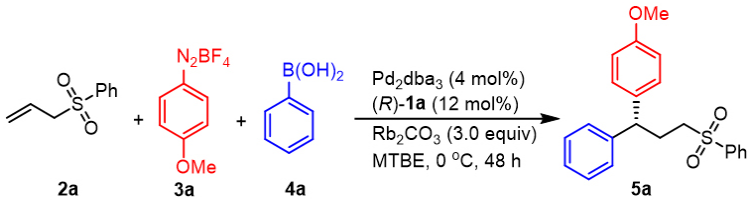

Scheme 2. The standard conditions of the catalytic asymmetric 1,1-diarylation of allylic sulfone.

Taking advantage of the optimized conditions, the reaction scope was first examined with a variety of arylboronic acids. In general, all arylboronic acids gave the desired product in a moderate yield with moderate to high levels of enantioselectivity [Scheme 3]. We found that the presence of methyl or fluorine groups at the 4-position of the phenyl ring slightly affected the yield and enantioselectivity, while electron-deficient substituents such as chlorine, ester and trifluoromethyl groups resulted in decreased yields and enantioselectivities (**5b**-**5f**). The reaction was also found to proceed with (4-hydroxyphenyl) boronic acid, giving the desired product **5g** in 96.5:3.5 er, albeit with a yield of 27%. Following these trials, phenylboronic acids bearing *meta* substituents such as methoxy and methyl groups were also applied to this reaction, and the corresponding products were obtained with moderate yields and high enantioselectivities (**5h**-**5i**). Interestingly, *ortho*-tolylboronic acid also worked well in this protocol, yielding product **5j** in 62% yield and 96:4 er. A multi-substituted phenylboronic acid was applied to this system and provided product **5k** with a high level of enantioselectivity. Naphthalen-2-ylboronic acid was also a suitable coupling partner and delivered product **5l** in 53% yield with 95.5:4.5 er. It is worth noting that a series of (heter)arylboronic acids were also examined in this reaction. In these trials, product **5m** was obtained in 60% yield with 86.5:13.5 er, while products **5n** and **5o** were generated in lower yields with moderate enantioselectivities (More results about (hetero)arylboronic acids, please see SI). Following the experiments described above, the reaction scope was examined by assessing different aryldiazonium salts (**5p**-**5s**). Changing the substituent of the model coupling partner **3a** from a methoxy to a benzyloxy group maintained high enantioselectivity and also gave a moderate yield. It should be noted that the absolute configuration of **5p** was assigned by X-ray crystallography[32]. It was also determined that the *meta*-methoxybenzene diazonium salt was compatible with this reaction, giving product **5q** with 40% yield and 95.5:4.5 er. In addition, using ethyl ether as the

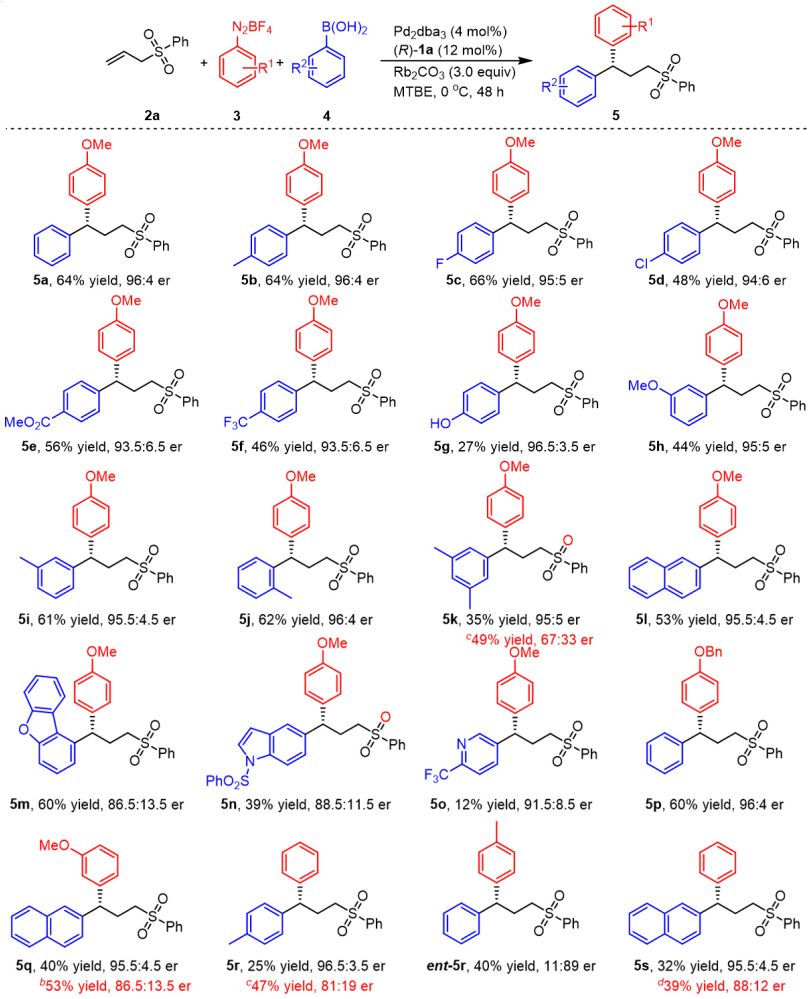

Scheme 3. Scope of arylboronic acids and aryldiazonium salts[a]. [a]Unless otherwise noted, the reaction was conducted with **2a** (0.2 mmol), **3** (0.2 mmol), **4** (0.1 mmol), Rb_2CO_3 (0.3 mmol), (*R*)-**1a** (0.012 mmol) and Pd_2dba_3 (0.004 mmol) in MTBE (2 mL) at 0 ºC for 48 h under Ar. Isolated yields are shown. The er values were determined by SFC. [b]Et_2O was used instead of MTBE as the solvent. [c]Guanidine carbonate was used instead of Rb_2CO_3. [d]Guanidine carbonate (1.0 equiv) and Rb_2CO_3 (1.0 equiv) were used instead.

solvent, product **5q** was produced in 53% yield with a lower er value. In further trials, *para*-tolylboronic acid and naphthalen-2-ylboronic acid were employed as coupling partners, and the corresponding products **5r** and **5s** were generated in moderate yields with good enantioselectivities. As expected, when the phenyl diazonium salt and 4-methylboronic acid were used as coupling partners, product *ent*-**5r** was obtained in 40% yield with 11:89 er. These results indicate that the range of aryldiazonium salts applicable to this process is relatively limited.

To further extend the scope of this reaction, we subsequently explored various allyl sulfone substrates [Scheme 4]. The steric effects of phenyl ring substituents were initially examined. A methyl group at the 4-position of the phenyl moiety was found not to affect the yield or enantioselectivity, while a tertiary butyl group decreased the yield (**5t**-**5u**). The electronic effect of substituents was also evaluated. Both an electron-rich methoxy substituent and electron-poor substituents such as fluorine, ester and trifluoromethyl groups slightly decreased the yield and enantioselectivity (**5v**-**5y**). Substrates bearing *meta*-methoxy-phenyl, 3,5-dichlorophenyl and 1-naphthyl moieties were also examined. In each case, the corresponding product was obtained with moderate efficiency and a high level of enantioselectivity (**5z**-**5ab**). However, a substrate with

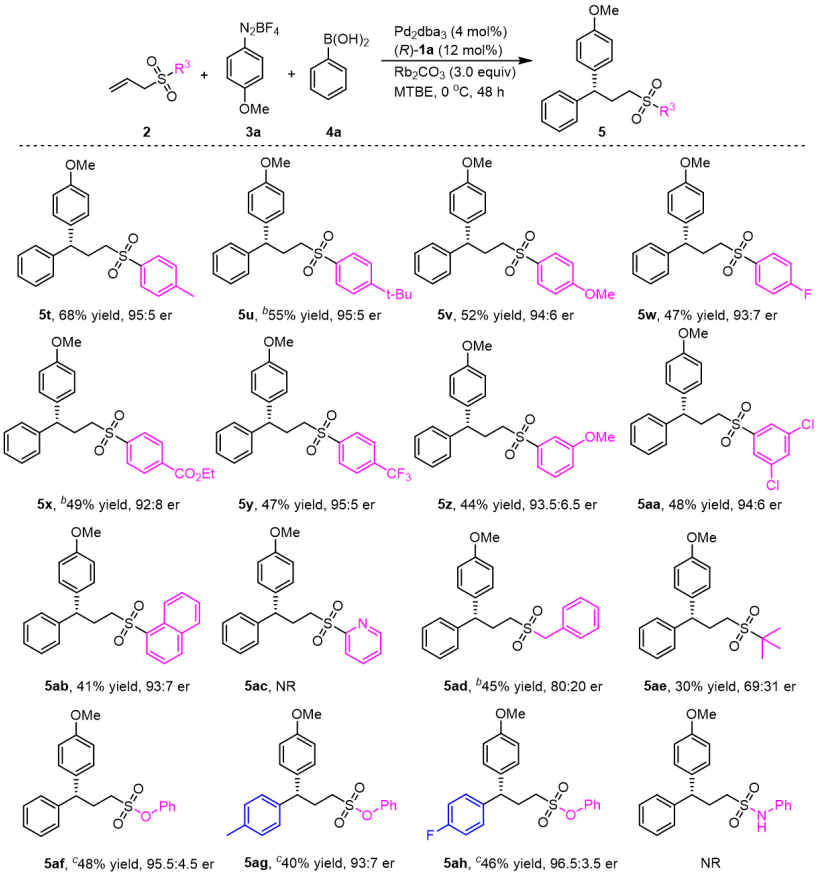

Scheme 4. Scope of allylic sulfones[a]. [a]Unless otherwise noted, the reaction was conducted with **2** (0.2 mmol), **3a** (0.2 mmol), **4a** (0.1 mmol), Rb_2CO_3 (0.3 mmol), (*R*)-**1a** (0.012 mmol) and Pd_2dba_3 (0.004 mmol) in MTBE (2 mL) at 0 ºC for 48 h under Ar. Isolated yields are shown. The er values were determined by SFC. [b]The reaction was performed at 10 ºC. [c]Cs_2CO_3 was used instead of Rb_2CO_3.

a SO_2Py group did not give the desired product (**5ac**), presumably because the pyridine group strongly coordinated with the palladium to suppress the reaction. Additionally, the use of alkyl groups, such as benzyl and tertiary butyl groups, instead of the phenyl group resulted in significant decreases in yield and enantioselectivity (**5ad**-**5ae**). From these data, it is evident that the sulfone group was a vital aspect of obtaining enantioselectivity and reactivity control. To our delight, allyl sulfonates were also suitable for this reaction. The products **5af**-**5ah** were always obtained in moderate yields with high enantioselectivities. As expected, allyl sulfonamide suppressed the transformation.

Because chiral β,β-diaryl sulfones can be readily transformed into bioactive pharmaceutical molecules such as (*R*)-CDP-840 and (*R*)-MCF-7[33,34], the extension of this catalytic system to the 1,1-diarylation of vinyl sulfones was investigated. The desired product **7a** was obtained in a 67% yield and with 95:5 er from the reaction of vinyl sulfone **6a**, 4-methoxybenzene diazonium salt **3a** and phenylboronic acid **4a**, using Cs_2CO_3 instead of Rb_2CO_3 [Scheme 5]. Following this, a number of arylboronic acids were applied to the reaction and the corresponding products were obtained in moderate yields with high enantioselectivities (**7b**-**7f**). It is of note that *ortho*-tolylboronic acid was also suitable for this protocol and gave product **7e** in 45% yield and 96:4 er. Phenyl aryldiazonium salt was employed in this reaction and product **7g** was obtained in 45% yield and 93.5:6.5 er. The absolute configuration of (*S*)-**7g** was determined by comparison with optical rotation data for the reported literature[26]. Likewise, the product **7h** was obtained in 30% yield with 96:4 er using vinyl sulfonate as the substrate. Finally, product *ent*-**7a** was produced in moderate yield with good

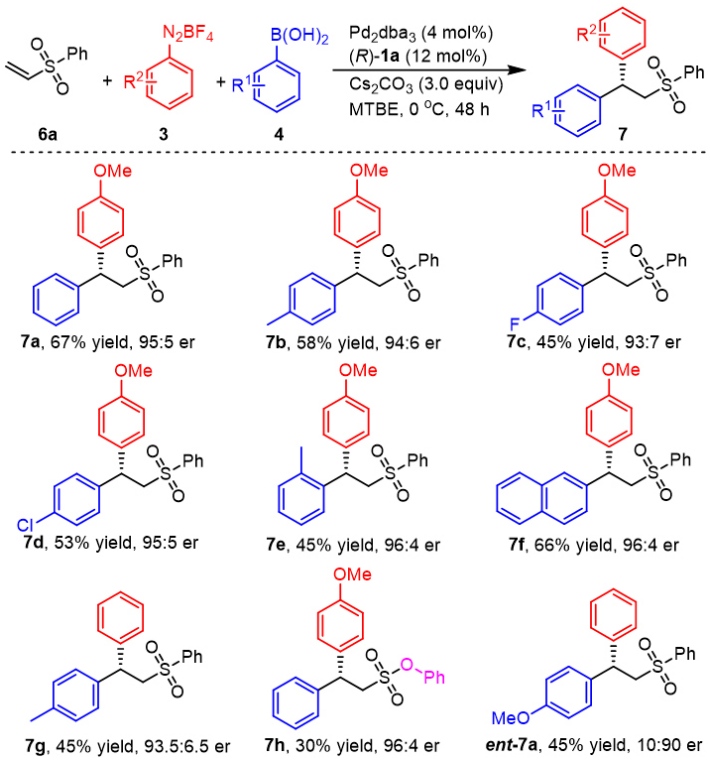

Scheme 5. Scopes of arylboronic acids and aryldiazonium salts[a]. [a]Unless otherwise noted, the reaction was conducted with **6a** (0.2 mmol), **3** (0.2 mmol), **4** (0.1 mmol), Cs_2CO_3 (0.3 mmol), (*R*)-**1a** (0.012 mmol) and Pd_2dba_3 (0.004 mmol) in MTBE (2 mL) at 0 ºC for 48 h under Ar. Isolated yields are shown. The er values were determined by SFC.

enantioselectivity.

The origin of the high enantioselectivities obtained from this reaction and the effect of the sulfone group were explored by carrying out the reaction using several different substrates [Scheme 6A]. These trials showed that increasing the length of the carbon chain between the sulfone group and the double bond greatly affected the yield and enantioselectivity (**5ai**-**5aj**). The reaction was also inhibited upon changing from a sulfone group to either a sulfoxide or thioether group (**5ak**, **5al**). Additionally, the reaction was suppressed after substituting a sulfoxide or thioether group for the sulfone (**5ak**, **5al**), possibly because of the strong coordination effects of the sulfoxide and thioether groups. When but-3-en-1-ylbenzene was used instead of **2a**, product **5am** was only obtained in 17% yield and 72:28 er. On the basis of these results, we suggest that the sulfone moiety serves as a directing group during this reaction. An internal alkene substrate was also tested, and the desired product **5an**, bearing a quaternary carbon center, was obtained in only a 20% yield with just a 63.5:36.5 er value. Thus, a terminal double bond is essential for high enantioselectivity. The effects of the boronic acid group on the reactivity and enantioselectivity of this process were first assessed by using esterified phenylboronic acid **9a** instead of phenylboronic acid and no desired product **5a** was obtained [Scheme 6B]. Product **5a** was obtained in 37% yield with 88:12 er [Scheme 6C]. The negative results established that the standard boronic acid group was crucial to this reaction. The use of $Pd(OAc)_2$ instead of Pd_2dba_3 as the catalyst afforded the desired product **5a** with 96:4 er, suggesting that the dba moieties did not participate in the asymmetric catalytic reaction [Scheme 6D]. Because the mass balance was the traditional Heck product **8a** in this transformation, this compound was employed as the starting material in a subsequent trial with the standard reaction conditions. The desired product **5a** was not obtained [Scheme 6E]. As shown in Scheme 6F, a cross-over experiment was further performed, but no

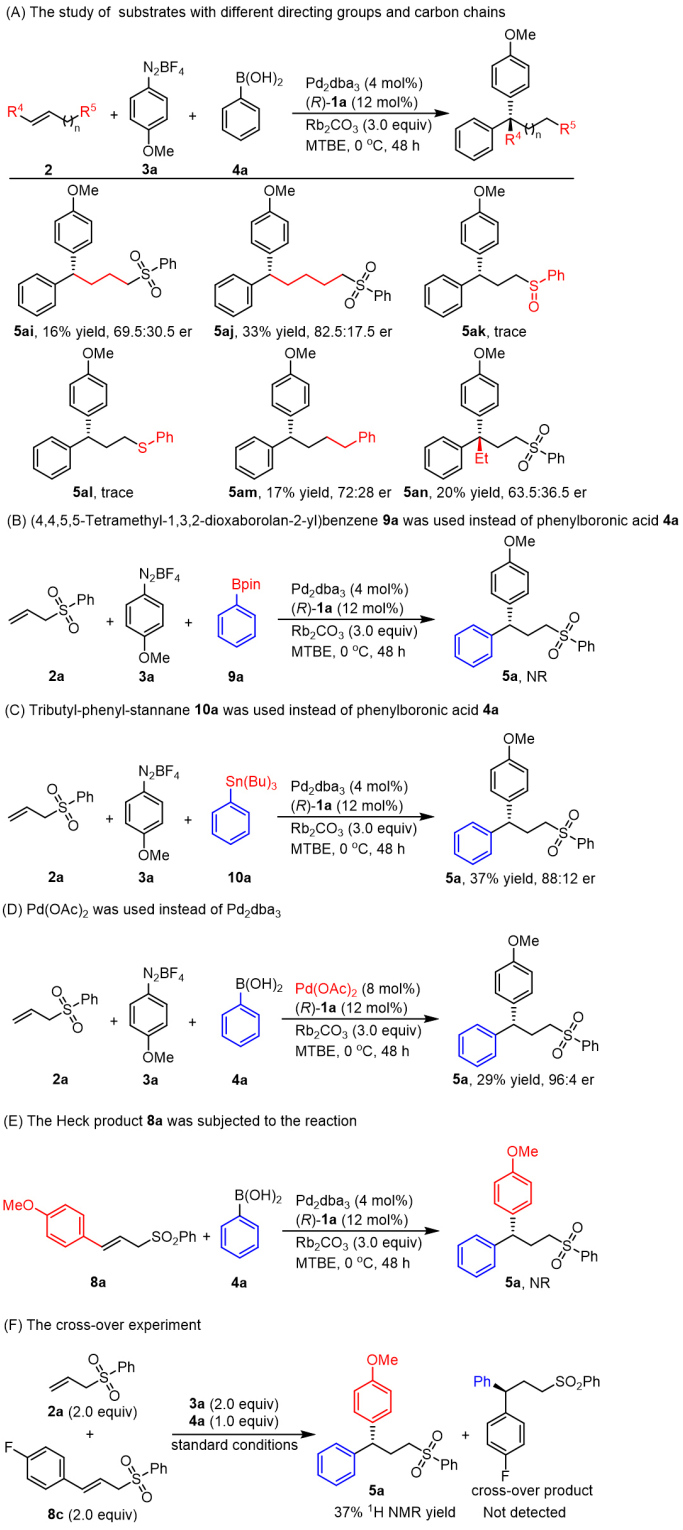

Scheme 6. Mechanistic studies.

cross-over product was obtained. Based on these observations, we believe that the Heck product was unable to participate in subsequent reactions with the arylboronic acid to form the 1,1-diarylation product.

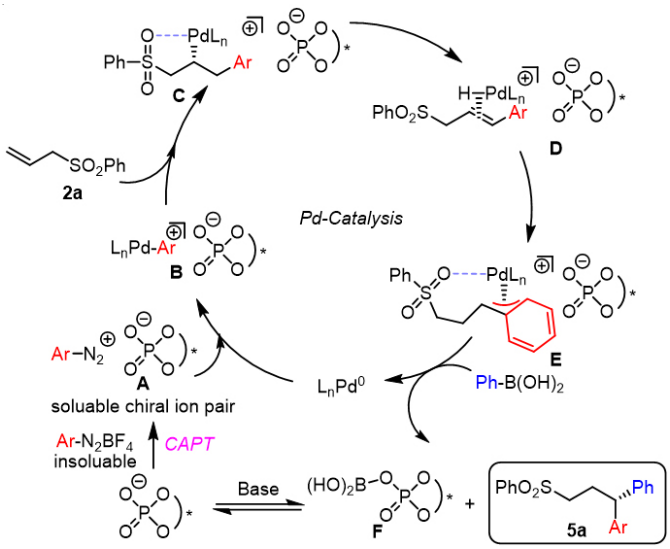

Scheme 7. Proposed catalytic cycle. CAPT: Chiral anion phase-transfer catalysis.

Based on these experimental results and previous work[10], a possible mechanism for the catalytic cycle was devised [Scheme 7]. In this mechanism, soluble chiral ion pair **A** is first generated from a chiral phosphate anion and the insoluble tetrafluoroborate aryldiazonium salt in the presence of Rb_2CO_3. Cationic Pd-aryl intermediate **B** is then formed via the oxidative addition of **A** in conjunction with Pd_2dba_3 and subsequently undergoes an enantioselective migratory insertion of **2a** to form intermediate **C**. Intermediate **E** is generated from **C** through β-hydride elimination and reinsertion. Finally, **E** reacts with phenylboronic acid **4a**, followed by reductive elimination, forming 1,1-diarylation product **5a**.

CONCLUSION

In conclusion, this work demonstrated the enantioselective 1,1-diarylation of allyl sulfones using a cooperative strategy based on a chiral SPINOL-derived phosphoric acid and Pd_2dba_3. This newly developed cooperative catalysis was also applied to the asymmetric 1,1-diarylation of vinyl sulfones. This catalytic system allows for the rapid construction of a variety of chiral sulfones containing a 1,1-diarylalkane motif and a remote stereocenter. Interestingly, we discovered that the sulfone group can function as a directing group and is important for achieving enantioselectivity and reactivity control. The investigation of detailed mechanisms and cooperative catalysis as a means of synthesizing other useful compounds is ongoing in our laboratory.

DECLARATIONS

Acknowledgments

We gratefully thank Prof. Changkun Li and Prof. Xiaohong Huo, Yicong Luo (Shanghai Jiao Tong University) for helpful suggestions and comments on this manuscript.

Authors' contributions

Designing the experiments, writing the manuscript, and being responsible for the whole work: Chen ZM
Performing the experiments: Ji K, Huang J
Synthesizing the substrates: Ji K, Huang J, Zhang XY

Availability of data and materials
Not applicable.

Financial support and sponsorship
We thank the NSFC (grant nos. 21871178 and 22071149) and the STCSM (grant no. 19JC1430100) for financial support. This research was also supported by The Program for Professor of Special Appointment (Eastern Scholar) at Shanghai Institutions of Higher Learning.

Conflicts of interest
All authors declared that there are no conflicts of interest.

Ethical approval and consent to participate
Not applicable.

Consent for publication
Not applicable.

REFERENCES
1. Ameen D, Snape TJ. Chiral 1,1-diaryl compounds as important pharmacophores. *Med Chem Commun* 2013;4:893. DOI
2. Malhotra B, Gandelman K, Sachse R, Wood N, Michel MC. The design and development of fesoterodine as a prodrug of 5-hydroxymethyl tolterodine (5-HMT), the active metabolite of tolterodine. *Curr Med Chem* 2009;16:4481-9. DOI PubMed
3. Wang H, Tong HR, He G, Chen G. An enantioselective bidentate auxiliary directed palladium-catalyzed benzylic C-H arylation of amines using a BINOL phosphate ligand. *Angew Chem Int Ed Engl* 2016;55:15387-91. DOI PubMed
4. Zhang W, Wu L, Chen P, Liu G. Enantioselective arylation of benzylic C-H bonds by copper-catalyzed radical relay. *Angew Chem Int Ed Engl* 2019;58:6425-9. DOI PubMed
5. Wu L, Wang F, Wan X, Wang D, Chen P, Liu G. Asymmetric Cu-catalyzed intermolecular trifluoromethylarylation of styrenes: enantioselective arylation of benzylic radicals. *J Am Chem Soc* 2017;139:2904-7. DOI PubMed
6. Wang D, Wu L, Wang F, et al. Asymmetric copper-catalyzed intermolecular aminoarylation of styrenes: efficient access to optical 2,2-diarylethylamines. *J Am Chem Soc* 2017;139:6811-4. DOI PubMed
7. Yin Y, Dai Y, Jia H, et al. Conjugate addition-enantioselective protonation of N-aryl glycines to α-branched 2-vinylazaarenes via cooperative photoredox and asymmetric catalysis. *J Am Chem Soc* 2018;140:6083-7. DOI PubMed
8. Belal M, Li Z, Lu X, Yin G. Recent advances in the synthesis of 1,1-diarylalkanes by transition-metal catalysis. *Sci China Chem* 2021;64:513-33. DOI
9. Li Y, Wu D, Cheng HG, Yin G. Difunctionalization of alkenes involving metal migration. *Angew Chem Int Ed Engl* 2020;59:7990-8003. DOI PubMed
10. Yamamoto E, Hilton MJ, Orlandi M, Saini V, Toste FD, Sigman MS. Development and analysis of a Pd(0)-catalyzed enantioselective 1,1-diarylation of acrylates enabled by chiral anion phase transfer. *J Am Chem Soc* 2016;138:15877-80. DOI PubMed PMC
11. Orlandi M, Hilton MJ, Yamamoto E, Toste FD, Sigman MS. Mechanistic investigations of the Pd(0)-catalyzed enantioselective 1,1-diarylation of benzyl acrylates. *J Am Chem Soc* 2017;139:12688-95. DOI PubMed PMC
12. Mukherjee S, List B. Chiral counteranions in asymmetric transition-metal catalysis: highly enantioselective Pd/Brønsted acid-catalyzed direct alpha-allylation of aldehydes. *J Am Chem Soc* 2007;129:11336-7. DOI PubMed
13. Mahlau M, List B. Asymmetric counteranion-directed catalysis: concept, definition, and applications. *Angew Chem Int Ed Engl* 2013;52:518-33. DOI PubMed
14. Ohmatsu K, Ito M, Kunieda T, Ooi T. Ion-paired chiral ligands for asymmetric palladium catalysis. *Nat Chem* 2012;4:473-7. DOI PubMed
15. Urkalan KB, Sigman MS. Palladium-catalyzed oxidative intermolecular difunctionalization of terminal alkenes with organostannanes and molecular oxygen. *Angew Chem Int Ed Engl* 2009;48:3146-9. DOI PubMed PMC
16. Saini V, Liao L, Wang Q, Jana R, Sigman MS. Pd(0)-catalyzed 1,1-diarylation of ethylene and allylic carbonates. *Org Lett* 2013;15:5008-11. DOI PubMed PMC
17. Li Z, Wu D, Ding C, Yin G. Modular synthesis of diarylalkanes by nickel-catalyzed 1,1-diarylation of unactivated terminal alkenes. *CCS Chem* 2021;3:576-82. DOI
18. Ilardi EA, Vitaku E, Njardarson JT. Data-mining for sulfur and fluorine: an evaluation of pharmaceuticals to reveal opportunities for

drug design and discovery. *J Med Chem* 2014;57:2832-42. DOI PubMed

19. Feng M, Tang B, Liang SH, Jiang X. Sulfur containing scaffolds in drugs: synthesis and application in medicinal chemistry. *Curr Top Med Chem* 2016;16:1200-16. DOI PubMed PMC
20. Scott KA, Njardarson JT. Analysis of US FDA-approved drugs containing sulfur atoms. *Top Curr Chem (Cham)* 2018;376:5. DOI PubMed
21. Giannetti AM, Wong H, Dijkgraaf GJ, et al. Identification, characterization, and implications of species-dependent plasma protein binding for the oral Hedgehog pathway inhibitor vismodegib (GDC-0449). *J Med Chem* 2011;54:2592-601. DOI PubMed
22. Tsui GC, Lautens M. Linear-selective rhodium(I)-catalyzed addition of arylboronic acids to allyl sulfones. *Angew Chem Int Ed Engl* 2010;49:8938-41. DOI PubMed
23. Nishimura T, Takiguchi Y, Hayashi T. Effect of chiral diene ligands in rhodium-catalyzed asymmetric addition of arylboronic acids to α,β-unsaturated sulfonyl compounds. *J Am Chem Soc* 2012;134:9086-9. DOI PubMed
24. So CM, Kume S, Hayashi T. Rhodium-catalyzed asymmetric hydroarylation of 3-pyrrolines giving 3-arylpyrrolidines: protonation as a key step. *J Am Chem Soc* 2013;135:10990-3. DOI PubMed
25. Lim KM, Hayashi T. Rhodium-catalyzed asymmetric arylation of allyl sulfones under the conditions of isomerization into alkenyl sulfones. *J Am Chem Soc* 2015;137:3201-4. DOI PubMed
26. Yan Q, Xiao G, Wang Y, Zi G, Zhang Z, Hou G. Highly efficient enantioselective synthesis of chiral sulfones by Rh-catalyzed asymmetric hydrogenation. *J Am Chem Soc* 2019;141:1749-56. DOI PubMed
27. Oxtoby LJ, Gurak JA Jr, Wisniewski SR, Eastgate MD, Engle KM. Palladium-catalyzed reductive heck coupling of alkenes. *Trends Chem* 2019;1:572-87. DOI PubMed PMC
28. Tao ZL, Adili A, Shen HC, Han ZY, Gong LZ. Catalytic enantioselective assembly of homoallylic alcohols from dienes, aryldiazonium salts, and aldehydes. *Angew Chem Int Ed Engl* 2016;55:4322-6. DOI PubMed
29. Zhang T, Li WA, Shen HC, Chen SS, Han ZY. Chiral-anion-mediated asymmetric heck-matsuda reaction of acyclic alkenyl alcohols. *Org Lett* 2021;23:1473-7. DOI PubMed
30. Werner EW, Sigman MS. Operationally simple and highly (E)-styrenyl-selective Heck reactions of electronically nonbiased olefins. *J Am Chem Soc* 2011;133:9692-5. DOI PubMed PMC
31. Zong Y, Hu J, Sun P, Jiang X. Synthesis of biaryl derivatives via a magnetic Pd-NPs-catalyzed one-pot diazotization - cross-coupling reaction. *Synlett* 2012;23:2393-6. DOI
32. CCDC 2152365 (**5p**) contains the supplementary crystallographic data for this paper. More detail, see supporting information chapter 6. The data can be obtained free of charge from The Cambridge Crystallographic Data Centre. Available from: www.ccdc.cam.ac.uk/structures [Last accessed on 12 Oct 2022].
33. Lin Y, Kuo Y, Kuei C, Chang M. Palladium-mediated synthesis of 1,1,2-triarylethanes. Application to the synthesis of CDP-840. *Tetrahedron* 2017;73:1275-82. DOI
34. Liang Q, Walsh PJ, Jia T. Copper-catalyzed intermolecular difunctionalization of styrenes with thiosulfonates and arylboronic acids via a radical relay pathway. *ACS Catal* 2020;10:2633-9. DOI

Liu *et al. Chem Synth* 2022;2:18
DOI: 10.20517/cs.2022.17

Chemical Synthesis

Short Communication

Open Access

β-cyclodextrin mediated construction of porous helical nanoribbons from oligoaniline derivatives

Si Yu Liu[1], Qing Qing Sun[1,*], Peng Yuan Hang[1], Xiao Huan Sun[1,*], Chuan Qiang Zhou[2], Jie Han[1,*], Rong Guo[1]

[1]School of Chemistry and Chemical Engineering, Yangzhou University, Yangzhou 225002, Jiangsu, China.
[2]Testing Center, Yangzhou University, Yangzhou 225002, Jiangsu, China.

***Correspondence to:** Dr. Qing Qing Sun, School of Chemistry and Chemical Engineering, Yangzhou University, 180 Siwangting Road, Yangzhou 225002, Jiangsu, China. E-mail: sunqingqing@yzu.edu.cn; Prof. Xiao Huan Sun, School of Chemistry and Chemical Engineering, Yangzhou University, 180 Siwangting Road, Yangzhou 225002, Jiangsu, China. E-mail: xhuansun@yzu.edu.cn; Prof. Jie Han, School of Chemistry and Chemical Engineering, Yangzhou University, 180 Siwangting Road, Yangzhou 225002, Jiangsu, China. E-mail: hanjie@yzu.edu.cn

How to cite this article: Liu SY, Sun QQ, Hang PY, Sun XH, Zhou CQ, Han J, Guo R. *β*-cyclodextrin mediated construction of porous helical nanoribbons from oligoaniline derivatives. *Chem Synth* 2022;2:18. https://dx.doi.org/10.20517/cs.2022.17

Received: 13 Aug 2022 **First Decision:** 29 Sep 2022 **Revised:** 8 Oct 2022 **Accepted:** 26 Oct 2022 **Published:** 31 Oct 2022

Academic Editor: Bao-Lian Su **Copy Editor:** Peng-Juan Wen **Production Editor:** Peng-Juan Wen

Abstract

A novel supramolecular self-assembly nanostructure of porous helical nanoribbons (PHNRs) was developed. PHNRs from oligoaniline derivatives were fabricated through the chemical oxidation of aniline in an *i*-propanol/water mixture as mediated by *β*-cyclodextrin (*β*-CD). The role of *β*-CD was considered vital through the modulation of the addition time point of *β*-CD and the molar ratio of *β*-CD/aniline. In addition, at the early stage of polymerization, the host-guest complex between oligoaniline and *β*-CD was formed, which was involved in the initial supramolecular assembly process. However, with the reorganization of the oligoaniline assemblies during the polymerization time, the abscission of *β*-CD from the helical nanoribbons was observed, which eventually induced the formation of PHNRs. We believe the supramolecular host-modulated assembly strategy presented herein will be instructive for the fabrication of porous supramolecular nanostructures.

Keywords: *β*-CD, oligoaniline derivatives, supramolecular assembly, porous helical nanoribbons

INTRODUCTION

Supramolecular nanostructures have emerged as promising materials in the field of drug delivery[1], catalysis[2], sensing[3], and luminescence[4]. In their construction, the self-assembly strategy has been

extensively used since it can afford unique hierarchical nanostructures through noncovalent interactions, such as hydrogen bonding, van der Waals interactions, and electrostatic interactions[5]. Owing to the reversible and dynamic nature of the noncovalent interactions, supramolecular nanostructures can be manipulated by other external stimuli, including solvent[6], light[7], and even extra components, such as host molecules[8], which can be employed to induce the reorganization of guest molecules and promote the achievement of diverse supramolecular nanostructures.

Cyclodextrin (CD), a typical host molecule with a hydrophobic cavity, is considered as an excellent candidate for the regulation of supramolecular structures. Sun and co-workers reported the photo-controlled morphology switch from nanoparticle to nanotube through the modulation of a *β*-CD-based host-guest complex[9]. It was also demonstrated that, during the RAFT dispersion polymerization of styrene, the introduction of CD can direct the controllable fabrication of spheres, worms, lamellae, and nanotubes[10]. However, the development of novel nanostructures, such as porous ones, remains a challenge.

Recently, we reported the fabrication of supramolecular helical nanoribbons from oligoaniline derivatives via the chemical oxidation of aniline in an alcohol/water mixture[11]. Inspired by the controllable self-assembly capability of oligoaniline, and taking into account that *β*-CD is suitable for the inclusion of oligoaniline, a novel supramolecular self-assembly nanostructure of porous helical nanoribbons (PHNRs) was developed. PHNRs from oligoaniline derivatives were fabricated through the chemical oxidation of aniline in an *i*-propanol/water mixture as mediated by *β*-cyclodextrin (*β*-CD). At the early stage of the polymerization of aniline, a supramolecular complex was formed between *β*-CD and tri-aniline derivatives and involved in the initial assembly of spindle nanoflakes. However, according to the morphological evolution of *β*-CD mediated oligoaniline assemblies, the combination of *β*-CD abscission from the helical nanoribbons and the reorganization of oligoanilines along with polymerization time eventually led to the formation of PHNRs [Scheme 1].

RESULTS AND DISCUSSION

β-CD mediated construction of PHNRs

According to our previous report, helical nanoribbons can be prepared from oligoaniline derivatives through the chemical oxidative polymerization of aniline in an *i*-propanol/water mixture, where right- or left-handed helical nanoribbons of oligoaniline derivatives can be obtained by controlling the *i*-propanol content of the mixed solution[11]. Inspired by the controllable self-assembly performance of oligoaniline, and taking into account that oligoaniline can form a host-guest inclusion complex with *β*-CD, *β*-CD was employed to further manipulate the supramolecular assembly process of oligoaniline. Specifically, aniline was oxidized using ammonium peroxodisulfate (APS) as an oxidant in an *i*-propanol/water mixture, where the *i*-propanol content at 40% was chosen as a typical example for the fabrication of helical nanoribbons of oligoaniline[12]. At the point of 4 min of polymerization, *β*-CD, of which the molar amount was kept the same as aniline, was added, and the reaction mixture was left for 12 h at 25 °C. After that, the product was centrifugated and washed with deionized water. Finally, the resulting solid was dried to afford the target black powder.

The morphology of the synthesized product was investigated using field emission scanning electron microscope (FESEM) and transmission electron microscope (TEM). As shown in Figure 1A-C, in the absence of *β*-CD, highly uniform and dense 1D helical nanoribbons with several microns in length were observed in both FESEM and TEM images, which is in high agreement with our previous report[11]. By contrast, surprisingly, when mediated by *β*-CD, the helical nanoribbons obtained were porous [Figure 1D-F and Supplementary Figure 1], with an almost unchanged size. These results indicate that *β*-CD participated

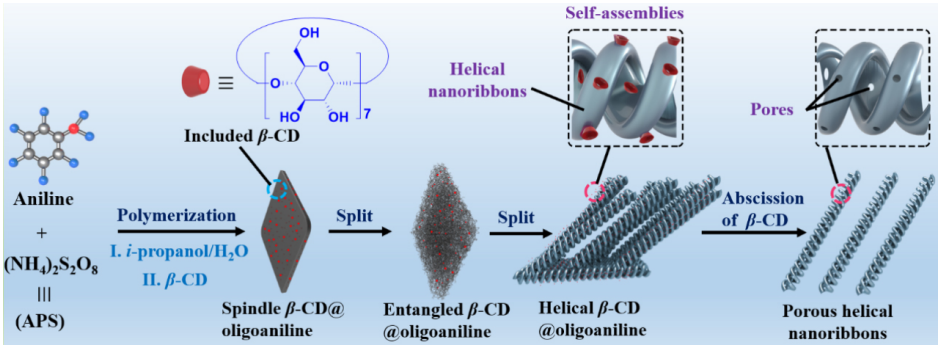

Scheme 1. Schematic illustration of the β-CD mediated formation of porous helical nanoribbons. The chemical structures of aniline and ammonium peroxodisulfate, as well as β-cyclodextrin, are presented. β-CD: β-cyclodextrin.

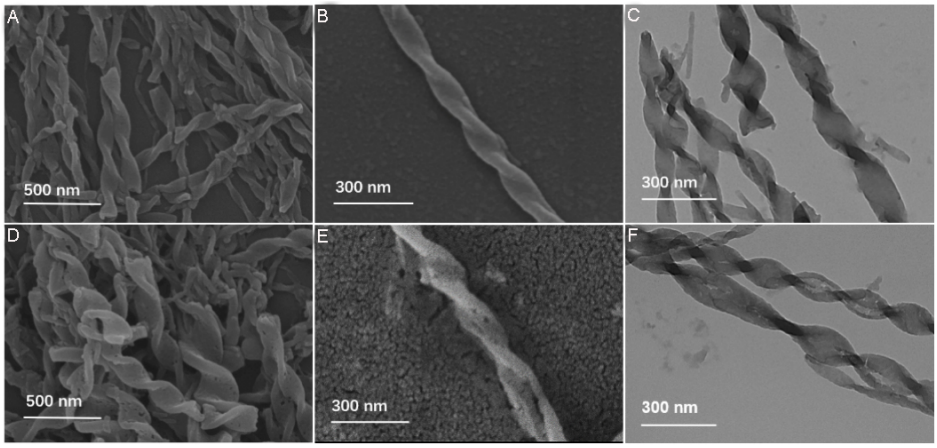

Figure 1. (A-E) FESEM and (C and F) TEM images of helical nanostructures synthesized (A-C) in the absence of β-CD and (D-F) in the presence of β-CD. FESEM: Field emission scanning electron microscope; TEM: transmission electron microscope; β-CD: β-cyclodextrin.

in the assembly process of oligoaniline and played a dominating role in the formation of porous helical nanoribbons (PHNRs).

The time point for the addition of β-CD during the polymerization of aniline was considered to be important for the fabrication of PHNRs. To verify this assumption, synthesis experiments were carried out on the modulation of the addition time of β-CD. The morphologies of the products obtained under different conditions were investigated by TEM. Interestingly, helical nanoribbons bearing large and relative uniform pore channels were observed upon the addition of β-CD at 4 min of polymerization [Figure 2B]. By contrast, the introduction of β-CD at shorter (1 min) [Figure 2A] and longer polymerization times (9 min) [Figure 2C] showed helical nanoribbons featuring small pore size and nonporous morphologies, respectively. According to the above results, it is logical to speculate that the dominating product at 1, 4, and 9 min of polymerization was different, and β-CD exhibited stronger binding capability towards the product formed at 4 min of polymerization of aniline. This deduction was supported by the UV-vis experiments. As shown in Supplementary Figure 2, the addition of 1 equiv. of β-CD at 1 min polymerization induced the observation of a singlet peak at 281 nm, which was ascribed to the monomer aniline. Remarkably, the absorption peak at 281 nm experienced an obvious decrease along with the appearance of a new peak at 374 nm after the addition of 1 equiv. of β-CD at 4 min polymerization. We assigned this new peak as oligoaniline[12]. The addition of β-CD at a longer polymerization time (9 min) led to the slight diminishment

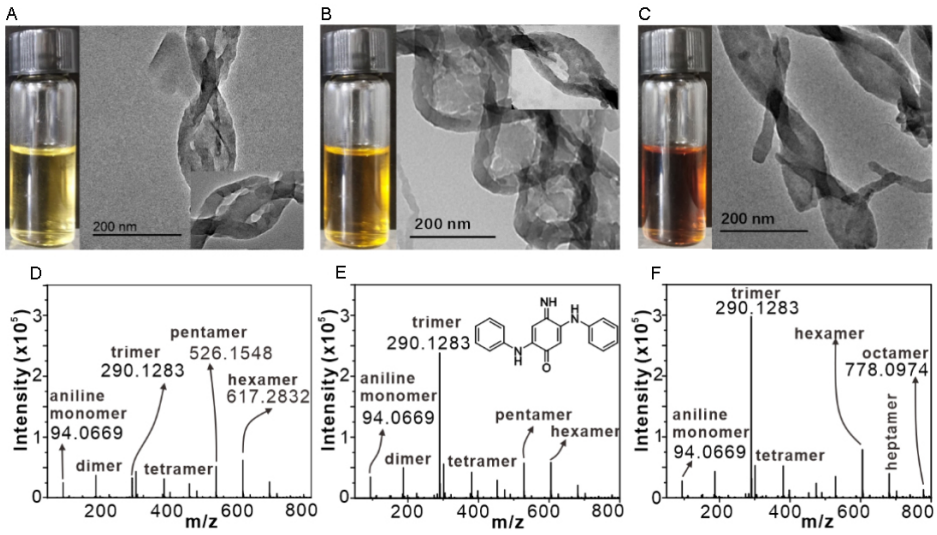

Figure 2. (A-C) (Left) Photographs of the polymerization mixture at the polymerization times of: (A) 1 min; (B) 4 min; and (C) 9 min. (Right) TEM images of *β*-CD mediated nanostructures assembled from oligoaniline for 12 h with the addition of *β*-CD at different polymerization times: (A) 1 min; (B) 4 min; and (C) 9 min. (A and B) (Inset) Magnified TEM images. (D-F) High-resolution mass spectra (HRMS with ESI mode) of the polymerization mixture at the polymerization times of: (D) 1 min; (E) 4 min; and (F) 9 min. Note that the aniline monomer and its oligomers (oligoaniline derivatives), such as dimer, trimer, tetramer, pentamer, hexamer, heptamer, and octamer, are carefully labeled in (D-F). TEM: Transmission electron microscope; *β*-CD: *β*-cyclodextrin; HRMS: high-resolution mass spectrometry.

of the aniline absorption and gradual enhancement of oligoaniline. This result not only illustrates the binding events between *β*-CD and oligoaniline formed at different polymerization times but also substantiates the importance of the additional time point of *β*-CD to the construction of porous nanostructures. Thus, the colors of the solutions obtained at different polymerization stages were also observed. The color changed from pale yellow to dark brown over time, as shown in Figure 2A-C (inset), which clearly confirmed the different polymerization degrees.

To further verify the possible structure of the oligoaniline obtained at different polymerization times, the mixtures from different polymerization times were investigated using high-resolution mass spectrometry (HRMS with ESI mode; Figure 2D-F and Supplementary Figure 3, Supplementary Table 1). The mass spectrum showed multiple ion peaks consistent with various oligoaniline derivatives for the sample that was polymerized for 1 min [Figure 2D]. Typically, an intense ion peak at m/z = 290.1283, corresponding to the mono-charged species of [tri-aniline+H]$^+$, was detected in addition to the free aniline ion peak at m/z = 94.0669. The ion peak of [tri-aniline+H]$^+$ evolved into the most intense one after 4 min of polymerization, indicating that the tri-aniline derivative $C_{18}H_{16}N_4$ was the main component at this polymerization stage [Figure 2E]. However, when the polymerization time reached 9 min, an ion peak at m/z = 778.0974, which could be assigned to the octa-aniline derivative, appeared [Figure 2F]. Based on the above results, we assume that at the early polymerization time (1 min), a lower amount of tri-aniline oligomer was produced. When *β*-CD was added at this time point, a lower degree of *β*-CD/tri-aniline oligomer complex was formed, leading to less involvement of *β*-CD in the polymerization process.

At the polymerization time of 4 min, a higher amount of tri-aniline oligomer was obtained, which led to the relative concentrated formation of *β*-CD/tri-aniline oligomer complex and, thus, a higher engagement of *β*-CD during the polymerization. However, at a longer polymerization time (9 min), the product with a higher polymerization degree, namely the octa-aniline derivative, was too bulky to interact with *β*-CD,

which led to a lower engagement of β-CD as well. In addition, the molar ratio of β-CD/aniline was modulated. As shown in Supplementary Figure 4, increasing the amount of β-CD led to a greater number of pores or even disruption of the helical nanoribbons. Above all, the involvement of β-CD in the initial polymerization process was considered to be the key factor for obtaining porous helical ribbons.

Morphological evolution of PHNRs

As discussed above, PHNRs with large pores were observed upon the addition of β-CD after 4 min polymerization of aniline; therefore, to clarify the role that β-CD played in the fabrication of PHNRs, this optimal condition was selected to monitor the formation process of PHNRs [Figure 3 and Supplementary Figure 5]. Figure 3 shows the nanostructures assembled from β-CD mediated oligoaniline derivatives at different time intervals. Spindle nanoflakes could be obtained after 1 h of polymerization. It is worth noting that the nanoflakes started to split and afford the nanofiber structures after 3 h. When the polymerization time was extended to 5 or 9 h, clusters of twisted nanoribbons, composed of entangled nanoribbons, were observed. Surprisingly, helical nanoribbons bearing multiple pore channels, namely PHNRs 100-150 nm in width and 200-250 nm in average pitch, were formed after 12 h of polymerization. As evidenced by the SEM and TEM images, we measured the pore sizes of the porous helical nanoribbons in the range of 15-35 nm. Based on these observations, we hypothesize that β-CD was involved in the early polymerization process to a certain extent and directed the formation of PHNRs through the abscission from the helical nanoribbons.

To investigate the size effect of the β-CD on the formation of the porous helical nanoribbons, we selected its analogs, α-CD and γ-CD, to mediate the nanostructure formation under the same conditions. As shown in Supplementary Figure 6, the addition of 1 equiv. of α-CD at the 4 min polymerization time point along with polymerization for 12 h induced the observation of porous helical nanoribbons with smaller pore sizes compared to those obtained by β-CD. In contrast, neither porous character nor helical nanostructures were detected in the presence of 1 equiv. of γ-CD. Taken together, these observations demonstrated that α-CD and β-CD displayed similar binding affinity towards the oligoaniline, while negligible binding existed in the case of γ-CD due to its larger size. However, γ-CD also damaged the polymerization of aniline, which eventually led to the disappearance of helical nanoribbons.

To investigate the helical sense discrepancy of the helical nanostructures, we performed circular dichroism experiments in an *i*-propanol/water solvent mixture [Supplementary Figure 7]. The helical nanoribbons formed in the absence of β-CD showed a positive Cotton effect at 202 nm, which is in agreement with the literature[11]. By contrast, the porous helical nanoribbons mediated by β-CD exhibited a positive Cotton signal with a blue-shift at 196 nm. This finding demonstrates that the emergence of the porous features did not affect the helical sense of the porous nanoribbons but enhanced the intermolecular π-π interaction to a certain extent.

Formation mechanism of PHNRs

To test the above formation hypothesis, fourier-transform infrared spectroscopy (FTIR) measurements were conducted. As shown in Figure 4, the spectrum of β-CD showed a typical -OH band at 3421 cm^{-1} (Figure 4F, left), and the spectrum of helical nanoribbons assembled from oligoanilines, obtained with 12 h polymerization in the absence of β-CD, showed two characteristic bands at 1572 and 1509 cm^{-1}, corresponding to C=C stretching vibration in quinonoid and benzenoid rings, respectively. In addition, the peak located around 1352 cm^{-1} could be ascribed to the C-N stretching mode of benzoquinone imine (Figure 4A, left). It is worth noting that, after the introduction of β-CD into the oligoaniline solution for 1 h, the three mentioned FTIR adsorption peaks of oligoaniline were slightly shifted to lower wavenumbers with reduced intensity compared to free oligoaniline (Figure 4B, left), indicating the establishment of a supramolecular complex between oligoaniline and β-CD. However, with the extension of the

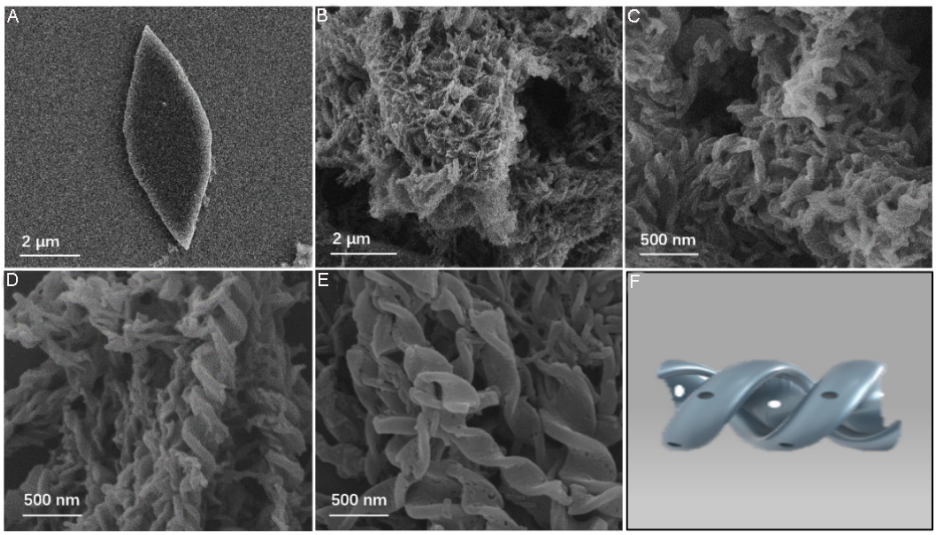

Figure 3. FESEM images of the nanostructures assembled from β-CD mediated oligoaniline derivatives at different polymerization times: (A) 1 h; (B) 3 h; (C) 5 h; (D) 9 h; and (E) 12 h. (F) A cartoon image of PHNR. FESEM: Field emission scanning electron microscope; β-CD: β-cyclodextrin; PHNR: porous helical nanoribbon.

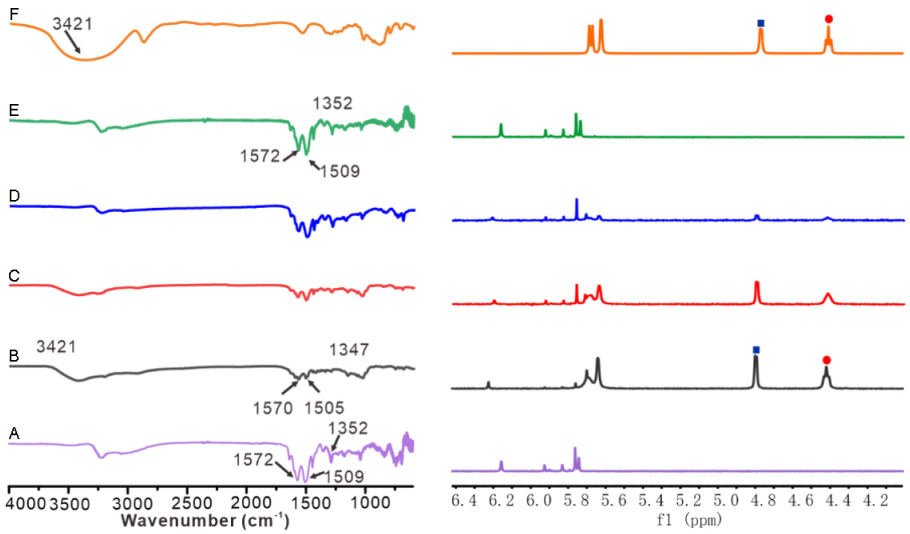

Figure 4. (Left) FTIR spectra and (Right) selected ^{1}H NMR spectra of (A) oligoanilines obtained with 12 h polymerization in the absence of β-CD. β-CD mediated polymerization product at various polymerization times: (B) 1 h; (C) 3 h; (D) 5 h; and (E) 12 h. (F) β-CD. FTIR: Fourier-transform infrared spectroscopy; NMR: nuclear magnetic resonance; β-CD: β-cyclodextrin.

polymerization time, the specific bound bands of both oligoaniline and β-CD started to diminish (Figure 4C and D, left) and completely disappeared after 12 h (Figure 4E, left). Moreover, the characteristic bands of free oligoaniline reappeared simultaneously, which indicated the disassociation of the β-CD/oligoaniline complex.

To further disclose the underlying mechanism of the β-CD mediated formation of PHNRs, the ^{1}H NMR spectra of β-CD, helical nanoribbons assembled from oligoanilines obtained with 12 h polymerization in the absence of β-CD, and the β-CD mediated polymerization product at various polymerization times in deuterated DMSO solution were obtained. Note that the samples taken from the polymerization system

were centrifuged and washed with water to remove free aniline, APS, and β-CD. As shown in Figure 4 (right), when β-CD was added into the polymerization system for 1 h, the hydroxyl protons of β-CD, located in the range of 4-5 ppm, from the resulting product experienced a slight downfield shift in comparison with that of free β-CD, an indication of the formation of the β-CD/oligoaniline complex. However, with the increase of the polymerization time, the signals arising from β-CD were largely attenuated for the β-CD mediated polymerization product and completely disappeared after 12 h. The above results further verify the abscission of β-CD from the oligoaniline assemblies with the extension of polymerization time, which was considered the crucial reason for the formation of PHNRs.

Taken together, the formation mechanism of the PHNRs was proposed as follows: A supramolecular complex was formed between β-CD and tri-aniline at the early stage of polymerization and involved in the assembly of spindle nanoflakes [Figure 3A]. However, with the reorganization of the oligoaniline assemblies over time, the abscission of β-CD from the helical nanoribbons was observed, which eventually induced the formation of PHNRs.

CONCLUSIONS

We describe the β-CD mediated fabrication of porous helical nanoribbons via the chemical oxidation of aniline in an *i*-propanol/water mixture. The effective formation of the β-CD/oligoaniline complex at the early stage of aniline polymerization was demonstrated, which was subsequently involved in the assembly of spindle nanoflakes. However, with the reorganization of the oligoaniline assemblies over time, the abscission of β-CD from the helical nanoribbons was observed, which eventually induced the formation of PHNRs. We believe the supramolecular host-modulated assembly presented herein may provide an alternative approach for the construction of unique porous nanostructures.

DECLARATIONS

Authors' contributions

Implemented synthesis, conducted morphology characterization and analyzed data: Liu SY
Performed data analysis, wrote and revised the manuscript: Sun QQ
Performed synthesis: Hang PY
Performed data analysis, wrote and revised the manuscript: Sun XH
Performed morphology characterization: Zhou CQ
Performed data analysis and revised the manuscript: Han J
Revised the manuscript: Guo R

Availability of data and materials

Not applicable.

Financial support and sponsorship

This work was supported by the National Natural Science Foundation of China (21922202 and 22272146 for Han J), Natural Science Foundation of the Higher Education Institutions of Jiangsu Province (20KJB150028 for Sun XH) and Chinese Postdoctoral Science Foundation (2021M692714 for Sun XH). Priority Academic Program Development of Jiangsu Higher Education Institutions.

Conflicts of interest

All authors declared that there are no conflicts of interest.

Ethical approval and consent to participate

Not applicable.

Consent for publication

Not applicable.

Copyright

REFERENCES

1. Wang Z, Wang Y, Sun X, et al. Supramolecular core-shell nanoassemblies with tumor microenvironment-triggered size and structure switch for improved photothermal therapy. *Small* 2022;18:e2200588. DOI PubMed
2. Feng Z, Zhang T, Wang H, Xu B. Supramolecular catalysis and dynamic assemblies for medicine. *Chem Soc Rev* 2017;46:6470-9. DOI PubMed PMC
3. Luo R, Xia Y. Fluorescent cadmium sulfide supraparticles: one-step in situ self-assembly fabrication and cationic surfactant chain length-dependent mitochondria targeting capacity. *J Anal Test* 2021;5:30-9. DOI
4. Zeng Y, Shi J, Li K, et al. Coordination-driven [2+2] metallo-macrocycles isomers: conformational control and photophysical properties. *Chem Synth* 2022;2:12. DOI
5. Zhou C, Sun X, Han J. Chiral conducting polymer nanomaterials: synthesis and applications in enantioselective recognition. *Mater Chem Front* 2020;4:2499-516. DOI
6. Moreno-Alcántar G, Aliprandi A, Rouquette R, et al. Solvent-driven supramolecular wrapping of self-assembled structures. *Angew Chem Int Ed Engl* 2021;60:5407-13. DOI PubMed PMC
7. Qin Y, Wang YT, Yang HB, Zhu W. Recent advances on the construction of diarylethene-based supramolecular metallacycles and metallacages via coordination-driven self-assembly. *Chem Synth* 2021;1:2. DOI
8. Kim Y, Lee M. Supramolecular capsules from bilayer membrane scission driven by corannulene. *Chem Eur J* 2015;21:5736-40. DOI PubMed
9. Sun HL, Chen Y, Zhao J, Liu Y. Photocontrolled reversible conversion of nanotube and nanoparticle mediated by β-cyclodextrin dimers. *Angew Chem Int Ed Engl* 2015;54:9376-80. DOI PubMed
10. Chen X, Liu L, Huo M, et al. Direct synthesis of polymer nanotubes by aqueous dispersion polymerization of a cyclodextrin/styrene complex. *Angew Chem* 2017;129:16768-72. DOI PubMed
11. Zhou C, Ren Y, Han J, et al. Controllable supramolecular chiral twisted nanoribbons from achiral conjugated oligoaniline derivatives. *J Am Chem Soc* 2018;140:9417-25. DOI PubMed
12. Zhou C, Ren Y, Han J, Xu Q, Guo R. Chiral polyaniline hollow nanotwists toward efficient enantioselective separation of amino acids. *ACS Nano* 2019;13:3534-44. DOI PubMed

Yin *et al. Chem Synth* 2022;2:19
DOI: 10.20517/cs.2022.20

Chemical Synthesis

Review

Open Access

Two-dimensional materials: synthesis and applications in the electro-reduction of carbon dioxide

Yaoyu Yin[1,2], Xinchen Kang[1,2,*], Buxing Han[1,2,3,*]

[1]Beijing National Laboratory for Molecular Sciences, Key Laboratory of Colloid and Interface and Thermodynamics, Institute of Chemistry, Chinese Academy of Sciences, Beijing 100190, China.
[2]School of Chemistry, University of Chinese Academy of Sciences, Beijing 100049, China.
[3]Shanghai Key Laboratory of Green Chemistry and Chemical Processes, School of Chemistry and Molecular Engineering, East China Normal University, Shanghai 200062, China.

***Correspondence to:** Prof. Xinchen Kang, Beijing National Laboratory for Molecular Sciences, Key Laboratory of Colloid and Interface and Thermodynamics, Institute of Chemistry, Chinese Academy of Sciences, Beijing 100190, China. E-mail: kangxinchen@iccas.ac.cn; Prof. Buxing Han, Beijing National Laboratory for Molecular Sciences, Key Laboratory of Colloid and Interface and Thermodynamics, Institute of Chemistry, Chinese Academy of Sciences, Beijing 100190, China. E-mail: hanbx@iccas.ac.cn

How to cite this article: Yin Y, Kang X, Han B. Two-dimensional materials: synthesis and applications in the electro-reduction of carbon dioxide. *Chem Synth* 2022;2:19. https://dx.doi.org/10.20517/cs.2022.20

Received: 28 Aug 2022 **First Decision:** 22 Sep 2022 **Revised:** 5 Oct 2022 **Accepted:** 9 Nov 2022 **Published:** 28 Nov 2022

Academic Editors: Bao-Lian Su, Da-Gang Yu **Copy Editor:** Peng-Juan Wen **Production Editor:** Peng-Juan Wen

Abstract

The emission of CO_2 has become an increasingly prominent issue. Electrochemical reduction of CO_2 to value-added chemicals provides a promising strategy to mitigate energy shortage and achieve carbon neutrality. Two-dimensional (2D) materials are highly attractive for the fabrication of catalysts owing to their special electronic and geometric properties as well as a multitude of edge active sites. Various 2D materials have been proposed for synthesis and use in the conversion of CO_2 to versatile carbonous products. This review presents the latest progress on various 2D materials with a focus on their synthesis and applications in the electrochemical reduction of CO_2. Initially, the advantages of 2D materials for CO_2 electro-reduction are briefly discussed. Subsequently, common methods for the synthesis of 2D materials and the role of these materials in the electrochemical reduction of CO_2 are elaborated. Finally, some perspectives for future investigations of 2D materials for CO_2 electro-reduction are proposed.

Keywords: 2D materials, material synthesis, electrochemical reduction of CO_2

INTRODUCTION

The concentration of greenhouse gas CO_2 has risen by 100 ppm since the industrial revolution. The average temperature has been rising at an average rate of 0.1 °C per decade for nearly half a century, which results in serious global warming[1-3]. From another perspective, CO_2 is an abundant, clean, and cheap feedstock for the production of value-added chemicals. Hence, it is of great ecological and social significance to utilize and convert CO_2 into high-value-added chemical products[4-6]. Nonetheless, CO_2 has thermodynamically stable and chemically inert properties, and thus its conversion is highly energy intensive. Considering the prominent role of CO_2 in global warming and the chemical characteristics of CO_2, numerous chemical technologies have been developed for CO_2 conversion, including thermal catalysis[7-9], photocatalysis[10-12], and electrocatalysis[13-15]. The development of highly effective catalysts and related equipment for CO_2 transformation has boomed in recent years[16]. Among them, the electro-reduction of CO_2 to value-added chemicals benefits from low investment in equipment, high efficiency, and environmental acceptance[17-20].

The electrochemical reduction of CO_2 is a multi-electron transfer process, which mainly occurs at the electrode and the electrolyte interface. This process consists of four steps: (i) CO_2 is chemically adsorbed on the electrode surface; (ii) CO_2 is converted into $CO_2^{\bullet-}$ by one-electron attacks; (iii) Multiple electrons and protons are transferred to $CO_2^{\bullet-}$ for the construction of C-H and C-C bonds; and (iv) Products are released from the electrode[21].The half-reactions and corresponding standard reduction potentials for the electro-reduction of CO_2 to various products have been elucidated through thermodynamic studies, as illustrated in Figure 1.

The electro-reduction of CO_2 to related products is a multi-step reduction. In spite of the low chemical reactivity of CO_2, the theoretical potential required for products is not a large negative value[22]. In fact, the first hurdle of CO_2 electro-reduction is the potential barrier for CO_2 activation ($CO_2 + e^- = CO_2^{\bullet-}$), which is -1.90 V *vs.* the standard hydrogen electrode (SHE). Because different products require similar thermodynamic potentials, it is challenging to obtain the desired product with high selectivity[23,24]. Accordingly, the development of electrode materials is significant to realize efficient electro-reduction with high selectivity toward target products.

Current density and selectivity are two evaluation indicators in CO_2 electro-reduction. A large current density indicates a fast reaction rate to provide a high yield of products from CO_2, and high selectivity can ease separation to reduce cost. Electrode materials play a decisive role in electrocatalytic performance. Hence, the design and synthesis of electrode materials with high activity, selectivity, and stability are significant for highly efficient CO_2 electro-reduction. 2D materials are defined as a type of nanomaterials with a layer-like morphology and small thickness (normally 1-100 nm) in which electrons move on the nanoscale in two dimensions[25]. 2D materials have been developed for various applications, such as energy conversion[26-28], catalysis[29-31], sensing[32-34], photodetector[35-37], and memristor[38-40], owing to their unique 2D geometry, nanoscale thickness, and high surface-to-volume ratio. 2D structures, such as nanoplates, nanosheets, and nanoflakes, have been using for preparation of various materials, including metals, metal oxides, metallic sulfides, and carbon materials[41-44]. Until now, numerous 2D materials have been designed and prepared for CO_2 electro-reduction[45-47]. For commercial applications of electrocatalysts, high yield and controllable fabrication techniques are essential. Versatile methods for the preparation of 2D materials, such as exfoliation, extraction, chemical or physical vapor deposition, and wet-chemical synthesis, have been developed. Different synthesis routes have different advantages. These strategies determine the morphology

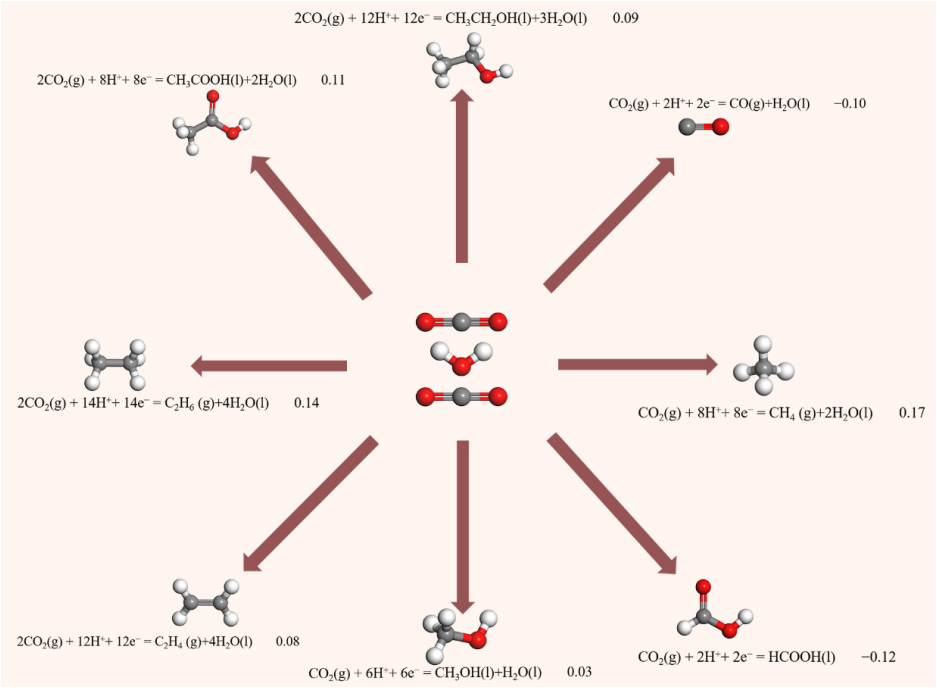

Figure 1. Half reactions and corresponding standard reduction potentials *vs.* reversible hydrogen electrode (RHE) (E^0/V *vs.* RHE) for the electrochemical reduction of CO_2 to various products.

of materials and further affect their properties, providing opportunities for their utilization in electrocatalysis.

This review covers the current progress on CO_2 electro-reduction using 2D material electrodes with a focus on the (i) advantages of 2D materials for CO_2 electro-reduction, (ii) strategies for 2D nanomaterial synthesis, and (iii) catalytic performance of 2D materials in the electrochemical reduction of CO_2.

ADVANTAGES OF 2D NANOSTRUCTURES FOR CO_2 ELECTRO-REDUCTION

Electrochemical reduction of CO_2 is a process involving gas-solid-liquid interactions[48,49], and its current density and Faradaic efficiency (FE) are largely affected by the specific surface area of electrode materials. Generally, a higher specific surface area guarantees more adsorption and active sites, leading to better catalytic performance. In addition, the concentration gradient of CO_2 and reaction intermediates are related to CO_2 diffusion on the electrode surface. The adsorption/desorption thermodynamics and kinetics of intermediates determine the selectivity and production rate of target products. Thus, materials with special morphologies and structures play a crucial role in catalyzing this process.

The electrochemical reduction of CO_2 is surface reaction, and thus 2D materials are suitable as catalysts because of the following advantages. First, 2D materials have a unique planar structure, which promotes interactions with the substrate or active components as well as the formation of heterojunctions to realize comprehensive regulation of electrocatalysis[50]. Second, 2D materials have enhanced electronic properties, such as high electron mobility and carrier concentration[51,52], which increase electron transfer from the electrode to CO_2. Third, 2D materials have a high proportion of uncoordinated sites and large specific surface areas, which increases interactions between CO_2 and the catalyst[53]. Exposed surface atoms in 2D materials can escape from their respective lattices to form defect sites, and these thermodynamically

unstable sites can trap electrons and shorten electron transport and ion diffusion distances[54,55]. Owing to the low atomic coordination number at the edge, the activity at the edge is higher than that at the basal plane in 2D materials[56]. Fourth, a multi-layer or single-layer structure increases the confinement effect, which improves the catalytic performance[57,58]. The surface of 2D materials can be modified to produce special gas trapping cavities, where interactions between the electrode, electrolyte, and CO_2 gas are enhanced[59,60]. Fifth, pores in 2D materials are fully exploited owing to the ultrathin structure. Porous structures in 2D materials can effectively amplify the differences in mass transfer efficiency as well as intermediate diffusion during CO_2 reduction.

In summary, 2D materials have geometries, electronic structures, and defects that are suitable for CO_2 electro-reduction. Owing to their large specific surface area, 2D materials can serve as supports for hybrid materials. In addition, the unique atomic-layer-thick structure provides an ideal platform for revealing atomic-scale mechanisms. The rational development and exploitation of distinct structural and electronic properties of 2D materials endow 2D materials with more opportunities for broad applications in the field of CO_2 electro-reduction.

SYNTHESIS OF 2D NANOSTRUCTURES

The electrocatalytic performances of 2D materials are mainly determined by the morphology, structure and chemical properties of the materials, which in turn are closely related to the synthesis methods. Since the discovery of graphene, many efficient routes have been developed for the synthesis of 2D materials, allowing researchers to design more promising 2D materials. Top-down and bottom-up routes are commonly used for the synthesis of 2D materials[61-63]. Top-down routes, such as exfoliation and extraction procedures, are easily performed without special equipment, and thus they are effective for the synthesis of inorganic materials, such as graphene and metal dichalcogenides. Bottom-up routes, including chemical/physical vapor deposition and wet-chemical syntheses, provide 2D materials with accurately controlled morphologies and structures, and thus they are frequently used to prepare materials with unique structures. In this section, several typical routes for the fabrication of 2D materials are briefly described.

Exfoliation

Exfoliation requires external mechanical forces to peel off 2D materials with a single or few layers from bulk objects. This method relies on driving forces, such as mechanical and ultrasonic forces, to overcome intermolecular interactions, such as the van der Waals force, between atomic layers. This process is simple to operate and produces few defects in the resulting material, although it suffers from low effectiveness and poor repeatability, which limits its practical applications.

Mechanical exfoliation has been a common method for the fabrication of emergent 2D materials [Figure 2A] since Geim obtained graphene by tearing off graphite from tape[64]. Other research groups have since developed similar methods for producing high-quality 2D materials. Li *et al.* used bulk materials to isolate desired products and prepare various single- and few-layer transition-metal dichalcogenide nanosheets with high crystallinity, including WSe_2, TaS_2, and $TaSe_2$[65]. However, the yield is low and the thickness and size of as-prepared materials are difficult to control using this strategy, thus inhibiting large-scale production. Huang *et al.* used a universal, one-step method via Au-assisted mechanical exfoliation to address the above problem [Figure 2B] and synthesize a series of 2D materials such as BP, $RuCl_3$, Fe_3GeTe_2, FeSe, MoS_2, and WSe_2[66] [Figure 2C]. This environmentally compliant route meets the requirements of green chemistry. Field-effect transistor devices have been fabricated using 2D MoS_2 and WSe_2. However, the use of noble metals undoubtedly increases the cost, thus hampering the implementation of this route for the fabrication of large devices.

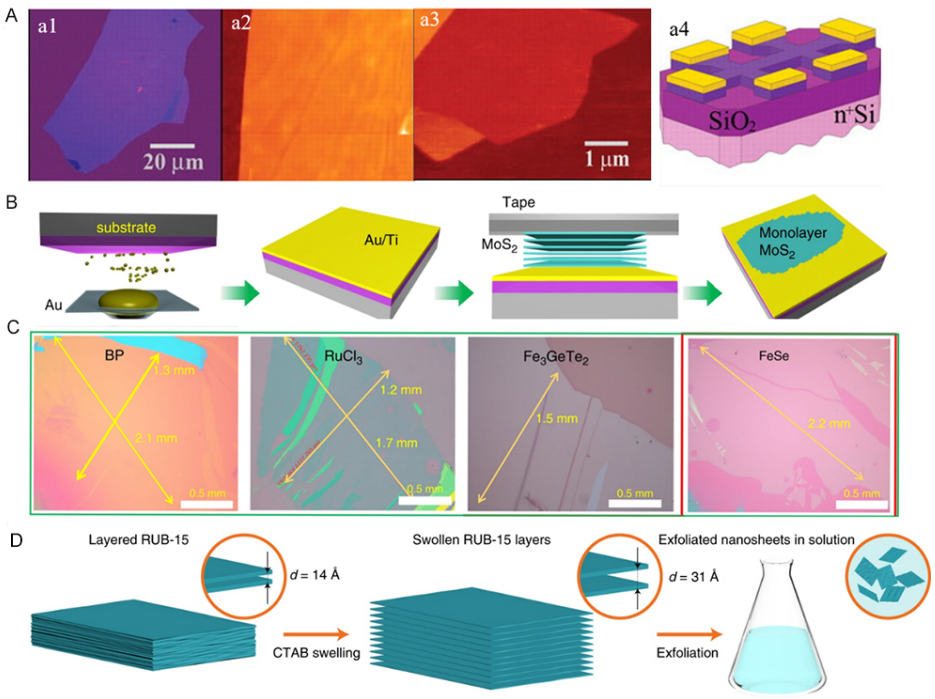

Figure 2. Synthesis of 2D materials by exfoliation. (A) Graphene films synthesized by mechanical exfoliation[64]. (B) Schematic diagram of Au-assisted mechanical exfoliation. (C) 2D materials synthesized by Au-assisted mechanical exfoliation[66]. (D) Schematic diagram of CTAB-assisted material swelling[69]. 2D: 2-dimensional; CTAB: hexadecyl trimethyl ammonium bromide.

Ultrasonic exfoliation in the liquid phase relies on the cavitation effect. When bulk materials are subjected to an ultrasonic wave in a suitable solvent, micro-gas core cavitation bubbles produced in the solvent expand the space between the layers of the material, thus producing the 2D material. Coleman *et al.* reported in detail that ultrasonic exfoliation of transition metal dichalcogenides, such as BN, MoS_2, WS_2, $MoSe_2$, $MoTe_2$, $TaSe_2$, $NbSe_2$, $NiTe_2$, and Bi_2Te_2, in organic solvents can be used to produce 2D materials with few layers[67]. Metal oxide and hydroxide with limited layers can also be produced by ultrasonic exfoliation. Compared with transition metal dichalcogenides, which are stabilized by weak intermolecular interactions, such as the van der Waals force, metal oxides and hydroxides are stabilized by strong ionic interactions, which makes exfoliation difficult[68]. Although ultrasonic exfoliation is the most promising strategy for the industrial production of 2D materials, this strategy has fatal defects. For example, (i) the number of layers and thickness are difficult to control and (ii) the recovery rate is low, which confines the method to the laboratory.

Intercalation-based exfoliation has been widely explored owing to the unique characteristics of high-yield monolayers. Suitable intercalation species are vital for effective intercalation and determine whether intercalation proceeds. For example, surfactants are often used for the production of 2D nanosheets. Dakhchoune *et al.* reported that intercalation of surfactant hexadecyl trimethyl ammonium bromide (CTAB) into sodalite precursors leads to material swelling[69]. Consequently, the lattice spacing increases from 1.4 nm to 3.1 nm [Figure 2D], indicating that interlayer interactions are weakened by the intercalation of CTAB.

Chemical vapor deposition

Chemical vapor deposition (CVD) is one of the most commonly used methods for the synthesis of 2D materials[70]. In this technique, a thin solid layer is deposited on the surface of a substrate through vapor-

phase chemical reactions in a high-temperature gas. Various solid-state layers (e.g., single crystals, continuous thin films, and heterojunctions) can be produced on substrates by adjusting the operating temperature, flow gas species, phase composition, and substrate. Numerous functional van der Waals heterostructures can also be created by this method[71] [Figure 3A-D]. In contrast to exfoliation and extraction, CVD allows control of the number of layers as well as the density and purity of products through changes in the synthesis conditions.

CVD has become an important method for the preparation of 2D materials since it was used to prepare graphene in 2009[72,73]. Browne *et al.* synthesized MoS_2 and WS_2 materials to serve as electrodes[74]. The surface of as-prepared MoS_2/WS_2 is rougher than that of commercial materials. Li *et al.* used methane to prepare graphene films with a large surface area on a copper substrate by CVD[73]. The as-prepared graphene film can be easily transferred to alternative substrates for the fabrication of functional devices. Yin *et al.* synthesized high-quality nonlayered Fe_2O_3 nanosheets with a thickness of 1.95 nm, which exhibit lattice relaxation owing to the ultrathin structure[75]. Although the growth of 2D materials on substrates is rapid, the direct growth of 2D metal/metal oxides onto substrates is restricted because of the high melting point of metals/metal oxides. Introducing molten salts as additives can effectively reduce the reaction temperature and promote the growth of high-quality 2D materials. For instance, Zhou *et al.* reported a new method to synthesize 47 compounds by adding NaCl and KI as adjuvants[76]. Despite various efforts focused on synthesizing 2D materials by CVD, poor repeatability and unscalable production restrict the industrial application of CVD.

As mentioned above, the thickness and size of 2D materials can be precisely controlled by adjusting the working temperature, carrier gas rate, and chamber pressure. Space-confined CVD can be used to achieve the growth of high-quality 2D materials. Recently, Li *et al.* used Te-assisted CVD to precisely synthesize 2D Fe single-crystal nanoflakes with different thicknesses[77] [Figure 3E-G]. Xu *et al.* used space-confined CVD to grow homogeneous 1T'-$MoTe_2$ monolayers with a lateral size of 100 μm in batches, demonstrating that the confined space can increase the vapor pressure of sulfur to extend the lifetime of monolayer tellurides from several minutes to at least 24 h[78].

Hydrothermal and solvothermal methods

Hydrothermal and solvothermal methods are widely used to prepare various 2D materials with high yields. Both methods are based on heterogeneous chemical reactions occurring at high temperature and pressure during which substances are dissolved and recrystallized. The difference between the two methods is the solvent. Water is used as the solvent in hydrothermal methods, while non-aqueous organic solvents are used in solvothermal methods. Materials prepared by hydro/solvothermal methods have advantageous characteristics, such as high crystallinity, small particle size, and uniform distribution.

Among various 2D materials, metal oxides have attracted considerable attention in the fields of catalysis, energy conversion, and electronics owing to their low cost and large surface area. Sun *et al.* developed a general solvothermal method to prepare various transition metal oxide nanosheets, such as ZnO, WO_3, Co_3O_4 and TiO_2, [Figure 4] in different solvents (water/ethanol/glycol) for use in photoelectric or photochemical devices[79]. The thickness of as-prepared nanosheets ranges from 1.6 nm to 5.2 nm. Metal-organic frameworks (MOFs) represent a class of hybrid materials comprising ordered networks formed by combining metal ions with organic ligands[80-82]. MOFs have been explored extensively to prepare 2D structures. As a bottom-up synthesis method, the templated hydrothermal strategy induces the confined growth of 2D MOF materials. Zheng *et al.* synthesized ultrathin 2D Co-MOF with a thickness of 2 nm by reacting precursors and polyvinyl pyrrolidone in DMF/C_2H_5OH solution at 80 °C for 80 h[83]. Moreover,

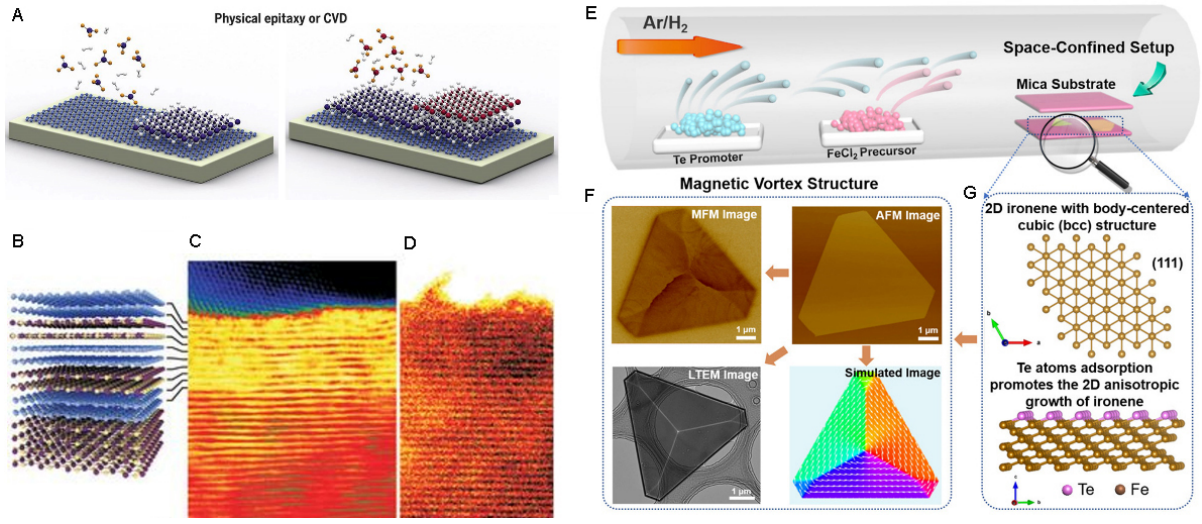

Figure 3. Synthesis of 2D materials by CVD. (A) Schematic diagram of the CVD method. (B-D) Schematic diagram and TEM images of graphene/hBN heterostructures. Here, carbon atoms are represented by blue spheres, boron is shown in yellow, and nitrogen is in purple[71]. (E-G) Synthesis of 2D Fe single-crystal nanoflakes by space-confined CVD[77]. 2D: 2-dimensional; CVD: chemical vapor deposition; TEM: transmission electron microscopy.

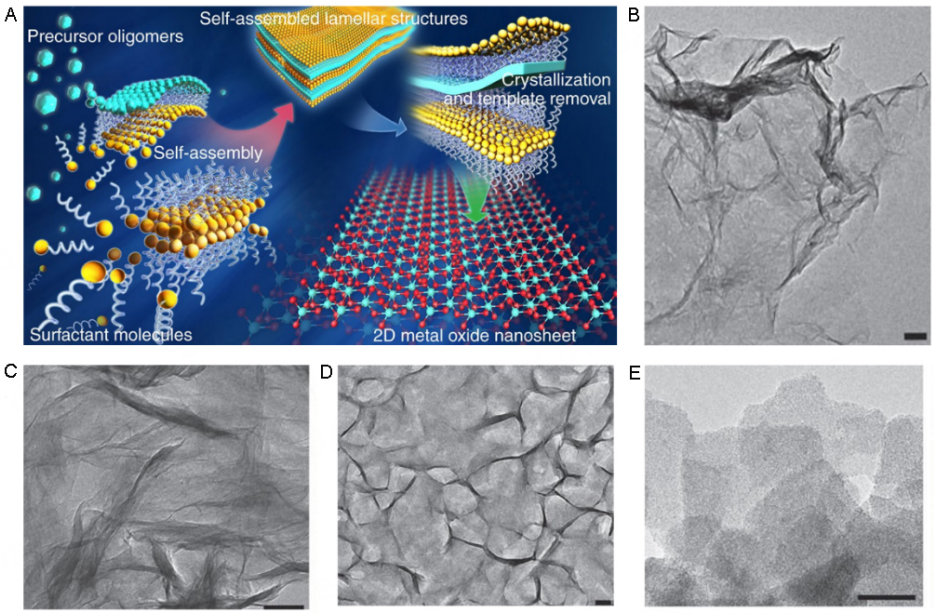

Figure 4. Synthesis of 2D metal oxide nanosheets by the hydrothermal method. (A) Schematic diagram of the synthesis route. TEM images of (B) Co_3O_4, (C) TiO_2, (D) ZnO, and (E) WO_3[79]. 2D: 2-dimensional; TEM: transmission electron microscopy.

various novel 2D materials, such as MoP@In-PC, Mo-Bi bimetallic, Sn_4P_3/rGO, have been synthesized by hydro/solvothermal methods[84-86].

Electrodeposition

Electrochemical deposition is a liquid-phase process based on redox reactions by which 2D materials are easily formed. This method has numerous advantages, including mild conditions, low cost, high safety, easy operation, and high controllability. The morphology, structure, and physicochemical property of products

can be controlled by adjusting various conditions, including the pH of the solution, potential, time, and temperature, during electrodeposition.

Electrodes prepared by electrodeposition have very low contact resistance, which promotes electron transfer in functional devices. Rabiee *et al.* grew uniform Bi-based nanosheets on a substrate by pulse electrodeposition[87]. In contrast, a Bi-based bulk material was obtained by continuous electrodeposition. Abdelazim *et al.* reported the lateral growth of MoS_2 on an insulating surface[88]. The highly anisotropic growth rate of MoS_2 can be controlled by simple electrodeposition to obtain a lateral to vertical growth ratio exceeding 20. This paves a new pathway to precisely control the growth direction to obtain 2D materials. Polymetallic alloys have shown great potential in various applications, and co-deposition of versatile metals can be realized with electrodeposition by adjusting the pH of the solution or applied voltage. For example, Feng *et al.* used electrodeposition in a solution of pH 10 to obtain an active borate-intercalated NiCoFe-LDH, which is susceptible to redeposition to recover catalytic activity, further confirming the advantage of electrodeposition[89]. Shen *et al.* synthesized amorphous 2D FeMn by electrodeposition using sodium citrate as a structure-directing agent[90] [Figure 5A-C]. OH^- is produced near the surface of the cathode, and metal ions are deposited with OH^- at the cathode to form hydroxides.

Despite recent achievements in the electrodeposition of 2D materials, the mechanism remains difficult to demonstrate. Tan *et al.* used transmission electron microscopy (TEM) to visualize material synthesis, including nucleation sites, growth mechanisms, and structures formed during electrochemical reactions[91]. This promising technology can be used to observe an electron beam-stable and low-contrast extended electrode area with high resolution [Figure 5D].

Extraction

To date, many new types of 2D materials have been developed for functional devices. 2D transition metal carbides and nitrides (MXenes) have good electrical properties owing to the inner conductive carbide layer and hydrophilic transition metal oxide surface, and thus they are promising materials for the fabrication of batteries and catalysts.

The most effective synthesis route of MXenes is the selective etching of "A" layers from an Al-containing MAX phase, where A represents a III A or IV A element (e.g., Al, Ga, Si, or Ge) and X represents either C or N. Lukatskaya *et al.* and Ghidiu *et al.* synthesized various MXenes by selective extraction, electrochemical etching, and ion intercalation[92-94]. The as-prepared 2D materials are applied in Li-ion batteries, which acquire excellent electricity performance.

In addition to the methods above, researchers have explored many other routes for the synthesis of 2D materials. Among the multitude of strategies, templated synthesis can easily and directly realize 2D materials with controlled structures. For example, Liu *et al.* synthesized a series of mesoporous materials with a single-layer structure[95]. Phenolic formaldehyde resin, a flexible template, is beneficial for the adsorption and subsequent confinement of inorganic precursors on the salt surface. Surface-limited cooperative assembly allows for large-scale production, and 14.1 g of mesoporous TiO_2 with single-layer structure can be synthesized per batch. Although templated synthesis has been extensively explored for the preparation of 2D materials, the long preparation time and high cost restrict its wide application in industry. Developing template-free preparation methods is of significance for the mass production of 2D materials. Zhang *et al.* developed a general method for control-oriented growth of MOF nanosheets with ultrathin thicknesses and abundant unsaturated coordination metal sites using CO_2 as a capping agent[96]. The process is template-free and CO_2 can be easily removed by depressurization after synthesis. Atomic

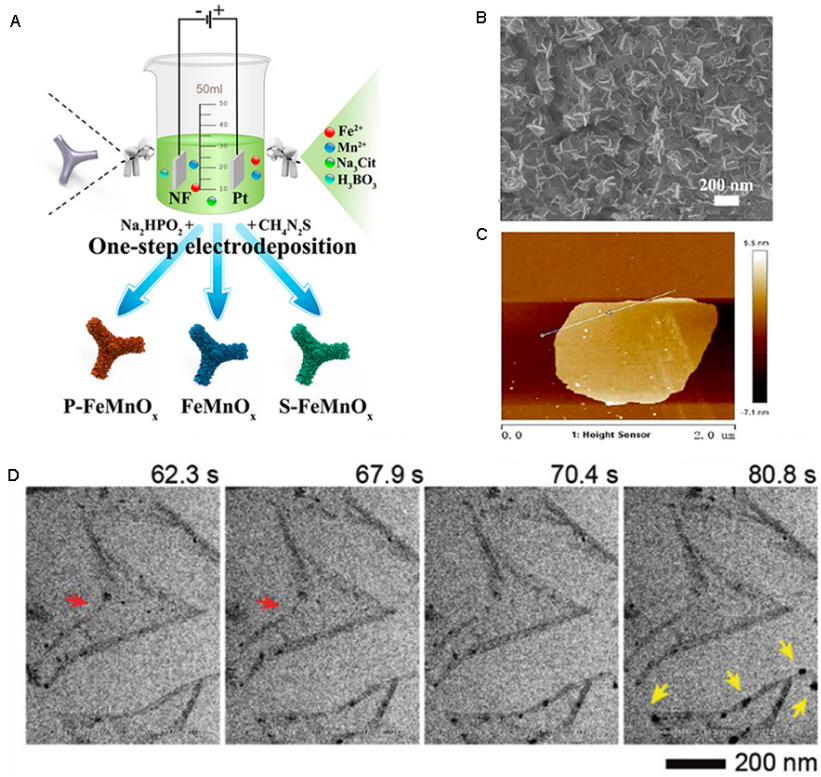

Figure 5. Synthesis of 2D materials by electrodeposition. (A) Schematic diagram of the preparation of FeMn-based nanosheets. (B) SEM image of $FeMnO_x$. (C) AFM image of $FeMnO_x$[90]. (D) TEM image of MoS_2 flake after exposure to the electron beam[91]. 2D: 2-dimensional; TEM: transmission electron microscopy.

layer deposition has emerged as a powerful technique to prepare nanofilms with a thickness approaching the Debye length. Ko *et al.* reported the preparation of a large-area WS_2 nanosheet with a precisely controlled number of layers by atomic layer deposition[97]. These methods can be used for reference and guidance in the development and application of 2D materials for CO_2 electrocatalytic reduction.

ELECTROCHEMICAL REDUCTION OF CO_2 OVER 2D NANOSTRUCTURES

Various 2D nanostructures have been extensively explored for the electro-reduction of CO_2 owing to their unique structure and properties. Versatile electrode materials, including metals, metal oxides, metal dichalcogenides, and carbon-based nanomaterials, have shown potential in CO_2 electrocatalytic reduction [Table 1]. In this section, advances in 2D materials for CO_2 electrocatalytic reduction a reviewed and the related mechanism is discussed.

Metal materials

Zero-valence metals are the most popular electrode materials for CO_2 electro-reduction owing to their high conductivity, high stability, controllable crystal faces, and ease of CO_2 activation.

Noble metals

Noble metals are considered the most effective catalysts[114,115], and electrochemical reduction of CO_2 over noble metal-based electrodes has been extensively studied in recent years[116,117]. The particle size determines the catalytic performance because larger particles have fewer active sites, whereas smaller particles favor H_2 evolution over CO_2 reduction. Noble metal nanosheets exhibit excellent catalytic performance in CO_2

Table 1. Summary of 2D-based materials developed for CO_2 electrocatalytic reduction

Catalysts	Electrolyte	Products	FE	Potential	*j* (mA cm^{-2})	Refs.
Ag nanosheet	0.5 M $NaHCO_3$	CO	95	-0.8 V *vs.* RHE	10	[98]
Ag foil			75		~0.3	
Zn nanosheet	0.5 M $NaHCO_3$	CO	86	-1.13 V *vs.* RHE	6	[99]
Zn foil			9.5		~1	
Sn sheet confined in graphene	0.1 M $NaHCO_3$	formate	89	-1.8 V *vs.* SCE	21.1	[100]
Bulk Sn			44.5		1.6	
Cu nanosheet	0.1 M K_2SO_4	ethylene	83.2	-1.18 V *vs.* RHE	58.8	[101]
Cu nanoparticles			37.2		36.4	
Sn nanosheet	0.5 M $NaHCO_3$	formate	83	-0.9 *vs.* RHE	14	[102]
Sn foil			25		6	
Cu plates	0.5 M KCl	ethylene	74.9	-0.9 *vs.* RHE	50	[103]
Cu nanoparticles			52		10	
Zn nanosheet	0.1 M $KHCO_3$	CO	90	-1.0 V *vs.* RHE	100	[104]
Zn nanoparticles			70		50	
Co nanosheet	0.1 M Na_2SO_4	formate	90.1	-0.85 V *vs.* SCE	10.59	[105]
Bulk Co			25		68.0	
Co_3O_4 nanosheets	0.1 M $KHCO_3$	formate	64.3	-0.88 V *vs.* SCE	0.68	[106]
Bulk Co_3O_4			18.5		0.034	
Bi nanosheet	0.5 M $NaHCO_3$	formate	~90	-1.74 V *vs.* SHE	24	[107]
Bi nanoparticles			~60		6	
ZnO nanosheet	0.1 M $KHCO_3$	CO	83	-1.1 V *vs.* RHE	16.1	[108]
Bi_2WO_6 nanosheet	0.5 M $BmimPF_6$/MeCN	CO	91	-2.4 V *vs.* Ag/Ag^+	43	[109]
N-codoped graphenes nanosheet	0.5 M $KHCO_3$	formate	64	-0.80 V *vs.* RHE	4	[110]
SnS_2	0.1 M $KHCO_3$	formate	93.3	-0.75 V *vs.* RHE	55	[111]
InN nanosheet	1 M KOH	formate	91	-0.9 V *vs.* RHE	46	[112]
Mo-Bi bimetallic chalcogenide nanosheet	0.5 M $BmimBF_4$/MeCN	methanol	71.2	-0.7 V *vs.* SHE	12.1	[85]
FeTPP[Cl]/Cu	1 M $KHCO_3$	ethanol	41	-0.82 V *vs.* SHE	124	[113]

2D: 2-dimensional; FE: Faradaic efficiency.

electro-reduction compared with their nanoparticles. For instance, Lee *et al.* prepared Ag nanosheets [Figure 6A] using a self-organized method and obtained an FE_{CO} of 95% over the Ag nanosheets at an overpotential of only 0.29 V[98] [Figure 6B and C]. The current density and surface area of the Ag nanosheets are 37 and 17 times higher than those of polycrystalline Ag, indicating that both the enlarged surface area and high current density promoted by the 2D structure determine the catalytic performance. According to scanning transmission electron microscopy (STEM) images, numerous twin crystals exist between and within individual grains of the Ag nanosheets, and these grain boundaries are considered active sites for CO_2 electro-reduction.

Different crystal planes exhibit different catalytic activities for the conversion of CO_2 to products, and thus regulation of the crystal planes of nanosheet is an effective strategy to obtain high current density and FE for certain products. For example, Zhao *et al.* demonstrated that Pd nanosheets prepared by co-precipitation exhibit excellent catalytic activity in the electro-reduction of CO_2 to CO at the moderate overpotential of 590 mV[118] [Figure 6D-F]. Pd nanosheets with dominant (111) facet sites are transformed into more active (100) sites after 1 h of electrolysis. The reconstruction of crystal planes not only increases the density of active sites but also reduces the binding energy with CO intermediates, leading to high CO selectivity [Figure 6G].

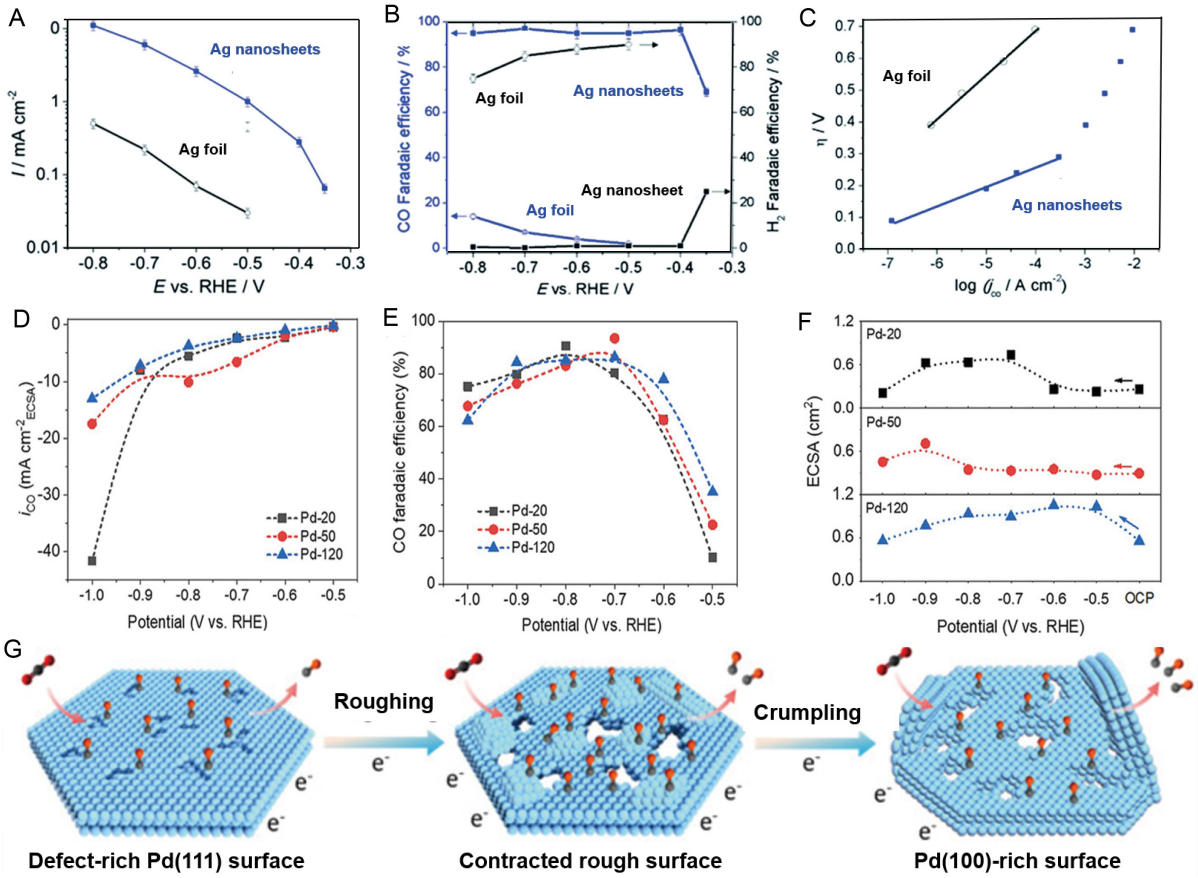

Figure 6. Electrochemical reduction of CO_2 over 2D noble metals. (A) Plot of current density *vs.* potential over Ag electrodes. (B) FE_{CO} and FE_{H2} *vs.* potential over Ag electrodes. (C) Tafel plots[98]. (D) Plot of current density *vs.* potential over Pd electrodes. (E) FE_{CO} *vs.* potential over Pd electrodes. (F) Electrochemical active surface area of different catalysts. (G) Schematic illustration of different Pd materials[118]. 2D: 2-dimensional.

It is worth mentioning that noble metal nanosheets favor CO over other carbon products of CO_2 electro-reduction because noble metals can strongly adsorb the *COOH intermediate, which is further reduced to CO* on the electrode surface. In addition, CO* is weakly adsorbed on the surface of noble metals, and thus CO easily desorbs from the surface of noble metal nanosheets.

Transition metals

Noble metals are expensive, and thus cost-effective transition metals are increasingly used for CO_2 electro-reduction[119]. For example, Zn nanosheets prepared by the hydrothermal method perform better than Zn-foil in the electro-reduction of CO_2 and show high selectivity toward CO[99]. 2D nanostructures exhibit high catalytic activity in CO_2 electro-reduction owing to the high density of edge sites. Xiao *et al.* reported that hexagonal Zn nanoplates prepared by cathodic electrochemical deposition [Figure 7A and B] are suitable for the electrochemical reduction of CO_2 to CO at a wide potential range[120]. FE_{CO} over Zn nanoplate can reach 94.2%, which is 2.2 times higher than that over Zn foil [Figure 7C]. The high catalytic performance of Zn nanoplates is attributed to the exposed Zn (100) facets and edges, where COOH* can form more easily than at any other facet, indicating that an increased edge-to-corner ratio can enhance the reactivity.

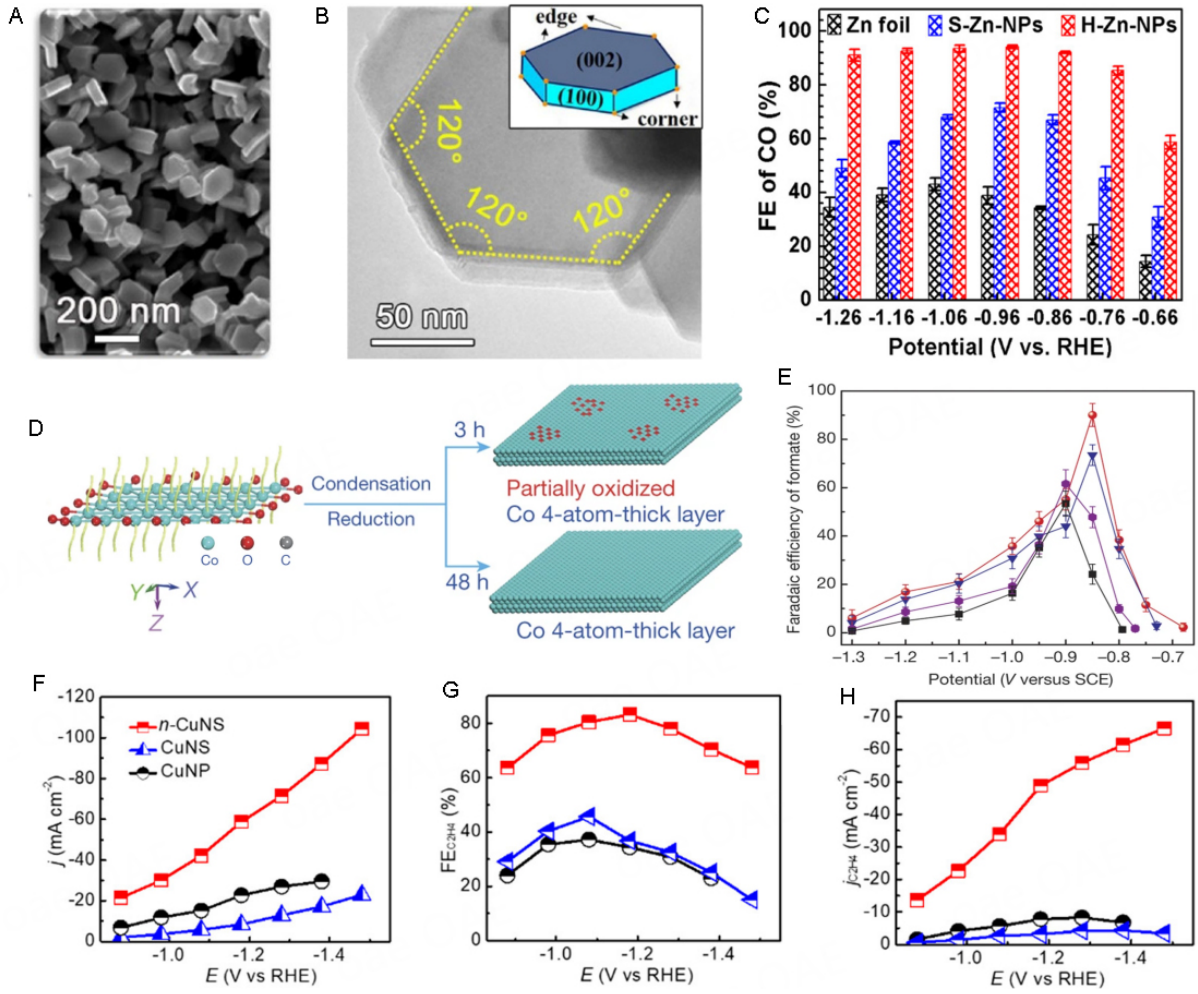

Figure 7. Electrochemical reduction of CO_2 over 2D transition metals. (A) SEM image of hexagonal Zn nanoplates. (B) TEM image of Zn nanoplates. (C) Plot of FE_{CO} *vs.* potential over different Zn electrodes[120]. (D) Schematic diagram of the partially oxidized and pure Co 4-atomic-layer. (E) Plot of $FE_{formate}$ *vs.* potential over different Co electrodes[105]. (F) Plot of current density *vs.* potential over different Cu electrodes. (G) Plot of FE_{C2H4} *vs.* potential over different Cu electrodes. (H) Plot of j_{C2H4} *vs.* potential over different Cu electrodes[101]. 2D: 2-dimensional; TEM: transmission electron microscopy.

Co is the first transition metal used in CO_2 electro-reduction. Gao *et al.* prepared a 4-atom-thick Co sheet with and without surface Co oxide for CO_2 electro-reduction [Figure 7D], achieving a high $FE_{formate}$ of 90.1% at a low overpotential of 0.85 V *vs.* SCE[105] [Figure 7E]. Moreover, the catalyst exhibits long-term stability, and FE_{HCOOH} remains at a high level of approximately 90% within 30 h. Volumetric CO_2 adsorption measurements were used to demonstrate that changes in the oxidation state of Co and increases in the surface area synergistically favor CO_2 adsorption, thereby enhancing catalytic performance. Porphyrin Co is one of the most efficient species for CO_2 electro-reduction because of the strong interaction between the metal and ligand. Han *et al.* prepared Co single-site catalysts by assembling Co-porphyrin molecules[121]. The catalyst can promote the conversion of CO_2 to CO with an FE of 96 % at an overpotential of 500 mV. This outstanding catalytic performance is attributed to the increase in the energy of d orbitals originating in the strong repulsive force between the ligand and electrons in the z-direction. Yin *et al.* recently prepared Co nanosheets for the conversion of CO_2 to C_{2+} products[122]. Co nanoparticles were first prepared by a hydrothermal reaction and then converted to Co nanosheets by exfoliation in formamide. Remarkably, ethanal is the main product of the Co nanosheet electrode with an $FE_{ethanal}$ of 60%. Ultraviolet photoelectron

spectroscopy was used to show that Co nanosheets have a wide electronic distribution near the Fermi level, resulting in rapid electron transfer. The electron-rich environment around Co 3d of Co nanosheets is beneficial for CO-CO coupling.

Bi is cheap and environmentally acceptable because of its low toxicity. Bi precursors are used to prepare Bi nanosheets *in situ* by a hydrothermal method[123], during which O is introduced into the Bi nanosheets. The as-prepared electrode can achieve an $FE_{formic\ acid}$ of > 90% with a current density of approximately 200 mA cm^{-2} in a flow cell. The catalytic performance remains unchanged when the Bi nanosheets are applied to a long-term test at -0.52 V *vs.* RHE for 10 h. Density functional theory (DFT) calculations suggest that the free energy for $*CO_2 \rightarrow *OCHO$ is respectively 0.46 eV and 0.17 eV over Bi and Bi-O, indicating that *in situ* construction of Bi nanosheets during electrode fabrication promotes the conversion of CO_2 to formic acid. Yang *et al.* prepared a Bi nanosheet-based catalyst by a solvothermal method, and the as-prepared electrode can achieve an $FE_{formate}$ of nearly 100% over a broad potential range[124]. Moreover, this electrode exhibits long-term stability at -0.8 V *vs.* RHE for 12 h. DFT calculations demonstrated that Bi(101) and Bi(111) planes can significantly stabilize the COOH* intermediate to promote the formation of formate.

Sn is another transition metal that can be used to convert CO_2 into valuable formate by electrochemical methods. A series of Sn nanosheets have been designed and synthesized for the electro-reduction of CO_2. Wu *et al.* prepared a very sensitive Sn nanosheet with a layer thickness of approximately 9.2 μm by directly spraying Sn catalyst ink onto a gas diffusion layer[125]. The Sn nanosheet electrode exhibits a high $FE_{formate}$, owing to the desirable proton concentration, electronic conduction, and gas diffusion of the 2D structure. The thickness of Sn nanosheets also influences the current density, FE, and operating potentials. An ultrathin Sn layer can significantly enhance these reduction-related properties, but an excessively thin layer may increase the oxidation rate of Sn, leading to poor stability. This problem can be resolved by confining metal layers into carbon materials[126,127]. Lei *et al.* reported a method to prepare Sn quantum sheets confined in graphene[100]. The confined nanostructure enhances CO_2 adsorption and rate-limiting electron transfer and stabilizes the $CO_2^{\bullet-}$ intermediate. As a result, the graphene confined Sn quantum sheet displays a current density of 21.1 mA cm^{-2} and $FE_{formate}$ of 89% at -1.8 V versus SCE, which is higher than that of the mixture of Sn nanoparticles and graphene. Electrochemical impedance spectroscopy was used to confirm the very low interfacial charge-transfer resistance, suggesting that the existence of 2D graphene can improve the conductivity of the electrocatalyst. Moreover, the electronic state of the complex interface can stabilize reaction intermediates, reducing the free energy barrier for the formation of products.

Among the elements, Cu is the most effective in harvesting various products, such as CO, HCOOH, and C_{2+} products, because Cu has a suitable binding energy between products and the surface of catalysts according to the Sabatier principle[128]. Thus, exploring Cu-based electrodes for CO_2 electro-reduction has become a vigorous research topic. Recently, numerous efforts have been dedicated to developing 2D Cu materials for the electro-reduction of CO_2 to hydrocarbons and alcohols [129].

In a pioneering work, Hori *et al.* reported the efficient electro-conversion of CO_2 to hydrocarbons and alcohols over an electrodeposited Cu sheet electrode in aqueous inorganic salt solutions[130]. KCl, K_2SO_4, $KClO_4$, and dilute HCO_3^- electrolytes favor the formation of ethylene and alcohols, while concentrated HCO_3^- and phosphate solutions prefer the generation of methane. Zhang *et al.* demonstrated that nanodefective Cu nanosheets (n-CuNS) effectively reduce CO_2 into C_2 products[101]. FE_{C2H4} over n-CuNS electrode is 83.2%, which is higher than that over Cu nanosheets with a smooth surface (CuNS, 45.7%) and Cu nanoparticles (CuNP, 37.2%). The current density and FE_{C2H4} over different electrodes at different applied potentials are shown in Figure 7F-H. Interestingly, n-CuNS does not produce CO, while CuNS and

CuNP convert CO_2 into CO in high quantities. Therefore, nano defects in Cu nanosheet significantly improve the current density because CO_2 adsorption and C-C coupling are boosted by the enrichment and confinement of reaction intermediates and OH^-. Chen *et al.* investigated the effects of grain boundary (GB) density and Cu^+/Cu^0 ratio during CO_2 electro-reduction[131]. As the GB density increases, $FE_{C_2H_4}$ first increases and then decreases, which is related to the content of Cu^+ in the catalyst during the reaction. Therefore, the GB density can activate CO_2 molecules, and Cu^+ can promote selectivity toward C_{2+} products.

2D metal nanomaterials have highly anisotropic characteristics, abundant coordination sites, and a special electronic structure. Moreover, 2D metals have a unique structure in the absence of external fields, which leads to special properties that can be exploited for electrocatalysis.

Metal oxide materials

Since the pioneering report on the catalytic behaviors of metal oxide semiconductor powders in the 1970s[132], the past decades have witnessed great progress in the fundamental study of metal oxide catalysts. Semiconductor metal oxides for CO_2 electro-reduction offer several advantages, including low cost, easy maintenance, and the potential to generate C_{2+} products. At present, many kinds of metal oxides have been used for CO_2 electro-reduction. It is worth pointing out that metal oxides are usually unstable and partially or entirely convert to low-valence metal oxide or zero-valence metallic species under negative potentials. Moreover, the final state and reconstruction of electrodes during electrolysis play important roles in CO_2 conversion[133,134].

Different ZnO nanosheets have been synthesized and employed as excellent electrodes for CO_2 electro-reduction[135,136]. A series of strategies, such as hydrothermal method, spray-coating, and electrodeposition, was used by Luo *et al.* to prepare ZnO precursors with different morphologies[137]. ZnO is reconstructed to a porous sheet-like structure, specifically hexagonal Zn crystals, regardless of the initial morphology and reduced to the metallic state during the electrochemistry process. ZnO nanosheets exhibit an FE_{CO} of 91.6% with a current density of 200 mA cm^{-2} at -0.62 V *vs.* RHE in a flow reactor. Overall, the reconstruction provides a high surface area, which enhances the catalytic activity and potentially promotes gas diffusion.

In addition to ZnO nanosheets, a number of other 2D metal oxide nanostructures, such as SnO_2, Co_3O_4, and CuO, have been tested for CO_2 electro-reduction. In particular, porous nanosheets are more advantageous. Han *et al.* synthesized porous SnO_2 nanosheets by a two-step method[102]. A precursor of SnS_2 nanosheets is first obtained by a hydrothermal method and subsequently annealed to obtain SnO_2 nanosheets with a highly porous architecture. The calcination step increases the surface area and active sites of SnO_2, resulting in a small onset potential, large current density, high FE_{HCOOH}, and high stability. Gao *et al.* prepared Co_3O_4 nanolayers for the selective electro-reduction of CO_2 to formate[138]. The catalyst exhibits good stability, and the current density negligibly changes within 40 h. The materials have abundant oxygen vacancies, which serve as active sites to stabilize reduction intermediates and reduce the activation energy barrier. Moreover, the valence of Co_3O_4 is retained, although the crystal structure is destroyed after the reaction owing to the existence of oxygen vacancies.

CuO is widely used in electro-reduction of CO_2 to C_{2+} products. CuO is reduced to Cu^+ and metallic Cu during CO_2 electro-reduction[139,140]. Liu *et al.* prepared an oxygen-rich ultrathin CuO nanoplate for the electro-reduction of CO_2 to C_2H_4 with an $FE_{C_2H_4}$ of 84.5%, which can be maintained for at least 55 h[103] [Figure 8A]. At the optimal current density of 75 mA cm^{-2} and a full-cell voltage of -3.1 V, the $FE_{C_2H_4}$ is 77.3% and the energy efficiency of C_2H_4 is 28.9% [Figure 8B and C]. Cu/Cu_2O heterogeneous interfaces are formed through the self-evolution of CuO nanoplate arrays during electrocatalysis. The impressive

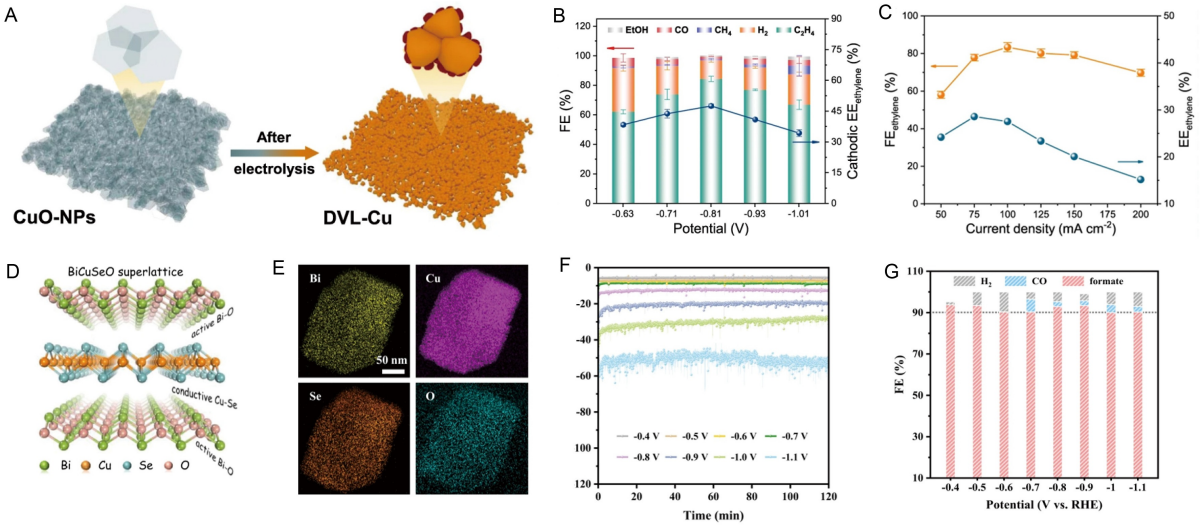

Figure 8. Electrochemical reduction of CO_2 over 2D metal oxides. (A) Schematic illustration of the electrochemical reconstruction of CuO nanosheets. (B) Plot of FE of various products *vs.* potential over the CuO electrode. (C) Plot of full cell potential and EE_{C2H4} *vs.* current density over the CuO electrode[103]. (D) Schematic illustration of the BiCuSeO superlattice. (E) EDS mapping images of BiCuSeO. (F) Chronoamperometric curves at different potentials over the BiCuSeO electrode. (G) $FE_{formate}$, FE_{CO}, and FE_{H2} *vs.* potential over the BiCuSeO electrode[142]. 2D: 2-dimensional; FE: Faradaic efficiency; EDS: energy dispersive spectroscopy.

performance is derived from Cu/Cu_2O interfaces. The enhanced adsorption of the *OCCOH intermediate on the surface of $Cu(110)/Cu_2O(110)$ facilitates the production of C_2H_4. A network comprising Ag and $S\text{-}Cu_2O/Cu$ is also formed by the reduction of CuO in Na_2S solution, followed by immersion in $AgNO_3$ solution[141]. The as-prepared catalyst exhibits an FE_{CH3OH} of 67.4% with a current density of approximately 122.7 mA cm^{-2} in a typical H-cell at -1.2 V *vs.* RHE using an ionic liquid (IL)-based electrolyte. Synergistic interaction of multiple atoms in the 2D nanostructure facilitates the practical electro-reduction of CO_2 to methanol. S can control the spatial position of adsorption to accommodate and stabilize the *CHO intermediate, while Ag supresses the hydrogen evolution reaction (HER) to provide a high FE_{CH3OH}.

Recently, polymetallic oxides have been developed for CO_2 electro-reduction owing to their structural flexibility. A tangible superlattice model of metal oxide and selenide for CO_2 electro-reduction was demonstrated by Duan *et al.*[142]. The as-prepared BiCuSeO (layer stacked superlattices) [Figure 8D and E] shows an $FE_{formate}$ of > 90% at a low overpotential [Figure 8F]. The outstanding catalytic activity is attributed to the active 2D $Bi_2O_2^{2+}$ sublayer. It is worth pointing out that the layer-stacked superlattices can inhibit the reduction of metal oxide and HER, resulting in long-term stability and a high $FE_{formate}$ over electrocatalysts [Figure 8G]. Zhao *et al.* reported that 2D $ZnGa_2O_4$ nanoplates prepared by an ion-exchange method can reduce CO_2 into CO at the relatively low applied potential of -1.4 V *vs.* Ag/AgCl, with a high FE_{CO} of 96%, owing to the high specific area of the nanoplates[143]. During CO_2 electro-reduction, partial Zn^{2+} reduces to Zn^+, and the Zn^{2+}/Zn^+ redox couple favors the activation of CO_2.

2D transition metal oxides have a large specific surface area, atomic-scale thickness, and abundant dangling bonds, leading to high catalytic performance in CO_2 electro-reduction. In principle, metal oxides are first reduced to the corresponding metals, and the as-reduced metal oxides become the active species for CO_2 electro-reduction. Defects and other active components are introduced into the final electrocatalysts during the reduction of metal oxides.

2D metal dichalcogenides

Transition metal dichalcogenides, such as MoS_2, WS_2, $MoSe_2$ and WSe_2, are common 2D nanostructures and can be easily prepared by simple exfoliation and CVD methods. These materials have a high surface-to-volume ratio and rich active sites, and thus they have the potential to convert CO_2 into valuable products.

During the past decades, MoS_2 has attracted considerable attention owing to its special 2D structure and property. Asadi *et al.* reported that excess d electrons on Mo-edge atoms and a low work function result in high catalytic performance[144] [Figure 9A and B]. The catalyst shows a current density of 65 mA cm^{-2} at -0.764 V *vs.* RHE, at which FE_{CO} reaches 98%. In contrast to bulk MoS_2, the edges of 2D MoS_2 are exposed to the electrolyte, leading to enhanced catalytic effectiveness. Additionally, by tailoring the edge structure of MoS_2, a low onset potential of 31 mV for CO_2 electro-reduction is achievable. 2D VA-$Mo_{1-x}M_xS_2$ (M = Nb and Ta) materials were prepared by a CVD method and applied as electrodes for CO_2 electro-reduction in an IL-based electrolyte[145]. The current density of Nb-doped MoS_2 is 50 times higher than that of pristine MoS_2 because doped Nb can shift the center of the d orbitals of Mo edge atoms, leading to weaker binding of CO. However, excessive Nb doping can increase the work function of MoS_2, which has a negative influence on the catalytic performance. Mao *et al.* demonstrated that modulating the MoS_2 edge structure by V, Zr, and Hf can promote the desorption of CO[146]. It is worth pointing out that dopants located close to the active Mo sites influence the catalytic activity.

Asadi *et al.* also synthesized a series of 2D transition metal dichalcogenides, including MoS_2, WS_2, $MoSe_2$ and WSe_2, by a chemical vapor transport method for CO_2 electro-reduction[147]. Among the as-prepared materials, WSe_2 shows the best catalytic performance, leading to an FE_{CO} of 24% with a current density of 18.95 mA cm^{-2} at -0.164 V *vs.* RHE (overpotential of 54 mV) in $EmimBF_4/H_2O$ (1:1) solution. The calculated work functions of the four catalysts decrease in the following sequence: MoS_2 > WS_2 > $MoSe_2$ > WSe_2, in agreement with experimental results.

In addition to 2D transition metal dichalcogenides, other 2D metal sulfides, such as SnS_2, also promote efficient electrochemical reduction of CO_2. Zheng *et al.* prepared SnS_2 nanosheets by an atomic layer deposition method[111]. Using over 2D SnS_2, the current density and $FE_{formate}$ at -0.75 V *vs.* RHE are 55 mA cm^{-2} and 93%, respectively. The catalyst also shows excellent stability, with $FE_{formate}$ decreasing by less than 2% after 40 h of electrolysis. The excellent catalytic performance is attributed to the presence of sulfur atoms on the catalyst surface, which increase the number of undercoordinated sites. A hybrid nanosheet consisting of SnS_2 and H [Figure 9C-F] was investigated by Zhang *et al.*[148]. The H-SnS_2 catalyst achieves a high $FE_{formate}$ of 93% at -0.9 V *vs.* RHE in 0.1 M $KHCO_3$ [Figure 9G-I], making it competitive in activity with pristine 2D metal dichalcogenides. The introduction of H onto the surface of the catalyst optimizes the structure of SnS_2 and increases the electron density in adjacent atoms, resulting in a lower reaction barrier for the formation of the HCOO* intermediate.

Transition metal dichalcogenides present a typical sandwich structure in which the metal atomic layer is sandwiched between two layers of sulfur atoms. Although the van der Waals force between each layer is very weak, strong covalent bonds in the plane ensure the stability of the 2D nanostructure. Therefore, 2D transition metal dichalcogenides exhibit excellent stability for long-term CO_2 electro-reduction.

2D carbon-based materials

Carbon-based materials represent a class of submetallic materials owing to the sp^2 hybrid state and the existence of metallized electrons on the surface. In the past decade, carbon-based materials have received increasing attention for electrocatalysis owing to their active edges, large surface area, and high charge carrier mobility[149-151]. The ultrahigh surface area and high electron transport along the carbon base plane

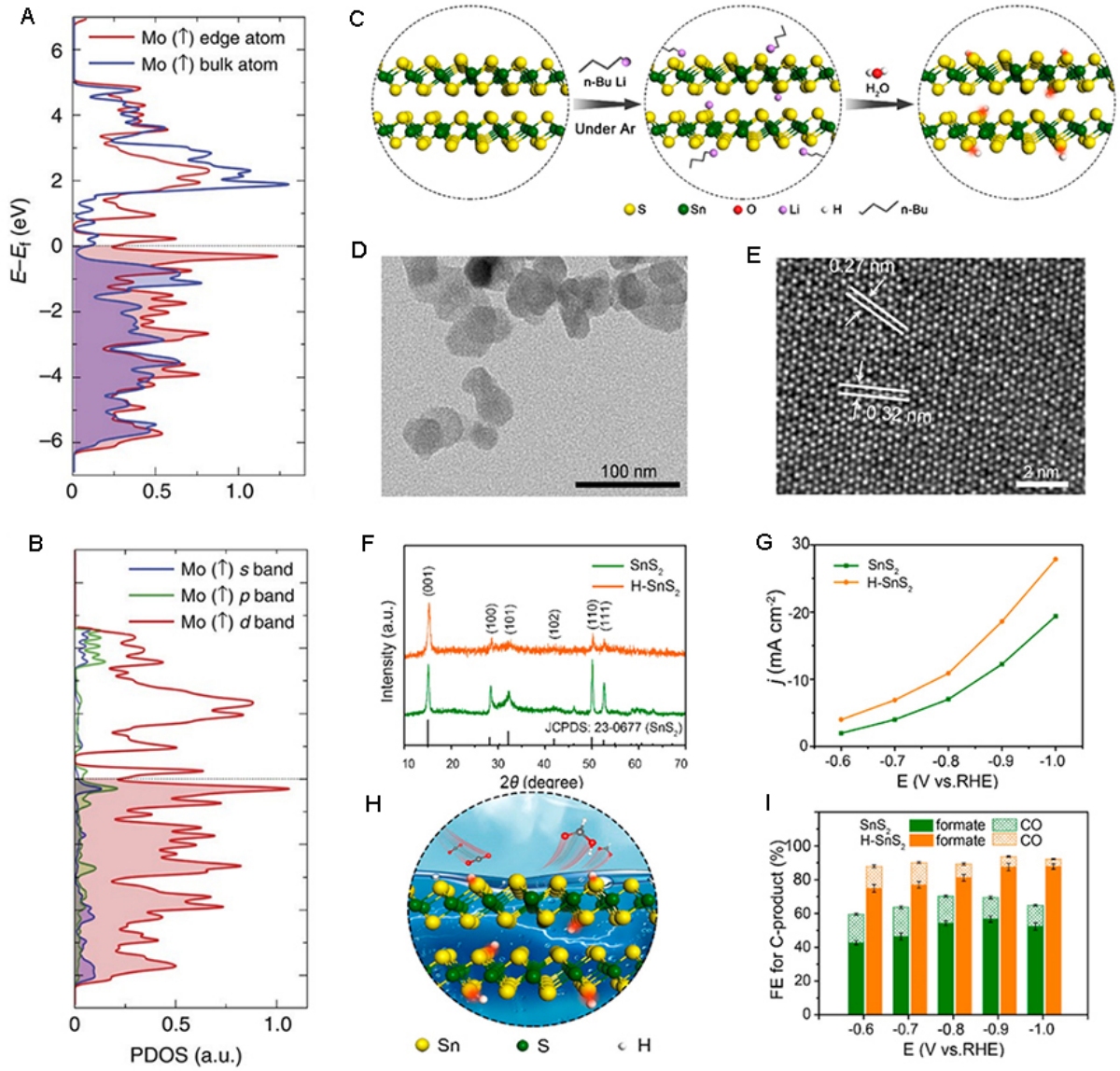

Figure 9. Electrochemical reduction of CO_2 over 2D metal dichalcogenides. (A) PDOS for the spin-up channel of Mo atoms at the edge and within the lattice. (B) PDOS for the spin-up channel of the s, p, and d orbitals of Mo-edge atoms[144]. (C) Schematic illustration of the synthesis of H-SnS_2 nanosheets. (D) TEM image of H-SnS_2 nanosheets. (E) HRTEM image of H-SnS_2 nanosheets. (F) XRD patterns of H-SnS_2 nanosheets. (G) Plot of current density *vs.* potential over SnS_2 and H-SnS_2 electrodes. (H) Structural model of H-SnS_2 nanosheets. (I) Plot of FE of products *vs.* potential over SnS_2 and H-SnS_2 electrodes[148]. 2D: 2-dimensional; PDOS: projected density of states; TEM: transmission electron microscopy; FE: Faradaic efficiency.

make 2D carbon-based materials suitable for the electrochemical reduction of CO_2.

Graphene is a representative of the carbon family and has been extensively explored in different research fields. Neither pure graphene nor graphene oxide (GO) is active in the electrochemical reduction of CO_2 because the π-π framework cannot effectively activate CO_2[152]. The electronic structure, physical structure, and morphology of graphene materials can be adjusted by heteroatom doping[153-155]. N-doped carbon has been widely studied because N is more electronegative than C. Four types of N exist in N-doped graphene: basal plane quaternary N, edge pyrrolic N, pyridinic N, and nitrilic N. Wang *et al.* prepared a nitrogen-doped graphene by high-temperature pyrolysis[110]. The nitrogen-doped graphene shows high catalytic

activity in the electrochemical conversion of CO_2 to formate, leading to an $FE_{formate}$ of 73%. Recently, many groups have reported that N-doped carbon materials can promote the conversion of CO_2 to C_2 products. For example, Song *et al.* developed a novel method to synthesize nitrogen-doped mesoporous carbon using a copolymer as the template[156] [Figure 10A]. Pyridinic N sites in this material facilitate the formation of CO*, which is subsequently coupled. Thus, an $FE_{ethanol}$ of 77% at -0.56 V *vs.* RHE is obtained [Figure 10B-D]. Hao *et al.* also confirmed that pyridinic N promotes efficient CO_2 electro-reduction[157]. DFT calculations showed that the catalytic activity of different N species in CO formation decreases according to the following sequence: pyridinic N > graphitic N > pyrrolic N [Figure 10E]. Moreover, pyridinic N can also induce C-C coupling[156], thus boosting the generation of C_{2+} products.

N-doped carbon hybrid nanosheets, normally prepared by wet chemical synthesis, have the advantages of feasible operation, low cost, and large-scale synthesis, and thus they are widely employed as electrodes for the electro-reduction of CO_2. Genovese *et al.* demonstrated that iron (III) oxyhydroxide on nitrogen-doped graphene exhibits an FE_{CH_3COOH} of 61% at -0.5 V *vs.* Ag/AgCl[158]. The N-doped graphene not only boosts the activation of CO_2 but also stabilizes Fe(II) species to suppress HER. Lu *et al.* reported that pyridinic N-rich carbon layers encapsulating Ni nanoparticles prepared by a hydrothermal method and pyrolysis exhibit a high FE_{CO} of 95% and long-term stability of 92 h at -1.05 V *vs.* RHE[159]. The excellent catalytic performance is attributed to the core-shell structure, which promotes mass transfer and the synergistic effect of N-C and metal oxides, while pyridinic-N increases the CO_2 adsorption capacity and decreases the reaction energy barrier for *COOH formation, the rate-determining step.

Single-atom loaded carbon-based materials are also attractive for CO_2 electro-reduction. Guo *et al.* reported that atomic indium on carbon (In/NC) exhibits a current density of 39.4 mA cm^{-2} and FE_{CO} of 97.2% in 0.5 M $BmimPF_6$/MeCN[160]. N-coordinated atomic indium catalysts [Figure 10F] can effectively activate CO_2 and hinder the formation of formic acid. In-N coordination is dominant in In/Ac [Figure 10G], indicating that atomic In is stabilized by the surrounding N. Owing to the high double-layer capacitance, large CO_2 adsorption capacity, and low interfacial charge transfer resistance, In/NC achieves a turnover frequency of approximately 40,000 h^{-1} without appreciable decrease during 24 h of electrolysis [Figure 10H]. DFT results show that the centers of the s and p orbitals of atomic In (In-N) downshift significantly compared with bulk In. A local alkaline environment is produced as the electron density reconfigures because of N coordination. Shi *et al.* reported that Cu single-site in graphdiyne enhances the electro-reduction of CO_2 to methane, with an FE_{CH_4} of 81% and high stability in 1.0 M KOH at -1.2 V *vs.* RHE[161]. The acetylenic bond in the catalyst suppresses the formation of multi-carbon products, and the as-constructed Cu-C bond favors the formation of the *OCHO intermediate, resulting in the high FE_{CH_4}.

2D carbon materials, such as graphene, have unique electronic properties, including the ambipolar electric field effect and quantum Hall effect. These unique electronic properties enable carbon materials to exhibit metal-like behaviors, which is beneficial for CO_2 electro-reduction. Moreover, 2D carbon materials are often used as substrates for doping or decoration, broadening their utilizations in CO_2 electro-reduction. Nevertheless, developing highly efficient 2D carbon based materials for CO_2 electro-reduction still has a long way to go.

Other 2D materials

In addition to traditional 2D materials, many other 2D nanostructures are potential candidates to realize highly efficient electro-conversion of CO_2 to valuable products. Recently, a series of novel 2D materials was applied to the electrochemical reduction of CO_2 to various products, and their special structure determines the catalytic performance.

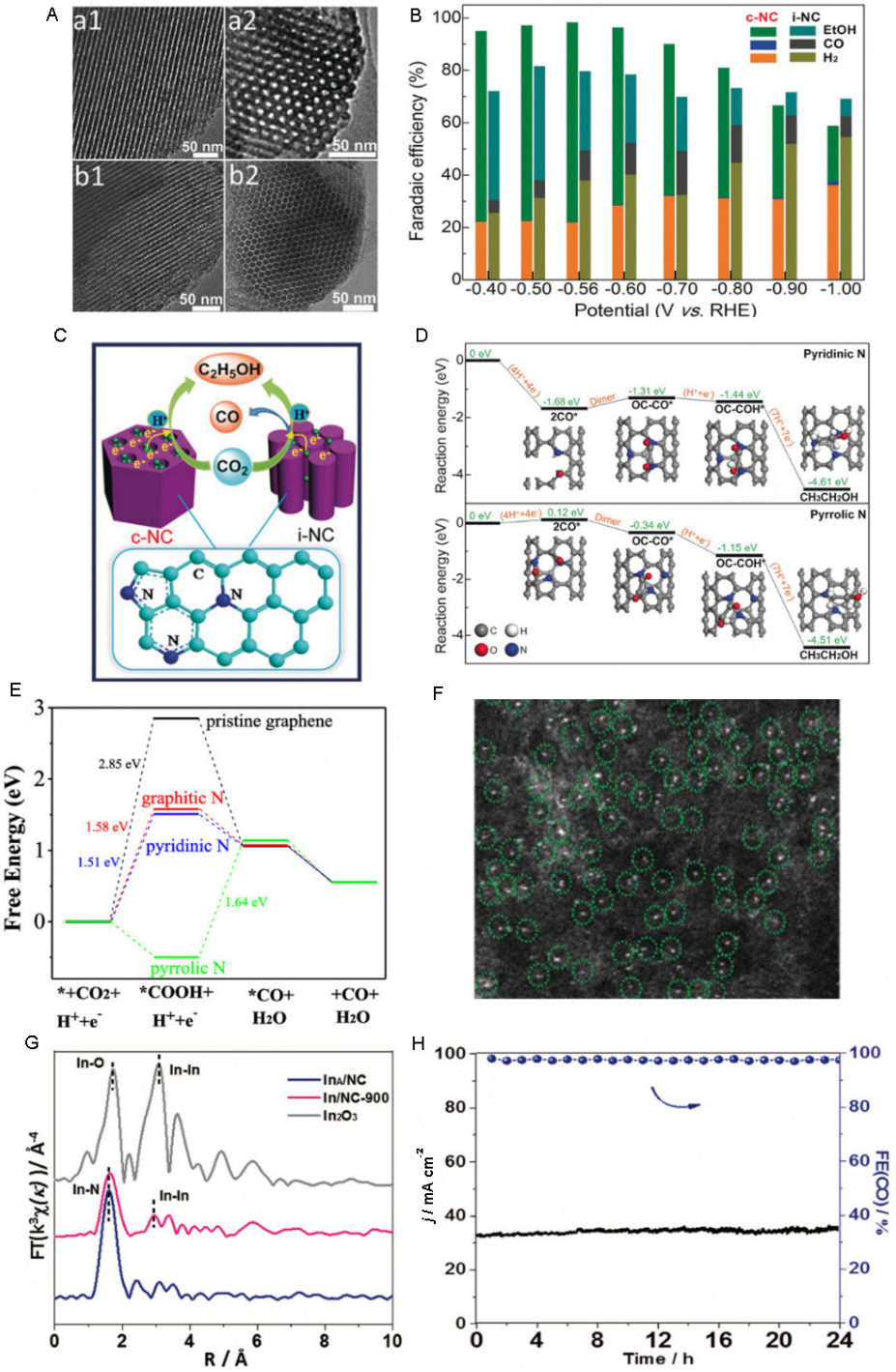

Figure 10. Electrochemical reduction of CO_2 over 2D carbon-based materials. (A) TEM images of nitrogen-doped mesoporous carbons. (B) FEs of various products *vs.* potential over nitrogen-doped mesoporous carbon electrodes. (C) Schematic illustration of CO_2 electro-reduction over nitrogen-doped mesoporous carbon electrodes. (D) DFT calculations of the electro-reduction of CO_2 to ethanol over different pyrrolic N sites[156]. (E) Free-energy diagrams of CO_2 electro-reduction over different N species[157]. (F) Magnified high-angle annular dark-field scanning transmission electron microscopy image of In/NC. (G) Fourier transform of In K-edge extended X-ray absorption fine structure spectra of different In-based catalysts. (H) Long-term stability of CO_2 electro-reduction over In/NC[160]. 2D: 2-dimensional; TEM: transmission electron microscopy; FE: Faradaic efficiency; DFT: density functional theory.

MOFs have attracted considerable attention in the field of catalysis and energy conversion owing to their

rich active sites, diverse structure, and controllable morphology. Kang *et al.* designed and synthesized a highly efficient MOF catalyst [Cu_2(L)-e/Cu] by *in situ* growth on Cu-foam substrates in IL-based solutions[162]. MOF particles with assemblies of approximately 50 nm on the surface of the Cu-foam form a thin film [Figure 11A-D]. The MOF thin film contains 15.3% of uncoupled Cu(II) sites, which are considered active sites for the electro-reduction of CO_2 to formic acid. The as-prepared catalyst achieves a high current density of 65.8 mA cm^2 and $FE_{formate}$ of 90.5% at -1.8 V *vs.* Ag/Ag^+ in an IL-based electrolyte [Figure 11E and F]. DFT calculations showed that free Cu(II) centers in defect Cu_2(L) are produced by the rupture of Cu-O bond to promote CO_2 binding.

With their specific layered structure, 2D transition metal carbides and nitrides (MXenes) show high conductivity, high chemical stability, and multiple catalytic sites. Li *et al.* calculated the catalytic activity of single-component MXenes by DFT, and the results showed that $Cr_3C_2T_x$ and $Mo_3C_2T_x$ are the best candidates for the electrochemical reduction of CO_2 to CH_4[163]. These two materials favor the activation of CO_2 rather than H_2O, resulting in highly efficient CO_2 electro-reduction and HER suppression. Qu *et al.* prepared N-doped Ti_3C_2 MXene nanosheets with abundant titanium vacancies (V_{Ti}) by a facile NH_3-etching pyrolysis approach to achieve an FE_{CO} of 92% and current density of 10 mA cm^{-2} at -0.7 V *vs.* RHE in seawater as the electrolyte[164]. The coexistence of N and V_{Ti} modulates the electronic structure, leading to a decrease in the reaction energy barriers for *COOH formation.

Molecule-metal catalysts are molecular adsorbates that can accumulate intermediates during CO_2 electro-reduction. Li *et al.* immobilized FeTPP[Cl] onto a Cu substrate to produce a molecular metal catalyst [Figure 11G-I], which was used as an electrode for the electrochemical reduction of CO_2[113]. FeTPP[Cl] does not reduce into iron nanoparticles or nanoclusters under the operating conditions, and the electrode can achieve an $FE_{ethanol}$ of 41% with a current density of 124 mA cm^{-2} at -0.82 V *vs.* RHE [Figure 11J and K]. *In situ* surface-enhanced Raman spectroscopy and DFT calculations were used to reveal that a local high concentration of CO induced by the electrode promotes C-C coupling to ethanol. Han *et al.* deposited N-substituted pyridinium additives as a film on a Cu electrode for the electro-reduction of CO_2 into C_{2+} products and, furthermore, demonstrated that the film promotes C-C coupling and impedes HER[165].

Substrates functionalized by molecular monolayers are considered a type of 2D electrodes, which have been extensively studied for CO_2 electro-reduction[166-169]. For instance, Fang *et al.* reported that a Au electrode modified with 4-pyridinylethanemercaptan(4-PEM) exhibits high CO_2 selectivity toward formate compared with pristine Au electrode[170]. The high surface concentration of H^+ impedes the first electron transfer to $CO_2^{\bullet-}$. Moreover, the organometallic complex was also modified as a gas diffusion layer to fabricate a 2D electrode, which was employed as a cathode in a flow cell microreactor for CO_2 electro-reduction. The electrode exhibits an FE_{HCOOH} of 76% and FE_{CO} of 10%[171].

Covalent organic frameworks (COFs), composed of organic monomers and hybrid atoms, are new porous organic materials with high crystallinity. Covalent bonds are formed through reversible chemical reactions. COFs have gradually been applied to CO_2 electrocatalysis owing to their designable structure, low density, adjustable pore structure, and easily modified structure. Bandomo *et al.* synthesized Mn^I tricarbonyl-based 2D COFs for CO_2 electro-reduction[172]. The as-prepared 2D COFs exhibit a low onset potential of 190 mV, at which a current density of 12 mA cm^{-2} and FE_{CO} of 72% are achieved, and the catalyst remains active even after 16 h. Zhu *et al.* developed metalloporphyrin-tetrathiafulvalene-based COFs (M-TTCOFs), which have impressive catalytic performance, achieving an FE_{CO} of > 90% and high cycling stability (> 40 h)[173]. Tetrathiafulvalene in the 2D nanostructure serves as an electron donor to construct an efficient pathway to accelerate electron transfer and obtain a low activation energy for CO_2 reduction.

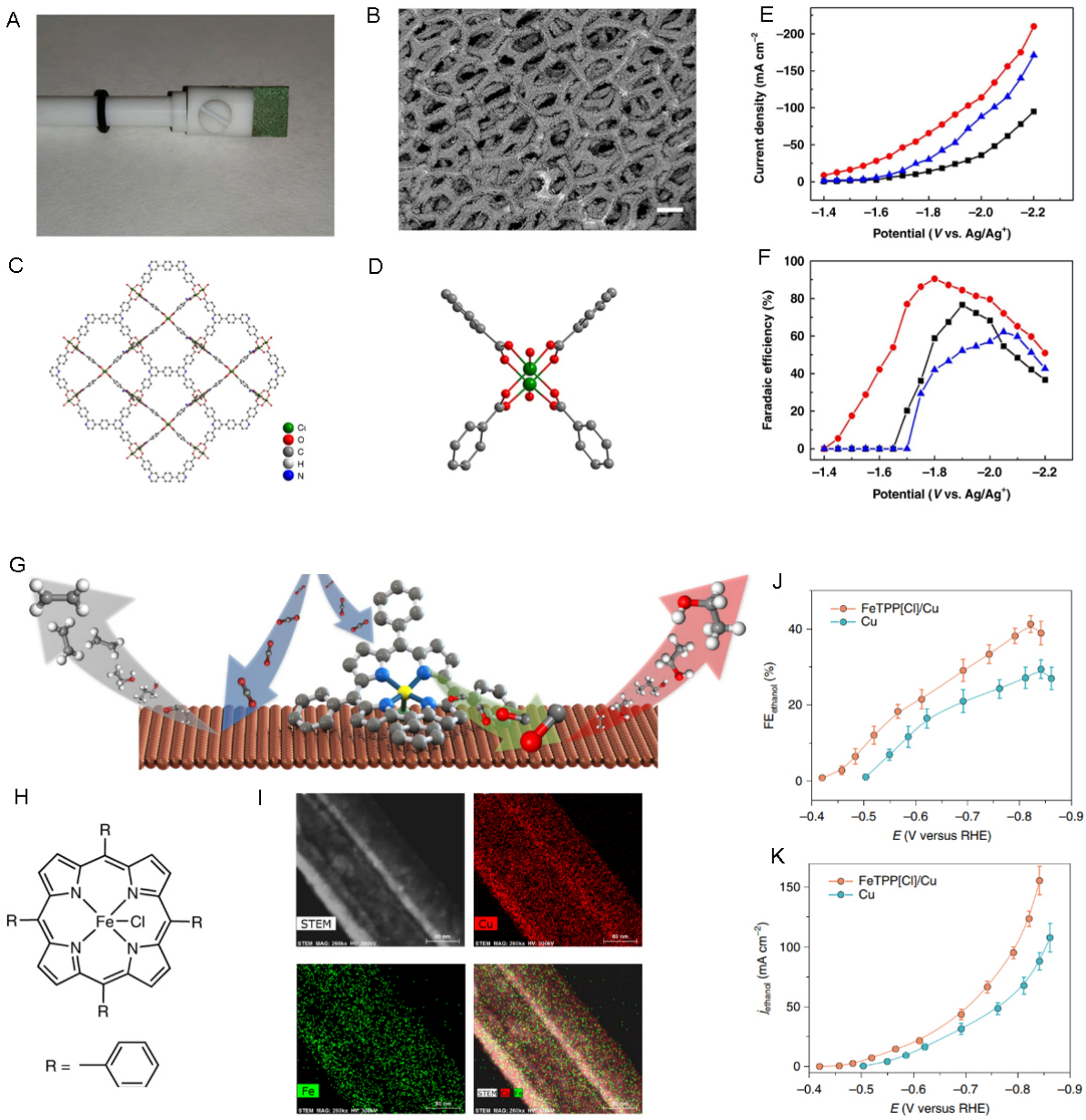

Figure 11. Electrochemical reduction of CO_2 over other 2D materials. (A) Photograph of Cu_2(L)-e/Cu. (B) SEM image of Cu_2(L)-e/Cu. (C and D) Views of the crystal structure of Cu_2(L). (E) Plot of current density *vs.* potential over Cu_2(L)-e/Cu. (F) Plot of FE_{HCOOH} *vs.* potential over Cu_2(L)-e/Cu[162]. (G) Schematic illustration of the heterogenization of molecular complexes on the Cu surface. (H) Molecular structure of FeTPP[Cl]. (I) Elemental mapping of FeTPP[Cl] on Cu. (J) Plot of $FE_{ethanol}$ and (K) $j_{ethanol}$ *vs.* potential over different electrodes[113]. 2D: 2-dimensional.

To understand the catalytic nature of 2D materials, the electrochemical properties of the same material with various nanostructures are summarized in Table 1. In general, 2D catalysts exhibit excellent catalytic performance compared with the corresponding bulk catalysts.

SUMMARY AND OUTLOOK

This review summarizes the progress on various 2D materials with a focus on preparation methods and applications to CO_2 electro-reduction. Without any doubt, advances in the synthesis of 2D materials over

the past decade have produced 2D materials that markedly enhance the efficiency of CO_2 electro-reduction.

Methods based on different principles for the preparation of 2D nanostructures have been reviewed. Wet-chemical synthesis and CVD are still the dominant methods for the mass production of 2D materials. It remains urgent to understand how to control the number of layers, flake dimensions, defect levels, and yield of 2D materials. Surface decoration is very important to broaden the application of 2D materials, and it is also an effective way to realize high catalytic performance for CO_2 electro-reduction. Selecting the electrode material is the first step of catalysis. The distribution and production rate of products are determined by the thermodynamic and kinetic energy barriers of reaction pathways. In principle, the electron distribution and the charge density of the catalyst surface affect the kinetic energy barriers. Therefore, selecting electrode materials with appropriate electronic properties can enhance the efficiency of CO_2 electroreduction.

Selectivity is an essential evaluation indicator of the catalytic performance of 2D materials. Although great progress has been made, the reaction pathway determined by the 2D structure is still unclear. In other words, catalytic performance as a function of structural parameters remains unexplored. Strategies such as morphology modification, doping, and surface decoration have been developed to achieve high catalytic performance of 2D materials. Nevertheless, designing *in situ* characterization techniques and developing theoretical calculations to unveil the effect of the structure of 2D materials on CO_2 electro-reduction are highly significant.

Nowadays, high current density can be easily realized by potential increase, structure design, surface functionalization, and cell modification. However, high potentials require high energy consumption, which is inconsistent with the concept of sustainable development. High potentials also influence the long-term stability and promote HER. The surface structure and activity of 2D materials also change under extremely negative potentials. Additionally, most cases of CO_2 electro-reduction over 2D materials are currently being investigated in laboratories owing to the high cost, difficulties in scale-up, and uncontrollable operation. Large-scale synthesis of 2D materials and the preparation of stable and large 2D material-based electrodes are the first important steps into industrialization. We believe that 2D nanostructures will gradually prevail in CO_2 electro-reduction and contribute to carbon neutrality worldwide.

DECLARATIONS

Authors' contributions

Prepared the manuscript: Yin Y
Performed manuscript correcting: Kang X, Han B

Availability of data and materials

Not applicable.

Financial support and sponsorship

This work is supported by National Natural Science Foundation of China (22273108, 22073104) and Beijing Natural Science Foundation (2222043).

Conflict of interest

All authors declared that there are no conflicts of interest.

Ethical approval and consent to participate

Not applicable.

Consent for publication

Not applicable.

REFERENCES

1. He M, Sun Y, Han B. Green carbon science: efficient carbon resource processing, utilization, and recycling towards carbon neutrality. *Angew Chem Int Ed Engl* 2022;61:e202112835. DOI PubMed
2. Mehla S, Kandjani AE, Babarao R, et al. Porous crystalline frameworks for thermocatalytic CO_2 reduction: an emerging paradigm. *Energy Environ Sci* 2021;14:320-52. DOI
3. Wu Y, Jiang Z, Lu X, Liang Y, Wang H. Domino electroreduction of CO_2 to methanol on a molecular catalyst. *Nature* 2019;575:639-42. DOI PubMed
4. Yang HB, Hung S, Liu S, et al. Atomically dispersed Ni(I) as the active site for electrochemical CO_2 reduction. *Nat Energy* 2018;3:140-7. DOI
5. Li CW, Ciston J, Kanan MW. Electroreduction of carbon monoxide to liquid fuel on oxide-derived nanocrystalline copper. *Nature* 2014;508:504-7. DOI PubMed
6. Li L, Li X, Sun Y, Xie Y. Rational design of electrocatalytic carbon dioxide reduction for a zero-carbon network. *Chem Soc Rev* 2022;51:1234-52. DOI PubMed
7. Zhang J, An B, Li Z, et al. Neighboring Zn-Zr sites in a metal-organic framework for CO_2 hydrogenation. *J Am Chem Soc* 2021;143:8829-37. DOI PubMed
8. Koshy DM, Nathan SS, Asundi AS, et al. Bridging thermal catalysis and electrocatalysis: catalyzing CO_2 conversion with carbon-based materials. *Angew Chem Int Ed Engl* 2021;60:17472-80. DOI PubMed
9. Sun Q, Wang N, Yu J. Advances in catalytic applications of zeolite-supported metal catalysts. *Adv Mater* 2021;33:e2104442. DOI PubMed
10. Rao H, Schmidt LC, Bonin J, Robert M. Visible-light-driven methane formation from CO_2 with a molecular iron catalyst. *Nature* 2017;548:74-7. DOI PubMed
11. Barman S, Singh A, Rahimi FA, Maji TK. Metal-free catalysis: a redox-active donor-acceptor conjugated microporous polymer for selective visible-light-driven CO_2 reduction to CH_4. *J Am Chem Soc* 2021;143:16284-92. DOI
12. Zhao W, Zhai D, Liu C, et al. Unblocked intramolecular charge transfer for enhanced CO_2 photoreduction enabled by an imidazolium-based ionic conjugated microporous polymer. *Appl Catal B-environ* 2022;300:120719. DOI
13. Ozden A, Wang Y, Li F, et al. Cascade CO_2 electroreduction enables efficient carbonate-free production of ethylene. *Joule* 2021;5:706-19. DOI
14. Qiu XF, Zhu HL, Huang JR, Liao PQ, Chen XM. Highly selective CO_2 electroreduction to C_2H_4 using a metal-organic framework with dual active sites. *J Am Chem Soc* 2021;143:7242-6. DOI
15. Ma W, Xie S, Liu T, et al. Electrocatalytic reduction of CO_2 to ethylene and ethanol through hydrogen-assisted C-C coupling over fluorine-modified copper. *Nat Catal* 2020;3:478-87. DOI
16. Cheng Y, Hou P, Wang X, Kang P. CO_2 electrolysis system under industrially relevant conditions. *Acc Chem Res* 2022;55:231-40. DOI PubMed
17. Gao D, Wei P, Li H, Lin L, Wang G, Bao X. Designing electrolyzers for electrocatalytic CO_2 reduction. *Acta Phys-Chim Sin* 2021;37:2009021. DOI
18. Li N, Si D, Wu Q, Wu Q, Huang Y, Cao R. Boosting electrocatalytic CO_2 reduction with conjugated bimetallic CO/Zn polyphthalocyanine frameworks. *CCS Chem* 2022. DOI
19. Jia S, Ma X, Sun X, Han B. Electrochemical transformation of CO_2 to value-added chemicals and fuels. *CCS Chem* 2022;4:3213-29. DOI
20. Cheng Y, Hou P, Pan H, Shi H, Kang P. Selective electrocatalytic reduction of carbon dioxide to oxalate by lead tin oxides with low overpotential. *Appl Catal B-environ* 2020;272:118954. DOI
21. Yang D, Zhu Q, Han B. Electroreduction of CO_2 in ionic liquid-based electrolytes. *Innovation* 2020;1:100016. DOI PubMed PMC
22. Schwarz HA, Dodson RW. Reduction potentials of CO_2- and the alcohol radicals. *J Phys Chem* 1989;93:409-14. DOI
23. Zhao K, Quan X. Carbon-based materials for electrochemical reduction of CO_2 to C_{2+} oxygenates: recent progress and remaining challenges. *ACS Catal* 2021;11:2076-97. DOI
24. Cheng Y, Hou J, Kang P. Integrated capture and electroreduction of flue gas CO_2 to formate using amine functionalized SnO_x nanoparticles. *ACS Energy Lett* 2021;6:3352-8. DOI
25. Chang C, Chen W, Chen Y, et al. Recent progress on two-dimensional materials. *Acta Phys-Chim Sin* 2021;37:2108017. DOI
26. Fu Q, Liu H, Tang X, Wang R, Chen M, Liu Y. Multifunctional two-dimensional polymers for perovskite solar cells with efficiency exceeding 24%. *ACS Energy Lett* 2022;7:1128-36. DOI
27. Song D, Chen X, Lin Z, et al. Usability identification framework and high-throughput screening of two-dimensional materials in

lithium ion batteries. *ACS Nano* 2021;15:16469-77. DOI PubMed

28. Wang J, Malgras V, Sugahara Y, Yamauchi Y. Electrochemical energy storage performance of 2D nanoarchitectured hybrid materials. *Nat Commun* 2021;12:3563. DOI PubMed PMC
29. Liang Q, Zhang Q, Zhao X, Liu M, Wee ATS. Defect engineering of two-dimensional transition-metal dichalcogenides: applications, challenges, and opportunities. *ACS Nano* 2021;15:2165-81. DOI PubMed
30. Shamzhy M, Gil B, Opanasenko M, Roth WJ, Čejka J. MWW and MFI frameworks as model layered zeolites: structures, transformations, properties, and activity. *ACS Catal* 2021;11:2366-96. DOI
31. Xu L, Ma T, Shen Y, et al. Rational manipulation of stacking arrangements in three-dimensional zeolites built from two-dimensional zeolitic nanosheets. *Angew Chem Int Ed Engl* 2020;59:19934-9. DOI PubMed
32. Li G, Shen Y, Zhao S, et al. Construction of rGO-SnO_2 heterojunction for enhanced hydrogen detection. *Appl Surf Sci* 2022;585:152623. DOI
33. Li S, Thiering G, Udvarhelyi P, Ivády V, Gali A. Carbon defect qubit in two-dimensional WS_2. *Nat Commun* 2022;13:1210. DOI PubMed PMC
34. Kovalska E, Antonatos N, Luxa J, Sofer Z. Edge-hydrogenated germanene by electrochemical decalcification-exfoliation of $CaGe_2$: Germanene-enabled vapor sensor. *ACS Nano* 2021;15:16709-18. DOI PubMed
35. Maiti R, Patil C, Saadi MASR, et al. Strain-engineered high-responsivity $MoTe_2$ photodetector for silicon photonic integrated circuits. *Nat Photonics* 2020;14:578-84. DOI
36. Liu R, Wang F, Liu L, et al. Band alignment engineering in two-dimensional transition metal dichalcogenide-based heterostructures for photodetectors. *Small Structures* 2021;2:2000136. DOI
37. An C, Nie F, Zhang R, et al. Two-dimensional material-enhanced flexible and self-healable photodetector for large-area photodetection. *Adv Funct Mater* 2021;31:2100136. DOI
38. Wang K, Chen J, Yan X. MXene Ti_3C_2 memristor for neuromorphic behavior and decimal arithmetic operation applications. *Nano Energy* 2021;79:105453. DOI
39. Cao G, Gao C, Wang J, Lan J, Yan X. Memristor based on two-dimensional titania nanosheets for multi-level storage and information processing. *Nano Res* 2022;15:8419-27. DOI
40. Tang B, Veluri H, Li Y, et al. Wafer-scale solution-processed 2D material analog resistive memory array for memory-based computing. *Nat Commun* 2022;13:3037. DOI PubMed PMC
41. Nguyen TN, Salehi M, Le QV, Seifitokaldani A, Dinh CT. Fundamentals of electrochemical CO_2 reduction on single-metal-atom catalysts. *ACS Catal* 2020;10:10068-95. DOI
42. Wang Y, Liu J, Wang Y, Al-Enizi AM, Zheng G. Tuning of CO_2 reduction selectivity on metal electrocatalysts. *Small* 2017;13:1701809. DOI PubMed
43. Shimoni R, Shi Z, Binyamin S, et al. Electrostatic secondary-sphere interactions that facilitate rapid and selective electrocatalytic CO_2 reduction in a fe-porphyrin-based metal-organic framework. *Angew Chem Int Ed Engl* 2022;61:e202206085. DOI PubMed PMC
44. Zhou P, Shen Y, Zhao S, et al. Hydrothermal synthesis of novel ternary hierarchical MoS_2/TiO_2/clinoptilolite nanocomposites with remarkably enhanced visible light response towards xanthates. *Appl Surf Sci* 2021;542:148578. DOI
45. Sun Z, Ma T, Tao H, Fan Q, Han B. Fundamentals and challenges of electrochemical CO_2 reduction using two-dimensional materials. *Chem* 2017;3:560-87. DOI
46. Fang W, Huang L, Zaman S, Wang Z, Han Y, Xia BY. Recent progress on two-dimensional electrocatalysis. *Chem Res Chin Univ* 2020;36:611-21. DOI
47. Li Z, Zhai L, Ge Y, et al. Wet-chemical synthesis of two-dimensional metal nanomaterials for electrocatalysis. *Natl Sci Rev* 2022;9:nwab142. DOI PubMed PMC
48. Ma Y, Shi R, Zhang T. Research progress on triphase interface electrocatalytic carbon dioxide reduction. *Acta Chimica Sinica* 2021;79:369. DOI
49. Pan F, Yang Y. Designing CO_2 reduction electrode materials by morphology and interface engineering. *Energy Environ Sci* 2020;13:2275-309. DOI
50. Gu H, Zhong L, Shi G, et al. Graphdiyne/Graphene heterostructure: a universal 2D scaffold anchoring monodispersed transition-metal phthalocyanines for selective and durable CO_2 electroreduction. *J Am Chem Soc* 2021;143:8679-88. DOI PubMed
51. Chen S, Kang Z, Hu X, et al. Delocalized spin states in 2D atomic layers realizing enhanced electrocatalytic oxygen evolution. *Adv Mater* 2017;29:1701687. DOI PubMed
52. Wang P, Zhao D, Yin L. Two-dimensional matrices confining metal single atoms with enhanced electrochemical reaction kinetics for energy storage applications. *Energy Environ Sci* 2021;14:1794-834. DOI
53. Li X, Wang S, Li L, Zu X, Sun Y, Xie Y. Opportunity of atomically thin two-dimensional catalysts for promoting CO_2 electroreduction. *Acc Chem Res* 2020;53:2964-74. DOI PubMed
54. Rong X, Wang HJ, Lu XL, Si R, Lu TB. Controlled synthesis of a vacancy-defect single-atom catalyst for boosting CO_2 electroreduction. *Angew Chem Int Ed Engl* 2020;59:1961-5. DOI PubMed
55. Pan J, Sun Y, Deng P, et al. Hierarchical and ultrathin copper nanosheets synthesized via galvanic replacement for selective electrocatalytic carbon dioxide conversion to carbon monoxide. *Appl Catal B-environ* 2019;255:117736. DOI
56. Chia X, Pumera M. Characteristics and performance of two-dimensional materials for electrocatalysis. *Nat Catal* 2018;1:909-21. DOI

57. Li Y, Chen J, Chen S, et al. In situ confined growth of bismuth nanoribbons with active and robust edge sites for boosted CO_2 electroreduction. *ACS Energy Lett* 2022;7:1454-61. DOI
58. Liu W, Qi J, Bai P, Zhang W, Xu L. Utilizing spatial confinement effect of N atoms in micropores of coal-based metal-free material for efficiently electrochemical reduction of carbon dioxide. *Appl Catal B-environ* 2020;272:118974. DOI
59. Niu ZZ, Gao FY, Zhang XL, et al. Hierarchical copper with inherent hydrophobicity mitigates electrode flooding for high-rate CO_2 Electroreduction to multicarbon products. *J Am Chem Soc* 2021;143:8011-21. DOI PubMed
60. Lv K, Teng C, Shi M, et al. Hydrophobic and electronic properties of the E-MoS_2 nanosheets induced by FAS for the CO_2 electroreduction to syngas with a wide range of CO/H_2 ratios. *Adv Funct Mater* 2018;28:1802339. DOI
61. Zeng L, You C, Hong N, Zhang X, Liang T. Large-scale preparation of 2D metal films by a top-down approach. *Adv Eng Mater* 2020;22:1901359. DOI
62. Xu Y, Sprick RS, Brownbill NJ, et al. Bottom-up wet-chemical synthesis of a two-dimensional porous carbon material with high supercapacitance using a cascade coupling/cyclization route. *J Mater Chem A* 2021;9:3303-8. DOI
63. Watts MC, Picco L, Russell-Pavier FS, et al. Production of phosphorene nanoribbons. *Nature* 2019;568:216-20. DOI PubMed
64. Novoselov KS, Geim AK, Morozov SV, et al. Electric field effect in atomically thin carbon films. *Science* 2004;306:666-9. DOI PubMed
65. Li H, Lu G, Wang Y, et al. Mechanical exfoliation and characterization of single- and few-layer nanosheets of WSe_2, TaS_2, and $TaSe_2$. *Small* 2013;9:1974-81. DOI PubMed
66. Huang Y, Pan YH, Yang R, et al. Universal mechanical exfoliation of large-area 2D crystals. *Nat Commun* 2020;11:2453. DOI PubMed PMC
67. Coleman JN, Lotya M, O'Neill A, et al. Two-dimensional nanosheets produced by liquid exfoliation of layered materials. *Science* 2011;331:568-71. DOI PubMed
68. Ma R, Sasaki T. Two-dimensional oxide and hydroxide nanosheets: controllable high-quality exfoliation, molecular assembly, and exploration of functionality. *Acc Chem Res* 2015;48:136-43. DOI PubMed
69. Dakhchoune M, Villalobos LF, Semino R, et al. Gas-sieving zeolitic membranes fabricated by condensation of precursor nanosheets. *Nat Mater* 2021;20:362-9. DOI PubMed
70. Obst M, Arnauts G, Cruz AJ, et al. Chemical vapor deposition of ionic liquids for the fabrication of ionogel films and patterns. *Angew Chem Int Ed Engl* 2021;60:25668-73. DOI PubMed
71. Novoselov KS, Mishchenko A, Carvalho A, Castro Neto AH. 2D materials and van der Waals heterostructures. *Science* 2016;353:aac9439. DOI PubMed
72. Kim KS, Zhao Y, Jang H, et al. Large-scale pattern growth of graphene films for stretchable transparent electrodes. *Nature* 2009;457:706-10. DOI PubMed
73. Li X, Cai W, An J, et al. Large-area synthesis of high-quality and uniform graphene films on copper foils. *Science* 2009;324:1312-4. DOI PubMed
74. Browne MP, Novotný F, Manzanares Palenzuela CL, Šturala J, Sofer Z, Pumera M. 2H and 2H/1T-transition metal dichalcogenide films prepared via powderless gas deposition for the hydrogen evolution reaction. *ACS Sustainable Chem Eng* 2019;7:16440-9. DOI
75. Yin C, Gong C, Chu J, et al. Ultrabroadband photodetectors up to 10.6 μm based on 2D Fe_3O_4 nanosheets. *Adv Mater* 2020;32:e2002237. DOI PubMed
76. Zhou J, Lin J, Huang X, et al. A library of atomically thin metal chalcogenides. *Nature* 2018;556:355-9. DOI PubMed
77. Li W, Qiu X, Lv B, et al. Free-standing 2D ironene with magnetic vortex structure at room temperature. *Matter* 2022;5:291-301. DOI
78. Xu T, Li S, Li A, et al. Structural evolution of atomically thin 1T'-$MoTe_2$ alloyed in chalcogen atmosphere. *Small Struct* 2022;3:2200025. DOI
79. Sun Z, Liao T, Dou Y, et al. Generalized self-assembly of scalable two-dimensional transition metal oxide nanosheets. *Nat Commun* 2014;5:3813. DOI PubMed
80. Peng Y, Tan Q, Huang H, et al. Customization of functional MOFs by a modular design strategy for target applications. *Chem Synth* 2022;2:15. DOI
81. Wang L, Saji SE, Wu L, et al. Emerging synthesis strategies of 2D MOFs for electrical devices and integrated circuits. *Small* 2022;18:e2201642. DOI PubMed
82. Pham HTB, Choi JY, Huang S, et al. Imparting functionality and enhanced surface area to a 2D electrically conductive MOF via macrocyclic linker. *J Am Chem Soc* 2022;144:10615-21. DOI PubMed
83. Zheng Y, Zheng S, Xu Y, Xue H, Liu C, Pang H. Ultrathin two-dimensional cobalt-organic frameworks nanosheets for electrochemical energy storage. *Chem Eng J* 2019;373:1319-28. DOI
84. Sun X, Lu L, Zhu Q, et al. MoP nanoparticles supported on indium-doped porous carbon: outstanding catalysts for highly efficient CO_2 electroreduction. *Angew Chem Int Ed Engl* 2018;57:2427-31. DOI PubMed
85. Sun X, Zhu Q, Kang X, et al. Molybdenum-bismuth bimetallic chalcogenide nanosheets for highly efficient electrocatalytic reduction of carbon dioxide to methanol. *Angew Chem Int Ed Engl* 2016;55:6771-5. DOI PubMed
86. Lu L, Guo W, Chen C, et al. Synthesis of Sn_4P_3/reduced graphene oxide nanocomposites as highly efficient electrocatalysts for CO_2 reduction. *Green Chem* 2020;22:6804-8. DOI
87. Rabiee H, Ge L, Zhang X, et al. Shape-tuned electrodeposition of bismuth-based nanosheets on flow-through hollow fiber gas

diffusion electrode for high-efficiency CO_2 reduction to formate. *Appl Catal B-environ* 2021;286:119945. DOI

88. Abdelazim NM, Noori YJ, Thomas S, et al. Lateral growth of MoS_2 2D material semiconductors over an insulator via electrodeposition. *Adv Electron Mater* 2021;7:2100419. DOI
89. Feng C, Wang F, Liu Z, et al. A self-healing catalyst for electrocatalytic and photoelectrochemical oxygen evolution in highly alkaline conditions. *Nat Commun* 2021;12:5980. DOI PubMed PMC
90. Shen L, Zhang Q, Luo J, et al. Heteroatoms adjusting amorphous FeMn-based nanosheets via a facile electrodeposition method for full water splitting. *ACS Sustainable Chem Eng* 2021;9:5963-71. DOI
91. Tan SF, Reidy K, Lee S, et al. Multilayer graphene - a promising electrode material in liquid cell electrochemistry. *Adv Funct Materials* 2021;31:2104628. DOI
92. Lukatskaya MR, Mashtalir O, Ren CE, et al. Cation intercalation and high volumetric capacitance of two-dimensional titanium carbide. *Science* 2013;341:1502-5. DOI PubMed
93. Lukatskaya MR, Halim J, Dyatkin B, et al. Room-temperature carbide-derived carbon synthesis by electrochemical etching of MAX phases. *Angew Chem Int Ed Engl* 2014;53:4877-80. DOI PubMed
94. Ghidiu M, Lukatskaya MR, Zhao MQ, Gogotsi Y, Barsoum MW. Conductive two-dimensional titanium carbide "clay" with high volumetric capacitance. *Nature* 2014;516:78-81. DOI PubMed
95. Liu L, Yang X, Xie Y, et al. A universal lab-on-salt-particle approach to 2D single-layer ordered mesoporous materials. *Adv Mater* 2020;32:e1906653. DOI PubMed
96. Zhang F, Zhang J, Zhang B, et al. CO_2 controls the oriented growth of metal-organic framework with highly accessible active sites. *Nat Commun* 2020;11:1431. DOI PubMed PMC
97. Ko KY, Song JG, Kim Y, et al. Improvement of gas-sensing performance of large-area tungsten disulfide nanosheets by surface functionalization. *ACS Nano* 2016;10:9287-96. DOI PubMed
98. Lee C, Zhao Y, Wang C, Mitchell DRG, Wallace GG. Rapid formation of self-organised Ag nanosheets with high efficiency and selectivity in CO_2 electroreduction to CO. *Sustain Energy Fuels* 2017;1:1023-7. DOI
99. Zhang T, Li X, Qiu Y, et al. Multilayered Zn nanosheets as an electrocatalyst for efficient electrochemical reduction of CO_2. *J Catal* 2018;357:154-62. DOI
100. Lei F, Liu W, Sun Y, et al. Metallic tin quantum sheets confined in graphene toward high-efficiency carbon dioxide electroreduction. *Nat Commun* 2016;7:12697. DOI PubMed PMC
101. Zhang B, Zhang J, Hua M, et al. Highly electrocatalytic ethylene production from CO_2 on nanodefective Cu nanosheets. *J Am Chem Soc* 2020;142:13606-13. DOI PubMed
102. Han N, Wang Y, Deng J, et al. Self-templated synthesis of hierarchical mesoporous SnO_2 nanosheets for selective CO_2 reduction. *J Mater Chem A* 2019;7:1267-72. DOI
103. Liu W, Zhai P, Li A, et al. Electrochemical CO_2 reduction to ethylene by ultrathin CuO nanoplate arrays. *Nat Commun* 2022;13:1877. DOI PubMed PMC
104. Liu K, Wang J, Shi M, Yan J, Jiang Q. Simultaneous achieving of high faradaic efficiency and CO Partial current density for CO_2 reduction via robust, noble-metal-free Zn nanosheets with favorable adsorption energy. *Adv Energy Mater* 2019;9:1900276. DOI
105. Gao S, Lin Y, Jiao X, et al. Partially oxidized atomic cobalt layers for carbon dioxide electroreduction to liquid fuel. *Nature* 2016;529:68-71. DOI PubMed
106. Gao S, Jiao X, Sun Z, et al. Ultrathin CO_3O_4 layers realizing optimized CO_2 electroreduction to formate. *Angew Chem Int Ed Engl* 2016;55:698-702. DOI PubMed
107. Han N, Wang Y, Yang H, et al. Ultrathin bismuth nanosheets from in situ topotactic transformation for selective electrocatalytic CO_2 reduction to formate. *Nat Commun* 2018;9:1320. DOI PubMed PMC
108. Geng Z, Kong X, Chen W, et al. Oxygen vacancies in ZnO nanosheets enhance CO_2 electrochemical reduction to CO. *Angew Chem Int Ed Engl* 2018;57:6054-9. DOI PubMed
109. Chu M, Chen C, Guo W, et al. Enhancing electroreduction of CO_2 over Bi_2 WO_6 nanosheets by oxygen vacancies. *Green Chem* 2019;21:2589-93. DOI
110. Wang H, Chen Y, Hou X, Ma C, Tan T. Nitrogen-doped graphenes as efficient electrocatalysts for the selective reduction of carbon dioxide to formate in aqueous solution. *Green Chem* 2016;18:3250-6. DOI
111. Zheng X, De Luna P, García de Arquer FP, et al. Sulfur-modulated tin sites enable highly selective electrochemical reduction of CO_2 to formate. *Joule* 2017;1:794-805. DOI
112. Zhang A, Liang Y, Li H, et al. In-situ surface reconstruction of InN nanosheets for efficient CO_2 electroreduction into formate. *Nano Lett* 2020;20:8229-35. DOI PubMed
113. Li F, Li YC, Wang Z, et al. Cooperative CO_2-to-ethanol conversion via enriched intermediates at molecule-metal catalyst interfaces. *Nat Catal* 2020;3:75-82. DOI
114. Yu Y, Lee SJ, Theerthagiri J, et al. Reconciling of experimental and theoretical insights on the electroactive behavior of C/Ni nanoparticles with AuPt alloys for hydrogen evolution efficiency and non-enzymatic sensor. *Chem Eng J* 2022;435:134790. DOI
115. Yu Y, Lee SJ, Theerthagiri J, Lee Y, Choi MY. Architecting the AuPt alloys for hydrazine oxidation as an anolyte in fuel cell: comparative analysis of hydrazine splitting and water splitting for energy-saving H_2 generation. *Appl Catal B-environ* 2022;316:121603. DOI
116. Lu Q, Rosen J, Zhou Y, et al. A selective and efficient electrocatalyst for carbon dioxide reduction. *Nat Commun* 2014;5:3242. DOI

PubMed

117. Mistry H, Reske R, Zeng Z, et al. Exceptional size-dependent activity enhancement in the electroreduction of CO_2 over Au nanoparticles. *J Am Chem Soc* 2014;136:16473-6. DOI PubMed
118. Zhao Y, Tan X, Yang W, et al. Surface reconstruction of ultrathin palladium nanosheets during electrocatalytic CO_2 reduction. *Angew Chem Int Ed Engl* 2020;59:21493-8. DOI PubMed
119. Wang Z, Li C, Yamauchi Y. Nanostructured nonprecious metal catalysts for electrochemical reduction of carbon dioxide. *Nano Today* 2016;11:373-91. DOI
120. Xiao J, Gao MR, Liu S, Luo JL. Hexagonal Zn nanoplates enclosed by Zn(100) and Zn(002) facets for highly selective CO_2 electroreduction to CO. *ACS Appl Mater Interfaces* 2020;12:31431-8. DOI
121. Han J, An P, Liu S, et al. Reordering d orbital energies of single-site catalysts for CO_2 electroreduction. *Angew Chem Int Ed Engl* 2019;58:12711-6. DOI PubMed
122. Yin J, Yin Z, Jin J, et al. A new hexagonal cobalt nanosheet catalyst for selective CO_2 conversion to ethanal. *J Am Chem Soc* 2021;143:15335-43. DOI PubMed
123. Yang J, Wang X, Qu Y, et al. Bi-based metal-organic framework derived leafy bismuth nanosheets for carbon dioxide electroreduction. *Adv Energy Mater* 2020;10:2001709. DOI
124. Yang H, Han N, Deng J, et al. Selective CO_2 reduction on 2D mesoporous Bi nanosheets. *Adv Energy Mater* 2018;8:1801536. DOI
125. Wu J, Sharma PP, Harris BH, Zhou X. Electrochemical reduction of carbon dioxide: IV dependence of the Faradaic efficiency and current density on the microstructure and thickness of tin electrode. *J Power Sources* 2014;258:189-94. DOI
126. Wu D, Wang X, Fu X, Luo J. Ultrasmall Bi nanoparticles confined in carbon nanosheets as highly active and durable catalysts for CO_2 electroreduction. *Appl Catal B-environ* 2021;284:119723. DOI
127. Shifa TA, Vomiero A. Confined catalysis: progress and prospects in energy conversion. *Adv Energy Mater* 2019;9:1902307. DOI
128. Xiao C, Zhang J. Architectural design for enhanced C_2 product selectivity in electrochemical CO_2 reduction using Cu-based catalysts: a review. *ACS Nano* 2021;15:7975-8000. DOI
129. Zhang Z, Bian L, Tian H, et al. Tailoring the surface and interface structures of copper-based catalysts for electrochemical reduction of CO_2 to ethylene and ethanol. *Small* 2022;18:e2107450. DOI PubMed
130. Hori Y, Murata A, Takahashi R. Formation of hydrocarbons in the electrochemical reduction of carbon dioxide at a copper electrode in aqueous solution. *J Chem Soc, Faraday Trans 1* 1989;85:2309. DOI
131. Chen C, Sun X, Yan X, et al. A strategy to control the grain boundary density and Cu^+/Cu^0 ratio of Cu-based catalysts for efficient electroreduction of CO_2 to C2 products. *Green Chem* 2020;22:1572-6. DOI
132. Inoue T, Fujishima A, Konishi S, Honda K. Photoelectrocatalytic reduction of carbon dioxide in aqueous suspensions of semiconductor powders. *Nature* 1979;277:637-8. DOI
133. Han Z, Han D, Chen Z, et al. Steering surface reconstruction of copper with electrolyte additives for CO_2 electroreduction. *Nat Commun* 2022;13:3158. DOI PubMed PMC
134. Sang J, Wei P, Liu T, et al. A reconstructed $Cu_2P_2O_7$ catalyst for selective CO_2 electroreduction to multicarbon products. *Angew Chem Int Ed Engl* 2022;61:e202114238. DOI
135. Xiang Q, Li F, Wang J, et al. Heterostructure of ZnO nanosheets/Zn with a highly enhanced edge surface for efficient CO_2 electrochemical reduction to CO. *ACS Appl Mater Interfaces* 2021;13:10837-44. DOI PubMed
136. Sikam P, Takahashi K, Roongcharoen T, et al. Effect of 3d-transition metals doped in ZnO monolayers on the CO_2 electrochemical reduction to valuable products: first principles study. *Appl Surf Sci* 2021;550:149380. DOI
137. Luo W, Zhang Q, Zhang J, Moioli E, Zhao K, Züttel A. Electrochemical reconstruction of ZnO for selective reduction of CO_2 to CO. *Appl Catal B-environ* 2020;273:119060. DOI
138. Gao S, Sun Z, Liu W, et al. Atomic layer confined vacancies for atomic-level insights into carbon dioxide electroreduction. *Nat Commun* 2017;8:14503. DOI PubMed PMC
139. Cheng D, Zhao ZJ, Zhang G, et al. The nature of active sites for carbon dioxide electroreduction over oxide-derived copper catalysts. *Nat Commun* 2021;12:395. DOI PubMed PMC
140. Yuan X, Chen S, Cheng D, et al. Controllable Cu^0-Cu^+ sites for electrocatalytic reduction of carbon dioxide. *Angew Chem Int Ed Engl* 2021;60:15344-7. DOI
141. Li P, Bi J, Liu J, et al. In situ dual doping for constructing efficient CO_2-to-methanol electrocatalysts. *Nat Commun* 2022;13:1965. DOI
142. Duan J, Liu T, Zhao Y, et al. Active and conductive layer stacked superlattices for highly selective CO_2 electroreduction. *Nat Commun* 2022;13:2039. DOI PubMed PMC
143. Zhao M, Gu Y, Chen P, et al. Highly selective electrochemical CO_2 reduction to CO using a redox-active couple on low-crystallinity mesoporous $ZnGa_2O_4$ catalyst. *J Mater Chem A* 2019;7:9316-23. DOI
144. Asadi M, Kumar B, Behranginia A, et al. Robust carbon dioxide reduction on molybdenum disulphide edges. *Nat Commun* 2014;5:4470. DOI PubMed
145. Abbasi P, Asadi M, Liu C, et al. Tailoring the edge structure of molybdenum disulfide toward electrocatalytic reduction of carbon dioxide. *ACS Nano* 2017;11:453-60. DOI PubMed
146. Mao X, Wang L, Xu Y, Li Y. Modulating the MoS_2 edge structures by doping transition metals for electrocatalytic CO_2 reduction. *J Phys Chem C* 2020;124:10523-9. DOI

147. Asadi M, Kim K, Liu C, et al. Nanostructured transition metal dichalcogenide electrocatalysts for CO_2 reduction in ionic liquid. *Science* 2016;353:467-70. DOI PubMed
148. Zhang A, Liang Y, Li H, et al. Electronic tuning of SnS_2 nanosheets by hydrogen incorporation for efficient CO_2 electroreduction. *Nano Lett* 2021;21:7789-95. DOI
149. Ma X, Du J, Sun H, et al. Boron, nitrogen co-doped carbon with abundant mesopores for efficient CO_2 electroreduction. *Appl Catal B-environ* 2021;298:120543. DOI
150. Tuci G, Rossin A, Zhang X, Pham-huu C, Giambastiani G. Exohedrally functionalized carbon-based networks as catalysts for electrochemical syntheses. *Curr Opin Green Sustain Chem* 2022;33:100579. DOI
151. Zhang X, Xue D, Jiang S, et al. Rational confinement engineering of MOF-derived carbon-based electrocatalysts toward CO_2 reduction and O_2 reduction reactions. *InfoMat* 2022:4. DOI
152. Hasani A, Teklagne MA, Do HH, et al. Graphene-based catalysts for electrochemical carbon dioxide reduction. *Carbon Energy* 2020;2:158-75. DOI PubMed PMC
153. Tao H, Gao Y, Talreja N, et al. Two-dimensional nanosheets for electrocatalysis in energy generation and conversion. *J Mater Chem A* 2017;5:7257-84. DOI
154. Wang ZL, Choi J, Xu M, et al. Optimizing electron densities of Ni-N-C complexes by hybrid coordination for efficient electrocatalytic CO_2 reduction. *ChemSusChem* 2020;13:929-37. DOI PubMed
155. Lee SJ, Theerthagiri J, Nithyadharseni P, et al. Heteroatom-doped graphene-based materials for sustainable energy applications: a review. *Renew Sust Energ Rev* 2021;143:110849. DOI
156. Song Y, Chen W, Zhao C, Li S, Wei W, Sun Y. Metal-free nitrogen-doped mesoporous carbon for electroreduction of CO_2 to ethanol. *Angew Chem Int Ed Engl* 2017;56:10840-4. DOI PubMed
157. Hao X, An X, Patil AM, et al. Biomass-derived N-doped carbon for efficient electrocatalytic CO_2 reduction to CO and Zn-CO_2 batteries. *ACS Appl Mater Interfaces* 2021;13:3738-47. DOI
158. Genovese C, Schuster ME, Gibson EK, et al. Operando spectroscopy study of the carbon dioxide electro-reduction by iron species on nitrogen-doped carbon. *Nat Commun* 2018;9:935. DOI PubMed PMC
159. Lu Q, Chen C, Di Q, et al. Dual role of pyridinic-N doping in carbon-coated Ni nanoparticles for highly efficient electrochemical CO_2 reduction to CO over a wide potential range. *ACS Catal* 2022;12:1364-74. DOI
160. Guo W, Tan X, Bi J, et al. Atomic indium catalysts for switching CO_2 electroreduction products from formate to CO. *J Am Chem Soc* 2021;143:6877-85. DOI PubMed
161. Shi G, Xie Y, Du L, et al. Constructing Cu-C bonds in a graphdiyne-regulated Cu single-atom electrocatalyst for CO_2 reduction to CH_4. *Angew Chem Int Ed Engl* 2022;61:e202203569. DOI
162. Kang X, Li L, Sheveleva A, et al. Electro-reduction of carbon dioxide at low over-potential at a metal-organic framework decorated cathode. *Nat Commun* 2020;11:5464. DOI PubMed PMC
163. Li N, Chen X, Ong WJ, et al. Understanding of electrochemical mechanisms for CO_2 capture and conversion into hydrocarbon fuels in transition-metal carbides (MXenes). *ACS Nano* 2017;11:10825-33. DOI
164. Qu D, Peng X, Mi Y, et al. Nitrogen doping and titanium vacancies synergistically promote CO_2 fixation in seawater. *Nanoscale* 2020;12:17191-5. DOI PubMed
165. Han Z, Kortlever R, Chen HY, Peters JC, Agapie T. CO_2 reduction selective for C(≥ 2) products on polycrystalline copper with N-substituted pyridinium additives. *ACS Cent Sci* 2017;3:853-9. DOI
166. Costentin C, Savéant JM. Molecular approach to catalysis of electrochemical reaction in porous films. *Curr Opin Electrochem* 2019;15:58-65. DOI
167. Stuardi FM, Tiozzo A, Rotundo L, Leclaire J, Gobetto R, Nervi C. Efficient electrochemical reduction of CO_2 to formate in methanol solutions by Mn-functionalized electrodes in the presence of amines. *Chem Eur J* 2022;28:e202104377. DOI PubMed PMC
168. McCarthy BD, Beiler AM, Johnson BA, Liseev T, Castner AT, Ott S. Analysis of electrocatalytic metal-organic frameworks. *Coord Chem Rev* 2020;406:213137. DOI PubMed PMC
169. Sun C, Gobetto R, Nervi C. Recent advances in catalytic CO_2 reduction by organometal complexes anchored on modified electrodes. *New J Chem* 2016;40:5656-61. DOI
170. Fang Y, Flake JC. Electrochemical reduction of CO_2 at functionalized Au electrodes. *J Am Chem Soc* 2017;139:3399-405. DOI PubMed
171. Filippi J, Rotundo L, Gobetto R, et al. Turning manganese into gold: efficient electrochemical CO_2 reduction by a fac-Mn(apbpy)$(Co)_3$Br complex in a gas-liquid interface flow cell. *Chem Eng J* 2021;416:129050. DOI
172. Dubed Bandomo GC, Mondal SS, Franco F, et al. Mechanically constrained catalytic $Mn(CO)_3$ Br single sites in a two-dimensional covalent organic framework for CO_2 electroreduction in H_2O. *ACS Catal* 2021;11:7210-22. DOI
173. Zhu HJ, Lu M, Wang YR, et al. Efficient electron transmission in covalent organic framework nanosheets for highly active electrocatalytic carbon dioxide reduction. *Nat Commun* 2020;11:497. DOI PubMed PMC

Ye *et al. Chem Synth* 2022;2:20
DOI: 10.20517/cs.2022.25

Chemical Synthesis

Research Article

Open Access

Check for updates

Alkalinity-controlled zeolite nucleation and growth: ultrafast synthesis of total-morphology zeolite L mesocrystals and adsorption evaluation

Zhaoqi Ye[1,#], Lingtao Kong[1,#], Yang Zhao[1], Chunna Zhang[1], Xue Yang[1], Kexin Yan[1], Yahong Zhang[1], Hongbin Zhang[2,*], Yi Tang[1,*]

[1]Department of Chemistry, Laboratory of Advanced Materials, Collaborative Innovation Center of Chemistry for Energy Materials and Shanghai Key Laboratory of Molecular Catalysis and Innovative Materials, Fudan University, Shanghai 200433, China.
[2]Institute for Preservation of Chinese Ancient Books, Fudan University Library, Fudan University, Shanghai 200433, China.
[#]Both authors contributed equally to this work.

***Correspondence to:** Prof. Yi Tang, Department of Chemistry, Laboratory of Advanced Materials, Collaborative Innovation Center of Chemistry for Energy Materials and Shanghai Key Laboratory of Molecular Catalysis and Innovative Materials, Fudan University, Shanghai 200433, China. E-mail: yitang@fudan.edu.cn; Dr. Hongbin Zhang, Institute for Preservation of Chinese Ancient Books, Fudan University Library, Fudan University, Shanghai 200433, China. E-mail: zhanghongbin@fudan.edu.cn

How to cite this article: Ye Z, Kong L, Zhao Y, Zhang C, Yang X, Yan K, Zhang Y, Zhang H, Tang Y. Alkalinity-controlled zeolite nucleation and growth: ultrafast synthesis of total-morphology zeolite L mesocrystals and adsorption evaluation. *Chem Synth* 2022;2:20. https://dx.doi.org/10.20517/cs.2022.25

Received: 8 Sep 2022 **First Decision:** 29 Sep 2022 **Revised:** 18 Oct 2022 **Accepted:** 9 Nov 2022 **Published:** 28 Nov 2022

Academic Editors: Bao-Lian Su, Jun Xu **Copy Editor:** Peng-Juan Wen **Production Editor:** Peng-Juan Wen

Abstract

Owing to the intrinsic complexity of crystallization and the heterogeneity of precursors, the specific stages and corresponding behaviors of an actual crystallization system remain ambiguous, which makes the univariate-controlled crystallization-kinetics-regulated synthesis and design of zeolite morphology and porosity an unrealized blueprint. In this study, a facile and univariate modulation (i.e., OH^-/SiO_2) strategy was developed to regulate zeolite crystallization kinetics, and zeolite L mesocrystals were synthesized rapidly (within 1-2 h) with almost all **LTL** morphologies (from cylindrical or disc-like shapes to nanoclusters or nanocrystals) in the simplest SiO_2-Al_2O_3-K_2O-H_2O system. Using time-resolved analysis of the change in the solid-liquid Si/Al nutrient and crystallinity evolution, the intertwined and complex crystallization processes of zeolite L were clearly distinguished into four distinct stages: induction, nucleation, growth, and ripening. Under alkalinity-controlled conditions, the reactivity, Si/Al distribution, and state of aluminosilicates were critical to the formation of short-range order in the amorphous matrix, which greatly influenced the nucleation frequency and assembly state. Subsequently, these nucleation differences evoked correspondingly different kinetic growth behaviors. A putative alkalinity-controlled nonclassical crystallization mechanism was uncovered, and its validity was evaluated by analyzing morphology

evolution, NH_4F etching, and the effects of modifiers. Furthermore, adsorption tests demonstrated the high adsorption capacity of a series of zeolite L for guest molecules with various sizes and properties (e.g., gaseous aromatic hydrocarbon, aqueous dye, and protein).

Keywords: Zeolite L, crystallization mechanism, morphology regulation, nonclassical crystallization, adsorption performance

INTRODUCTION

Exploring the crystallization mechanism is one of the most fundamental and vital parts of research on crystalline materials because it leads to endless possibilities for the engineering and functionalization of material structures[1-7]. In the crystallization system of inorganic materials, such as zeolites, it is widely accepted that crystal growth not only depends on the addition of simple ions or small molecules (classical crystallization mechanism[8,9]) but also involves the assembly of a series of more complex and evolvable "particles"[9,10] - including crystalline[11], semi-crystalline[12] or amorphous oligomers, clusters, and nanoparticles[13] (nonclassical crystallization mechanism). These particles attach to the surface of nuclei with a certain spatial orientation[14-16], forming orderly assembled superstructure crystals with nanoparticles as the basic unit, i.e., mesocrystals[17-19]. If we can comprehensively understand and effectively control the nonclassical assembly behavior of crystal materials, then it will be possible to pre-design mesocrystal products with configurable morphologies targeting specific applications.

With the aim of reducing the diffusion limitation of zeolites and regulating the properties of zeolites for macromolecular adsorption and liquid-phase reactions, the last two decades have witnessed researchers devising different ways to introduce mesopores into zeolitic microporous systems[20], such as designing novel organic structure-directing agents[21-23], using mesopore-directing templates[24-26], and implementing post-treatments[27-29]. Compared with these intricate methods, it is a more promising approach to construct zeolite mesocrystals with special morphologies and pore structures solely and simply based on nonclassical crystallization mechanisms, which is a low-cost and green alternative requiring neither special templates nor re-dissolving of the crystalline part. There has been excellent progress in developing novel zeolite materials under this blueprint. For instance, Zhang *et al.* revealed the evolution of the structure and size of precursor particles in the nonclassical crystallization process of ZSM-5[30-33]. Meanwhile, Kumar *et al.* modulated the size and morphology of SSZ-13[34], zeolite L[35], and SAPO-34[36] by using recyclable organic modifiers to regulate the aggregation growth of precursor particles. In our previous works, a series of ZSM-5 mesocrystals were synthesized under the seed-induced synthesis route by using inorganic cations to modulate the assembly behavior[37,38], and ZSM-12 mesocrystals with a clustered, fractal, or finned structure were obtained by tuning the concentration-dependent crystallization kinetics[39-41]. However, owing to the intrinsic complexity of the zeolite synthesis system, different stages of the crystallization process - namely induction, nucleation, growth, and ripening - are often intertwined and exhibit significant interplay[30]. Ambiguous understanding of the crystallization behavior of zeolites hinders the realization of thermodynamic and kinetic control of the crystallization process.

According to current studies on the crystallization mechanism, zeolite L (**LTL** type) is a potential model of zeolite growth owing to its widely tunable morphology and special crystallization habit. Specifically, as a typical zeolite with a Si/Al ratio (denoted as SAR) of 2.0-4.0, zeolite L generally needs to be produced in a precursor system with a higher SAR (≥ 10), and the elemental composition of the product is relatively fixed and unaffected by the synthesis conditions[42-44]. Therefore, the crystallization stage can be monitored by simply tracking SAR changes. Moreover, as a 1D channeled zeolite (12-membered ring, ~0.7 nm in width,

oriented axially along the *c*-axis) with a hexagonal crystal structure, zeolite L exhibits anisotropic growth along the *c*-axis, which facilitates determination of the crystal axis direction of both the products and intermediates under electron microscopes[45]. In addition, past studies have reported zeolite L with multiple morphologies, from nanoclusters to micron-sized cylinders[42-44,46], which provides sufficient space to explore and clarify intrinsic factors and mechanisms for crystal regulation. Although nonclassical particle-assemble crystallization (CPA) of zeolite L with particular morphologies, especially micron-sized cylinders, has been observed and preliminarily exploited[35,47], more specific nucleation and growth behaviors at different crystallization stages under differential synthesis conditions are still missing, and thus the intrinsic factors leading to different morphologies remain uncovered.

In this study, alkalinity-controlled crystallization kinetics regulation was developed to achieve ultrafast and total-morphology synthesis of zeolite L mesocrystals with widely tunable sizes and morphologies, from cylindrical or disc-like shapes to nanoclusters or nanocrystals. This novel strategy entails simply and strategically changing KOH/SiO_2. Serendipitously, by investigating the relative crystallinity of intermediates and the dynamic concentration change of nutrient species in the solid and liquid phases, we found that the crystallization process of zeolite L can be divided clearly and explicitly into four stages: induction, nucleation, growth, and ripening. By systematically detecting the formation of microstructures and thoroughly investigating crystallization and dissolution processes, we established that the nucleation-growth process is thermodynamically and kinetically regulated through the alkalinity of the synthesis system. Moreover, a related nonclassical crystallization mechanism was revealed, and its validity was evaluated by investigating morphology evolution, NH_4F etching, and the effects of modifiers and K^+. Furthermore, the high adsorption capacities of zeolite L mesocrystals with different morphologies for gaseous aromatic hydrocarbons, liquid dye, and protein molecules were confirmed, which further demonstrated the effectiveness and potential utility of this method in tailoring the zeolite size and morphology.

EXPERIMENTAL

Materials

Fumed silica (Aerosil400, Shanghai Chlorine Alkali Industry), aluminum foil (SP grade, Aladdin), potassium hydroxide (KOH, semiconductor grade, Aladdin), sodium hydroxide (NaOH, AR grade, Aladdin), and deionized water were employed for the preparation of zeolite L. Poly dimethyl diallyl ammonium chloride (PDDAC, M.W. 100-200 k, 20 wt% in water, Aladdin), *n*-butylamine (*n*-$BuNH_2$, GC grade, Aladdin), and ammonium fluoride (NH_4F, AR grade, Aladdin) were used to verify the crystallization mechanism. Additionally, *o*-xylene (GC grade, Aladdin), 1,3,5-triethyl benzene (GC grade, Aladdin), methylene blue (AR grade, Macklin), myoglobin (from horse skeletal muscle, salt-free, lyophilized powder, Sigma), ammonium acetate (NH_4OAc, 40 wt% aqueous solution, Aladdin), potassium phosphate monobasic (KH_2PO_4, AR grade, Aladdin), and phosphoric acid (H_3PO_4, AR grade, Aladdin) were employed in multiple adsorption tests.

Synthesis of samples

Zeolite samples were synthesized in a xKOH/0.0667Al/1.00SiO_2/20.0H_2O system, where x (OH^-/SiO_2 ratio, BSR) = 0.65-1.35, and the resulting samples are denoted as **LTL-*x***. In detail, a certain amount of KOH was dissolved in water, and the resulting solution was divided equally into two parts. Then, a clear aluminate solution was prepared by adding the aluminum foil to one part of the KOH solution. Meanwhile, the fumed silica was added to the other part of the KOH solution with stirring and heating at 80 °C for 1 h to dissolve SiO_2 completely, and a clear silicate solution was obtained. After cooling to room temperature, the above-mentioned clear aluminate solution was slowly added to the clear silicate solution with vigorous stirring. The obtained clear solution was aged at room temperature with stirring for 12 h and then heated to 190 °C in a Teflon-lined autoclave for a certain time (see Supplementary Table 1). After hydrothermal treatment,

the zeolite L products were separated by centrifugation (15,000 rpm for 40 min with a relative centrifugal force of 19118 × *g*) and washed with deionized water several times. To study the difference in the crystallization behavior of zeolite L in different basicity ranges, two typical samples were selected and further denoted as **LTL-LB** (x = 0.75) and **LTL-HB** (x = 1.15). The crystallization intermediates were extracted at the pre-determined time and denoted as **LTL-LB/HB-*t***, where t (min) refers to the heating time. To minimize structural changes in the collected samples, especially the intermediates, all washed samples were freeze-dried in a vacuum at -50 °C.

Characterization

Powder X-ray diffraction (XRD) experiments of the as-synthesized samples were conducted on a Bruker D2 diffractometer (Cu-K_α, 10 kV, 30 mA) from 5° to 50°. The morphologies and surface features of the samples were monitored by using field-emission scanning electron microscopy (FE-SEM, Hitachi S-4800), and structural features were visualized by using field-emission transmission electron microscopy (FE-TEM, Tecnai G2 F20 S-Twin). Selected area electron diffraction (SAED) and spot elemental analysis by energy dispersive spectroscopy (EDS) was conducted on a Tecnai G2 F20 S-Twin instrument to investigate the fine structure of the products. Fourier transform infrared spectra (FT-IR) were recorded on a PerkinElmer Frontier IR instrument with a resolution of 4 cm^{-1} in the range of 1000-400 cm^{-1}. The physical parameters and porous structure of the products and intermediates were determined by using a Quantachrome iQ-2 instrument to conduct N_2-sorption experiments at 77 K and Ar-sorption experiments at 87 K after outgassing at 573 K for 8 h. Changes in the concentration of species in the supernatant liquid separated from the mixture by centrifugation and the element ratio in the solid phase were analyzed by using inductively coupled plasma-atomic emission spectrometry (ICP-AES, iCAP 7400). Raman spectra were recorded with a Horiba Jobin Yvon XploRA confocal microscope equipped with a 532 nm laser. ^{27}Al MAS NMR spectra were acquired on a Bruker DSX 300 spectrometer.

Zeolite adsorption tests

Adsorption of *o*-xylene (0.65 nm) and 1,3,5-triethyl benzene (0.82 nm) in zeolite L was evaluated by using a gravimetric gas sorption analyzer (IGA, Hiden Analytical). The sample was degassed under a vacuum of less than 10^{-3} Pa at 673 K for 2 h before the adsorption measurement.

The adsorption capacity of the zeolites was determined by measuring the ultraviolet-visible (UV-vis, PE-Lamnda 35, PerkinElmer) absorption spectra of methylene blue (1.43 nm × 0.61 nm × 0.40 nm) over zeolite L samples and by calculating the concentrations of methylene blue from the absorption peak at λ = 661 nm. In detail, 20 mg of LTL mesocrystals were added to a conical flask, and then 10 mL of methylene blue (1.00-35.0 mg/L, in 0.02 mol/L NH_4OAc aqueous solution, pH = 7.0) was added quickly. After that, the suspensions were stirred vigorously at room temperature for a pre-determined time (for the isotherm measurement, the adsorption time was 12 h). The protein adsorption capability of zeolite L was determined by incubating myoglobin (0.1 mg/mL, 4.5 nm × 3.5 nm × 2.5 nm) and zeolite L (0.1 mg/mL) mixtures in phosphate-buffered saline (PBS, 20 mmol/L, pH = 5.0) for 1.0 h at room temperature. After centrifugation, the UV-vis absorbance value (λ = 409 nm) of the supernatant was measured to calculate the amounts of protein adsorbed on zeolite L.

RESULTS AND DISCUSSION

Fast synthesis of zeolite L with total morphologies

By optimizing the mixing and aging of K^+-contained aluminosilicate precursors, univariate modulation (OH^-/SiO_2 ratio, denoted as BSR) of the crystallization process was achieved for the fabrication of a series of L zeolites [Figure 1] in the simplest SiO_2-Al_2O_3-K_2O-H_2O system. Herein, the resulting products are denoted as LTL-x, where x is the BSR value. The obtained zeolite L mesocrystals display widely tunable sizes and

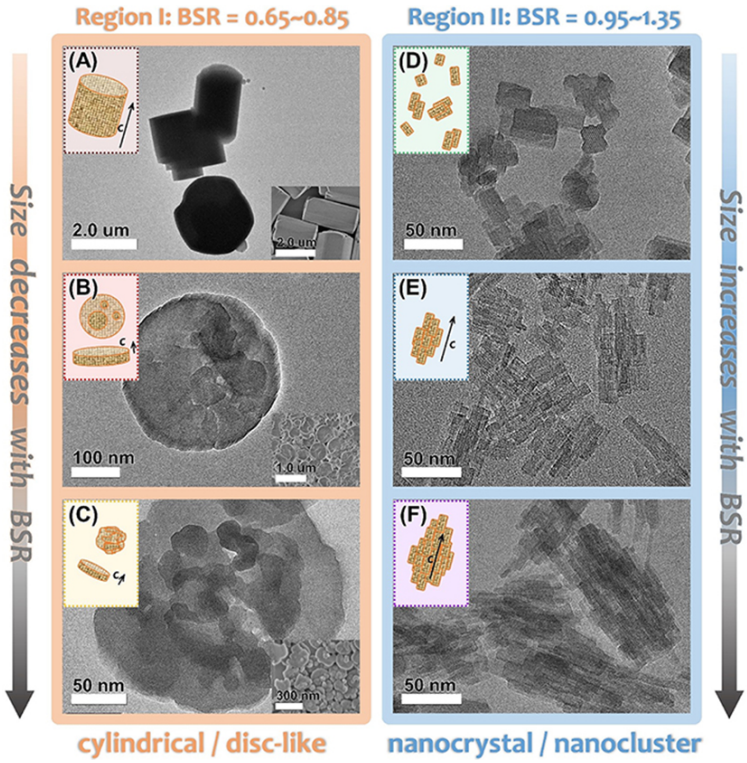

Figure 1. TEM images of zeolite L products synthesized under different alkalinity conditions. BSR equals (A) 0.65, (B) 0.75, (C) 0.85, (D) 0.95, (E) 1.15, and (F) 1.35. Inset of (A)-(C): corresponding SEM images.

morphologies, from cylindrical or disc-like shapes to nanoclusters or nanocrystals, covering all morphologies reported so far. Moreover, most morphologies can be rapidly prepared with a heating time as short as 1 to 2 h at 190 °C. Compared with reported synthesis conditions [Supplementary Table 1], the overall crystallization rate of the optimized system is faster, and K^+ is used as the only inorganic structure-directing agent without additional organic modifiers.

Interestingly, with the adjustment of alkalinity (BSR from 0.65 to 1.35), the architectural feature of zeolite L seems to obey a piecewise size-change rule in two BSR regions with different dominant morphologies. When BSR ≤ 0.85 [Figure 1A-C], the morphology of zeolite L products is cylindrical or disc-shaped. Additionally, the particle size undergoes a dramatic decline from ~(1.5-2.0) μm × (1.5-2.0) μm (diameter along *a*/*b*-axis × length along *c*-axis, denoted as *d* × *l*) to ~300 nm × 100 nm and ~200 nm × (50-60) nm as the alkalinity increases from 0.65 to 0.75 and 0.85. In detail, for LTL-0.65 and LTL-0.75, the product crystals have smooth and regular edges [Figure 1A and B]. High-resolution TEM (HR-TEM) images further reveal aligned and coherent lattice fringes, and SAED results also show pure **LTL**-phase diffraction patterns [Supplementary Figure 1A and B], indicating that LTL-0.65/0.75 have single-crystal-like structures and dense, coherent textures. When BSR reaches 0.85, the corresponding zeolite product remains disc-like but becomes partially fragmented [Figure 1C]. In the high alkalinity region (BSR ≥ 0.95), however, zeolite L nanoparticles and nanoclusters are obtained, and a converse change in the size is observed. The products reach the minimum size of ~15 nm × (30-35) nm when BSR = 0.95 [Figure 1D]. Further increasing the alkalinity reduces the size of the crystal domains to some extent but also increases the tendency of these nanoparticles to form clusters. As the BSR increases to 1.15 and 1.35, the overall size of the nanoclusters improves to ~(30-40) nm × (60-80) nm and ~(60-70) nm × (100-120) nm, respectively [Figure 1E and F]. Notably, within a single cluster assembly, the lattice orientations of adjacent domains are aligned

[Supplementary Figure 1C and D], indicating oriented growth instead of random aggregation for these nano-units.

The XRD patterns of all samples contain only diffraction peaks corresponding to the **LTL** phase [Figure 2A], and broadening of the diffraction peaks is mainly due to the nanosized crystal domains, especially under high BSR. Moreover, N_2-sorption experiments show that the porosity of the products is effectively regulated by simply adjusting the system basicity [Figure 2B]. Except for LTL-0.65, the other five samples show typical isotherms with type I and IV features, which indicates the coexistence of micro- and mesopores[48]. The isotherm of LTL-0.65 exhibits only type I characteristics, which indicates a micron-sized and dense zeolite structure[48]. As BSR gradually increases, the uptake at high p/p_0 increases, suggesting gradual enrichment of mesoporosity. Detailed texture data [Supplementary Table 2] further confirm the above results. In the BSR range of 0.65 to 1.35, the mesopore volume (V_{meso}) of the obtained products increases from 0.012 to 0.755 cm^3/g, and the external surface area (S_{ext}) grows from 9 to 246 m^2/g. It is worth noting that, although the overall particle sizes of zeolites slightly increase in the high BSR region, V_{meso} and S_{ext} do not decrease but enlarge, indicating that adjacent domains are loosely combined rather than fully fused. In addition, the rise in alkalinity somehow affects the microporosity of products because of the drop in the micropore volume (V_{micro}) from ~0.14 to ~0.09 cm^3/g. Increasing the alkalinity significantly reduces the size of LTL zeolites and simultaneously produces many defects inside the LTL crystal, such as point defects and dislocations, leading to the existence of mesopores and macropores among adjacent domains, as shown in the inset of Figure 2B (pore size distribution of LTL-HB). These gradually increasing defects and decreasing LTL zeolite size largely lead to a reduction in the micropore volume.

LTL-LB (BSR = 0.75) and LTL-HB (BSR = 1.15) were selected as representative samples for further pore structure analysis. The mesopore size distribution (Figure 2B, inset) shows that the mesopore size in LTL-HB is distributed over 5-30 nm, attributed to the assembly structure of ultra-small nanocrystals [Figure 1E]. LTL-LB has fewer meso- and macropores, which is related to its larger particle size, denser crystal structure, and smoother surface features. Moreover, the micropore size distribution by Ar-sorption [Supplementary Figure 2] shows that both products have characteristic **LTL** micropores of 0.7-0.8 nm, which are slightly larger in LTL-HB than in LTL-LB, suggesting that more crystal defects and incomplete pore walls are created at higher alkalinity conditions. Additionally, the micropore distribution of LTL-HB exhibits a more pronounced maximum in the range of 1.0-1.5 nm [Supplementary Figure 2], which may originate from the voids between adjacent nanodomains.

The **LTL** structure of samples is further confirmed by FT-IR experiments [Supplementary Figure 3]. The absorption bands at 609 and 648 cm^{-1} are attributed to the double six-membered ring (***d6r***) vibration due to the external linkage, and the absorption bands at 725 and 772 cm^{-1} can be assigned to the symmetric T-O (T = Si or Al) stretching vibrations from the external tetrahedral linkage[49,50]. Moreover, the intensity and frequency of these absorption bands are sensitive to the chemical composition of zeolite[51]. As BSR increases, the above-mentioned absorption bands gradually shift to lower wavenumbers accompanied with weaker intensities, indicating a decrease in product SAR[51]. This tendency is also revealed through the elemental analysis. As BSR increases sharply from 0.65 to 1.35, the SAR of the samples decreases slightly from 2.60 to 2.29 [Supplementary Table 2], showing that the system basicity does have a certain effect on the SAR of zeolite L (but not significant), which is consistent with previous reports[42-44].

Time-resolved investigation of zeolite L crystallization

Identification of different stages in the crystallization process

To elucidate the detailed discrepancies in the crystallization mechanism in different BSR regions, we tracked

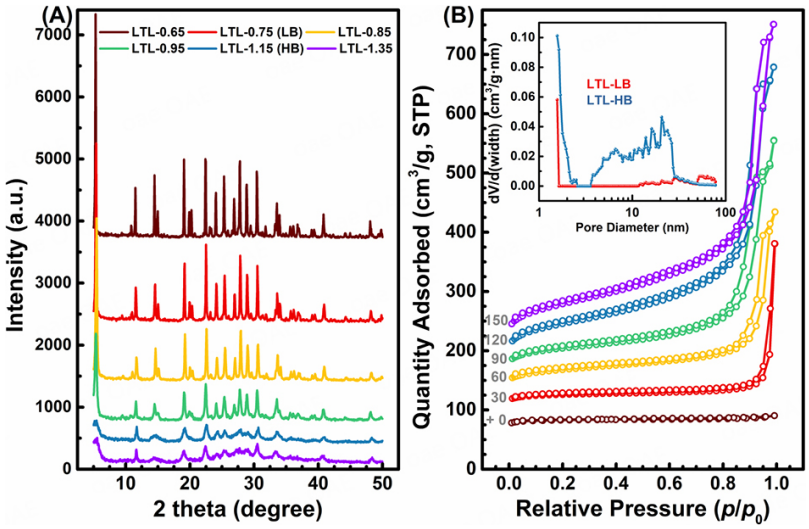

Figure 2. (A) XRD patterns and (B) N_2-sorption isotherms of different zeolite L samples. Inset of (B): mesopore size distribution of LTL-LB and LTL-HB.

the evolution of precursor structures and the distribution of nutrient species in the solid and liquid phases using two typical samples, LTL-LB (BSR = 0.75) and LTL-HB (BSR = 1.15). The intermediates at various crystallization intervals were collected and investigated (denoted as LTL-LB/HB-*t*, where *t* refers to the time of hydrothermal treatment; photographs with corresponding solid yields are displayed in Supplementary Figure 4). The solid-phase yield of the product is stable at approximately 32% in the LTL-LB system and 30% in the LTL-HB system.

The crystallization kinetic curves of LTL-LB and LTL-HB [Figure 3A and C] were obtained by the solid-phase XRD analysis [Supplementary Figure 5]. For LTL-LB-*t* [Figure 3A], the intermediates show no LTL characteristic peaks in the first 60 min of heating. Additionally, the relative crystallinity (RC) of the solid phase slowly increases to approximately 12% and then rapidly grows to 92% in the following 30 min (90 min of heating). For LTL-HB-*t* [Figure 3B], however, the higher alkalinity accelerates the crystallization process markedly, and RC increases by approximately 87% between t = 22 min and t = 44 min. Moreover, the compositions of the supernatant liquid were monitored together with the solid-phase SAR (i.e., changes in the Si-Al distribution). As shown in Supplementary Table 3, more than 2/3 of Al species in the clear precursor solution transfer into the solid phase when the gel network starts to form, and as RC increases, more Al species enter the solid phase synchronously. In contrast, changes in the concentration of Si species in the supernatant are not significantly different between the low and high BSR groups. The utilization rate of Al is more than 95% and that of Si is less than 30%; thus, further analysis of SAR changes in the solid and liquid phases provides a more intuitive picture of nutrient migration [Figure 3C and D]. As a result, a two-stage rise in the liquid-phase SAR and a corresponding piecewise fall in the solid-phase SAR can be clearly observed.

To determine the key nodes of the crystallization process and the cause of the plateau in the SAR curve, we analyzed the lower turning points of the above two curves. Serendipitously, we found that in this zeolite L system, the crystallization behaviors are strongly SAR-dependent. That is, the nucleation and subsequent growth of zeolites can occur only with an appropriate solid-phase SAR value, and thus the induction, nucleation, growth, and ripening stages of the crystallization process can be clearly distinguished [Figure 3]. After room temperature aging, both the low and high BSR systems become clear and transparent solutions.

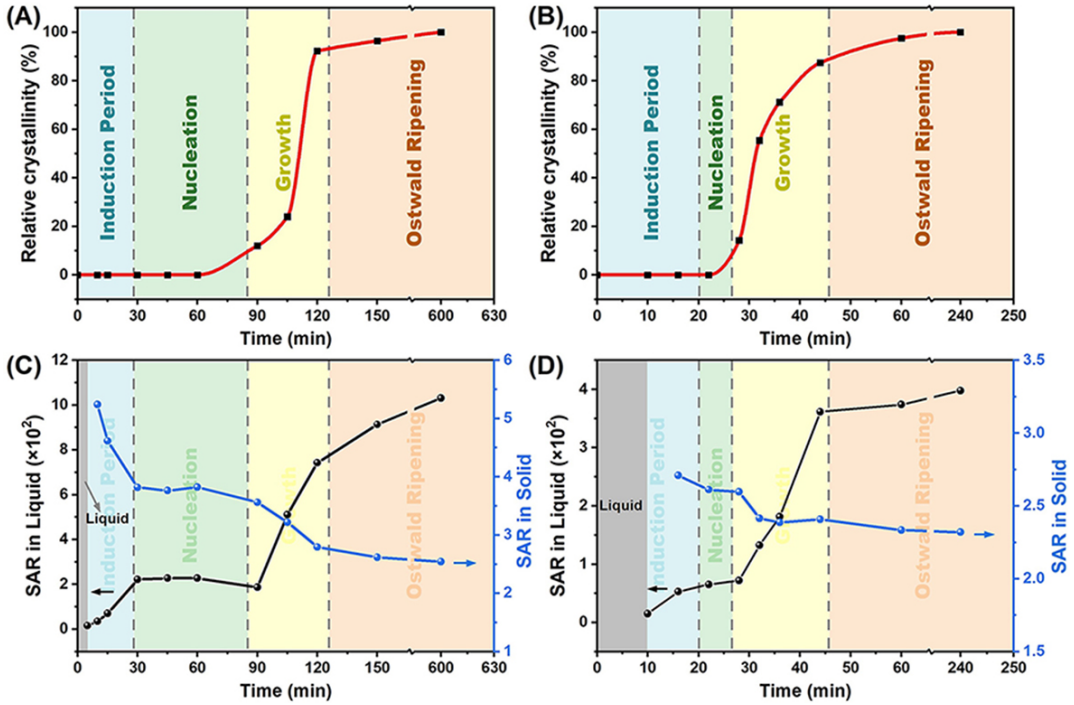

Figure 3. Kinetic curves of the crystal growth of (A) LTL-LB-*t* and (B) LTL-HB-*t*, according to the XRD data in Supplementary Figure 5. Related migration of Si and Al nutrients in the supernatant and solid phase of (C) LTL-LB-*t* and (D) LTL-HB-*t*, according to the data in Supplementary Table 3. The different colored regions represent four detailed stages of the crystallization process.

DLS measurements revealed that the clear liquid contains sol particles with a size of approximately 10 nm. For LTL-LB-*t* [Figure 3C], the solid gel phase is first observed when the clear initial sol is heated for 5 min. After that, the ICP-AES data shows a two-stage increase in SAR in the supernatant. Additionally, the data shows a relevant two-stage decline in SAR from 5.24 to 3.80 and then to 2.79 in the solid phase. Moreover, a rapid increase in crystallization can be observed from 60 to 120 min, which corresponds to the second changing period of SAR and indicates fast growth of **LTL**-type crystals. For LTL-HB-*t* [Figure 3D], a similar tendency of SAR in the liquid and solid occurs with a smaller change scale and in a shorter timeframe. Additionally, the increase in RC and the decrease in solid-phase SAR support the second SAR growth. Accordingly, the second SAR growth and solid-phase RC jump can be attributed to the "growth period" of zeolite crystallization (Figure 3, yellow regions).

It is generally accepted that **LTL** zeolites have a relatively low SAR and a limited regulation interval, similar to **FAU** and **LTA** zeolites with abundant 4-membered rings (4MRs)[52]. Because of this characteristic, **LTL** crystals can only form with a fixed SAR of 2-4 even for an initial mixture with a SAR above 10. Therefore, at the beginning of gel crosslinking, SAR in the solid phase is too high for the formation of LTL-type sub-units with short-range order (e.g., ***d6r*** and ***can*** containing 4MRs) in the amorphous matrix. The first decline of solid-phase SAR indicates an "induction period" in which the Si and Al nutrients exchange between the solid and liquid phases to reach the ratio for nucleation (Figure 3, blue regions). Subsequently, crystal nuclei form in concentrated areas with a suitable SAR, and SAR in the solid and liquid phases reaches a plateau (Figure 3, green region, "nucleation stage"). At the end of the "nucleation stage" and the beginning of the "growth stage", the characteristic Bragg peaks of **LTL** appear, and the peak intensity increases rapidly with increasing time. At this stage (Figure 3, yellow region), SAR of the solid phase shows a "secondary decline" until it is close to the final product, which suggests that for low-silica zeolites like **LTL**, further construction

of long-range order has more stringent elemental composition requirements than the formation of local nucleation domains. As RC increases to more than 80%, the change in SAR slows down again, indicating that the crystallization process reaches the final "Ostwald ripening stage" (Figure 3, orange region). At this stage, the crystal is formed to a large extent, and some small defects left by the rapid growth will be perfected through the slow liquid phase exchange process, which makes RC rise slowly and slightly. Moreover, as shown in Supplementary Figure 4, the solid-phase yield of time-resolved intermediates in the LTL-LB system shows a distinct two-stage descending feature. Specifically, the first stage is from 10 to 30 min, corresponding to the "Induction Period," and the second stage is from 90 to 120 min, corresponding to the "Growth Period." The two-stage descending feature indicates that there is significant element migration from the solid phase to the liquid phase during the induction and growth stages. However, the distinct two-stage descending feature does not emerge in the LTL-LB system, which can be attributed to the high alkalinity. The distribution of precursor species is fully optimized during the induction and growth periods due to the fast rate of material exchange, thus avoiding obvious fluctuations.

The start and end times of different stages in the whole crystallization process of LTL-LB and LTL-HB were successfully obtained. To further study the reasons for the formation of different morphologies, it is necessary to focus on two key stages - the nucleation stage and the growth stage - to figure out the detailed differences in the evolution behavior of intermediates under different BSR.

Investigation of the effects of BSR on Si-Al distribution/state

The Raman spectra of solid-phase intermediates were acquired to determine the effects of BSR on Si-Al distribution/state at the induction and nucleation stages [Figure 4A and D]. The band observed at 498 cm^{-1} with a shoulder at 470 cm^{-1} is attributed to the T-O-T bending mode of 4MRs in the LTL structure. Additionally, the increase in the band intensity represents the formation and evolution of short-range order[53]. For LTL-HB-*t*, compared with the XRD patterns [Supplementary Figure 5B] and RC curves [Figure 3B], the Raman spectra [Figure 4D] show that construction of the short-range structure starts early (t = 16 min, RC stays at 0% until t = 22 min) is approximately 80% complete within the next 16 min (t = 32 min, when RC = 55%). In contrast, for LTL-LB-*t*, progress starts at a late point (t = 60 min) and increases almost synchronously with the rise of RC (Figure 4A for Raman spectra, Figure 3A for RC curves).

The above results show that the length of the induction period is closely related to the formation of short-range order in the amorphous matrix. The different alkalinity conditions lead to distinct thermodynamic saturability of Si species, and thus the gel-network precipitated from the initial sol has dissimilar SAR values and different dynamic evolution phenomena. In the high alkalinity system (LTL-HB-*t*), the gel formed at 16 min with a SAR = 2.71 is suitable for the formation of **LTL**-type sub-units (e.g., 4MR-riched ***can*** cage), allowing rapid establishment of short-range order with a minor adjustment of nutrient distribution. For LTL-LB-*t*, however, the gel precipitated at 10 min contains too many Si species to form nuclei for zeolite L. Hence, a more significant and slower exchange of nutrients is detected between the solid and liquid phases as SAR in solid drops from ~5.2 to ~3.8 during the induction period. Consequently, a tediously long nucleation stage of more than 30 min is observed.

The chemical state of the Al atoms of the intermediates was investigated using solid-state ^{27}Al MAS NMR, as shown in Figure 4B and E. The signal of the tetrahedrally coordinated Al atoms of zeolite frameworks appears at a lower field than that of amorphous aluminosilicate, and the former is narrower than the latter due to improved homogeneity[39,54]. Therefore, the chemical shift and the corresponding full width at half maximum (FWHM) of the peaks of the intermediates obtained with different heating times are displayed in Figure 4C and F to evaluate the ordering process and the overall short-range uniformity, respectively. All

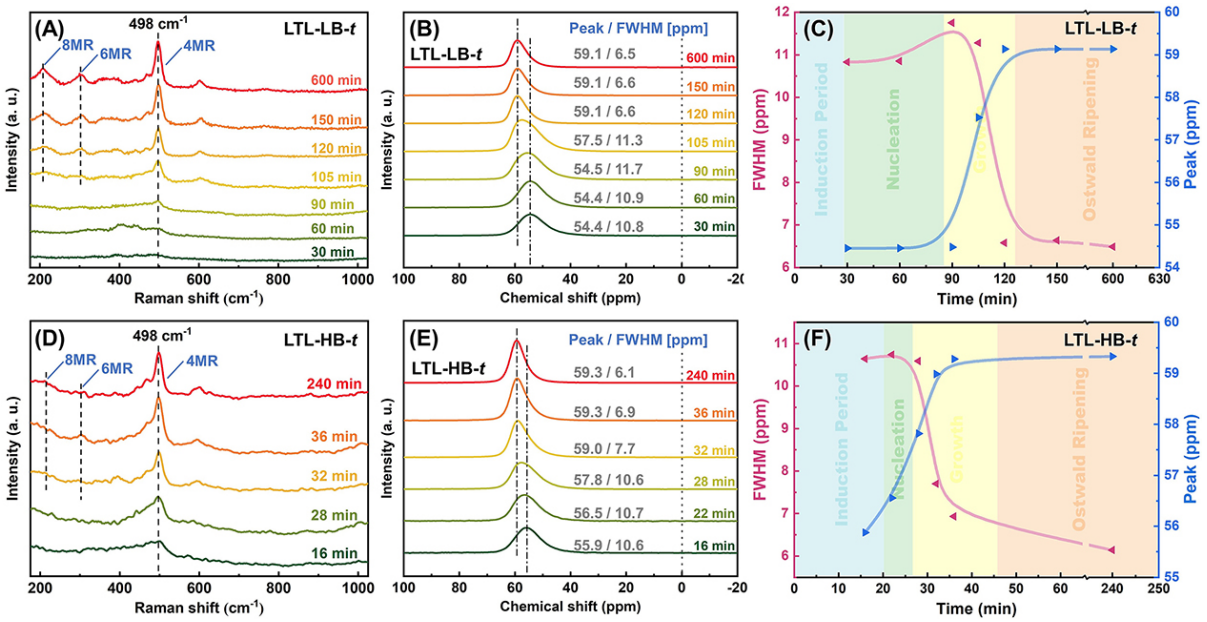

Figure 4. (A) Raman spectra, (B) ^{27}Al MAS NMR, and (C) related changes in the peak position and FWHM for LTL-LB-*t*. (D) Raman spectra, (E) ^{27}Al MAS NMR, and (F) related changes in the peak position and FWHM for LTL-HB-*t*.

samples show no peak at 0 ppm, indicating that all solid-phase Al atoms are tetrahedrally coordinated even in the amorphous precursors[39]. During the crystallization process, the ^{27}Al MAS NMR peaks of both systems shift to a lower field (from 54 to 59 ppm for LTL-LB-*t*, and 56 to 59 ppm for LTL-HB-*t*), which is consistent with reported results[54]. It is worth noting that in the LTL-LB system, signal shift begins at the start of the growth stage and continues until the end of this stage [Figure 4C]. In the LTL-HB system, the corresponding shift starts even before the middle of the nucleation stage and ends before the middle of the growth stage [Figure 4F]. Moreover, unlike the gradual decline in the FWHM of the LTL-HB-*t* peak [Figure 4F], the FWHM of the LTL-LB peak shows abnormal broadening in the nucleation stage and the early growth stage [Figure 4C]. The above results indicate that **LTL**-type sub-units can be established earlier and distributed widely in the gel network in the high alkalinity system, and the generation of more nucleation sites is conducive to rapid induced crystallization. In the low alkalinity system, however, relatively slower formation of less short-range ordered structures give birth to fewer nuclei and initial crystals, and other disordered species need to be assembled on the surface of these nuclei and initial crystals to become crystals gradually. Therefore, short-range order divergence under low and high alkalinity conditions directly leads to different crystallization kinetic behaviors.

Exploring the differentiated nucleation/growth behaviors of LTL-LB/HB-t

Different alkalinity conditions not only affect the nucleation speed/amount, they also change the detailed evolution mode of the precursors in the pre-nucleation stage. Visual evidence was obtained using TEM and dynamic light scatter (DLS) measurements. For LTL-LB, worm-like particles (WLPs) are formed by the crosslinking and collapsing processes of the gel networks, and the corresponding particle width increases from approximately 10 nm (t = 10 min) to 100-300 nm at t = 60 min [Supplementary Figures 6 and 7A]. This is accompanied with a few initial crystals of 5-20 nm in size [Figure 5A] at the gel-liquid boundary at 60 min. In the next 30 min, these small nuclei gradually grow to 50-100 nm in size, which is close to the width of WLPs [Figure 5B]. Moreover, the size of WLPs with a localized LTL crystalline phase gradually increases to 500 nm with larger aggregates (around 5 μm in size) at 90 min. During the growth and Ostwald ripening stages, from 90 to 600 min, the size of particles with increasing crystallinity remains at

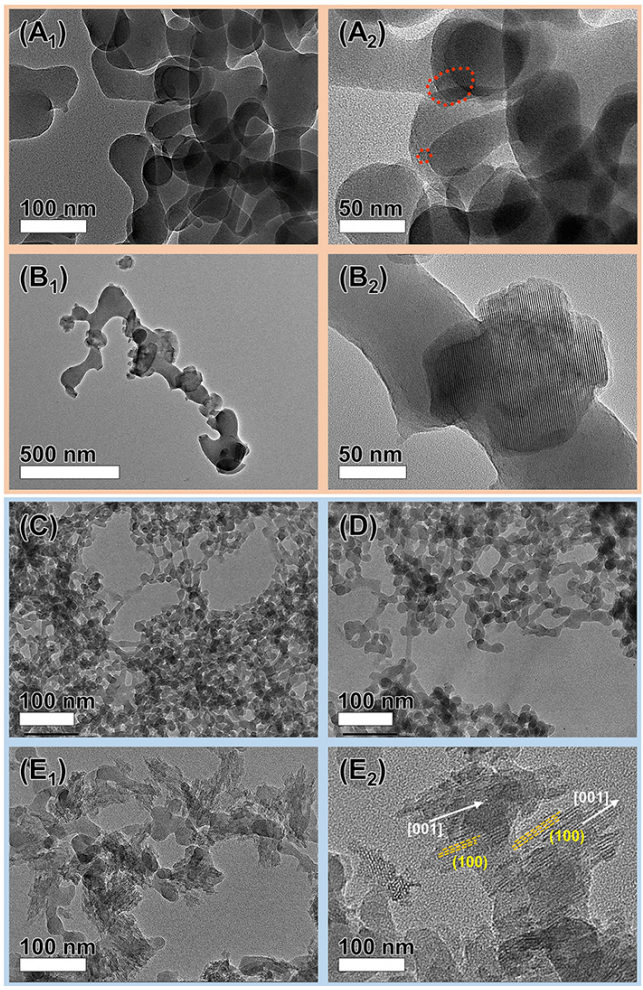

Figure 5. TEM images of LTL-LB-*t* in the nucleation stage and early growth stage: *t* = (A) 60 and (B) 90 min. TEM images of LTL-HB-*t* in the induction and nucleation stage: *t* = (C) 16, (D) 22, and (E) 28 min.

approximately 700 nm. In contrast, in the LTL-HB batch, WLPs formed at 16 min maintain the width of 15-20 nm throughout the induction period [Figure 5C and D, Supplementary Figure 7B] and give birth to abundant small crystals with a cluster-like morphology at 28 min (RC = 14%), of which the size is approximately 30 nm in width and approximately 50 nm in length [Figure 5E]. In the following stages, the particle size stays at 100-200 nm, which is significantly smaller than that of the LTL-LB system. A comparison of the above nucleation phenomena under different alkalinity conditions indicates that a relatively small number of nuclei (small crystals) are formed in the LTL-LB system. These initial crystals are generally located at the solid-liquid edges and show a single-crystal-like structure. In contrast, a large number of crystal nuclei can be formed in one WLP in the LTL-HB system, and it is notable that these adjacent nuclei mutually grow and adjust orientation, forming a prototype of nanocluster-like mesocrystals.

Prolonging the crystallization time to the growth stage leads to a rapid increase in RC, and the second change period of SAR can be observed. At this stage, the adjustment of solid-phase SAR in the high alkalinity system (from ~2.6 to ~2.4) [Figure 3D] is significantly smaller than that in the low alkalinity system (from ~3.6 to ~2.8) [Figure 3C], and the growth of corresponding relative Raman peak is also much faster, as mentioned above. It seems that the Si-Al nutrient distribution/state caused by different BSRs

further affects the growth stage. As our previous work revealed, differences in short-range order may lead to different assembly and/or induced growth modes between the amorphous and crystalline parts[37]. This conjecture was confirmed by TEM tracking. For LTL-LB-105, amorphous WLPs attach to the crystal surface and become crystalline through induced crystallization [Figure 6A]. A typical amorphous-to-crystalline conversion is displayed in Figure 6B. The composite structure with a crystalline core and an amorphous shell supports this "assembly, and induced crystallization" growth that occurs from inside the nuclei/crystal to outside the WLPs. In the following 15 min, WLPs in the LTL-LB system are consumed, and the corresponding RC value reaches approximately 92%. The morphology and size of the crystal are close to those of the final products [Figure 6C], suggesting the end of the rapid growth stage.

The induced crystallization process of LTL-HB in the growth stage is rather fast and somehow "*in-situ*". That is, in contrast to the "several WLPs"-to-"one crystal" assembly process in the low BSR system, one WLP may fracture to form several final crystals in the high BSR system. The TEM images show that abundant nucleation sites are generated in every single WLP (t = 28 min) [Figure 5E], and the subsequent induced crystallization process occurs rapidly along each WLP with multiple starts in the next 4 min, leading to the breakdown of WLPs and the formation of cluster-like products [Figure 7A]. This unique growth behavior also explains why the final products have a similar diameter and a significantly shorter length than WLP precursors. For LTL-HB-32, the RC value reaches approximately 55% without the appearance of an amorphous region, and the size/morphology of the crystals is similar to that of the final ones [Figure 1E]. This relatively low crystallinity suggests that there may be defects in the crystals. In the following growth and ripening stages, unused liquid Si and Al species grow on the crystals (inferred from the concentration change shown in Supplementary Table 3), which gives the zeolite smoother and sharper crystal edges and slightly increases the size of domains (Figure 7B for t = 60 min, Figure 1E for t = 240 min).

The formation of **LTL**-type microstructures is sensitive to the distribution/state of precursors Si and Al. Therefore, we further explored the distribution of the solid elements of two key intermediates. EDS results for LTL-LB-105 show an uneven distribution of Si and Al in the solid phase, and some Si-excess spheres can be observed (spot SAR = 4.3-7.2) [Supplementary Figure 8A]. Li *et al.* reported that zeolite synthesis systems commonly contain nonhomogeneous gel networks with Si-rich and Al-rich areas, especially when fumed silica or silica gel is used as the Si source[55]. Therefore, we postulated that the second drop in solid-phase SAR is due to nutrient exchange between the liquid phase and the Si-rich segments in WLPs to gain a suitable SAR for further crystal growth. As a result, parts of WLPs-located Si species undergo dynamic dissolution into the liquid phase during the induced crystallization process [Supplementary Table 3] or are extruded integrally (which eventually dissolves because no such particle is observed when the time is prolonged to more than 120 min). For LTL-HB-28 [Supplementary Figure 8B], conversely, EDS results show a fairly uniform distribution of Si and Al in the solid phase, and the detailed SAR value matches the final framework SAR. This uniformity and compatibility ensure the rapid and extensive formation of **LTL** microstructure at the thermodynamic level.

The texture of intermediates was characterized using N_2-sorption experiments [Supplementary Figure 9 and Supplementary Table 4]. Generally, the zeolitic micropore surface and volume (S_{micro} and V_{micro}) grow with a relative lag as the RC value increases. To quantify the magnitude of the hysteresis, the relative V_{micro} (RV, which is defined as the ratio of "V_{micro} of the intermediate" to "V_{micro} of the final product") of intermediates was calculated and compared with the corresponding RC values [Supplementary Table 4]. It can be seen that this delayed formation of zeolitic micropores is more obvious in the low BSR system (LTL-LB-t) because the RV/RC ratio remains low (< 0.3) throughout the early growth stage ($t \leq$ 105 min). That is, at this stage, the generated small crystals/nuclei in the LTL-LB-t system have a relatively complete **LTL**-type

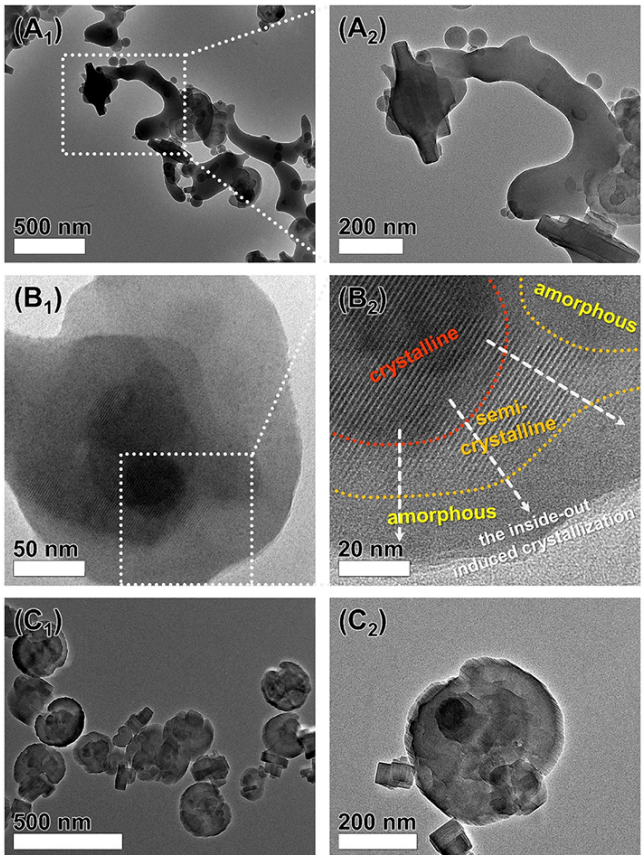

Figure 6. TEM images of (A) the assembly behavior between WLPs and crystals for LTL-LB-105. (B) Inside-out induced crystallization process for LTL-LB-105. (C) Crystals in LTL-LB-120.

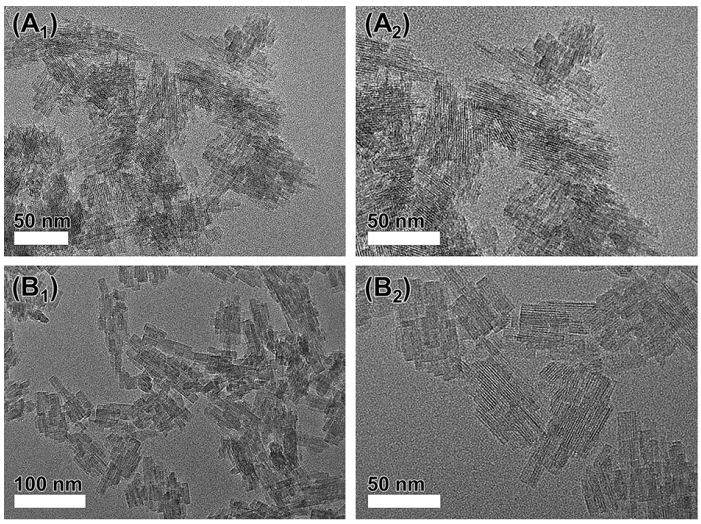

Figure 7. TEM images of LTL-HB in the growth and ripening stages: *t* = (A) 32 and (B) 60 min.

crystalline structure, while there are almost no initial zeolitic pores in the amorphous parts. When these disordered WLPs start to wrap around the outside of the crystalline part, the outermost amorphous layer hinders connectivity to the inner crystal micropores, making the measured RV relatively low. Subsequently,

corresponding with the rapid rise in RC, a sharp increase in V_{micro} from 0.009 to 0.140 cm^3/g can be seen between 105-120 min, which is attributed to the inside-out induced crystallization of WLPs and the re-opening of microporous channels. In contrast, subsequent ripening only results in a reduction in the mesoporous volume and surface (V_{meso} and S_{ext}). For the high BSR group (LTL-HB-*t*), in contrast, the lag of RV is smaller than that of RC. After the lattice fringes are first observed in the TEM images (t = 28 min, RC = 14%), the RV/RC ratio remains high (> 0.55) [Supplementary Table 4]. This indicates that the amorphous WLPs in the LTL-HB system have a good microstructure. With the rapid occurrence of *in situ* induced crystallization, **LTL**-type micropores can be constructed and penetrated rapidly. This behavior is consistent with the short-range ordering information obtained through Raman and NMR experiments.

Putative crystallization mechanism and its validation

Uncovering the nonclassical crystallization mechanism of LTL-LB/HB-t

By comparing the evolution behaviors under different alkalinity conditions, it is evident that BSR influences the solubility of Si species, which in turn affects the thermodynamic properties of amorphous precursors, such as the non/uniformity of Si and Al distributions and the high/low potential to form **LTL**-type microstructures, leading to different crystallization kinetics and products with various morphologies. In the aging stage, the reaction mixture in both systems is a clear solution owing to the relatively high pH [Scheme 1A(i) and Scheme 1B(i)]. As the temperature rises, colloidal silica particles aggregate, the gel network begins to form [Scheme 1A(ii) and Scheme 1B(ii)], and tetra-coordinated Al enters the solid-phase gel network. At this gel formation stage, BSR affects the solubility of Si species and the stability of the ≡Si-O-Si≡ bond. Under low alkalinity conditions (LTL-LB), the gel network has a higher degree of crosslinking, with more Si species entering the solid phase and producing a coarser gel network [Scheme 1A(ii)]. Moreover, owing to the low solubility of Si and the relatively slow exchange rate between the solid and liquid phases, the distribution of Si and Al in the solid phase is not uniform, and some localized Si-rich zones exist [Supplementary Figure 8A]. Conversely, as the alkalinity increases (LTL-HB), the solubility of Si species increases, and mass exchange is also faster, resulting in a narrower-sized gel network with a relatively homogeneous distribution of elements [Scheme 1B(ii) and Supplementary Figure 8B].

After the rearrangement of elements in the gel network and the formation of WLPs by fracture of the gel network, regions of solid-phase particles with more suitable SAR show a preference for nucleation late in the induction period. Since the SAR of LTL-HB precursors closely matches the **LTL** structure, a large number of nucleation sites rapidly form in adjacent regions, which are subsequently adjusted to produce oriented cluster-like nuclei [Scheme 1B(iii)]. For LTL-LB, however, the unsuitable initial SAR of the solid phase and the relatively slow mass transfer lead to a significantly longer induction period, and the nucleation sites are fewer and located mainly at the solid-liquid junction, where mass exchange, element adjustment, and the formation of 4MR sub-units occur easily [Scheme 1A(iii)].

In the subsequent growth stage, amorphous WLPs in the LTL-LB system aggregate on the nuclei surface [Scheme 1A(iv)]. Owing to the unsuitable SAR and the lack of short-range ordered microstructure, the inside-out induced crystallization process [Scheme 1A(v)] is assisted by solid-liquid element transfer, leading to a significant change in SAR in the gel and solution phases [Figure 3C]. In contrast, in the LTL-HB system, the amorphous part shows good short-range order. As a result, direct and rapid induced crystallization occurs *in situ* [Scheme 1B(iv) and (v)], along with a relatively less involved liquid-phase process (because changes in the elements in solution are smaller) [Figure 3D].

Mechanism validation by analyzing morphology evolution, NH_4F etching, and the effects of modifiers and K^+

The above assumptions are supported by the changes in crystal morphology under different alkalinity

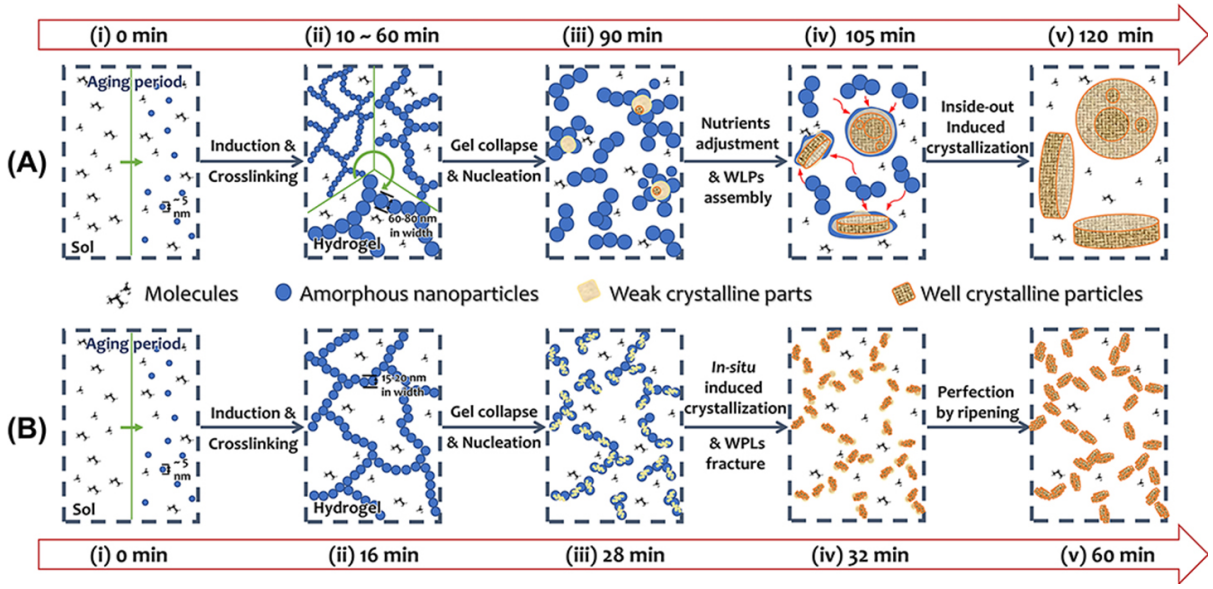

Scheme 1. Putative nonclassical crystallization pathways of (A) LTL-LB and (B) LTL-HB.

conditions. In the cylindrical/disc-like morphology region (Figure 1A-C, BSR ≤ 0.85), low alkalinity amplifies the unsuitable initial SAR and slow adjustment of elements in the solid phase, which drastically decreases the crystallization rate [Supplementary Table 1]. Moreover, the nonuniform Si-Al distribution and poor short-range order in amorphous precursors greatly inhibit nucleation. That is, the number of WLPs assembled on each nucleus increases, leading to a significant enlargement of the final products. Additionally, owing to the slower attachment and internal reorganization of WLPs, the classical mechanism (growth via the addition of simple species) of crystallization is prominent, resulting in a dense product and a rise in the *c*/*a*-axis ratio. A previous study found that in the growth of disc-shaped zeolite L, the attachment of simple molecules preferentially occurs along the *c*-axis[44]. In the nanocrystal/nanocluster region (Figure 1D-F, BSR ≥ 0.85), however, high alkalinity boosts nucleation, resulting in a decrease in the size of each domain. Moreover, the proximity of nucleation sites to one WLP facilitates interlacing, leading to the formation of large oriented clusters.

To further verify this crystallization mechanism, NH_4F etching experiments and synthesis in the presence of modifiers were carried out for LTL-LB and LTL-HB. NH_4F tends to etch high-energy interfaces in zeolite, thus revealing hidden building blocks[28]. After NH_4F etching of LTL-LB, the remaining parts show a cashew-like shape with a width of 50-80 nm, which is similar to WLPs [Figure 8A], confirming that crystals are formed by the assembly and fusion of WLPs. In contrast, after NH_4F etching of LTL-HB, the particles retain their overall shape, while the nanoclusters become looser and the pores between adjacent domains are larger [Figure 8B], which is consistent with the assumption that neighboring nuclei form interlaced nanoclusters in a single WLP.

During the assembly of WLPs to form micron-sized zeolite L, the product aspect ratio can be altered by using modifiers *n*-$BuNH_2$ and PDDAC to suppress WLPs-crystal deposition along the *c*-axis and *a*/*b*-axis, respectively[35]. Experiments were conducted in which modifiers *n*-$BuNH_2$ and PDDAC were introduced into the LTL-LB and LTL-HB systems. The results show that the morphology of LTL-LB is sensitive to both *n*-$BuNH_2$ [Figure 8C] and PDDAC [Figure 8E], while that of LTL-HB is unaffected by the modifiers [Figure 8D and F]. These results further confirm that one cylindrical/disc-shaped zeolite crystal may

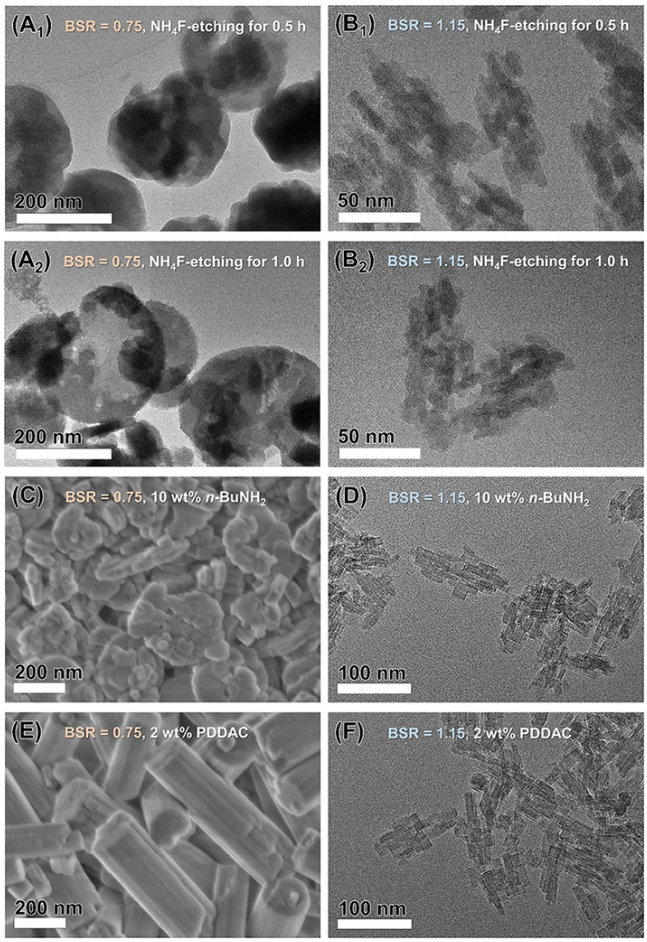

Figure 8. TEM images of (A) NH_4F-etched LTL-LB and (B) NH_4F-etched LTL-HB. Products obtained under (C and E) BSR = 0.75 and (D and F) BSR = 1.15 with the addition of modifiers *n*-$BuNH_2$ (C and D) and PDDAC (E and F).

originate from the aggregation of multiple WLPs, while the formation of one nanocluster zeolite L does not involve the assembly of WLPs but originates from a single WLP with *in situ* interleaved nucleation and induced crystallization.

In addition, the presence of KOH affects the concentration of K^+ in the system, although the above discussion is mainly focused on the thermodynamic and kinetic effects of system alkalinity (OH^- concentration) on the crystallization mechanism. Therefore, it is also necessary to consider whether changes in the K^+ concentration affect the product morphology. In the original LTL-HB system (BSR = 1.15), an equimolar amount of NaOH was used to replace a proportion of KOH. This operation has a slight effect on the product morphology; specifically, the products remain nanoclusters, although the overall particle size and domain size increase slightly with the decrease in K^+/SiO_2 from 1.15 to 0.75 and 0.55 [Supplementary Figure 10]. Moreover, EDS results show that the Na^+/K^+ molar ratios in the two products with the feeding NaOH/KOH ratios of 0.4:0.75 and 0.6:0.55 are respectively 0.033 and 0.060, indicating that the counterion is mainly K^+. It should be noted that if a greater proportion of K^+ is replaced with Na^+ (K^+/SiO_2 < 0.5, when OH^-/SiO_2 = 1.15), then pure **LTL** phase zeolite is unavailable because it is generally believed that K^+ can just hold the ***can*** cage and acts as a special structure-directing agent for **LTL**[56]. These experiments indicate that as long as sufficient K^+ participates in the formation of microstructures, it is the alkalinity (OH^-) that plays a dominant role in the regulation of crystallization and morphologies of zeolite L. Further increasing or

decreasing excessive K^+ has no obvious effect on morphology control.

Adsorption performances of zeolite L mesocrystals with different morphologies

Changing BSR in the synthesis system also changes the morphology, including texture, size, exposed crystal face, and micropore length, of the obtained zeolite L, which affects the properties of the zeolite. Morphological and architectural changes in zeolite L can be reflected in the adsorption of probe molecules with various sizes and properties, thus further guiding the preparation of purpose-directed zeolite adsorbents and functional materials. Therefore, the adsorption of gaseous aromatic hydrocarbons, dye solutions, and proteins was investigated as three typical applications with environmental or biological value.

For the gas-phase adsorption of aromatic hydrocarbons, LTL-HB with a larger S_{ext} exhibits a higher adsorption capacity for both *o*-xylene (kinetic diameter = 0.65nm) and 1,3,5-triethyl benzene (kinetic diameter = 0.82 nm) than LTL-LB [Supplementary Figure 11A]. The rapid adsorption of *o*-xylene (which can enter the micropore channels of zeolite L) by the nanocluster-shaped L zeolite is an obvious advantage (Figure 9A and Supplementary Figure 11B, inset). The characteristic diffusion time (L_0^2/D, see the discussion for Supplementary Figure 11 in the supporting information) was calculated. LTL-HB (L_0^2/D = 0.888 s) has a significantly shorter characteristic diffusion time than LTL-LB (L_0^2/D = 76.9 s) [Figure 9A], which correlates with the length of the micropore channels along the [001] direction, specifically the former is approximately 1/7 the length of the latter. The above results indicate that nanocluster-shaped zeolite L is more suitable than cylindrical/disc-shaped zeolite L for the adsorption of gas phase aromatic hydrocarbons because the former has a shorter *c*-axis length and larger specific surface area than the latter.

For the liquid-phase adsorption of methylene blue (molecular dimensions: 1.43 nm × 0.61 nm × 0.40 nm), similar dynamic phenomena were observed [Figure 9B]. Specifically, adsorption by clustered zeolite L (LTL-HB) is significantly faster than adsorption by disc-shaped zeolite (LTL-LB). For LTL-HB, the adsorption efficiency reaches 73.6% in 20 s and 100% in 20 min. For LTL-LB, the efficiency is only 41.5% in the first 20 s and below 90% in 60 min [Figure 9B]. The effect of the initial probe concentration on the equilibrium adsorption capacity of LTL-HB and LTL-LB was also evaluated [Supplementary Figure 12A-C]. The adsorption curve of methylene blue on LTL-LB has typical characteristics of the Langmuir model, while that of methylene blue on LTL-HB has mixed features of the Langmuir and multi-layer adsorption models[57,58]. This thermodynamic adsorption feature indicates that the dye molecules are simultaneously adsorbed on the microporous channels and the external surface of the zeolite. Additionally, the dye adsorption capacities of all six zeolite L samples were evaluated. The results show that the LTL-1.35 sample with the largest S_{ext} and smallest domain size exhibits the highest adsorption capacity [Supplementary Figure 12D].

Nanocrystal zeolite L obtained with BSR = 0.95 displays the highest adsorption capacity for myoglobin (molecular dimensions: 4.5 nm × 3.5 nm × 2.5 nm), while nanoclusters with higher S_{ext} have lower adsorption capacities for myoglobin [Supplementary Figure 13A]. Because proteins such as myoglobin are large, they can only be adsorbed on the outermost surface of the crystal, and the gaps between adjacent domains in the nanoclusters become inaccessible. Additionally, our previous work showed that the protein adsorption capacity of the (001) face of zeolite L is approximately 10 times that of the (100)/(010) face[59]. An analysis of the adsorption data using the definition of the effective adsorption specific area ($A_{eff} = 5/L+1/R$, see the discussion for Supplementary Figure 13) revealed a good linear relationship between the amount of adsorbed myoglobin and the A_{eff} of zeolite L with different morphologies [Figure 9C]. This finding facilitates future designs of zeotype supports with suitable morphologies for protein and enzyme immobilization.

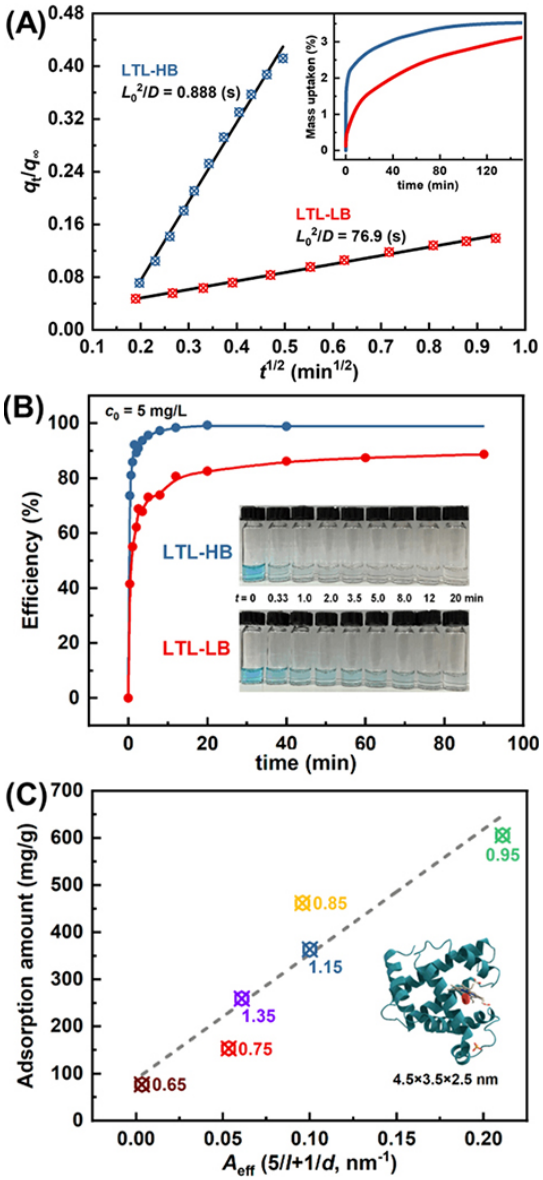

Figure 9. (A) Characteristic diffusion times of *o*-xylene on different zeolite L calculated using the kinetic uptake profiles (inset) in the short time domain (p/p_0 = 0→0.05). (B) Adsorption kinetic curves of methylene blue on LTL-LB/HB. Inset: corresponding photographs. (C) Relationship between the defined factor A_{eff} of different zeolite L with the corresponding adsorption capacity of myoglobin. Inset: molecular structure and size of myoglobin.

CONCLUSIONS

By simply adjusting the alkalinity of the synthesis system, a series of **LTL** mesocrystals with almost all morphologies (from cylindrical/disc-like shapes to nanoclusters/nanocrystals) were synthesized rapidly (1-2 h). The obtained zeolite products with different molecular dimensions and states exhibited excellent adsorption performance. Comprehensive tracking of the evolution of long-range/short-range order and the distribution of solid/ liquid nutrients throughout the crystallization process revealed that the above morphological shift is achieved by a two-step thermodynamic/kinetic co-regulation mechanism: First, different basicity conditions lead to thermodynamic differences in the precursors, such as non/uniformity of elemental distribution and high/low potential for microstructure formation. Subsequently, these

thermodynamic differences in the precursors induce different crystallization kinetic behaviors. That is, the assembly of WLPs on discrete single crystal-like nuclei in the low BSR system, and *in situ* induced crystallization along a single WLP in the high BSR system. Notably, an analysis of crystal growth and nutrient migration in these systems provided a standardized model for zeolite formation comprising four stages of crystallization, namely induction, nucleation, growth, and ripening. A related nonclassical crystallization mechanism was uncovered for zeolite L when different alkalinity conditions were employed, and its validity was evaluated by analyzing morphology evolution, NH_4F etching of the obtained mesocrystals, and effects of modifiers and K^+. The results presented herein not only provide insight into an understanding of the evolution of crystalline materials but also pave a new way for the economical and green synthesis of target-oriented zeotype materials.

DECLARATIONS

Authors' contributions

Conceptualization, investigation, data curation, formal analysis, writing - original draft, visualization: Ye Z
Formal analysis, validation, data curation, writing - review & editing: Kong L
Formal analysis, validation, data curation: Zhao Y
Investigation, methodology, validation: Zhang C, Yang X, Yan K
Resources, formal analysis, writing - review & editing: Zhang Y
Resources, conceptualization, formal analysis, visualization, writing - review & editing: Zhang H
Resources, formal analysis, writing - review & editing, supervision, project administration: Tang Y

Availability of data and materials

Not applicable.

Financial support and sponsorship

This work was supported by the National Key R&D Program of China (2018YFA0209402, 2021YFC1523403), NSFC (22088101, 22072028, and 22175040) and China Postdoctoral Science Foundation (2021M700812).

Conflicts of interest

The authors declared that they have no known competing financial interests or personal relationships that could have appeared to influence the work reported in this paper.

Ethical approval and consent to participate

Not applicable.

Consent for publication

Not applicable.

REFERENCES

1. Rimer JD, Chawla A, Le TT. Crystal engineering for catalysis. *Annu Rev Chem Biomol Eng* 2018;9:283-309. DOI PubMed
2. Dandekar P, Kuvadia ZB, Doherty MF. Engineering crystal morphology. *Annu Rev Mater Res* 2013;43:359-86. DOI
3. Lai WH, Wang YX, Wang Y, et al. Morphology tuning of inorganic nanomaterials grown by precipitation through control of electrolytic dissociation and supersaturation. *Nat Chem* 2019;11:695-701. DOI PubMed
4. Görke M, Garnweitner G. Crystal engineering of nanomaterials: current insights and prospects. *CrystEngComm* 2021;23:7916-27. DOI

5. Brammer L. Developments in inorganic crystal engineering. *Chem Soc Rev* 2004;33:476-89. DOI PubMed
6. Zhou W. Reversed crystal growth: implications for crystal engineering. *Adv Mater* 2010;22:3086-92. DOI PubMed
7. Desiraju GR. Crystal engineering: a holistic view. *Angew Chem Int Ed Engl* 2007;46:8342-56. DOI PubMed
8. Jain R, Mallette AJ, Rimer JD. Controlling nucleation pathways in zeolite crystallization: seeding conceptual methodologies for advanced materials design. *J Am Chem Soc* 2021;143:21446-60. DOI PubMed
9. Olafson KN, Li R, Alamani BG, Rimer JD. Engineering crystal modifiers: bridging classical and nonclassical crystallization. *Chem Mater* 2016;28:8453-65. DOI
10. De Yoreo JJ, Gilbert PU, Sommerdijk NA, et al. Crystal growth. Crystallization by particle attachment in synthetic, biogenic, and geologic environments. *Science* 2015;349:aaa6760. DOI PubMed
11. Kirschhock CEA, Ravishankar R, Jacobs PA, Martens JA. Aggregation mechanism of nanoslabs with zeolite MFI-type structure. *J Phys Chem B* 1999;103:11021-7. DOI
12. Sheng Z, Li H, Du K, et al. Observing a zeolite nucleus (subcrystal) with a uniform framework structure and its oriented attachment without single-molecule addition. *Angew Chem Int Ed Engl* 2021;60:13444-51. DOI PubMed
13. Davis TM, Drews TO, Ramanan H, et al. Mechanistic principles of nanoparticle evolution to zeolite crystals. *Nat Mater* 2006;5:400-8. DOI PubMed
14. He G, Dahl T, Veis A, George A. Nucleation of apatite crystals in vitro by self-assembled dentin matrix protein 1. *Nat Mater* 2003;2:552-8. DOI PubMed
15. Fang Y, Hu H, Chen G. In situ assembly of zeolite nanocrystals into mesoporous aggregate with single-crystal-like morphology without secondary template. *Chem Mater* 2008;20:1670-2. DOI
16. Zhang H, Ma Y, Song K, Zhang Y, Tang Y. Nano-crystallite oriented self-assembled ZSM-5 zeolite and its LDPE cracking properties: Effects of accessibility and strength of acid sites. *J Catal* 2013;302:115-25. DOI
17. Niederberger M, Cölfen H. Oriented attachment and mesocrystals: non-classical crystallization mechanisms based on nanoparticle assembly. *Phys Chem Chem Phys* 2006;8:3271-87. DOI PubMed
18. Song RQ, Cölfen H. Mesocrystals-ordered nanoparticle superstructures. *Adv Mater* 2010;22:1301-30. DOI PubMed
19. Sturm Née Rosseeva EV, Cölfen H. Mesocrystals: structural and morphogenetic aspects. *Chem Soc Rev* 2016;45:5821-33. DOI PubMed
20. Shamzhy M, Opanasenko M, Concepción P, Martínez A. New trends in tailoring active sites in zeolite-based catalysts. *Chem Soc Rev* 2019;48:1095-149. DOI PubMed
21. Choi M, Na K, Kim J, Sakamoto Y, Terasaki O, Ryoo R. Stable single-unit-cell nanosheets of zeolite MFI as active and long-lived catalysts. *Nature* 2009;461:246-9. DOI PubMed
22. Zhang Y, Che S. π-π interactions between aromatic groups in amphiphilic molecules: directing hierarchical growth of porous zeolites. *Angew Chem Int Ed Engl* 2020;59:50-60. DOI PubMed
23. Korde A, Min B, Kapaca E, et al. Single-walled zeolitic nanotubes. *Science* 2022;375:62-6. DOI PubMed
24. Jacobsen CJH, Madsen C, Houzvicka J, Schmidt I, Carlsson A. Mesoporous zeolite single crystals. *J Am Chem Soc* 2000;122:7116-7. DOI
25. Azhati A, Xie S, Wang W, et al. Ordered, highly zeolitized mesoporous aluminosilicates produced by a gradient acidic assembly growth strategy in a mixed template system. *Chem Mater* 2016;28:4859-66. DOI
26. Sun MH, Chen LH, Yu S, et al. Micron-sized zeolite beta single crystals featuring intracrystal interconnected ordered macro-meso-microporosity displaying superior catalytic performance. *Angew Chem Int Ed Engl* 2020;59:19582-91. DOI PubMed
27. Jung J, Jo C, Mota FM, Cho J, Ryoo R. Acid catalytic function of mesopore walls generated by MFI zeolite desilication in comparison with external surfaces of MFI zeolite nanosheet. *Appl Catal A-Gen* 2015;492:68-75. DOI
28. Qin Z, Melinte G, Gilson JP, et al. The mosaic structure of zeolite crystals. *Angew Chem Int Ed Engl* 2016;55:15049-52. DOI PubMed
29. Zhang B, Zhang Y, Hu Y, et al. Microexplosion under microwave irradiation: a facile approach to create mesopores in zeolites. *Chem Mater* 2016;28:2757-67. DOI
30. Ren N, Subotić B, Bronić J, et al. Unusual pathway of crystallization of zeolite ZSM-5 in a heterogeneous system: phenomenology and starting considerations. *Chem Mater* 2012;24:1726-37. DOI
31. Zhang Q, Mayoral A, Terasaki O, et al. Amino acid-assisted construction of single-crystalline hierarchical nanozeolites via oriented-aggregation and intraparticle ripening. *J Am Chem Soc* 2019;141:3772-6. DOI PubMed
32. Zhang Q, Chen G, Wang Y, et al. High-quality single-crystalline MFI-type nanozeolites: a facile synthetic strategy and MTP catalytic studies. *Chem Mater* 2018;30:2750-8. DOI
33. Zhang H, Zhao Y, Zhang H, et al. Tailoring zeolite ZSM-5 crystal morphology/porosity through flexible utilization of silicalite-1 seeds as templates: unusual crystallization pathways in a heterogeneous system. *Chem Eur J* 2016;22:7141-51. DOI PubMed
34. Kumar M, Luo H, Román-Leshkov Y, Rimer JD. SSZ-13 crystallization by particle attachment and deterministic pathways to crystal size control. *J Am Chem Soc* 2015;137:13007-17. DOI PubMed
35. Lupulescu AI, Kumar M, Rimer JD. A facile strategy to design zeolite L crystals with tunable morphology and surface architecture. *J Am Chem Soc* 2013;135:6608-17. DOI PubMed
36. Zheng J, Zhang W, Liu Z, et al. Unraveling the non-classic crystallization of SAPO-34 in a dry gel system towards controlling meso-structure with the assistance of growth inhibitor: growth mechanism, hierarchical structure control and catalytic properties.

Microporous Mesoporous Mater 2016;225:74-87. DOI

37. Ye Z, Zhao Y, Zhang H, et al. Mesocrystal morphology regulation by "alkali metals ion switch": re-examining zeolite nonclassical crystallization in seed-induced process. *J Colloid Interface Sci* 2022;608:1366-76. DOI PubMed
38. Zhang H, Zhang H, Zhao Y, Shi Z, Zhang Y, Tang Y. Seeding bundlelike MFI zeolite mesocrystals: a dynamic, nonclassical crystallization via epitaxially anisotropic growth. *Chem Mater* 2017;29:9247-55. DOI
39. Zhao Y, Zhang H, Wang P, et al. Tailoring the morphology of MTW zeolite mesocrystals: intertwined classical/nonclassical crystallization. *Chem Mater* 2017;29:3387-96. DOI
40. Wang L, Zhu SC, Shen MK, et al. Fractal MTW zeolite crystals: hidden dimensions in nanoporous materials. *Angew Chem Int Ed Engl* 2017;56:11764-8. DOI PubMed
41. Wang P, Zhao Y, Zhang H, Yu T, Zhang Y, Tang Y. Effect of pyrazolium-derived compounds as templates in zeolite synthesis. *RSC Adv* 2017;7:23272-8. DOI
42. Ruiz AZ, Brühwiler D, Ban T, Calzaferri G. Synthesis of zeolite L. Tuning size and morphology. *Monatsh Chem* 2005;136:77-89. DOI
43. Hu Y, Liu C, Zhang Y, Ren N, Tang Y. Microwave-assisted hydrothermal synthesis of nanozeolites with controllable size. *Microporous Mesoporous Mater* 2009;119:306-14. DOI
44. Larlus O, Valtchev VP. Crystal morphology control of LTL-type zeolite crystals. *Chem Mater* 2004;16:3381-9. DOI
45. Meier WM, Olson DH, Baerlocher C. Atlas of zeolite structure types. *Zeolites* 1996;17:1-2. DOI
46. Itani L, Bozhilov KN, Clet G, Delmotte L, Valtchev V. Factors that control zeolite L crystal size. *Chem Eur J* 2011;17:2199-210. DOI PubMed
47. Kumar M, Li R, Rimer JD. Assembly and evolution of amorphous precursors in zeolite L crystallization. *Chem Mater* 2016;28:1714-27. DOI
48. Thommes M, Kaneko K, Neimark AV, et al. Physisorption of gases, with special reference to the evaluation of surface area and pore size distribution (IUPAC Technical Report). *Pure Appl Chem* 2015;87:1051-69. DOI
49. Devi R, Borah R, Deka RC. Design of zeolite catalysts for nitroaldol reaction under mild condition. *Appl Catal A-Gen* 2012;433-434:122-7. DOI
50. Tangale NP, Sonar SK, Niphadkar PS, Joshi PN. Hierarchical K/LTL zeolites: synthesis by alkali treatment, characterization and catalytic performance in Knoevenagel condensation reaction. *J Ind Eng Chem* 2016;40:128-36. DOI
51. Joshi PN, Jacob NE, Shiralkar VP. Physicochemical characterization of the intermediate phases obtained during the hydrothermal crystallization of LTL zeolites. *J Phys Chem* 1995;99:4225-9. DOI
52. Oleksiak MD, Soltis JA, Conato MT, Penn RL, Rimer JD. Nucleation of FAU and LTA zeolites from heterogeneous aluminosilicate precursors. *Chem Mater* 2016;28:4906-16. DOI
53. Dutta PK, Shieh DC. Crystallization of zeolite A: a spectroscopic study. *J Phys Chem* 1986;90:2331-4. DOI
54. Chen CT, Iyoki K, Hu P, et al. Reaction kinetics regulated formation of short-range order in an amorphous matrix during zeolite crystallization. *J Am Chem Soc* 2021;143:10986-97. DOI PubMed
55. Li R, Linares N, Sutjianto JG, Chawla A, Garcia-Martinez J, Rimer JD. Ultrasmall zeolite L crystals prepared from highly interdispersed alkali-silicate precursors. *Angew Chem Int Ed Engl* 2018;57:11283-8. DOI PubMed
56. Ohgushi T, Matsuo T, Satoh H, Matsumoto T. Cation distribution in K,H-L zeolite prepared through ion-exchange with TMA ion. *Microporous Mesoporous Mater* 2009;117:472-7. DOI
57. Bulut E, Özacar M, Şengil İA. Adsorption of malachite green onto bentonite: Equilibrium and kinetic studies and process design. *Microporous Mesoporous Mater* 2008;115:234-46. DOI
58. Choy KKH, Porter JF, Mckay G. Langmuir isotherm models applied to the multicomponent sorption of acid dyes from effluent onto activated carbon. *J Chem Eng Data* 2000;45:575-84. DOI
59. Hu Y, Zhang Y, Ren N, Tang Y. Crystal plane- and size-dependent protein adsorption on nanozeolite. *J Phys Chem C* 2009;113:18040-6. DOI

Liu *et al. Chem Synth* 2022;2:21
DOI: 10.20517/cs.2022.26

Chemical Synthesis

Review

Open Access

Check for updates

Fundamentals of the catalytic conversion of methanol to hydrocarbons

Zhaohui Liu, Jianfeng Huang*

State Key Laboratory of Coal Mine Disaster Dynamics and Control, Institute of Advanced Interdisciplinary Studies, School of Chemistry and Chemical Engineering, Chongqing University, Chongqing 400044, China.

***Correspondence to:** Prof. Jianfeng Huang, State Key Laboratory of Coal Mine Disaster Dynamics and Control, Institute of Advanced Interdisciplinary Studies, School of Chemistry and Chemical Engineering, Chongqing University, Chongqing 400044, China. E-mail: jianfeng.huang@cqu.edu.cn

How to cite this article: Liu Z, Huang J. Fundamentals of the catalytic conversion of methanol to hydrocarbons. *Chem Synth* 2022;2:21. https://dx.doi.org/10.20517/cs.2022.26

Received: 12 Sep 2022 **First Decision:** 4 Nov 2022 **Revised:** 19 Nov 2022 **Accepted:** 25 Nov 2022 **Published:** 6 Dec 2022

Academic Editor: Ying Wan **Copy Editor:** Peng-Juan Wen **Production Editor:** Peng-Juan Wen

Abstract

For more than four decades, the methanol-to-hydrocarbons (MTH) reaction has been a successful route to producing valuable fuels and chemicals from non-petroleum feedstocks. This review provides the most comprehensive summary to date of recent research concerning the mechanistic fundamentals of this important reaction, covering different reaction stages. Mechanisms that have been proposed to explain the initial C-C bond formation during the induction stage of the MTH reaction are introduced, including the methoxymethyl cation, Koch carbonylation, carbene and methane-formaldehyde processes. At present, there is no consensus regarding these hypothetical mechanisms as a consequence of the limited amount of conclusive experimental evidence. The steady state of the MTH reaction is also examined with a focus on the widely accepted indirect hydrocarbon pool mechanism and the dual cycle concept that provides a mechanistic basis for the effects of zeolite structures and reaction conditions on product distribution. In the following section, advanced characterization techniques capable of providing new insights into the formation of coke species during the MTH reaction and innovative approaches effectively inhibiting coke formation are introduced. Finally, a summary is provided and perspectives on current challenges and the future development of this area are presented.

Keywords: Methanol to hydrocarbons, zeolite, reaction mechanism, C-C bond formation, product selectivity, catalyst deactivation

INTRODUCTION

The methanol-to-hydrocarbons (MTH) reaction catalyzed by zeolites was first discovered by Mobil scientists in 1977[1] and subsequently commercialized for the first time in New Zealand in 1985[2]. This process then became an important platform for the production of various high-demand chemical commodities, such as via methanol to gasoline (MTG)[3,4], methanol to olefins (MTO)[5-9], methanol to propene (MTP)[10-12] and methanol to aromatics (MTA) systems[13-15]. Since the MTH reaction uses methanol or dimethyl ether (DME) as the feedstock, both of which can be readily produced from nonpetrochemical resources such as natural gas, coal and biomass[16-18], this process provides an alternative to current petroleum-based synthetic routes and has thus attracted extensive attention[19-21].

In addition to obvious economic benefits[22,23], understanding the complex MTH reaction mechanism as a means of improving efficiency represents an important fundamental research goal. Over the past several decades, numerous studies of MTH have been reported and various reaction mechanisms have been proposed. There have also been several review articles in the literature that focus on different aspects of the MTH reaction, including the effects of zeolite pores on product selectivity[4,22], the sub-reactions associated with the dual cycle mechanism[20], the analysis of chemical kinetics using molecular modeling[24] and principles for the design of catalysts[21].

This review aims to provide a comprehensive summary of the MTH reaction mechanisms reported to date. To this end, the mechanisms associated with the different reaction stages are separately elucidated. We first discuss four direct mechanisms explaining the formation of the first C-C bond during the induction period. These comprise the methoxymethyl cation, Koch carbonylation, carbene and methane-formaldehyde mechanisms. These discussions primarily focus on the differences between the proposed mechanisms as well as areas where there is a lack of consensus. Advances in characterization techniques that have provided new experimental evidence and an improved understanding of these long-standing issues are also assessed. The next section examines the MTH process when in the steady state, which primarily determines product selectivity, with a focus on the widely accepted indirect hydrocarbon pool mechanism and the dual cycle concept. On the basis of the well-developed dual cycle mechanism, the effects of zeolite structures and reaction conditions on product distribution are explained. In particular, the enhanced production of propene based on optimizing the extent to which the aromatic and olefin cycles proceed is discussed. Subsequently, the deactivation of MTH catalysts is assessed. This section presents the most recent works investigating the mechanisms by which coke species [comprising primarily polycyclic aromatic hydrocarbons (PAHs) and oxygen-containing species] are formed and introduces some effective approaches to reducing coke formation. Finally, we conclude this review with a summary and share our vision for the future of MTH research.

FORMATION OF THE INITIAL C-C BOND

Since the 1970s, numerous scientists have devoted considerable effort to determining the mechanism of the MTH reaction and more than twenty different theories have been proposed. However, the precise route to the formation of the first C-C during the induction stage of the MTH reaction is still being debated. Initially, it was believed that trace impurities (potentially originating from the methanol feed, incomplete combustion of organics in the zeolite, the carrier gas or other sources) were responsible for the conversion of methanol in any direct mechanism that converts methanol/DME to hydrocarbons via a coupling process[25]. This concept was dominant for a long time, primarily because of a lack of convincing experimental data to support a direct mechanism. More recently, there has been much research devoted to the analysis of the first C-C bond formed in the initial reaction stage. Several years ago, Yarulina *et al.* and Olsbye *et al.* discussed potential mechanisms in high-quality reviews[21,26]. The present review provides more

recent discoveries based on the use of advanced characterization techniques, with a particular focus on elaborating on the reasons for the ongoing lack of consensus. Four firmly supported direct mechanisms are discussed in this section.

Methoxymethyl cation mechanism

In 2003, Wang *et al.* found that methanol or DME molecules are adsorbed on Brønsted acid sites to produce surface methoxy species (SMSs) that are highly active with regard to hydrocarbon generation[27]. This prior work indicated that, rather than organic impurities affecting product distribution or the hydrocarbon pool species, these SMS sites could promote the initial C-C bond formation during the MTH reaction[28]. With the ongoing development of spectroscopic techniques, many investigations of the first C-C bond formation have been performed and the facile generation of SMSs as active intermediates on catalytic sites has often been confirmed. As an example, Li *et al.* observed the formation of methoxy groups on the zeolite SAPO-34 using infrared (IR) spectroscopy and proposed that methoxymethyl cations ($CH_3OCH_2^+$) generated by the reaction of SMSs with DME served as intermediates[29]. These cations are coupled with additional DME/methanol molecules to produce various compounds incorporating C-C bonds (such as 1,2-dimethoxyethane and 2-methoxyethanol)[29]. In 2017, Wu *et al.* successfully observed a surface metheneoxy analog species on ZSM-5 with the aid of a solid-state nuclear magnetic resonance (NMR) technique and hypothesized that the strong interaction of the active C-H bond in DME/methanol adsorbed on the zeolite with SMSs played a crucial role in the initial C-C bond formation process[30]. In 2018, Wang *et al.* observed the bonding of SMSs to extra-framework Al atoms on ZSM-5 using ^{13}C-{^{27}Al} solid-state NMR, thus establishing the possibility of interactions between these Al atoms and SMSs[31]. In addition, SMSs adsorbed on the 8-MR pore windows of the zeolite SAPO-34 were detected by Lo *et al.* using synchrotron X-ray powder diffraction-mass spectrometry (MS) with Rietveld refinement of the data[32]. This prior work demonstrated that the presence of SMSs limited the diffusion of C_4 species through the pore openings of the SAPO-34 and thus facilitated the production of light olefins during the MTO reaction[32]. More recently, Sun *et al.* reported the first observation of surface ethoxy species serving as ethene precursor on a CHA zeolite during an MTH reaction using *in situ* solid-state NMR[33]. Ab initio molecular dynamics simulations were also applied to simulate the dynamics of the first C-C bond generation. As shown in Figure 1, the presence of a reactive SMS intermediate on an active site was determined by NMR analysis and a short-range collision between a DME molecule and this SMS was found to activate the DME. Subsequently, the first C-C bond was formed via an electrophilic attack to produce a C_2 precursor[33]. These previous studies confirmed the formation of methoxymethyl cations as a consequence of the reactions between SMSs and methanol/DME, representing the methoxymethyl cation mechanism.

Koch carbonylation mechanism

The electrophilic C in methanol/DME and the nucleophilic C in CO readily undergo an addition reaction to form a C-C bond. In 2016, Liu *et al.* proposed that the carbonylation of SMSs contributes to the first C-C bond formation to generate an acetyl species that then dissociates to produce methyl acetate or acetic acid, which can be detected as intermediates [Figure 2][34]. While monitoring the MTH reaction over ZSM-5 at 400 °C, this same group detected an increased conversion rate following the addition of CO to the methanol feedstock. Since here the involved carbonylation is similar to the Koch-type carbonylation by which carboxylic acids can be produced from the reaction of high-pressure CO with alcohols/olefins and H_2O, the mechanism for the C-C bond formation was recognized as the Koch carbonylation mechanism. The feasibility of the Koch carbonylation mechanism has also been supported by theoretical calculations that have shown a relatively low energy barrier of 80 kJmol^{-1} compared with the value of 330 kJmol^{-1} for the ylide-type mechanism[34,35]. Using solid-state NMR and operando UV-visible diffuse reflectance spectroscopy, Chowdhury *et al.* identified a direct C-C bond-containing species, i.e., surface-bound acetate, a known Koch carbonylation product that can be obtained from SMSs[36]. The surface-bound acetate species

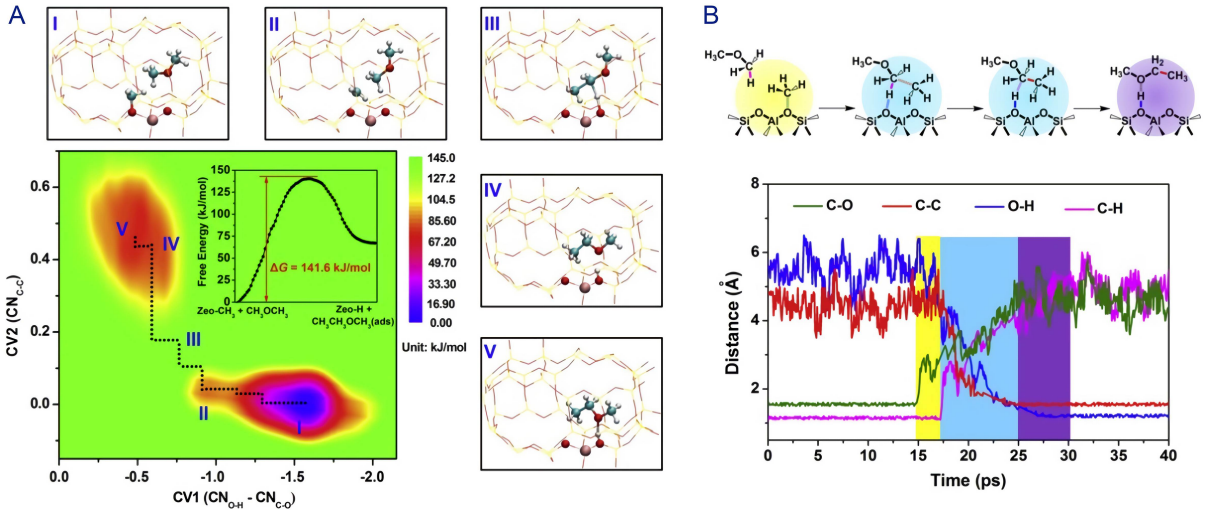

Figure 1. An ab initio molecular dynamics simulation of C-C bond formation subsequent to the collision of DME with an SMS. (A) The two-dimensional free energy surface and minimal energy path associated with the first C-C bond formation. The images show five (meta-) stable states: (I) reactant basin, (II) approaching state, (III) activation state, (IV) product state and (V) product basin. (B) Changes in the C-O, C-C, O-H and C-H bond distances in DME and the SMS over the SSZ-13 zeolite. Reproduced with permission from ref. 33[33]. Copyright 2021, Elsevier. DME: Dimethyl ether; SMS: surface methoxy specie.

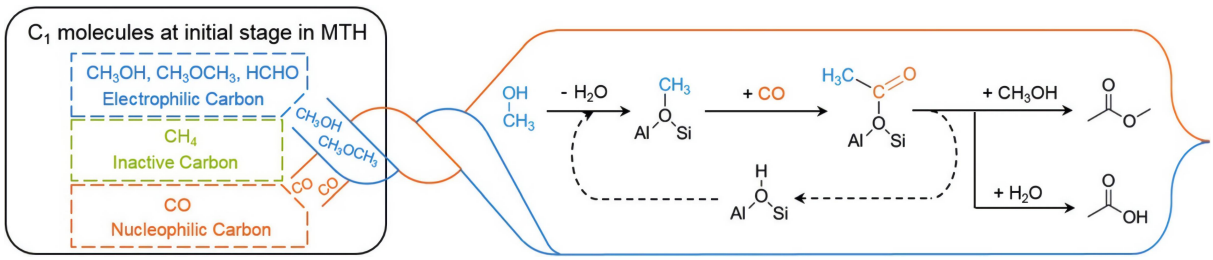

Figure 2. A diagram showing the initial C-C bond formation via the Koch carbonylation mechanism. Reproduced with permission from ref. 34[34]. Copyright 2016, Wiley-VCH. MTH: Methanol-to-hydrocarbons.

reacted with methanol to produce methyl acetate, as confirmed by the ^{13}C NMR signals at 55.2 and 178.5 ppm[36]. Very recently, using *in situ* Fourier transform IR spectroscopy, Airi *et al.* tracked the roto-vibrational CO signal throughout a methanol conversion reaction over the catalyst CoAlPO-18 and the resulting data provided support for a Koch carbonylation process involving SMSs and CO[37]. Plessow *et al.* also provided theoretical evidence for the Koch carbonylation mechanism using a model in which CO was formed from the dehydrogenation of methanol via a formaldehyde intermediate[38]. In 2019, Yang *et al.* confirmed the formation of acetaldehyde as a result of the reaction of SMSs, CO and H_2 based on a combination of online MS and NMR spectroscopy[39]. In addition, using the advanced operando synchrotron photoelectron-photoion coincidence technique, Wu *et al.* observed the production of a ketene from methyl acetate, further confirming the occurrence of carbonylation during the MTH reaction[40].

Carbene mechanism

In addition to reacting with cations (such as methoxymethyl cation) and CO, SMSs can also serve as methylation agents via the formation of carbene-like species. In 2008, Wang *et al.* reported that the C-H bonds of SMSs can be activated at high reaction temperatures to generate active compounds possessing carbene/ylide-like properties[41]. Indirect evidence for this phenomenon was also obtained from a carbene trapping experiment in which cyclohexane was used as the probe molecule and a typical carbene insertion

reaction generated a methylcyclohexane indicator[41]. Following this early work, Yamazaki *et al.* obtained direct evidence of a carbene-like intermediate using IR spectroscopy. Monitoring the IR spectra of samples obtained during the reaction of surface-bound deuterated methoxy (OCD_3) with ethene at 250 °C over ZSM-5 indicated that the intensities of the C-D stretching bands decreased while a peak related to an acidic O-D group appeared at 2655 cm^{-1} and increased in intensity, demonstrating the attachment of a D atom to a neighboring O[42]. Additional evidence for this process was obtained by reacting OCD_3 with DME at 200 °C[43]. In 2016, Chowdhury *et al.* provided further support for the carbene mechanism on the basis of analyses by two-dimensional magic angle spinning ^{1}H-^{13}C and ^{13}C-^{13}C solid-state NMR spectroscopy[36]. As shown in Figure 3A and B, the peaks at 57.7 ppm in the ^{13}C NMR spectrum and at 3.54 ppm in the ^{1}H NMR spectrum were assigned to SMSs and the strong cross-peak between ^{13}C NMR signals revealed the proximity of the SMSs to adsorbed methanol molecules. The close proximity of the 57.7 and 52.2 ppm peaks in the ^{13}C NMR spectrum was attributed to interactions of the polarized C-H bonds in the SMSs with neighboring O atoms [Figure 3C]. This result indicated the insertion of carbenes into the sp^3 C-H bonds of methanol molecules. Dimethoxymethane and its hydrolysis product methanediol were also detected in this prior work [Figure 3D and E][36]. More recently, Minova *et al.* employed Fourier transform IR spectroscopy with a mass spectrometer to directly observe the deprotonation of SMSs in large single crystals of SAPO-34[44]. This process was thought to initiate the first C-C bond formation via the insertion of a carbene into an adjacent methoxy group[44].

Methane-formaldehyde mechanism

In 1984, Kubelková *et al.* demonstrated the formation of formaldehyde and methane as a result of methanol disproportionation on ZSM-5 at 400 °C, working at low methanol pressures[45]. In 1987, Hutchings *et al.* observed the formation of methane prior to C_{2+} hydrocarbons in conjunction with low methanol coverage of the catalyst[46]. Based on these findings, the methane-formaldehyde mechanism has been postulated as yet another theory regarding the initial C-C bond formation process during the MTH reaction[46,47]. In this mechanism, methanol and SMS first react to produce formaldehyde and methane, after which the C-C coupling of the formaldehyde with a CH_3^- anion generated by the donation of an H^+ cation from CH_4 to ZO^- (i.e., deprotonated zeolite) occurs to produce ethanol [Figure 4][26]. Several recent studies using advanced analytical techniques have also confirmed the formation of methane and formaldehyde. As an example, Liu *et al.* identified the formation of olefins following the reaction of CH_4, HCHO and CO using *in situ* IR spectroscopy in conjunction with MS[48]. Wen *et al.* employed *in situ* synchrotron radiation photoionization MS to quantify the amount of formaldehyde generated during the reaction[49]. Data such as these provide solid evidence to support the methane-formaldehyde mechanism.

HYDROCARBON POOL MECHANISM AND THE DUAL CYCLE CONCEPT

An autocatalytic process occurring during the induction stage of the MTH reaction and related to the direct mechanisms has attracted much attention from researchers. Several excellent reviews have fully summarized the development of these mechanisms[21,26]. Although a general agreement has been reached regarding the formation of the initial C-C bond via a direct mechanism involving the direct coupling of methanol with its derivatives (e.g., methoxymethyl cations, CO, carbene, formaldehyde), the exact mechanistic process for each direct mechanism has not yet been fully established. Moreover, computational results have shown that the energy barrier to the direct coupling mechanism is very high and the reaction intermediates are labile, making direct C-C bond formation difficult to achieve[35,50]. While there are ongoing debates regarding the initial C-C bond formation mechanism, an indirect hydrocarbon pool mechanism which is responsible for the later stages after the initial C-C bond formation in MTH reactions has now been widely accepted with abundant supporting evidences.

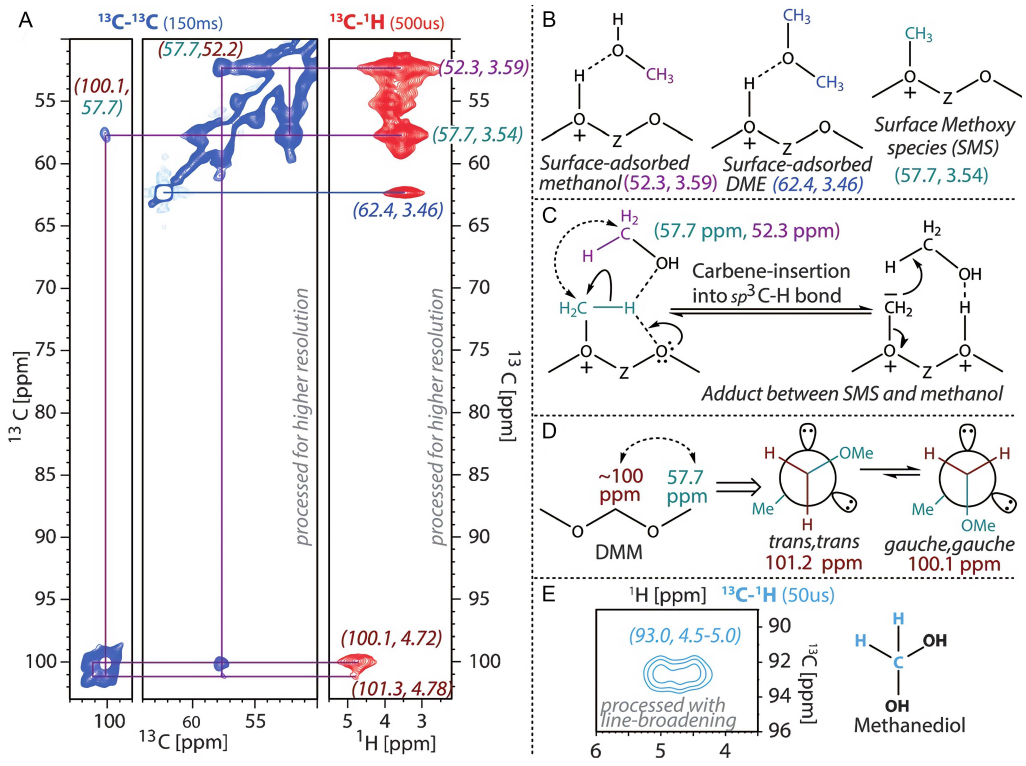

Figure 3. NMR spectra of methanol, SMSs and acetal species on SAPO-34. (A) Magnifications of two-dimensional ^{13}C-^{13}C (blue) and ^{13}C-^{1}H (red) solid-state NMR spectra acquired with a mixing time of 150 ms and a cross-polarization contact time of 500 µs. (B) Structures associated with peaks related to different surface species including methanol, DME and SMSs. (C) Identification of a surface adduct between an SMS and methanol (solid arrows: electron flows, dotted arrows: ^{13}C-^{13}C NMR correlation). (D) Chemical exchange of anomeric conformations of DMM as evident from the ^{13}C-^{13}C NMR data. (E) Identification of methanediol from the ^{13}C-^{1}H NMR data with a cross-polarization contact time of 50 µs. Reproduced with permission from ref. 36[36]. Copyright 2016, Wiley-VCH. NMR: Nuclear magnetic resonance; DME: dimethyl ether; SMSs: surface methoxy species.

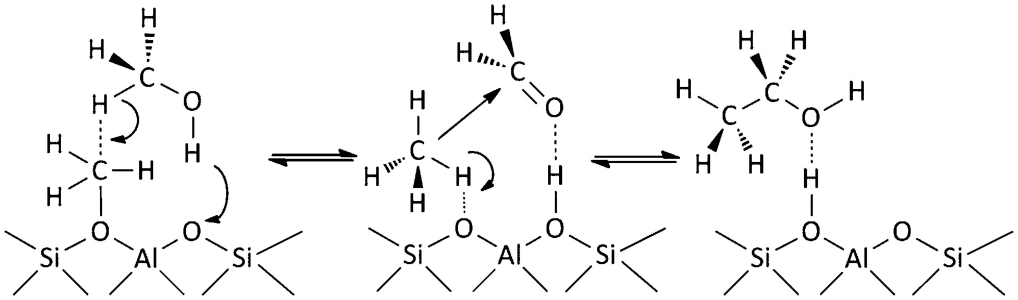

Figure 4. A diagram summarizing the methane-formaldehyde mechanism. Reproduced with permission from ref. 26[26]. Copyright 2015, Royal Society of Chemistry.

The proposed hydrocarbon pool mechanism and the dual cycle concept

In the 1990s, Dahl *et al.* first proposed the hydrocarbon pool mechanism for the MTH reaction[51,52]. In this process [Figure 5A], methanol molecules first generate a pool of hydrocarbon species [$(CH_2)_n$]. These species are active and further react with the reactant methanol to generate multiple products, including olefins, alkanes and aromatics. Simultaneously, coke is produced from the hydrocarbon pool species[52]. This indirect hydrocarbon pool mechanism has been widely studied and the associated theory has evolved considerably over time. In 2000, Song *et al.* found that the use of pretreated SAPO-34 containing

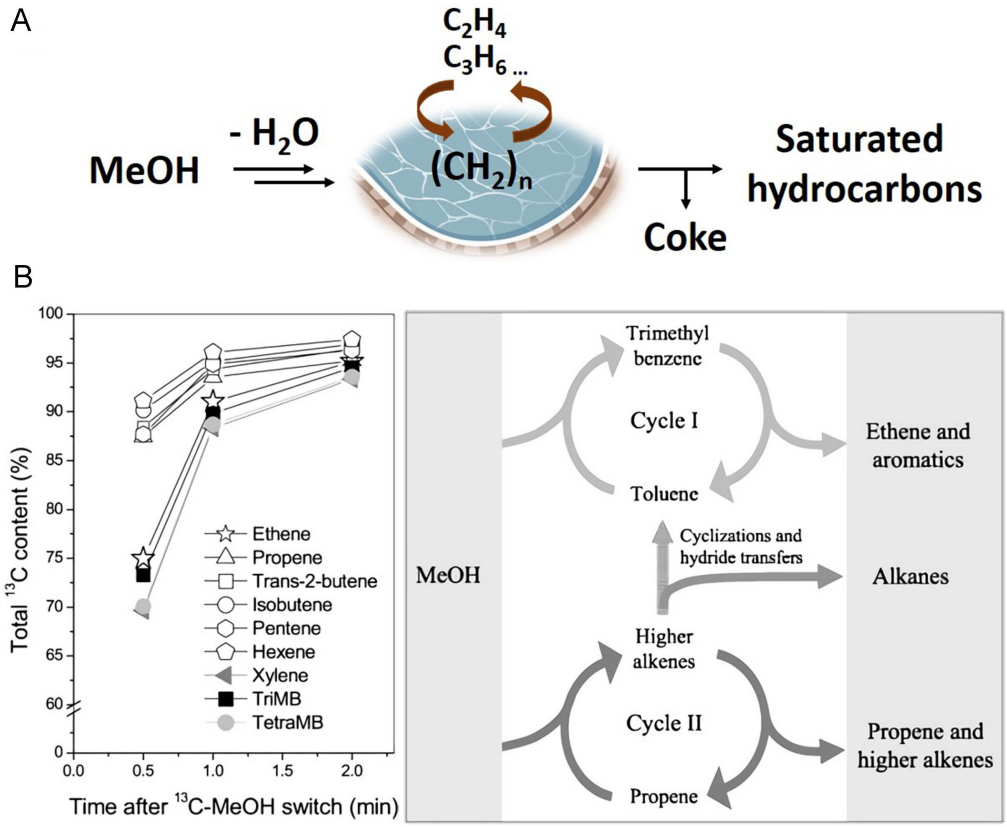

Figure 5. (A) The hydrocarbon pool mechanism for MTH conversion. Adapted with permission from ref. 52[52]. Copyright 1996, Elsevier. (B) The total ^{13}C concentrations in the reaction products (left) and the proposed dual cycle concept for the MTH reaction on ZSM-5 (right). Reproduced with permission from ref. 55[55]. Copyright 2007, Elsevier. MTH: Methanol-to-hydrocarbons.

methylbenzenes greatly increased the extent of methanol conversion from just 14% in the case of fresh catalyst to approximately 100%, suggesting that methylbenzenes were the active intermediates in the hydrocarbon pool[5]. Based on the co-reaction of ^{13}C-methanol with ^{12}C-benzene, which yields methylbenzenes, in a beta zeolite, Bjørgen *et al.* demonstrated the insertion of ^{12}C atoms in both the reaction effluent and identified the compounds retained in the catalyst, providing concrete evidence for the active nature of methylbenzenes[53].

Another important theory that evolved from the hydrocarbon pool mechanism is the dual cycle concept. Isotopic switching experiments in which a ^{12}C-methanol feedstock was switched to ^{13}C-methanol during the steady state of the MTH process by Bjorgen *et al.* indicated that the amount of ^{13}C inserted into ethene closely matched that in the methylbenzenes while the amounts of ^{13}C in propene and higher olefins were highly similar [Figure 5B][54,55]. These results demonstrated that there were two different groups of active intermediates in the MTH hydrocarbon pool, leading to the dual cycle concept. In this mechanism, aromatic intermediates and olefins simultaneously react to generate complex products, representing a modification of the hydrocarbon pool mechanism[54,55]. Notably, this isotopic switching technique is commonly accepted and widely applied to the study of dual cycle reaction routes.

Elementary reactions

The proposed dual cycle mechanism has made a significant contribution to our understanding of the effect of the hydrocarbon pool on product selectivity. However, many different elementary reactions comprise the

overall MTH process and an assessment of the kinetics of the pool species and the associated sub-reactions can help to elucidate links between the dual cycle mechanism and various products. In this regard, Ilias *et al.* produced an excellent review focusing on the chemistry of the MTH reaction[20]. Here, we provide a brief introduction to the sub-reactions and primarily concentrate on the effects of these sub-reactions on product distribution. Based on the dual cycle mechanism, six important elementary reactions may be associated with the MTH process, as discussed in the following paragraphs.

Olefin methylation, generating higher olefins by incorporating methyl groups into light olefins, is the main way for the C-C chain growth in MTH reactions. A prior kinetic study established that such reactions are primarily affected by the olefin pressure with only a minimal effect from methanol/DME[56-61], on the basis of the relationship between olefin methylation rate and the partial pressure of reactants (i.e., light olefin and methanol/DME) which implies that, during this process, the active sites on the catalyst are fully saturated by methyl groups obtained from methanol or DME[20]. Additionally, with increases in olefin size, the activation energy barrier decreases and the methylation rate increases, such that highly branched aliphatic compounds are favored as intermediates during MTH conversion[56-61]. Interestingly, the oligomerization of light olefins is also an effective source of the C-C chain growth of hydrocarbons and can be catalyzed by the Brønsted acid sites of zeolites. Similar to the olefin methylation reaction, the formation of heavy olefins via this route is promoted by moderate temperatures and high pressures[62,63].

Olefin cracking was first reported by Dessau and LaPierre[64,65] and was proposed as an important means of increasing the yield of propene in Lurgi's MTP reaction on ZSM-5[20]. During this process, alkoxides formed by the protonation of long-chain olefins generate short-chain olefins and small alkoxides through β-scission. The small alkoxides subsequently desorb from the catalyst and acquire protons. The competition between methylation and cracking is a critical factor that decides the resulting product distribution. Specifically, more rapid olefin cracking tends to produce lower molecular weight olefins, while a slower reaction gives higher molecular weight olefins that eventually generate aromatics via cyclization reactions. The rates of β-scission also affect the proportion of olefins in the product mixture[66-68]. Simonetti *et al.* found that the rate of C_5 methylation was more than 100 times that of β-scission, but the C_8 olefin (i.e., 3,4,4-trimethyl-2-pentene) had a higher rate of β-scission[66]. Buchanan *et al.* also revealed that the olefin cracking process was enhanced by elongating the olefin chains[68].

Hydrogen transfer and cyclization reactions can function as bridges between olefin- and aromatic-based cycles in MTH reactions. Higher olefins tend to produce aromatic compounds via hydrogen transfer together with the formation of stoichiometric amounts of alkanes. This process can be quantified using the hydrogen transfer index[69-72]. Specifically, this index can be used as an indicator for the formation of aromatics and the participation extent of the associated catalytic cycle (i.e., aromatic-based cycle)[73]. It should also be noted that cycloalkanes and cycloolefins are unstable products that quickly dehydrogenate to produce aromatics, so the cyclization process also contributes to the propagation of the aromatic cycle. Fan *et al.* found that dienes and monoenes can also form methylcyclohexenes via the Diels-Alder reaction based on assessments using solid-state NMR and gas chromatography (GC)-MS[74]. The same group also demonstrated that the Diels-Alder process exhibited much lower energy barriers than the oligomerization and cyclization reactions along the route to the construction of large molecules[74].

The methylation of aromatics is similar to that of olefins, but the dealkylation of the former can follow two different routes: the paring and side-chain mechanisms [Figure 6][75]. These two mechanisms both begin with the gem-methylation of methylbenzene. In the former, this step results in a ring contraction to generate a five-membered ring with an alkyl substituent that can produce either ethene or propene via

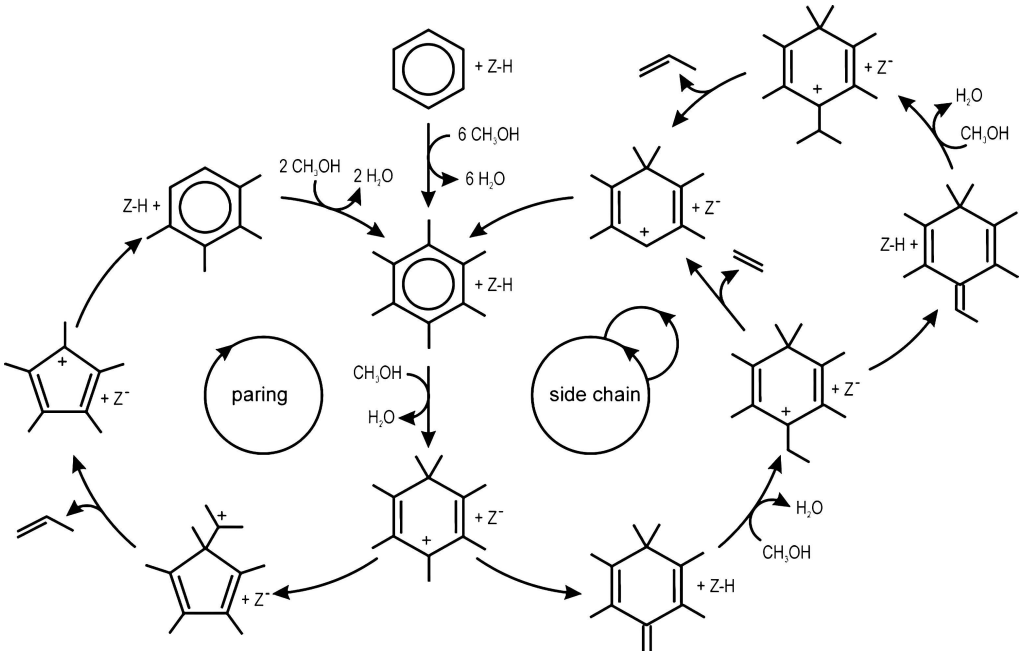

Figure 6. A diagram summarizing the paring and side-chain mechanisms. Reproduced with permission from ref. 75[75]. Copyright 2009, Wiley-VCH.

dealkylation[76-78]. The participation of cyclopentenyl cations in this mechanism has previously been confirmed by IR and NMR analyses[77-79]. In the case of the side-chain mechanism, following the release of a proton, an exocyclic double bond is formed that then undergoes stepwise side chain methylation and dealkylation[75,80]. Hexamethenecyclohexadiene and a heptamethylbenzenium cation have also been identified using GC-MS and NMR, providing direct evidence for the side-chain mechanism[81].

Contribution of catalytic cycles to product formation

In-depth investigations of the dual cycle mechanism have been performed in attempts to assess the relative contributions of the two cycles to the product distribution generated by the MTH reaction. As discussed above, each catalytic cycle contains different elementary sub-reactions that will vary with the reaction conditions and catalysts employed. Careful kinetic studies of these different sub-reactions have provided much knowledge regarding the effects of these elementary steps on product distribution and the dominant catalytic cycle.

Hill *et al.* recently carried out a detailed study of the dual cycle mechanism[59-61,82]. They first systematically investigated the rate constants for ethene and propene methylation over four zeolites (MFI, BEA, MOR and FER) and found that propene methylation had higher rate constants (by an order of magnitude) and lower activation energies compared with ethene methylation[59]. On the basis of isotopic switching experiments that showed that ethene was a product of the aromatic dealkylation process[55], this group proposed that ethene was an end product and could be used as an indicator of the progression of the aromatic cycle. Similarly, because alkanes formed during the MTH reaction are inactive, these compounds can serve as indicators of the occurrence of the olefin catalytic cycle. However, alkanes are also formed via a hydrogen transfer process that is related to aromatic formation. To exclude this effect, the same group proposed that the total yield of 2-methylbutane and 2-methyl-2-butene could serve as an indicator of the progression of the olefin-based cycle, while the ethylene/(2-methylbutane + 2-methyl-2-butene) ratio could be used to assess the extent to which aromatic-/olefin-based cycles occurred during the MTH reaction over ZSM-5[82].

Building on Bhan's work, Sun *et al.* suggested slightly different indicators for the dual cycles[83,84]. In the case of the aromatic-based cycle, they concluded that methane can also be formed via the dealkylation of methylbenzene and represents a terminal product of this catalytic cycle, meaning that the formation of this compound should exhibit the same trend as ethene. In contrast, the selectivity for C_4-C_7 aliphatics, which readily diffuse out of ZSM-5, can be employed as an indicator for the olefin-based cycle[83,84]. It is known that propene can be produced in both catalytic cycles and is also able to react with methanol as an olefin intermediate. Another important feature of the dual cycle mechanism is that the two catalytic cycles compete for acidic sites. Based on such fundamental information concerning the dual-cycle mechanism, researchers are trying many different approaches to achieving the selective propagation of one specific cycle as a means of obtaining product selectivity from the MTH reaction[20,82,83].

PRODUCT SELECTIVITY

The product distribution obtained from the MTH reaction during its steady state is an important aspect of the process and has therefore been extensively studied. Many factors, including the raw material feed, reaction conditions and zeolite structure, can have significant effects on the reaction routes and subsequently on product distribution. In the following section, we elaborate on the influences of these factors on product formation during the MTH reaction with a particular focus on the effects of zeolite structure.

Active intermediates in the raw material feed

According to the dual cycle concept, increasing the relative amounts of specific active species in the feedstock should enhance certain catalytic cycles to promote the formation of desired products. As an example, the addition of toluene or p-xylene to the methanol feedstock has been found to increase the formation of methane, ethene and aromatic products while decreasing the amounts of C_4-C_7 aliphatics [Figure 7A]. These results can be attributed to promotion of the aromatic-based cycle and inhibition of the olefin catalytic cycle upon adding active aromatic compounds. Interestingly, the addition of a low concentration of C_{3-6} olefins cannot effectively restrain the aromatic-based catalytic cycle as a result of the rapid transformation of these compounds to aromatics[83]. Bhan's group also found that the addition of small amounts of acetaldehyde (1-4 C%) to the methanol stream led to a monotonic enhancement of the ethene selectivity, ranging from 9.3 C% to 15 C% in trials with bulk ZSM-5 and from 1.4 C% to 6.4 C% in trials with diffusion-free ZSM-5 nanosheets. In addition, methylbenzene selectivities from 4.9 C% to 7.8 C% with bulk ZSM-5 and from 2.6 C% to 5.3 C% with ZSM-5 nanosheets were observed. Although acetaldehyde is not a direct active hydrocarbon pool species, it can produce aromatics through a multistep aldol-condensation reaction[85]. Zhang *et al.* also recently reported a kinetics study showing that the addition of olefins (such as in the case of olefin recycling) to the feedstock enhanced the olefin methylation and cracking processes, facilitating the formation of propylene during the MTP reaction[86].

Reaction conditions

Elementary reactions have varied kinetic orders and active energies, so the reaction temperature and pressure will affect the rates of these sub-reactions differently and thus modify the product distribution. For example, Goetze *et al.* found that 1-methylnaphthalene deactivated the MTH reaction at 350 °C on the zeolite DDR but functioned as a catalytically active intermediate at 450 °C[87]. The same group established that the primary active intermediates during the MTO reaction over CHA zeolites varied at different temperatures. Specifically, methylbenzenes were the main active species at low temperatures (300-350 °C), whereas methylated naphthalenes were the primary active intermediates at higher temperatures (350-500 °C)[88,89]. However, Qi *et al.* reported that naphthalene species can also serve as active intermediates at a lower temperature of 290 °C in trials using ZSM-5[90]. In addition, Yarulina *et al.* found that adjusting the temperature from 380 to 475 °C changed the ethene: propene ratio obtained from the MTO reaction

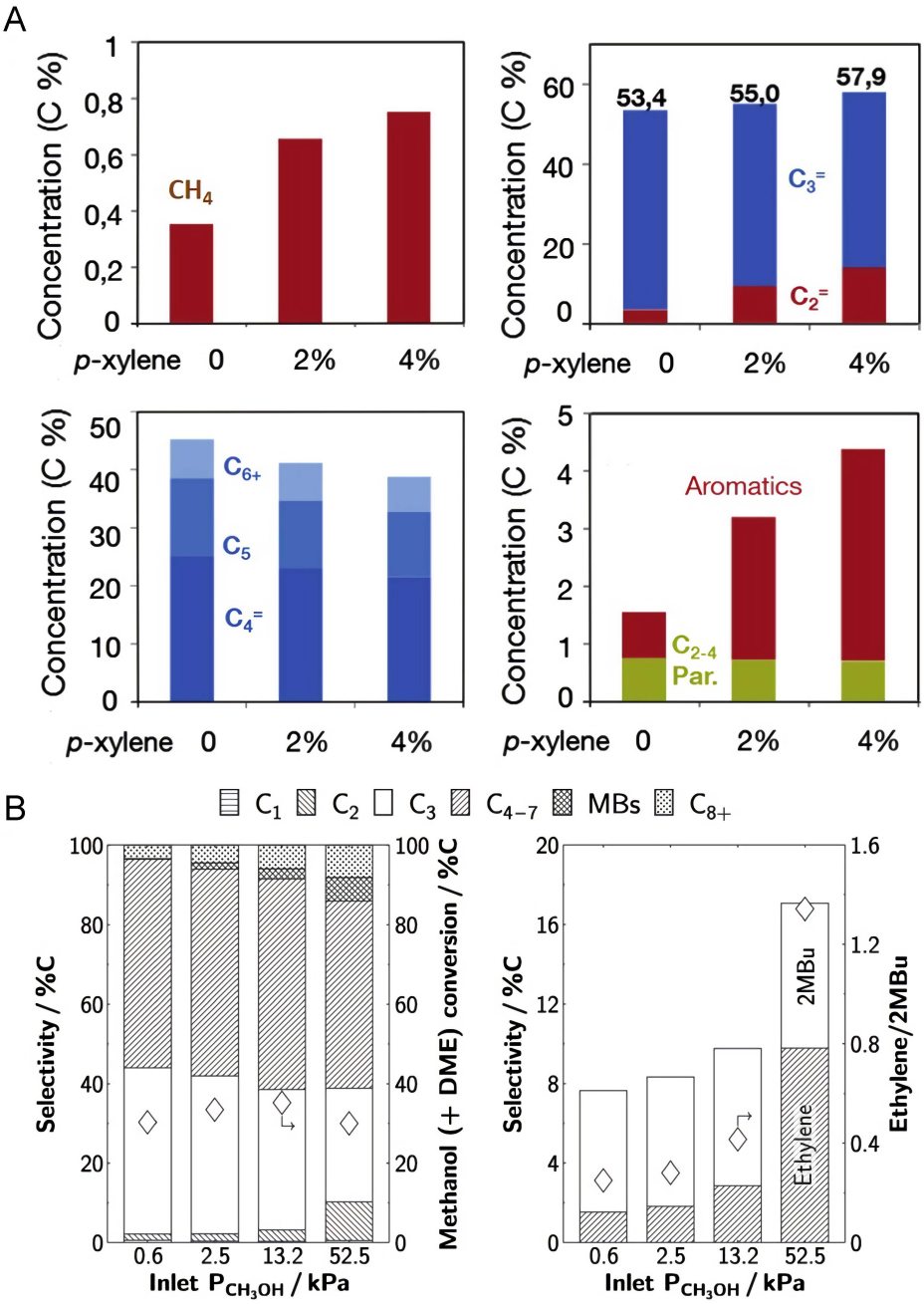

Figure 7. (A) The effect of co-feeding p-xylene on product distribution. Reproduced with permission from ref. 83[83]. Copyright 2014, Elsevier. (B) Product selectivity and methanol conversion (left), selectivities for ethene and 2-methyl-2-butene + methylbutane (right). Reproduced with permission from ref. 73[73]. Copyright 2017, Elsevier.

over a Sigma-1 zeolite from 0.5 to 1.6[91]. This same reaction gave a butene yield of 14 C% at 380 °C but yields of less than 5 C% at a higher temperature of 475 °C[91].

Arora *et al.* demonstrated the effect of the methanol partial pressure on the product distribution [Figure 7B][73]. As a typical example, increasing the methanol pressure from 0.6 to 52.5 kPa during the MTH process over ZSM-5 at 400 °C increased the selectivities for methylbenzenes and ethene from 0.1 C% to 5.9 C% and from 1.5 C% to 9.8 C%, respectively. In contrast, the propene selectivity decreased from 41.8 C%

to 28.7 C% such that the propene/ethene (P/E) ratio was decreased by a factor of 9. It was concluded that a higher methanol pressure facilitated the hydrogen transfer reaction which, in turn, generated large amounts of aromatics during the MTH reaction[73].

Zeolite structure

As a result of the rapid development of crystalline zeolites with ordered micropores having sizes in the range of 0.3-1 nm, such materials have been widely used as catalysts or sorbents. These inorganic substances include aluminosilicates, aluminophosphates and silicates, and the International Zeolite Association database currently contains over 200 different types of zeolites. Their topologies (based on the presence of cavities and channels), morphologies (that is, the crystal dimensions and mesoporosities) and compositions (the relative amounts of Si, Al, P, Ti and other elements) of these materials vary greatly and all these factors can affect catalytic performance in the MTH reaction.

The first factor assessed herein is topology. As an example, ZSM-22 has one-dimensional 10-MR channels that are too narrow to allow the formation of methylbenzene intermediates, thus inhibiting the aromatic catalytic cycle but promoting the olefin-based cycle to produce a high proportion of branched C_{5+} paraffins[92,93]. The ZSM-5 zeolite, which has an MFI structure containing three-dimensional 10-MR pores approximately 5.6 Å in size, produces a mixture of olefins, paraffins and aromatics, while the small-pore CHA-structured SAPO-34 containing pore opening of only approximately 3.8 Å mainly produces C_2-C_4 alkenes under similar reaction conditions[19]. Moreover, the primary active hydrocarbons during the MTH reaction over zeolites also vary in morphology. Hexa- and penta-methylbenzenes were found to be the main active hydrocarbon pool intermediates in trials using a beta zeolite, facilitating the production of propene and butenes[53]. In contrast, the reaction intermediates were restricted to xylenes and tri-methylbenzenes in work with ZSM-5, which produced ethene and propene[54].

The texture of the zeolite is another important factor determining the MTH reaction mechanism. In particular, the transport of reactants and products across the channels in the zeolite plays a vital role[94]. A Fickian diffusion model in which the zeolite is assumed to be a spherical crystal without any other transport restrictions can be used to calculate the adsorption properties of a zeolite under isothermal conditions[95,96]. This method allows a quantitative comparison of the difference between zeolite sizes, which can have a remarkable effect on product selectivity during the MTH reaction[97,98]. Studies have shown that increasing the ZSM-5 particle size increases the selectivity for ethene while reducing that for C_4-C_7 aliphatics. The same trend in product selectivity was also observed in trials in which access to ZSM-5@SiO_2 was blocked by the formation of a SiO_2 shell. These results show that a large effective crystallite size prolongs the residence time of large active methylbenzenes in the catalyst particles, facilitating the aromatic-based cycle to produce light olefins[97]. Work with the self-pillared pentasil ZSM-5 having a diffusion length of only 1 nm indicated that the ethene selectivity resulting solely from olefin interconversion was limited to 1.1% because the aromatic cycle essentially did not proceed in the zeolite[98]. The effects of using a mesoporous beta zeolite as the catalyst in the MTH reaction were previously examined. The results indicated that intracrystalline mesoporosity provided much shorter diffusion lengths than those in the standard material, leading to better catalytic performance in terms of conversion capacity, reaction rate and lifetime. More importantly, methylbenzenes could easily diffuse out of the mesoporous catalyst so that less ethylene but more long-chain aliphatics were obtained compared with the conventional beta zeolite[99].

In addition to the diffusion effect, the product distribution is also sensitive to the acidity of the zeolite. In 2011, Wei *et al.* reported that ZSM-5 zeolites with different SiO_2/Al_2O_3 ratios all showed high MTH activity, but the propene selectivity was 45.9% greater on a Na-ZSM-5 specimen having a high SiO_2/Al_2O_3 ratio of

220[100]. In 2017, Zhao *et al.* achieved an elevated propene selectivity of 58.3% using a high-Si structured beta zeolite-catalyzed MTP process because the olefin-based catalytic cycle was the dominant reaction route[101]. In 2018, Yarulina *et al.* determined that ZSM-5 modified with alkaline earth metals had a lower density of Brønsted acidic sites[102]. This suppressed the accumulation of aromatics but allowed the olefin methylation/cracking process to proceed, leading to the generation of more propene and less ethene than were obtained using pure ZSM-5[102]. In cooperation with Bhan's group, the authors also investigated the effects of the SiO_2/Al_2O_3 ratio in ZSM-5 zeolites on the formation of ethene during DME conversion. This work indicated that a high aluminum content increased the interactions between aromatics and catalytic sites before these compounds exited the crystalline particles, providing higher selectivity for ethene. As noted above, increasing the catalyst particle size can also increase the interactions between aromatics and catalytic sites by prolonging the residence time of the methylbenzenes. These two factors were therefore combined to produce a single descriptor (N_{H+}) for ethene selectivity. Increasing the N_{H+} value was found to promote both catalytic cycles, although the aromatic cycle was promoted to a larger extent than the olefin cycle, meaning that ethene formation was enhanced[103]. Very recently, Liang *et al.* proposed that the relationship between the acid site density and the aromatic-based cycle is more complicated than is presently thought[104]. Isotopic tracing experiments by this group showed that the acid site density had a negligible impact on the reactivity of active aromatics that were preferentially transformed into coke precursors and thus caused deactivation of the catalytic sites[104]. Moreover, Yuan *et al.* showed that active Al atoms located on the external surfaces of ZSM-11 promoted rapid coke formation, while the uniformly distributed Al species in the micropores inhibited the aromatic-based cycle during the MTO reaction[105].

Zeolites having small pores tend to exhibit high selectivity for light olefins because they are able to confine larger organic compounds produced during the MTO reaction. The MTO process is an important reaction in C1 chemistry and is capable of producing valuable olefin-based chemicals via non-petroleum routes. Many fundamental investigations of this process have also recently been performed. Initially, aromatic-based species were widely believed to function as active intermediates during the MTO reaction because of the shape-selective effect of the small pores in the catalysts. Isotopic studies have also demonstrated that methylbenzenes make the main contribution to the production of olefins[106]. Analyses by GC-MS and solid-state NMR have produced evidence for the presence of active hexamethenecyclohexadiene and the heptamethylbenzenium cation[81]. In addition, operando UV-visible spectra have indicated that methylated aromatic species are the major active species[88,89]. However, variations in the specific aromatic compounds in the hydrocarbon pool can have a significant effect on the MTO products. Kang *et al.* systematically established the correlations between the cage sizes of small-pore zeolites and the MTO product distribution[107]. This work compared 30 different zeolites having 14 different cage-type topologies and found that the MTO reaction proceeded in a similar manner on specific topologies independent of the composition[107]. As shown in Figure 8, an ellipsoidal model was initially defined based on three axes, with *ab* denoting the cage-defining ring and *b* being the ring size. As the ellipsoidal cage size was increased from 12-ring to 16-ring, the primary light olefin product changed from ethene to butene, so a relationship between ring size and product selectivity could be established. These results suggest that the ellipsoidal cages in small-pore zeolites determine the sizes of methylated aromatic intermediates during the MTO process[107].

In addition to aromatic active species, olefin-based catalytic intermediates formed during the MTO process are also of interest. Based on an analysis of ^{1}H and ^{13}C NMR spectra, Dai *et al.* identified several olefin-like species in trials using SAPO-34 during the induction period of the MTO reaction, and suggested that these compounds evolved into aromatic intermediates when the reaction was in the steady state[8]. However, the functioning of these olefin-like species as active intermediates was not assessed[8]. Hwang *et al.* showed that active olefin intermediates appeared during the MTO reaction in an early stage but also established that

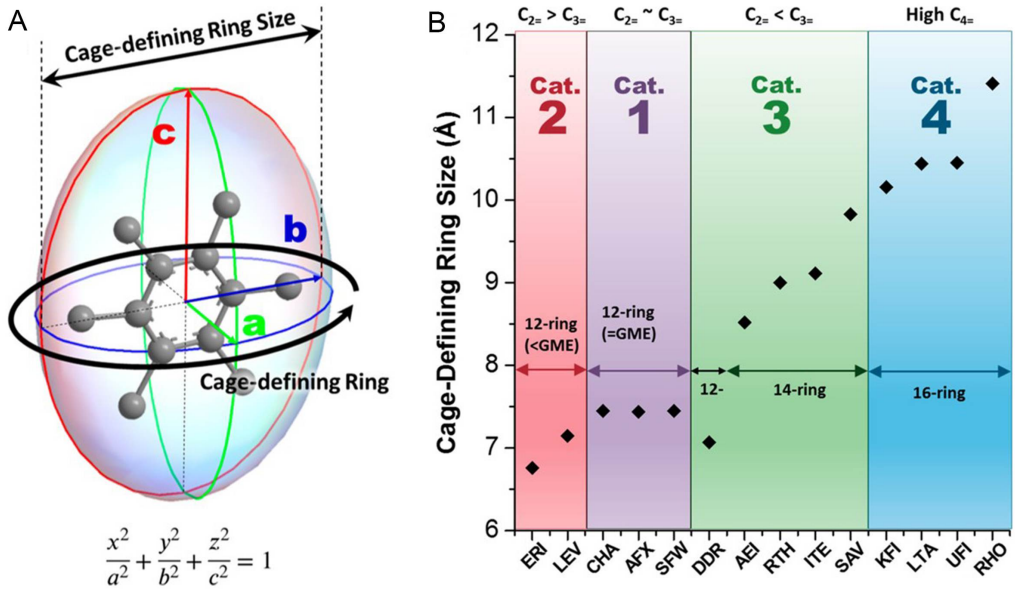

Figure 8. (A) The ellipsoidal model of a cage-defining ring. (B) Correlations between cage-defining ring sizes and olefin distributions. Reproduced with permission from ref. 107[107]. Copyright 2019, American Chemical Society.

accumulated aromatics dominated the catalytic process and increased the turnover number[108]. More recently, the authors found that propene selectivity underwent a monotonic increase with decreases in the aluminum content or crystal size of DDR zeolites[109]. As shown in Figure 9A, $^{12}C/^{13}C$ methanol switch results indicated that the formation of propene was closely associated with the propagation of the olefin-based cycle, an effect that has been neglected in most studies. The authors have proposed that catalytic behavior during this process is related to the presence of small pores in the zeolite that restrict the diffusion of both aromatics and long-chain olefin intermediates. The effect of olefin-related β-scission reactions during the entire process was also determined to be significant[109]. Yang *et al.* prepared a SAPO-14 zeolite with ultrasmall cages (5.3 × 10.05 Å) and an AFN topology and reported 77.3% propene selectivity from a one-pass methanol conversion process with a time-on-stream of 3 min, representing the highest value up to that point [Figure 9B][110]. Using $^{12}C/^{13}C$-methanol switch experiments, the same group established that the olefin-based route, rather than a mechanism based on aromatics, dominated the conversion of methanol [Figure 9C] and thus maximized the selectivity for propene based on the effect of limited diffusion[110]. Zhou *et al.* fabricated a SAPO-14 zeolite with a high Si content and achieved a P/E ratio of 4.17 during the MTO reaction at 450 °C[111]. These studies served to fill gaps in the body of knowledge regarding the effect of the olefin-based cycle on MTO reactions.

MTP reaction

Ethene, propene and aromatics are the main value-added products that can be obtained from the MTH process. The dual cycle mechanism indicates that the formation of ethene and aromatics is largely associated with the aromatic-based cycle, while the production of propene is connected with either the olefin-based or aromatic-based cycles. Because of the complexity of the MTH reaction network, adjusting the single-pass selectivity for propene to achieve a high selectivity value is highly desirable. Based on the preceding discussions of the reaction mechanism, effective means of enhancing the propene yield are discussed below.

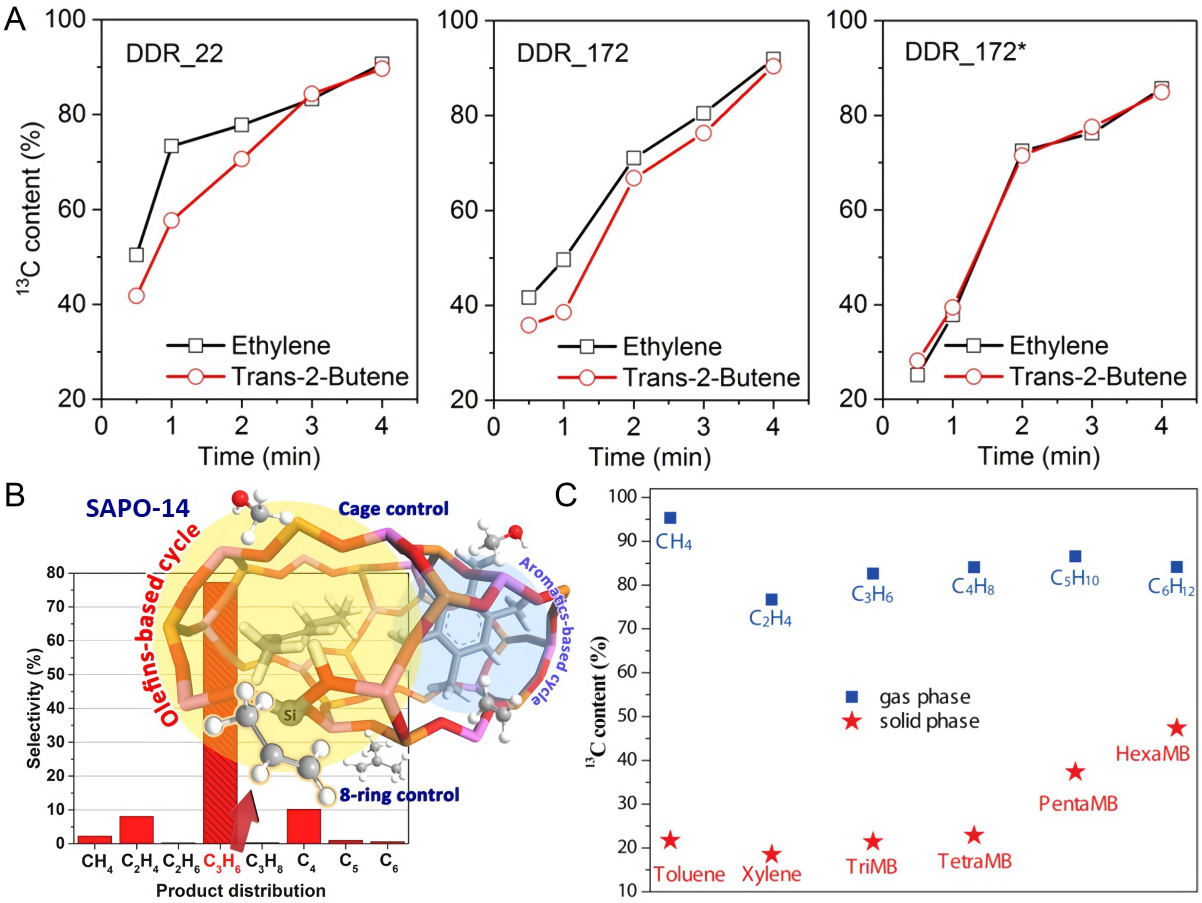

Figure 9. (A) The ^{13}C concentrations in ethene and trans-2-butene over time during ^{12}C/^{13}C-methanol switch experiments using various DDR zeolites. Reproduced with permission from ref. 109[109]. Copyright 2020, American Chemical Society. (B) Product distribution and (C) ^{13}C concentrations in effluents and residual methylbenzenes during the MTO reaction over SAPO-14. Reproduced with permission from ref. 110[110]. Copyright 2020, American Chemical Society. MTO: Methanol to olefins.

In general, the MTH process can take place only in the cages and interconnected channels of zeolites. Therefore, the structures of zeolites have a substantial effect on the catalytic route and affect the final product selectivity. Dyballa *et al.* compared three different 10-MR zeolites having varying structures (ZSM-5, ZSM-11 and ZSM-22) in MTP reactions and demonstrated that propene selectivity, coke formation and catalyst lifetime were highly dependent on the acid density of the material[112]. As indicated by the data in Table 1, a propene selectivity greater than 50% could be achieved over ZSM-5 (130) (here, the number 130 in the bracket indicates the Si/Al ratio of the zeolite) and ZSM-11 (200). Moreover, regardless of the morphology, the propene selectivity and the P/E ratio increased with increasing Si/Al ratio[112]. Adding a binder[113] and heteroatoms such as B[114], Mn[12] and Ca[102] had a similar effect to that of increasing the Si/Al ratio to dilute the acid density, and greatly enhanced propene selectivity. This phenomenon was especially noticeable in trials using the catalysts B-CON[115] (with a propene selectivity of 60%) and Mn-ZSM-5 (200)[12] (with a propene selectivity of 58.4%). This research showed that decreasing the density of Brønsted acid sites hindered the hydrogen transfer process and changed the main catalytic route during the MTH process. As a result, the olefin-based cycle became dominant, leading to a high propene selectivity.

Hierarchically structured zeolites (also referred to as mesoporous zeolites) combine the advantages of micropores and mesopores to provide an enhanced molecular diffusion rate. As discussed above in Section

Table 1. Propene selectivities over different zeolites

Catalyst[a]	Temperature (℃)	Conversion (%)	Propene Sel. (C%)	Ethene Sel. (C%)	P/E ratio	Refs. (year)
ZSM-5 (20)	450	100	27	15	1.8	[112] (2016)
ZSM-5 (130)	450	100	51	5	10.2	[112] (2016)
ZSM-11 (30)	450	94	14	10	1.4	[112] (2016)
ZSM-11 (200)	450	100	51	3	17	[112] (2016)
ZSM-22 (30)	450	100	43	9	4.8	[112] (2016)
ZSM-22 (50)	450	100	45	8	5.6	[112] (2016)
Binder-ZSM-5 (40)	450	100	41.9	5.2	8	[113] (2010)
B-ZSM-5 (162)	460	> 80	43	/	/	[114] (2014)
Mn-ZSM-5 (200)	480	100	58.4	10.6	5.5	[12] (2015)
Ca-ZSM-5 (46)	500	100	51	7.5	6.8	[102] (2018)
B-CON[b]	500	100	60	4.5	13.3	[115] (2015)
Meso-ZSM-5 (78)	470	99.6	42.2	4.18	10.1	[10] (2008)
Meso-beta (277)	550	> 99	55.5	5.6	10	[116] (2018)
2 nm ZSM-5 (87.5)	350	~50	20.5	1.5	13.7	[97] (2015)
17 μm ZSM-5 (38.0)	350	~50	26.2	20.3	1.3	[97] (2015)
100 nm ZSM-22 (46)	450	100	53	21	2.6	[117] (2014)
300 nm ZSM-22 (46)	450	100	50	21	2.4	[117] (2014)
Beta (125)	450	100	46.0	3.3	14.1	[118] (2017)
SAPO-17 (6)	425	> 98	27	55	0.5	[107] (2019)
SAPO-34 (0.123)	400	> 98	39	30	1.3	[107] (2019)
SAPO-18 (0.063)	400	> 98	46	24	1.9	[107] (2019)
DDR (22)	400	~50	38.1	36.6	1.0	[109] (2020)
DDR (172)	400	~50	48.3	27.8	1.7	[109] (2020)
Meso DDR (172)	400	~50	50.6	26.4	1.9	[109] (2020)
SAPO-14[c]	400	89.2	77.3	8.0	9.7	[110] (2020)
SAPO-14[c]	450	99.3	65.7	15.9	4.1	[110] (2020)

[a]The number in brackets is the Si/Al ratio of the zeolite. [b]Si/B = 22. [c]Al:P:Si = 0.50:0.48:0.02.

"Zeolite structure", mesoporous zeolites have very short diffusion lengths of only a few nanometers and show promise as catalysts when applied to the MTP process. As reported previously, meso-ZSM-5[10] and meso-beta[116] zeolites produce more propene than their counterparts because the short diffusion lengths in these materials favor the olefin-based cycle and limit the aggregation of aromatics[97]. However, Khare *et al.* achieved a propene selectivity of only 20.5% with 2 nm ZSM-5 (87.5) particles at 350 °C, albeit with a high P/E ratio of 13.7[97]. These results were attributed to the relatively low reaction temperature, at which the methylation and oligomerization of low alkenes proceeded rather than the cracking process that would be expected to produce light olefins. Therefore, a high temperature (typically above 400 °C)[117,118] is needed for the MTP reaction, as indicated in Table 1.

Small-pore zeolites are highly selective for both ethene and propene because the smaller openings in these catalysts easily trap large products. As the aromatic-based cycle proceeds, ethene is inevitably produced via the dealkylation of branched aromatics and subsequently competes with the formation of propene. As such, the P/E ratio is usually less than 2 [Table 1][107]. However, many groups have recently made efforts to tune the P/E ratio obtained during the MTO reaction. Kang *et al.* established that the topology of a small-pore zeolite can determine the branching of aromatics in the cages and release different olefins through dealkylation[107]. Tuning the acid content and crystallization size of small-pore zeolites is also an effective strategy to regulate the relative extents to which the two catalytic cycles proceed[109,110] and this approach has

previously been used in work with medium-/large-pore zeolites. Notably, Liu's group achieved the highest-ever propene selectivity of 77.3% using a newly developed small-pore SAPO-14 zeolite[110]. Compared with the complex outflows from medium- or large-pore zeolites, the main products of the MTO process over small-pore zeolites are limited to light olefins. As a consequence, it is easier to adjust the selectivity for propene when using small-pore zeolites. The data discussed in this paragraph therefore suggest innovative approaches to designing and engineering catalysts for the MTP process.

CATALYST DEACTIVATION

Pore blocking by polycyclic aromatic hydrocarbons

The deactivation of catalysts is another issue with equal importance to the product selectivity of the MTH reaction. As the MTH reaction proceeds over molecular sieve catalysts, many cross-linked PAHs featuring graphene-like structures are formed via the cage-passing growth of confined hydrocarbon pool species. This phenomenon suppresses mass transfer, blocks the catalytic centers and deactivates the catalyst. According to the mechanism described in Section "FORMATION OF THE FIRST C-C BOND", the MTH reaction proceeds based on a pool of hydrocarbons that produce needed light olefins but also undesirable heavy molecules that cause catalyst deactivation[119-124]. Much effort has been devoted to understanding this deactivation phenomenon. In 2020, Lezcano-Gonzalez *et al.* tracked the formation of carbonaceous species during the MTO reaction using a newly developed operando Kerr-gated Raman spectroscopic technique that discriminated between Raman signals and fluorescence[125]. This work examined the formation of heavy hydrocarbons at different stages of the MTO reaction and showed that small branched polyenes with reduced mobility [Figure 10A-C] eventually underwent a cyclization process to form PAHs within large cages [Figure 10D]. However, an MFI topology that provided steric constraint inhibited the cyclization of polyenes and thus the generation of PAHs, increasing the catalyst lifetime[125]. Using a single-crystal electron diffraction technique, Wennmacher *et al.* found that the nucleation of coke began at channel intersections while large PAHs were preferentially formed in straight pores[119].

Similar to the outcomes of many other reactions, the coke generated during the MTH process is a complex mixture of various polycyclic aromatics with broad mass distributions[126-129]. However, in the case of the MTH reaction, the deactivating species are uncertain in terms of their exact compositions and chemical structures and are largely related to the pore structure of the zeolite. For example, hexamethylbenzene is an active pool species in reactions over beta and SAPO-34 zeolites but can also function as a deactivation species in conjunction with other topologies such as ZSM-22 (with a pore size of 4.6 × 5.7 Å)[26]. Interestingly, the hydrocarbon pool species undergo spatial interactions with the zeolite framework and thus cause the zeolite cells to expand[130-132]. Yang *et al.* investigated the dynamic structural evolution of SAPO-34 induced by organic compounds using ^{27}Al and ^{31}P NMR spectroscopy[132]. The ^{31}P NMR signal was found to shift from -30.1 to -30.8 ppm with the accumulation of deposits, indicating an increase in the P-O-Al bond angle[132]. In addition to expanding the unit cells in the zeolite, coke can grow by traversing the windows of zeolitic cages to form cross-links with neighboring coked cells and therefore generate large interconnected multicore PAHs[133]. Based on analyses by matrix-assisted laser desorption ionization-Fourier transform ion cyclotron resonance (MALDI-FT-ICR) with MS and isotope labeling, Wang *et al.* developed a so-called aromatic cage-passing deactivation mechanism occurring in MTO reactions over different small-pore zeolites[133]. In these materials, aromatics with three or four rings are initially formed in the cages and then cross the opening windows and link together as the reaction proceeds. As shown in Figure 11, the chemical composition of the coke will vary with changes in the zeolite cavity shape, suggesting that the coke formation/deactivating processes in zeolite-type catalysts are also associated with a shape-selective effect similar to product selectivity[133].

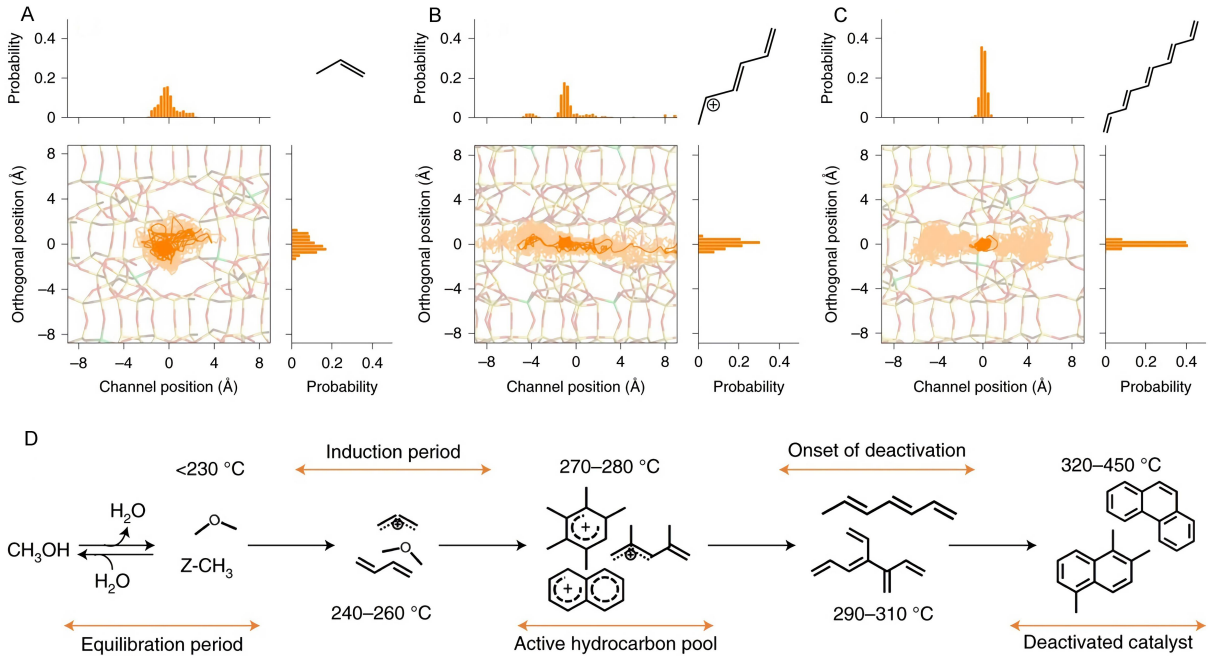

Figure 10. (A-C) The mobility of polyene species and (D) hydrocarbon species evolution during the MTO reaction. Reproduced with permission from ref. 125[125]. Copyright 2020, Nature Publishing Group. MTO: Methanol to olefins.

Conventional zeolites with ordered cavities and microporous channels can serve as molecular sieves, explaining the unique shape selectivity function within the MTH reaction. However, micropores also impose restrictions on molecular diffusion throughout the zeolite crystals. Hierarchical zeolites containing mesopores provide enhanced mass transfer and exhibit prolonged lifetimes during the MTH reaction[120,134]. Choi *et al.* prepared thin ZSM-5 nanosheets that showed reaction times five times that of bulk ZSM-5 particles as a consequence of the rapid mass diffusion and high coke tolerance of the sheets[135]. Liu *et al.* fabricated single-crystalline hierarchical ZSM-5 zeolites via a protozeolite seeding method[136]. These materials contained faceted mesopores and possessed high hydrothermal stability, exhibiting a remarkable lifetime of 18 h and an impressive propylene selectivity of up to 52.7%[136]. Using high-resolution electron energy loss spectroscopy, the authors probed the distribution of coke species in a mesoporous beta zeolite (Beta-MS) and a conventional beta zeolite (Beta-C) following the MTH reaction [Figure 12]. A significant difference observed in elemental carbon mapping data is that coke species were uniformly distributed throughout each entire Beta-MS crystal, while the coke in Beta-C crystals was mainly concentrated close to the particle exteriors [Figure 12B and E]. This same work examined the chemical compositions of carbon-based coke compounds at different locations. These analyses showed that H-rich coke with low molecular weights was deposited in the micropores but the intracrystalline mesopores in Beta-MS accommodated heavy graphite-like species [Figure 12C and F][99]. The data also suggested that micropores containing methylbenzenes and long-chain aliphatics may remain active during the MTH reaction even if the channels are blocked by large coke molecules. Liang *et al.* reported that the high density of surface acid sites on the H-MCM-22 zeolite promoted coke deposition on the external surfaces of the material[137]. In contrast, the acid sites in the sinusoidal channels in this zeolite were highly resistant to coke formation, providing additional evidence for the effects of acid site density and distribution on deactivation[137].

Oxygen-containing species promoting coke formation

In 2015, Müller *et al.* investigated the deactivation of a catalyst in a plug-flow reactor (PFR) and a fully back-mixed reactor (CSTR) and found more rapid deactivation of ZSM-5 in the PFR [Figure 13A][124]. This work

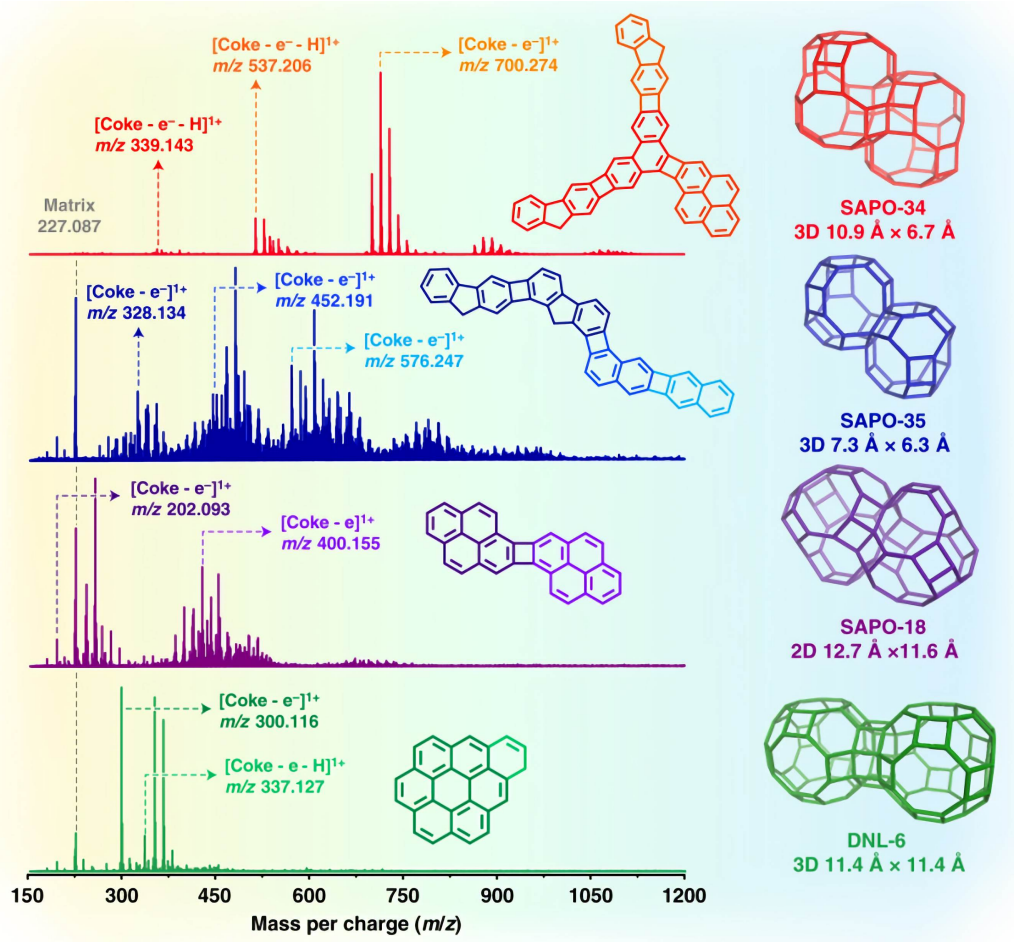

Figure 11. Molecular structures of coke species in different cage-structured zeolites and the associated MALDI FT-ICR mass spectra. Reproduced with permission from ref. 133[133]. Copyright 2020, Nature Publishing Group. MALDI FT-ICR: Matrix-assisted laser desorption ionization-Fourier transform ion cyclotron resonance.

established that the local methanol pressure in the top layer of the PFR was high, while the mixing of products with feedstock in the CSTR resulted in a more moderate methanol pressure. A mechanism was proposed to explain this phenomenon and is summarized in Figure 13B. At the start of the reaction, the relatively high methanol pressure leads to the formation of oxygen-containing compounds that strongly bind with active Brønsted acid sites on the catalyst, resulting in rapid deactivation. As the reaction continues, the O-containing surface compounds evolve into aromatics and eventually grow into typical coke molecules such as PAHs. This pioneering work established the important effect of O-containing compounds on catalyst deactivation throughout the MTH reaction[124]. In 2016, our own group observed the formation of various O-containing compounds comprising cyclopentenone derivatives during the MTH reaction by isotopic tracing with ^{13}C-methanol. As shown in Figure 13C, co-feeding this labeled compound along with the methanol feedstock showed that the presence of certain species inhibited methanol conversion by competing for adsorption on catalytic acid sites, where they were readily converted to heavy aromatics and coke species[138]. Notably, many subsequent reports following this pioneering work confirmed the appearance of the same O-containing compounds [Figure 13D][39,139].

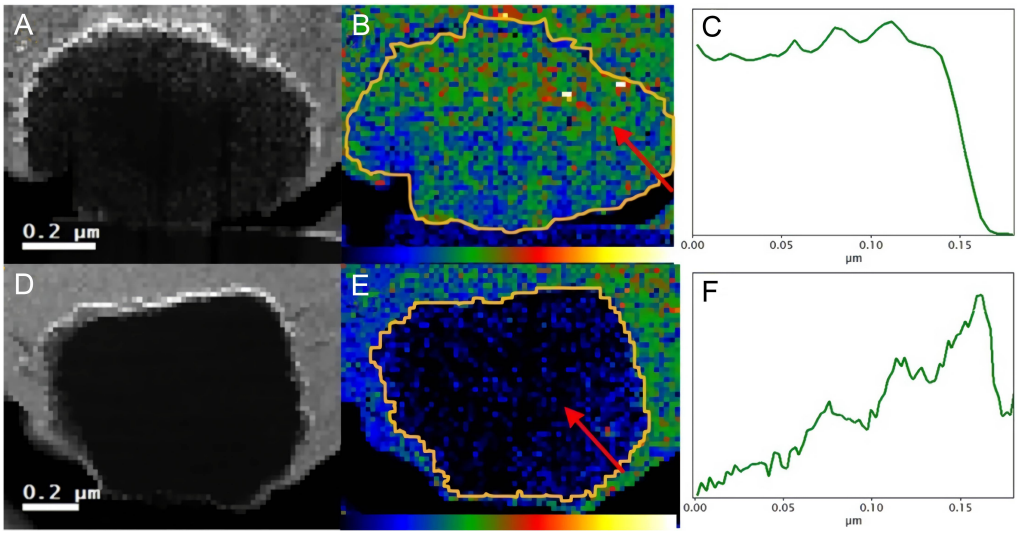

Figure 12. HAADF-STEM images (left), carbon mapping data (middle) and line profiles (right) for Beta-MS (A-C) and Beta-C (D-F). The carbon concentrations in (B) and (E) are indicated by the color bar and the red arrows show the locations at which line profiles were acquired. Reproduced with permission from ref. 99[99]. Copyright 2015, American Chemical Society.

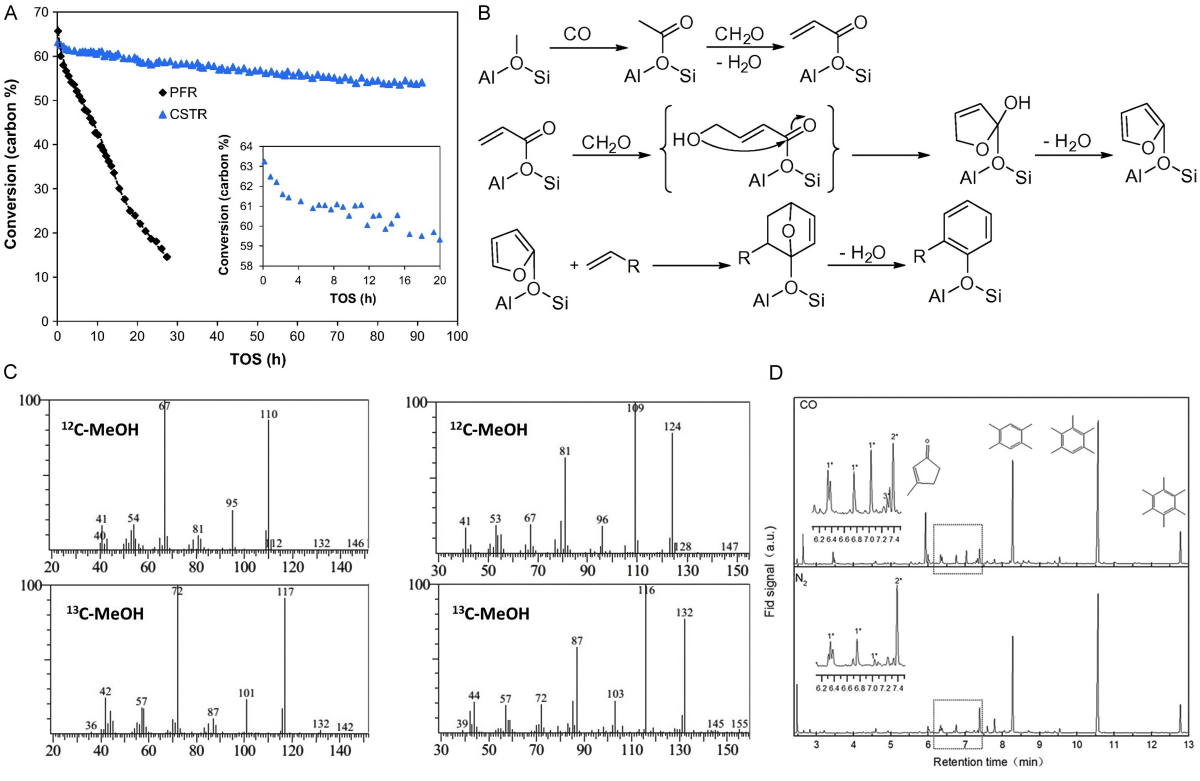

Figure 13. (A) Deactivation characteristics of a catalyst in PFR and CSTR trials and (B) proposed pathway for O-containing coke formation. Reproduced with permission from ref. 124[124]. Copyright 2015, Elsevier. (C) Mass spectra of O-containing coke compounds. Reproduced with permission from ref. 138[138]. Copyright 2016, Royal Society of Chemistry. (D) Mass spectra of organic materials retained in ZSM-5 catalysts during methanol conversion under N_2 and CO. Reproduced with permission from ref. 139[139]. Copyright 2018, Wiley-VCH. PFR: Plug-flow reactor; CSTR: continuous stirred-tank reactor.

Formaldehyde has also attracted attention as another O-containing compound that could be related to

catalyst deactivation during the MTH reaction[49,140]. Because formaldehyde readily undergoes nucleophilic addition, either the Prins or aldol-condensation reactions could produce coke precursors from this molecule[48,85]. In 2017, Martinez-espin *et al.* compared the use of methanol and DME as feedstocks for MTH reactions on ZSM-5, SSZ-24 and SAPO-5 zeolites and found that a methanol feed caused faster deactivation, which they attributed to the formation of formaldehyde[141]. More recently, Shi *et al.* reported that SSZ-13 had a shorter lifetime than SAPO-34, even though both materials have the same CHA framework[140]. The greater acid strength of the former was thought to promote the generation of formaldehyde, which subsequently transformed active intermediates into inactive polycyclic species[140,142]. This same work investigated means of circumventing formaldehyde-mediated chain carrier termination by adding Y_2O_3 to the zeolite to decompose formaldehyde[143] or combining high-pressure H_2 with the feedstock to hydrogenate the formaldehyde to methanol[144,145].

Transformation of coke to active species

Methylbenzenes, which promote the formation of light olefins in the hydrocarbon pool, can also evolve into PAHs through cyclization and cross-linking reactions. In many reactions that are known to be accompanied by coke deposition, air calcination or steam gasification is used to remove coke species as an approach to catalyst regeneration. Zhou *et al.* demonstrated that coke species confined in SAPO-34 can be directly transformed to active naphthalenic species by steam cracking, which ultimately enhances the light olefin selectivity of the process[146]. As shown in Figure 14A, increasing the treatment time applied to a coked ZEOS specimen gradually increased the concentration of naphthalene even though the total coke amount was reduced. These results suggest the stability of naphthalene under steam cracking conditions at 680 °C. More importantly, the average molecular weight of the carbonaceous species was decreased after steam treatment, indicating that H_2O could serve as an active agent to hydrogenate coke species [Figure 14B]. The Raman spectra in Figure 14C contain bands at 1360, 1415 and 1630 cm^{-1} assigned to PAHs and at 1600 cm^{-1} corresponding to the G band of amorphous carbon, all of which decreased in intensity during the early stage of steam cracking. Simultaneously, bands at 1240 and 1125 cm^{-1} assigned to branched exocyclic aromatics appeared. These results confirm that coke compounds underwent ring-opening as the catalyst was regenerated. Steam treatment has also been found to regenerate blocked micropores such that they become accessible again [Figure 14D][146]. In another study, Wang *et al.* created active naphthalenic species in SAPO-34 by ethylene pre-coking and reported that subsequent steaming of the material significantly promoted the selectivity for lower olefins and prolonged the catalyst lifetime during the MTO reaction[147].

CONCLUSION AND OUTLOOK

Over the 40-year time span during which the MTH process has been developed, this method has been recognized as an extremely important research area in the catalysis community. Several industrial plants using this process are already operated successfully, especially in China, attracting much more interest from both academia and industry. However, the fundamentals of the initial C-C bond formation mechanism are still debated. As discussed in the first part of this review, many active species have recently been discovered using advanced analytical techniques. Even so, details regarding the transformation of active species in this process remain elusive. More work is needed to investigate the mechanism responsible for the initial C-C bond formation during the MTH reaction using these advanced methods.

Understanding the mechanism of the MTH reaction and the effect of the zeolite structure will facilitate the design and synthesis of new high-performance catalysts. Based on the proposed indirect hydrocarbon pool mechanism, the direct mechanism seems unnecessary because the product distribution obtained from the MTH process can be clearly explained with the indirect mechanism, especially the dual cycle mechanism. As discussed in the second part of this review, assessments of the complexity of the catalyst compositions

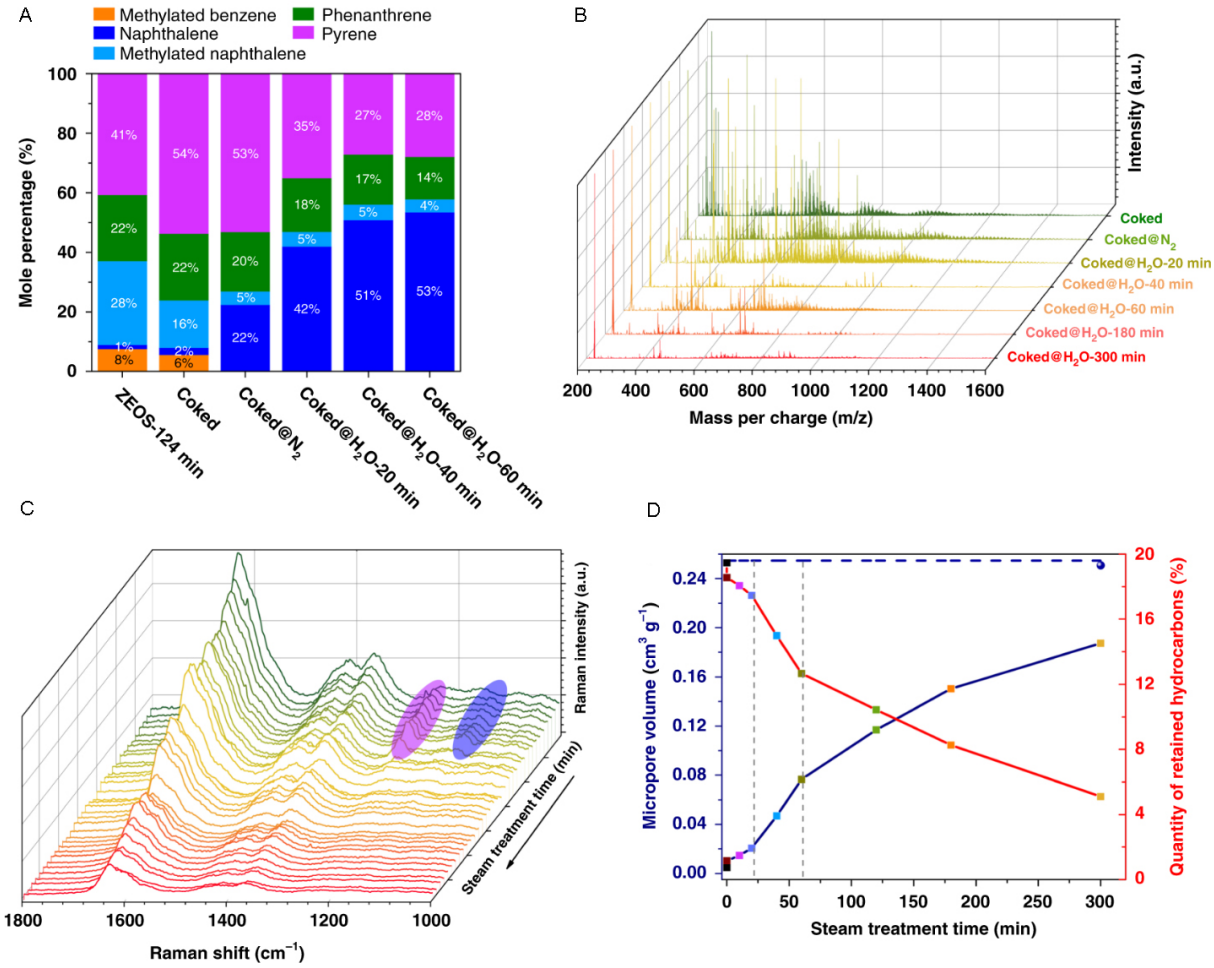

Figure 14. The formation of coke species with molecular masses (A) less than 200 Da and (B) greater than 200 Da under various conditions. (C) Operando UV-Raman spectra of a coked ZEOS specimen during steam treatment. (D) Micropore volume and coke mass of a ZEOS specimen over time during steam treatment. Reproduced with permission from ref. 146[146]. Copyright 2021, Nature Publishing Group.

and the multiple elementary sub-reactions occurring within the MTH system can provide basic knowledge that allows control of the reaction routes and product distributions. With much effort, the MTG and MTO reactions have been commercialized but not the MTP and MTA reactions. Studies of the MTP process have shown that small-pore zeolites with weak acidity show promise as catalysts for the olefin-based catalytic cycle and can increase the propene yield. The MTA process can also efficiently produce aromatics[148,149] that are very important platform molecules for high-value commodity chemicals[150]. Although the MTA reaction was not addressed in detail in this review, highly acidic zeolites having large pore channels may be able to promote this reaction based on prior research regarding the dual cycle mechanism.

Coke formation is another severe problem that cannot be avoided in the MTH reaction. Currently, the commercially available catalyst SAPO-34 is used for the MTO process with only a very short time for the one-pass reaction, after which coke deposits must be burned off by heating at high temperatures in air. This process, unfortunately, generates a considerable amount of CO_2 that is released into the atmosphere. A number of advanced techniques, such as operando Kerr-gated Raman and NMR spectroscopy, MALDI FT-ICR MS and electron energy loss spectroscopy, have provided detailed insights into the formation of coke

species. Further work, already being performed by many groups (including Olsbye, Bhan and Lercher), is required to find effective protocols to slow coke formation as a prerequisite for industrial applications.

Ever-increasing CO_2 emissions have resulted in many environmental challenges and the catalytic conversion of CO_2 to produce valuable fuels and chemicals, such as via CO_2 hydrogenation to methanol, has become one of the most effective approaches to addressing this issue. Commercial CO_2-to-renewable-methanol plants have been established in China, Iceland, Japan and elsewhere[151]. Considering the well-developed methanol-to-hydrocarbon technologies that are available, the catalytic hydrogenation of CO_2 to C_{2+} chemicals (such as olefins and aromatics) via methanol-mediated routes is especially desirable because these compounds possess higher energy densities and greater value than C_1 products[152-154]. It is our hope that this review will inspire new research intended to mitigate existing challenges associated with CO_2 hydrogenation and methanol conversion.

DECLARATIONS

Authors' contributions

Manuscript preparation and correction: Liu Z, Huang J

Availability of data and materials

Not applicable.

Financial support and sponsorship

This work was supported by the Fundamental Research Funds for the Central Universities (2020CDJQY-A072), the Venture and Innovation Support Program for Chongqing Overseas Returnees (cx2020107), the Thousand Talents Program for Distinguished Young Scholars, Natural Science Foundation of Chongqing (cstc2021jcyj-msxmX0945), and the Postdoctoral Science Foundation of China (2021M700579).

Conflicts of interest

Both authors declared that there are no conflicts of interest.

Ethical approval and consent to participate

Not applicable.

Consent for publication

Not applicable.

REFERENCES

1. Chang C. The conversion of methanol and other O-compounds to hydrocarbons over zeolite catalysts. *J Catal* 1977;47:249-59. DOI
2. Yurchak S. Development of Mobil's fixed-bed methanul-to-gasoline (MTG) process. Methane Conversion, Proceedings of a Symposium on the Production of Fuels and Chemicals from Natural Gas. Elsevier; 1988. p. 251-72. DOI
3. Lunsford JH. Catalytic conversion of methane to more useful chemicals and fuels: a challenge for the 21st century. *Catal Today* 2000;63:165-74. DOI
4. Olsbye U, Svelle S, Bjørgen M, et al. Conversion of methanol to hydrocarbons: how zeolite cavity and pore size controls product selectivity. *Angew Chem Int Ed Engl* 2012;51:5810-31. DOI PubMed
5. Song W, Haw JF, Nicholas JB, Heneghan CS. Methylbenzenes are the organic reaction centers for methanol-to-olefin catalysis on HSAPO-34. *J Am Chem Soc* 2000;122:10726-7. DOI
6. Wang C, Wang Y, Du Y, Yang G, Xie Z. Similarities and differences between aromatic-based and olefin-based cycles in H-SAPO-34 and H-SSZ-13 for methanol-to-olefins conversion: insights from energetic span model. *Catal Sci Technol* 2015;5:4354-64. DOI

7. Wang Y, Chen S, Gao Y, et al. Enhanced methanol to olefin catalysis by physical mixtures of SAPO-34 molecular sieve and MgO. *ACS Catal* 2017;7:5572-84. DOI
8. Dai W, Wang C, Dyballa M, et al. Understanding the early stages of the methanol-to-olefin conversion on H-SAPO-34. *ACS Catal* 2015;5:317-26. DOI
9. Deimund MA, Harrison L, Lunn JD, et al. Effect of heteroatom concentration in SSZ-13 on the methanol-to-olefins reaction. *ACS Catal* 2016;6:542-50. DOI
10. Mei C, Wen P, Liu Z, et al. Selective production of propylene from methanol: mesoporosity development in high silica HZSM-5. *J Catal* 2008;258:243-9. DOI
11. Firoozi M, Baghalha M, Asadi M. The effect of micro and nano particle sizes of H-ZSM-5 on the selectivity of MTP reaction. *Catal Commun* 2009;10:1582-5. DOI
12. Rostamizadeh M, Taeb A. Highly selective Me-ZSM-5 catalyst for methanol to propylene (MTP). *J Ind Eng Chem* 2015;27:297-306. DOI
13. Ni Y, Sun A, Wu X, et al. The preparation of nano-sized H[Zn, Al]ZSM-5 zeolite and its application in the aromatization of methanol. *Microporous Mesoporous Mater* 2011;143:435-42. DOI
14. Williams CL, Chang C, Do P, et al. Cycloaddition of biomass-derived furans for catalytic production of renewable p-Xylene. *ACS Catal* 2012;2:935-9. DOI
15. Zhang J, Qian W, Kong C, Wei F. Increasing para-Xylene selectivity in making aromatics from methanol with a surface-modified Zn/P/ZSM-5 catalyst. *ACS Catal* 2015;5:2982-8. DOI
16. Olah GA. Beyond oil and gas: the methanol economy. *Angew Chem Int Ed Engl* 2005;44:2636-9. DOI PubMed
17. Usman M, Daud WMAW. Recent advances in the methanol synthesis via methane reforming processes. *RSC Adv* 2015;5:21945-72. DOI PubMed PMC
18. Lebarbier VM, Dagle RA, Kovarik L, Lizarazo-adarme JA, King DL, Palo DR. Synthesis of methanol and dimethyl ether from syngas over Pd/ZnO/Al_2O_3 catalysts. *Catal Sci Technol* 2012;2:2116. DOI
19. Haw JF, Song W, Marcus DM, Nicholas JB. The mechanism of methanol to hydrocarbon catalysis. *Acc Chem Res* 2003;36:317-26. DOI PubMed
20. Ilias S, Bhan A. Mechanism of the catalytic conversion of methanol to hydrocarbons. *ACS Catal* 2013;3:18-31. DOI
21. Yarulina I, Chowdhury AD, Meirer F, Weckhuysen BM, Gascon J. Recent trends and fundamental insights in the methanol-to-hydrocarbons process. *Nat Catal* 2018;1:398-411. DOI
22. Zhong J, Han J, Wei Y, Liu Z. Catalysts and shape selective catalysis in the methanol-to-olefin (MTO) reaction. *J Catal* 2021;396:23-31. DOI
23. Tian P, Wei Y, Ye M, Liu Z. Methanol to olefins (MTO): from fundamentals to commercialization. *ACS Catal* 2015;5:1922-38. DOI
24. Speybroeck V, De Wispelaere K, Van der Mynsbrugge J, Vandichel M, Hemelsoet K, Waroquier M. First principle chemical kinetics in zeolites: the methanol-to-olefin process as a case study. *Chem Soc Rev* 2014;43:7326-57. DOI PubMed
25. Song W, Marcus DM, Fu H, Ehresmann JO, Haw JF. An oft-studied reaction that may never have been: direct catalytic conversion of methanol or dimethyl ether to hydrocarbons on the solid acids HZSM-5 or HSAPO-34. *J Am Chem Soc* 2002;124:3844-5. DOI PubMed
26. Olsbye U, Svelle S, Lillerud KP, et al. The formation and degradation of active species during methanol conversion over protonated zeotype catalysts. *Chem Soc Rev* 2015;44:7155-76. DOI PubMed
27. Wang W, Buchholz A, Seiler M, Hunger M. Evidence for an initiation of the methanol-to-olefin process by reactive surface methoxy groups on acidic zeolite catalysts. *J Am Chem Soc* 2003;125:15260-7. DOI PubMed
28. Jiang Y, Wang W, Reddymarthala V, Huang J, Sulikowski B, Hunger M. Effect of organic impurities on the hydrocarbon formation via the decomposition of surface methoxy groups on acidic zeolite catalysts. *J Catal* 2006;238:21-7. DOI
29. Li J, Wei Z, Chen Y, et al. A route to form initial hydrocarbon pool species in methanol conversion to olefins over zeolites. *JJ Catal* 2014;317:277-83. DOI
30. Wu X, Xu S, Zhang W, et al. Direct mechanism of the first carbon-carbon bond formation in the methanol-to-hydrocarbons process. *Angew Chem Int Ed Engl* 2017;56:9039-43. DOI PubMed
31. Wang C, Chu Y, Xu J, et al. Extra-framework aluminum-assisted initial C-C bond formation in methanol-to-olefins conversion on zeolite H-ZSM-5. *Angew Chem Int Ed Engl* 2018;57:10197-201. DOI PubMed
32. Lo B, Ye L, Chang G, et al. Dynamic modification of pore opening of SAPO-34 by adsorbed surface methoxy species during induction of catalytic methanol-to-olefins reactions. *Appl Catal B: Environ* 2018;237:245-50. DOI
33. Sun T, Chen W, Xu S, et al. The first carbon-carbon bond formation mechanism in methanol-to-hydrocarbons process over chabazite zeolite. *Chem* 2021;7:2415-28. DOI
34. Liu Y, Müller S, Berger D, et al. Formation mechanism of the first carbon-carbon bond and the first olefin in the methanol conversion into hydrocarbons. *Angew Chem Int Ed Engl* 2016;55:5723-6. DOI PubMed
35. Blaszkowski SR, van Santen RA. Theoretical study of C-C bond formation in the methanol-to-gasoline process. *J Am Chem Soc* 1997;119:5020-7. DOI
36. Chowdhury AD, Houben K, Whiting GT, et al. Initial carbon-carbon bond formation during the early stages of the methanol-to-olefin process proven by zeolite-trapped acetate and methyl acetate. *Angew Chem Int Ed Engl* 2016;55:15840-5. DOI PubMed PMC
37. Airi A, Damin A, Xie J, Olsbye U, Bordiga S. Catalyst sites and active species in the early stages of MTO conversion over cobalt

AlPO-18 followed by IR spectroscopy. *Catal Sci Technol* 2022;12:2775-92. DOI

38. Plessow PN, Studt F. Unraveling the mechanism of the initiation reaction of the methanol to olefins process using ab initio and DFT calculations. *ACS Catal* 2017;7:7987-94. DOI
39. Yang L, Yan T, Wang C, et al. Role of acetaldehyde in the roadmap from initial carbon-carbon bonds to hydrocarbons during methanol conversion. *ACS Catal* 2019;9:6491-501. DOI
40. Wu X, Zhang Z, Pan Z, Zhou X, Bodi A, Hemberger P. Ketenes in the induction of the methanol-to-olefins process. *Angew Chem Int Ed Engl* 2022;61:e202207777. DOI PubMed
41. Wang W, Hunger M. Reactivity of surface alkoxy species on acidic zeolite catalysts. *Acc Chem Res* 2008;41:895-904. DOI PubMed
42. Yamazaki H, Shima H, Imai H, Yokoi T, Tatsumi T, Kondo JN. Evidence for a "carbene-like" intermediate during the reaction of methoxy species with light alkenes on H-ZSM-5. *Angew Chem Int Ed Engl* 2011;50:1853-6. DOI PubMed
43. Yamazaki H, Shima H, Imai H, Yokoi T, Tatsumi T, Kondo JN. Direct production of propene from methoxy species and dimethyl ether over H-ZSM-5. *J Phys Chem C* 2012;116:24091-7. DOI
44. Minova IB, Bühl M, Matam SK, et al. Carbene-like reactivity of methoxy groups in a single crystal SAPO-34 MTO catalyst. *Catal Sci Technol* 2022;12:2289-305. DOI
45. Kubelková L, Nováková J, Jírů P. Reaction of small amounts of methanol on Hzsm-5, Hy and modified Y zeolites. Structure and Reactivity of Modified Zeolites, Proceedings of an International Conference. Elsevier; 1984. p. 217-24. DOI
46. Hutchings GJ, Gottschalk F, Hall MVM, Hunter R. Hydrocarbon formation from methylating agents over the zeolite catalyst ZSM-5. Comments on the mechanism of carbon-carbon bond and methane formation. *J Chem Soc., Faraday Trans* 1987;83:571-83. DOI
47. Tajima N, Tsuneda T, Toyama F, Hirao K. A new mechanism for the first carbon-carbon bond formation in the mtg process: a theoretical study. *J Am Chem Soc* 1998;120:8222-9. DOI
48. Liu Y, Kirchberger FM, Müller S, et al. Critical role of formaldehyde during methanol conversion to hydrocarbons. *Nat Commun* 2019;10:1462. DOI PubMed PMC
49. Wen W, Yu S, Zhou C, et al. Formation and fate of formaldehyde in methanol-to-hydrocarbon reaction: *in situ* synchrotron radiation photoionization mass spectrometry study. *Angew Chem Int Ed Engl* 2020;59:4873-8. DOI PubMed
50. Lesthaeghe D, Van Speybroeck V, Marin GB, Waroquier M. Understanding the failure of direct C-C coupling in the zeolite-catalyzed methanol-to-olefin process. *Angew Chem Int Ed Engl* 2006;45:1714-9. DOI PubMed
51. Dahl I, Kolboe S. On the reaction mechanism for hydrocarbon formation from methanol over SAPO-34. *J Catal* 1994;149:458-64. DOI
52. Dahl IM, Kolboe S. On the reaction mechanism for hydrocarbon formation from methanol over SAPO-34. *J Catal* 1996;161:304-9. DOI
53. Bjørgen M. The methanol-to-hydrocarbons reaction: insight into the reaction mechanism from [^{12}C]benzene and [^{13}C]methanol coreactions over zeolite H-beta. *J Catal* 2004;221:1-10. DOI
54. Svelle S, Joensen F, Nerlov J, et al. Conversion of methanol into hydrocarbons over zeolite H-ZSM-5: ethene formation is mechanistically separated from the formation of higher alkenes. *J Am Chem Soc* 2006;128:14770-1. DOI PubMed
55. Bjorgen M, Svelle S, Joensen F, et al. Conversion of methanol to hydrocarbons over zeolite H-ZSM-5: on the origin of the olefinic species. *J Catal* 2007;249:195-207. DOI
56. Van Speybroeck V, Van der Mynsbrugge J, Vandichel M, et al. First principle kinetic studies of zeolite-catalyzed methylation reactions. *J Am Chem Soc* 2011;133:888-99. DOI PubMed
57. Svelle S, Rønning PO, Kolboe S. Kinetic studies of zeolite-catalyzed methylation reactions1. Coreaction of [^{12}C]ethene and [^{13}C]methanol. *Journal of Catalysis* 2004;224:115-23. DOI
58. Svelle S, Ronning P, Olsbye U, Kolboe S. Kinetic studies of zeolite-catalyzed methylation reactions. Part 2. Co-reaction of [^{12}C]propene or [^{12}C]n-butene and [^{13}C]methanol. *J Catal* 2005;234:385-400. DOI PubMed
59. Hill IM, Hashimi SA, Bhan A. Kinetics and mechanism of olefin methylation reactions on zeolites. *J Catal* 2012;285:115-23. DOI
60. Hill IM, Hashimi SA, Bhan A. Corrigendum to "kinetics and mechanism of olefin methylation reactions over zeolites". *J Catal* 2012;291:155-7. DOI
61. Hill IM, Ng YS, Bhan A. Kinetics of butene isomer methylation with dimethyl ether over zeolite catalysts. *ACS Catal* 2012;2:1742-8. DOI
62. Nozik D, Bell AT. Role of Ga^{3+} Sites in Ethene Oligomerization over Ga/H-MFI. *ACS Catal* 2022;12:14173-84. DOI
63. Kim YT, Chada JP, Xu Z, et al. Low-temperature oligomerization of 1-butene with H-ferrierite. *J Catal* 2015;323:33-44. DOI
64. Dessau R. On the mechanism of methanol conversion to hydrocarbons over HZSM-5. *J Catal* 1982;78:136-41. DOI
65. Dessau R. On the H-ZSM-5 catalyzed formation of ethylene from methanol or higher olefins. *J Catal* 1986;99:111-6. DOI
66. Simonetti DA, Ahn JH, Iglesia E. Mechanistic details of acid-catalyzed reactions and their role in the selective synthesis of triptane and isobutane from dimethyl ether. *J Catal* 2011;277:173-95. DOI
67. Hay P, Redondo A, Guo Y. Theoretical studies of pentene cracking on zeolites: C-C β-scission processes. *Catal Today* 1999;50:517-23. DOI
68. Buchanan J, Santiesteban J, Haag W. Mechanistic considerations in acid-catalyzed cracking of olefins. *J Catal* 1996;158:279-87. DOI
69. Mikkelsen Ø, Kolboe S. The conversion of methanol to hydrocarbons over zeolite H-beta. *Microporous Mesoporous Mater* 1999;29:173-84. DOI

70. Teketel S, Skistad W, Benard S, et al. Shape selectivity in the conversion of methanol to hydrocarbons: the catalytic performance of one-dimensional 10-ring zeolites: ZSM-22, ZSM-23, ZSM-48, and EU-1. *ACS Catal* 2012;2:26-37. DOI
71. Yarulina I, Bailleul S, Pustovarenko A, et al. Suppression of the aromatic cycle in methanol-to-olefins reaction over ZSM-5 by post-synthetic modification using calcium. *ChemCatChem* 2016;8:3057-63. DOI
72. Martínez-espín JS, De Wispelaere K, Janssens TVW, et al. Hydrogen transfer versus methylation: on the genesis of aromatics formation in the methanol-to-hydrocarbons reaction over H-ZSM-5. *ACS Catal* 2017;7:5773-80. DOI
73. Arora SS, Bhan A. The critical role of methanol pressure in controlling its transfer dehydrogenation and the corresponding effect on propylene-to-ethylene ratio during methanol-to-hydrocarbons catalysis on H-ZSM-5. *J Catal* 2017;356:300-6. DOI
74. Fan S, Wang H, He S, et al. Formation and evolution of methylcyclohexene in the initial period of methanol to olefins over H-ZSM-5. *ACS Catal* 2022;12:12477-87. DOI
75. Lesthaeghe D, Horré A, Waroquier M, Marin GB, Van Speybroeck V. Theoretical insights on methylbenzene side-chain growth in ZSM-5 zeolites for methanol-to-olefin conversion. *Chemistry* 2009;15:10803-8. DOI PubMed
76. Xu T, Haw JF. Cyclopentenyl carbenium ion formation in acidic zeolites: an *in situ* NMR study of cyclic precursors. *J Am Chem Soc* 1994;116:7753-9. DOI
77. Haw JF, Nicholas JB, Song W, et al. Roles for cyclopentenyl cations in the synthesis of hydrocarbons from methanol on zeolite catalyst HZSM-5. *J Am Chem Soc* 2000;122:4763-75. DOI
78. Long J, Wang X, Ding Z, et al. Cyclopentadiene transformation over H-form zeolites: TPD and IR studies of the formation of a monomeric cyclopentenyl carbenium ion intermediate and its role in acid-catalyzed conversions. *J Catal* 2008;255:48-58. DOI
79. Wang C, Chu Y, Hu M, et al. Insight into carbocation-induced noncovalent interactions in the methanol-to-olefins reaction over ZSM-5 zeolite by solid-state NMR spectroscopy. *Angew Chem Int Ed Engl* 2021;60:26847-54. DOI PubMed
80. Arstad B, Nicholas JB, Haw JF. Theoretical study of the methylbenzene side-chain hydrocarbon pool mechanism in methanol to olefin catalysis. *J Am Chem Soc* 2004;126:2991-3001. DOI PubMed
81. Li J, Wei Y, Chen J, et al. Observation of heptamethylbenzenium cation over SAPO-type molecular sieve DNL-6 under real MTO conversion conditions. *J Am Chem Soc* 2012;134:836-9. DOI PubMed
82. Ilias S, Khare R, Malek A, Bhan A. A descriptor for the relative propagation of the aromatic- and olefin-based cycles in methanol-to-hydrocarbons conversion on H-ZSM-5. *J Catal* 2013;303:135-40. DOI
83. Sun X, Mueller S, Shi H, et al. On the impact of co-feeding aromatics and olefins for the methanol-to-olefins reaction on HZSM-5. *J Catal* 2014;314:21-31. DOI
84. Sun X, Mueller S, Liu Y, et al. On reaction pathways in the conversion of methanol to hydrocarbons on HZSM-5. *J Catal* 2014;317:185-97. DOI
85. Khare R, Arora SS, Bhan A. Implications of cofeeding acetaldehyde on ethene selectivity in methanol-to-hydrocarbons conversion on MFI and Its Mechanistic Interpretation. *ACS Catal* 2016;6:2314-31. DOI
86. Zhang C, Ng KLA, Yan L, et al. Kinetic Perspective on methanol to propylene process via HZSM-5 catalyst: balancing between reaction and diffusion. *Ind Eng Chem Res* 2022;61:2055-67. DOI
87. Goetze J, Meirer F, Yarulina I, et al. Insights into the activity and deactivation of the methanol-to-olefins process over different small-pore zeolites as studied with operando uv-vis spectroscopy. *ACS Catal* 2017;7:4033-46. DOI PubMed PMC
88. Borodina E, Meirer F, Lezcano-González I, et al. Influence of the reaction temperature on the nature of the active and deactivating species during methanol to olefins conversion over H-SSZ-13. *ACS Catal* 2015;5:992-1003. DOI
89. Borodina E, Sharbini Harun Kamaluddin H, Meirer F, et al. Influence of the reaction temperature on the nature of the active and deactivating species during methanol-to-olefins conversion over H-SAPO-34. *ACS Catal* 2017;7:5268-81. DOI PubMed PMC
90. Qi L, Li J, Wei Y, Xu L, Liu Z. Role of naphthalene during the induction period of methanol conversion on HZSM-5 zeolite. *Catal Sci Technol* 2016;6:3737-44. DOI
91. Yarulina I, Goetze J, Gücüyener C, et al. Methanol-to-olefins process over zeolite catalysts with DDR topology: effect of composition and structural defects on catalytic performance. *Catal Sci Technol* 2016;6:2663-78. DOI
92. Teketel S, Svelle S, Lillerud K, Olsbye U. Shape-selective conversion of methanol to hydrocarbons over 10-ring unidirectional-channel acidic H-ZSM-22. *ChemCatChem* 2009;1:78-81. DOI
93. Teketel S, Olsbye U, Lillerud K, Beato P, Svelle S. Selectivity control through fundamental mechanistic insight in the conversion of methanol to hydrocarbons over zeolites. *Microporous Mesoporous Mater* 2010;136:33-41. DOI
94. Cnudde P, Demuynck R, Vandenbrande S, Waroquier M, Sastre G, Speybroeck VV. Light olefin diffusion during the MTO process on H-SAPO-34: a complex interplay of molecular factors. *J Am Chem Soc* 2020;142:6007-17. DOI PubMed
95. Crank J. The mathematics of diffusion. 2nd edition. Oxford University Press; 1979. DOI
96. Koller H, Kärger J, Ruthven DM. Theodorou DN. Sorption kinetics. In “Diffusion in nanoporous materials”. Wiley-VCH: Weinheim; 2012. p. 1433-7851. DOI
97. Khare R, Millar D, Bhan A. A mechanistic basis for the effects of crystallite size on light olefin selectivity in methanol-to-hydrocarbons conversion on MFI. *J Catal* 2015;321:23-31. DOI
98. Khare R, Bhan A. Mechanistic studies of methanol-to-hydrocarbons conversion on diffusion-free MFI samples. *J Catal* 2015;329:218-28. DOI
99. Liu Z, Dong X, Zhu Y, et al. Investigating the influence of mesoporosity in zeolite beta on its catalytic performance for the conversion of methanol to hydrocarbons. *ACS Catal* 2015;5:5837-45. DOI

100. Wei R, Li C, Yang C, Shan H. Effects of ammonium exchange and Si/Al ratio on the conversion of methanol to propylene over a novel and large partical size ZSM-5. *J Nat Gas Chem* 2011;20:261-5. DOI
101. Zhao X, Wang L, Li J, et al. Investigation of methanol conversion over high-Si beta zeolites and the reaction mechanism of their high propene selectivity. *Catal Sci Technol* 2017;7:5882-92. DOI
102. Yarulina I, De Wispelaere K, Bailleul S, et al. Structure-performance descriptors and the role of Lewis acidity in the methanol-to-propylene process. *Nat Chem* 2018;10:804-12. DOI PubMed
103. Khare R, Liu Z, Han Y, Bhan A. A mechanistic basis for the effect of aluminum content on ethene selectivity in methanol-to-hydrocarbons conversion on HZSM-5. *J Catal* 2017;348:300-5. DOI
104. Liang T, Chen J, Qin Z, et al. Insight into induction period of methanol conversion reaction: reactivity of ethene-precursors over H-ZSM-5 zeolite is independent of Brϕnsted acid site density. *Fuel* 2023;332:126062. DOI
105. Yuan K, Jia X, Wang S, et al. Regulating the distribution of acid sites in ZSM-11 zeolite with different halogen anions to enhance its catalytic performance in the conversion of methanol to olefins. *MicroporousMesoporous Mater* 2022;341:112051. DOI
106. Hereijgers BP, Bleken F, Nilsen MH, et al. Product shape selectivity dominates the methanol-to-olefins (MTO) reaction over H-SAPO-34 catalysts. *J Catal* 2009;264:77-87. DOI
107. Kang JH, Alshafei FH, Zones SI, Davis ME. Cage-defining ring: a molecular sieve structural indicator for light olefin product distribution from the methanol-to-olefins reaction. *ACS Catal* 2019;9:6012-9. DOI
108. Hwang A, Prieto-centurion D, Bhan A. Isotopic tracer studies of methanol-to-olefins conversion over HSAPO-34: the role of the olefins-based catalytic cycle. *J Catal* 2016;337:52-6. DOI
109. Hua J, Dong X, Wang J, et al. Methanol-to-olefin conversion over small-pore ddr zeolites: tuning the propylene selectivity via the olefin-based catalytic cycle. *ACS Catal* 2020;10:3009-17. DOI
110. Yang M, Li B, Gao M, et al. High Propylene selectivity in methanol conversion over a small-pore SAPO molecular sieve with ultra-small cage. *ACS Catal* 2020;10:3741-9. DOI
111. Zhou Y, Zhang J, Ma W, et al. Small pore SAPO-14-based zeolites with improved propylene selectivity in the methanol to olefins process. *Inorg Chem Front* 2022;9:1752-60. DOI
112. Dyballa M, Becker P, Trefz D, et al. Parameters influencing the selectivity to propene in the MTO conversion on 10-ring zeolites: directly synthesized zeolites ZSM-5, ZSM-11, and ZSM-22. *AAPPL CATAL A-GEN* 2016;510:233-43. DOI
113. Lee K, Lee H, Ihm S. Influence of catalyst binders on the acidity and catalytic performance of HZSM-5 zeolites for methanol-to-propylene (MTP) process: single and binary binder system. *Top Catal* 2010;53:247-53. DOI
114. Hu Z, Zhang H, Wang L, et al. Highly stable boron-modified hierarchical nanocrystalline ZSM-5 zeolite for the methanol to propylene reaction. *Catal Sci Technol* 2014;4:2891-5. DOI
115. Yoshioka M, Yokoi T, Tatsumi T. Development of the CON-type aluminosilicate zeolite and its catalytic application for the MTO reaction. *ACS Catal* 2015;5:4268-75. DOI
116. Zhao X, Wang L, Guo P, et al. Synthesis of high-Si hierarchical beta zeolites without mesoporogen and their catalytic application in the methanol to propene reaction. *Catal Sci Technol* 2018;8:2966-74. DOI
117. Jamil AK, Muraza O, Yoshioka M, Al-amer AM, Yamani ZH, Yokoi T. Selective production of propylene from methanol conversion over nanosized ZSM-22 zeolites. *Ind Eng Chem Res* 2014;53:19498-505. DOI
118. Zhang J, Huang Z, Li P, et al. Elucidating the reaction pathway for ethene and propene formation in the methanol-to-hydrocarbons reaction over high silica H-Beta. *Catal Sci Technol* 2017;7:2194-203. DOI
119. Wennmacher JTC, Mahmoudi S, Rzepka P, et al. Electron diffraction enables the mapping of coke in ZSM-5 micropores formed during methanol-to-hydrocarbons conversion. *Angew Chem Int Ed Engl* 2022;61:e202205413. DOI PubMed PMC
120. Schmidt F, Hoffmann C, Giordanino F, et al. Coke location in microporous and hierarchical ZSM-5 and the impact on the MTH reaction. *J Catal* 2013;307:238-45. DOI
121. Urata K, Furukawa S, Komatsu T. Location of coke on H-ZSM-5 zeolite formed in the cracking of n-hexane. *AAPPL CATAL A-GEN* 2014;475:335-40. DOI
122. Milina M, Mitchell S, Cooke D, Crivelli P, Pérez-Ramírez J. Impact of pore connectivity on the design of long-lived zeolite catalysts. *Angew Chem Int Ed Engl* 2015;54:1591-4. DOI PubMed
123. Astafan A, Benghalem M, Pouilloux Y, et al. Particular properties of the coke formed on nano-sponge *BEA zeolite during ethanol-to-hydrocarbons transformation. *J Catal* 2016;336:1-10. DOI
124. Müller S, Liu Y, Vishnuvarthan M, et al. Coke formation and deactivation pathways on H-ZSM-5 in the conversion of methanol to olefins. *Journal of Catalysis* 2015;325:48-59. DOI
125. Lezcano-Gonzalez I, Campbell E, Hoffman AEJ, et al. Insight into the effects of confined hydrocarbon species on the lifetime of methanol conversion catalysts. *Nat Mater* 2020;19:1081-7. DOI PubMed
126. Bjørgen M. Coke precursor formation and zeolite deactivation: mechanistic insights from hexamethylbenzene conversion. *J Catal* 2003;215:30-44. DOI
127. Magnoux P, Roger P, Canaff C, Fouche V, Gnep N, Guisnet M. New technique for the characterization of carbonaceous compounds responsible for zeolite deactivation. Catalyst Deactivation 1987, Proceedings of the 4th International Symposium. Elsevier; 1987. p. 317-30. DOI
128. Aramburo LR, Teketel S, Svelle S, et al. Interplay between nanoscale reactivity and bulk performance of H-ZSM-5 catalysts during the methanol-to-hydrocarbons reaction. *J Catal* 2013;307:185-93. DOI

129. Wei Y, Yuan C, Li J, et al. Coke formation and carbon atom economy of methanol-to-olefins reaction. *ChemSusChem* 2012;5:906-12. DOI PubMed
130. Wragg DS, O'Brien MG, Bleken FL, Di Michiel M, Olsbye U, Fjellvåg H. Watching the methanol-to-olefin process with time- and space-resolved high-energy operando X-ray diffraction. *Angew Chem Int Ed Engl* 2012;51:7956-9. DOI PubMed
131. Wang C, Wang Q, Xu J, et al. Direct detection of supramolecular reaction centers in the methanol-to-olefins conversion over zeolite H-ZSM-5 by ^{13}C-^{27}Al solid-state NMR spectroscopy. *Angew Chem Int Ed Engl* 2016;55:2507-11. DOI
132. Yang L, Wang C, Zhang L, et al. Stabilizing the framework of SAPO-34 zeolite toward long-term methanol-to-olefins conversion. *Nat Commun* 2021;12:4661. DOI PubMed PMC
133. Wang N, Zhi Y, Wei Y, et al. Molecular elucidating of an unusual growth mechanism for polycyclic aromatic hydrocarbons in confined space. *Nat Commun* 2020;11:1079. DOI PubMed PMC
134. Wang C, Yang M, Tian P, et al. Dual template-directed synthesis of SAPO-34 nanosheet assemblies with improved stability in the methanol to olefins reaction. *J Mater Chem A* 2015;3:5608-16. DOI
135. Choi M, Na K, Kim J, Sakamoto Y, Terasaki O, Ryoo R. Stable single-unit-cell nanosheets of zeolite MFI as active and long-lived catalysts. *Nature* 2009;461:246-9. DOI PubMed
136. Liu Y, Zhang Q, Li J, et al. Protozeolite-seeded synthesis of single-crystalline hierarchical zeolites with facet-shaped mesopores and their catalytic application in methanol-to-propylene conversion. *Angew Chem Int Ed Engl* 2022;61:e202205716. DOI PubMed
137. Liang T, Chen J, Wang S, et al. Conversion of methanol to hydrocarbons over H-MCM-22 zeolite: deactivation behaviours related to acid density and distribution. *Catal Sci Technol* 2022;12:6268-84. DOI
138. Liu Z, Dong X, Liu X, Han Y. Oxygen-containing coke species in zeolite-catalyzed conversion of methanol to hydrocarbons. *Catal Sci Technol* 2016;6:8157-65. DOI
139. Chen Z, Ni Y, Zhi Y, et al. Coupling of methanol and carbon monoxide over H-ZSM-5 to form aromatics. *Angew Chem Int Ed Engl* 2018;57:12549-53. DOI PubMed
140. Shi Z, Arora SS, Trahan DW, Hickman D, Bhan A. Methanol to hydrocarbons conversion: Why dienes and monoenes contribute differently to catalyst deactivation? *Chem Eng J* 2022;437:134229. DOI
141. Martinez-espin JS, Mortén M, Janssens TVW, Svelle S, Beato P, Olsbye U. New insights into catalyst deactivation and product distribution of zeolites in the methanol-to-hydrocarbons (MTH) reaction with methanol and dimethyl ether feeds. *Catal Sci Technol* 2017;7:2700-16. DOI
142. Shi Z, Neurock M, Bhan A. Methanol-to-olefins catalysis on HSSZ-13 and HSAPO-34 and Its relationship to acid strength. *ACS Catal* 2021;11:1222-32. DOI
143. Hwang A, Bhan A. Bifunctional strategy coupling Y_2O_3-catalyzed alkanal decomposition with methanol-to-olefins catalysis for enhanced lifetime. *ACS Catal* 2017;7:4417-22. DOI
144. Arora SS, Nieskens DLS, Malek A, Bhan A. Lifetime improvement in methanol-to-olefins catalysis over chabazite materials by high-pressure H_2 co-feeds. *Nat Catal* 2018;1:666-72. DOI
145. Hwang A, Bhan A. Deactivation of zeolites and zeotypes in methanol-to-hydrocarbons catalysis: mechanisms and circumvention. *Acc Chem Res* 2019;52:2647-56. DOI PubMed
146. Zhou J, Gao M, Zhang J, et al. Directed transforming of coke to active intermediates in methanol-to-olefins catalyst to boost light olefins selectivity. *Nat Commun* 2021;12:17. DOI PubMed PMC
147. Wang C, Yang L, Gao M, et al. Directional construction of active naphthalenic species within SAPO-34 crystals toward more efficient methanol-to-olefin conversion. *J Am Chem Soc* 2022;144:21408-16. DOI PubMed
148. Gao P, Wang Q, Xu J, et al. Brønsted/lewis acid synergy in methanol-to-aromatics conversion on ga-modified zsm-5 zeolites, as studied by solid-state NMR spectroscopy. *ACS Catal* 2018;8:69-74. DOI
149. Wang N, Li J, Sun W, et al. Rational design of zinc/zeolite catalyst: selective formation of p-Xylene from methanol to aromatics reaction. *Angew Chem Int Ed Engl* 2022;61:e202114786. DOI PubMed
150. Wang H, Wang L, Luo Q, et al. Two-dimensional manganese oxide on ceria for the catalytic partial oxidation of hydrocarbons. *Chem Synth* 2022;2:2. DOI
151. Wang D, Xie Z, Porosoff MD, Chen JG. Recent advances in carbon dioxide hydrogenation to produce olefins and aromatics. *Chem* 2021;7:2277-311. DOI
152. Zhang W, Wang S, Guo S, et al. Effective conversion of CO_2 into light olefins over a bifunctional catalyst consisting of La-modified ZnZrO. *Catal Sci Technol* ;12:2566-77. DOI
153. Xie J, Firth DS, Cordero-Lanzac T, et al. MAPO-18 catalysts for the methanol to olefins process: influence of catalyst acidity in a high-pressure syngas (CO and H_2) environment. *ACS Catal* 2022;12:1520-31. DOI PubMed PMC
154. Wang S, Zhang L, Wang P, et al. Highly selective hydrogenation of CO_2 to propane over $GaZrO_x$/H-SSZ-13 composite. *Nat Catal* 2022;5:1038-50. DOI

Su. *Chem Synth* 2022;2:22
DOI: 10.20517/cs.2022.39

Chemical Synthesis

Editorial

Open Access

Chemical Synthesis: Happy Birthday!

Bao-Lian Su[1,2,*]

[1]State Key Laboratory of Advanced technology for Materials Synthesis and Processing, Wuhan University of Technology, Wuhan 430074, Hubei, China.
[2]Laboratory of Inorganic Materials Chemistry, University of Namur, Namur B-5000, Belgium.

***Correspondence to:** Prof. Bao-Lian Su, Laboratory of Inorganic Materials Chemistry, University of Namur, Rue de Bruxelles 61, Namur B-5000, Belgium. E-mail: bao-lian.su@unamur.be

How to cite this article: Su BL. *Chemical Synthesis*: Happy Birthday! *Chem Synth* 2022;2:22. https://dx.doi.org/10.20517/cs.2022.39

Received: 5 Dec 2022 **Accepted:** 5 Dec 2022 **Published:** 7 Dec 2022

Academic Editor: Bao-Lian Su **Copy Editor:** Peng-Juan Wen **Production Editor:** Peng-Juan Wen

Our journal *Chemical Synthesis* is celebrating its first anniversary of releasing the first issue in November 2021 and the second anniversary of its creation. We also would like to take this opportunity to congratulate our author, Prof. Karl Barry Sharpless, for his second Nobel Prize in Chemistry in 2022.

This year, *Chemical Synthesis* became a member of the Committee on Publication Ethics (COPE) and STM (International Association of Scientific, Technical, and Medical Publishers). We also have some cooperating conferences, such as the 2023 International Conference on Materials Science and Engineering (CoMSE 2023), the International Conference on Catalysis and Chemical Science, The 44th International Conference on Coordination Chemistry, and The 20th National Congress on Catalysis of China. In addition, we have three cooperating partners: Researchgate, TrendMed, and Clarivate. As of now, all published articles have been indexed by Google Scholar, Dimensions, and Lens. We also plan to apply for CAS, J-GATE, EBSCO, INSPEC, ESCI, Scopus, *etc*.

Chemical Synthesis has published 36 high-quality papers since November 2021, including 3 Editorials, 6 Research Articles, 11 Reviews, 2 Previews, 3 Editor's Choices, 3 Research Highlights, 1 Commentary, 1 Perspective, 3 News, 2 Short Communications and 1 Feature Article. According to statistics, the published articles have 35,523 views and 10,214 downloads. The authors are internationally well-known chemists. The Webinar on "Dynamic network assembly and multipolar structural transformation" with three lectures chaired by Prof. Guangshan Zhu from Northeastern Normal University and delivered by three eminent

scientists: Prof. Minghua Zeng from Hubei University, Prof. Chen Wang from East China Normal University and Prof. Teng Ben from Zhejiang Normal University was a great success and attracted more than 21,000 attendees. The second Webinar focused on "Catalysis" with Prof. Peijun Hu from East China University of Science Technology, Prof. Yuefeng Liu from Dalian Institute of Chemical Physics, Chinese Academy of Sciences, and Prof. Lin He from Lanzhou Institute of Chemical Physics, Chinese Academy of Sciences as Speakers, which broke the record and attracted more than 76,000 attendees. Our journal gained widespread attention around the world! We sincerely thank the editorial staff for their hard work, for the quality control of our section editors, and for the active participation of our youth editorial committee members.

This year, the number of international Editorial Board Members has been expanded to 65, covering 14 countries, 23 Section Editors and 43 Youth Editorial Board Members.

Next year, our journal will be more diversified. In addition to the regular issues, six Special Issues are programmed on "50 Years Selenium Organic Chemistry", "Celebrating the 45th Anniversary of Changzhou University - Applications and Future Prospects of Asymmetric Organocatalysis", "Molecular Based Magnetic Materials, Synthesis of Advanced Material for Novel Fuel Cells", "Self-Assembled Nanostructures and Materials" and "Carbon-Based Materials for Electrocatalytic Energy Conversion and Storage: From Understanding to Designing". We welcome your contributions and will provide you with more information on the latest developments in Chemistry.

On this momentous occasion, the release of the first issue and the second anniversary of our journal's founding, there are no words to express my gratitude to our authors for their trust and high-quality contributions to our journal. Special thanks to our reviewers for giving their expertise and time to review manuscripts. We really appreciate their commitment to the first, second, third and sometimes even fourth and fifth rounds of review. They set an excellent example of scientific professionalism. We know that we can continue to count on them. The success of our journal is owing to our authors, reviewers and editorial staff.

In this fourth issue of 2022, you will find two excellent review articles. One is on a very hot topic related to two-dimensional materials: synthesis and applications in the electro-reduction of carbon dioxide contributed by the team led by Prof. Xinchen Kang and Prof. Buxing Han from the Institute of Chemistry, Chinese Academy of Sciences. It is really a state-of-the-art review that can give you essential information. The other is on the fundamentals of the catalytic conversion of methanol to hydrocarbons by Prof. Jianfeng Huang and Dr. Zhaohui Liu from Chongqing University. Two research articles are in this issue. One is from Prof. Yi Tang's group, Fudan University, on alkalinity-controlled zeolite nucleation and growth: ultrafast synthesis of total-morphology zeolite L mesocrystals and adsorption evaluation. Zeolites, as one of the most important materials in petroleum processing, remain the focus of catalysis research. In this high-quality research paper, a facile and univariate modulation strategy was developed to regulate zeolite crystallization kinetic to develop advanced catalysts and adsorbents. Another is on Enantioselective 1,1-diarylation of terminal alkenes catalyzed by palladium with a chiral phosphoric acid from Prof. Zhi-Min Chen's group at Shanghai Jiao Tong University. This paper, for the first time, reports the enantioselective 1,1-diarylation of allyl sulfones and vinyl sulfones. A short communication from Prof. Jie Han's team at Yangzhou University highlights β-cyclodextrin mediated construction of porous helical nanoribbons from oligoaniline derivatives. This work demonstrates how the supramolecular host-modulated assembly strategy can be instructive for the fabrication of porous supramolecular nanostructures.

Chemical Synthesis is seeking important breakthroughs and significant scientific insights. With the joint efforts of our editorial staff, we do our best to bring you more information on chemical developments. We are waiting for you to join us to promote chemical research via our journal and realize our *Chemical Synthesis* dream.

Finally, Merry Christmas and Happy New Year to all!

DECLARATIONS

Author's contribution

The author contributed solely to this manuscript.

Availability of data and materials

Not applicable.

Financial support and sponsorship

None.

Conflicts of interest

The author declared that there are no conflicts of interest.

Ethical approval and consent to participate

Not applicable.

Consent for publication

Not applicable.

AUTHOR INSTRUCTIONS

1. Submission Overview

Before you decide to publish with *Chemical Synthesis*, please read the following items carefully and make sure that you are well aware of Editorial Policies and the following requirements.

1.1 Topic Suitability

The topic of the manuscript must fit the scope of the journal. Please refer to Aims and Scope for more information.

1.2 Open Access and Copyright

The journal adopts Gold Open Access publishing model and distributes content under the Creative Commons Attribution 4.0 International License. Copyright is retained by authors. Please make sure that you are well aware of these policies.

1.3 Publication Fees

Chemical Synthesis is an open access journal. When a paper is accepted for publication, authors are required to pay Article Processing Charges (APCs) to cover its editorial and production costs. The APC for each submission is $600. There are no additional charges based on color, length, figures, or other elements. For more details, please refer to OAE Publication Fees.

1.4 Language Editing

All submissions are required to be presented clearly and cohesively in good English. Authors whose first language is not English are advised to have their manuscripts checked or edited by a native English speaker before submission to ensure the high quality of expression. A well-organized manuscript in good English would make the peer review even the whole editorial handling more smoothly and efficiently.
If needed, authors are recommended to consider the language editing services provided by Charlesworth to ensure that the manuscript is written in correct scientific English before submission. Authors who publish with OAE journals enjoy a special discount for the services of Charlesworth via the following two ways.

Submit your manuscripts directly at http://www.charlesworthauthorservices.com/~OAE;
Open the link http://www.charlesworthauthorservices.com/, and enter Promotion Code “OAE” when you submit.

1.5 Work Funded by the National Institutes of Health

If an accepted manuscript was funded by National Institutes of Health (NIH), the authors may inform Editors of the NIH funding number. The Editors are able to deposit the paper to the NIH Manuscript Submission System on behalf of the authors.

2. Submission Preparation

2.1 Cover Letter

A cover letter is required to be submitted accompanying each manuscript. It should be concise and explain why the study is significant, why it fits the scope of the journal, and why it would be attractive to readers, etc.
Here is a guideline of a cover letter for authors’ consideration:
In the first paragraph: include the title and type (e.g., Original Article, Review, Case Report, etc.) of the manuscript, a brief on the background of the study, the question the author sought out to answer and why;
In the second paragraph: concisely explain what was done, the main findings and why they are significant;
In the third paragraph: indicate why the manuscript fits the Aims and Scope of the journal, and why it would be attractive to readers;
In the fourth paragraph: confirm that the manuscript has not been published elsewhere and not under consideration of any other journal. All authors have approved the manuscript and agreed on its submission to the journal. Journal’s specific requirements have been met if any.
If the manuscript is contributed to a Special Issue, please also mention it in the cover letter.
If the manuscript was presented partly or entirely in a conference, the author should clearly state the background information of the event, including the conference name, time and place in the cover letter.

2.2 Types of Manuscripts

The journal publishes Research Article, Review Article, Short Communication, Feature Article, Commentary, Editorial, News, Research Highlight, Perspective, *etc*. For more details about paper type, please refer to the following table.

Manuscript Type	Definition	Abstract	Keywords	Main Text Structure
Research Article	A Research Article is a seminal and insightful research study and showcases that often involves modern techniques or methodologies. Authors should justify that their work are of novel findings.	The abstract should state briefly the purpose of the research, the principal results and major conclusions. No more than 250 words.	3-6 keywords.	The main content should include four sections: Introduction, Experimental, Results and discussion, and Conclusions.
Review Article	A Review Article should be an authoritative, well balanced and critical survey of recent progresses in an attractive or a fundamental chemical research field.	Unstructured abstract. No more than 250 words.	3-6 keywords.	The main text may consist of several sections with unfixed section titles. We suggest that the author include an "Introduction" section at the beginning, several sections with unfixed titles in the middle part, and a "Conclusion and outlook" section in the end. Corresponding authors are requested to provide a short biography (up to 200 words) and headshot for inclusion at the end of the published article.
Short Communication	Short Communications are for the urgent publication of a research which is of outstanding significance and interest to experts in the field and also to general chemistry readership. Authors should write in a clear and concise way to demonstrate the necessity of an urgent publication.	Unstructured abstract. No more than 150 words.	3-6 keywords.	The short Communication is a one body text with maximum 4 items (figures and tables) and 12 references.
Feature Article	A Feature Article is not a typical review. Feature article should highlight the author's contribution to a key field with a balanced discussion of related work from the field. A Feature Article should not, in principle, contain original research.	Unstructured abstract. No more than 250 words.	3-6 keywords.	The main text may consist of several sections with unfixed section titles. We suggest that the author include an "Introduction" section at the beginning, several sections with unfixed titles in the middle part, and a "Conclusion and outlook" section in the end.
Commentary	A Commentary is to provide comments on a newly published article or an alternative viewpoint on a certain topic.	Unstructured abstract. No more than 250 words.	3-6 keywords.	/
Editorial	An Editorial can be a comment about an important event in the world related or not to chemistry or a particular discovery in chemistry, needing a particular attention of chemistry community.	None required.	None required	/
News	A News comments an important event in the world related or not to chemistry, or a particular discovery in chemistry, needing a particular attention of chemistry community.	None required.	None required	/
Research Highlight	A Research Highlight article is peer-reviewed paper and highlights work recently published in the journal or in a recent issue of another journal.	None required.	3-6 keywords.	/
Perspective	A Perspective provides personal points of view on the state-of-the-art of a specific area of knowledge and its future prospects.	Unstructured abstract. No more than 150 words.	3-6 keywords.	/

2.3 Manuscript Structure

2.3.1 Front Matter

2.3.1.1 Title

The title of the manuscript should be concise, specific and relevant, with no more than 16 words if possible. When gene or protein names are included, the abbreviated name rather than full name should be used.

2.3.1.2 Authors and Affiliations

Authors' full names should be listed. The initials of middle names can be provided. Institutional addresses and email addresses for all authors should be listed. At least one author should be designated as corresponding author. In addition, corresponding authors are suggested to provide their Open Researcher and Contributor ID upon submission. Please note that any change to authorship is not allowed after manuscript acceptance.

2.3.1.3 Highlights

Highlights are mandatory because they can help increase the discoverability of your article through search engines. They consist of a short collection of bullet points that capture the novel results of your research as well as new methods that were used during the study (if any). They should be submitted in a separate editable file in the online submission system. Please use 'Highlights' in the file name and include 3 to 5 bullet points (maximum 85 characters per bullet point, including spaces).

2.3.1.4 Abstract

The abstract should be a single paragraph with word limitation and specific structure requirements (for more details please refer to Types of Manuscripts). It usually describes the main objective(s) of the study, explains how the study was done, including any model organisms used, without methodological detail, and summarizes the most important results and their significance. The abstract must be an objective representation of the study: it is not allowed to contain results which are not presented and substantiated in the manuscript, or exaggerate the main conclusions. Citations should not be included in the abstract.

2.3.1.5 Graphical Abstract

The graphical abstract is essential as this can catch first view of your publication by readers. We recommend you to submit an eye-catching figure. It should summarize the content of the article in a concise graphical form. It is recommended to use it because this can make online articles get more attention. The graphic abstract should be submitted as a separate document in the online submission system. Please provide an image with a minimum of 531 × 1,328 pixels (h × w) or proportionally more. The image should be readable at a size of 5 × 13 cm using a regular screen resolution of 96 dpi. Preferred file types: tiff, psd, AI, jpeg and eps files.

2.3.1.6 Keywords

Three to six keywords should be provided, which are specific to the article, yet reasonably common within the subject discipline.

2.3.2 Main Text

Manuscripts of different types are structured with different sections of content. Please refer to Types of Manuscripts to make sure which sections should be included in the manuscripts.

2.3.2.1 Introduction

The introduction should contain background that puts the manuscript into context, allow readers to understand why the study is important, include a brief review of key literature, and conclude with a brief statement of the overall aim of the work and a comment about whether that aim was achieved. Relevant controversies or disagreements in the field should be introduced as well.

2.3.2.2 Experimental

Experimental should contain sufficient details to allow others to fully replicate the study. New methods and protocols should be described in detail while well-established methods can be briefly described or appropriately cited. Experimental participants selected, the drugs and chemicals used, the statistical methods taken, and the computer software used should be identified precisely. Statistical terms, abbreviations, and all symbols used should be defined clearly. Protocol documents for clinical trials, observational studies, and other non-laboratory investigations may be uploaded as supplementary materials.

2.3.2.3 Results and Discussion

This section should contain the findings of the study and discuss the implications of the findings in context of existing research and highlight limitations of the study. Future research directions may also be mentioned. Results of statistical analysis should also be included either as text or as tables or figures if appropriate. Authors should emphasize and summarize only the most important observations. Data on all primary and secondary outcomes identified in the section Methods should also be provided. Extra or supplementary materials and technical details can be placed in supplementary documents.

2.3.2.4 Conclusions

It should state clearly the main conclusions and include the explanation of their relevance or importance to the field.

2.3.3 Back Matter

2.3.3.1 Acknowledgments

Anyone who contributed towards the article but does not meet the criteria for authorship, including those who provided professional writing services or materials, should be acknowledged. Authors should obtain permission to acknowledge from all those mentioned in the Acknowledgments section. This section is not added if the author does not have anyone to acknowledge.

2.3.3.2 Authors' Contributions

Each author is expected to have made substantial contributions to the conception or design of the work, or the acquisition, analysis, or interpretation of data, or the creation of new software used in the work, or have drafted the work or substantively revised it.

Please use Surname and Initial of Forename to refer to an author's contribution. For example: made substantial contributions to conception and design of the study and performed data analysis and interpretation: Salas H, Castaneda WV; performed data acquisition, as well as provided administrative, technical, and material support: Castillo N, Young V.

If an article is single-authored, please include "The author contributed solely to the article." in this section.

2.3.3.3 Availability of Data and Materials

In order to maintain the integrity, transparency and reproducibility of research records, authors should include this section in their manuscripts, detailing where the data supporting their findings can be found. Data can be deposited into data repositories or published as supplementary information in the journal. Authors who cannot share their data should state that the data will not be shared and explain it. If a manuscript does not involve such issue, please state "Not applicable." in this section.

2.3.3.4 Financial Support and Sponsorship

All sources of funding for the study reported should be declared. The role of the funding body in the experiment design, collection, analysis and interpretation of data, and writing of the manuscript should be declared. Any relevant grant numbers and the link of funder's website should be provided if any. If the study is not involved with this issue, state "None." in this section.

2.3.3.5 Conflicts of Interest

Authors must declare any potential conflicts of interest that may be perceived as inappropriately influencing the representation or interpretation of reported research results. If there are no conflicts of interest, please state "All authors declared that there are no conflicts of interest." in this section. Some authors may be bound by confidentiality agreements. In such cases, in place of itemized disclosures, we will require authors to state "All authors declare that they are bound by confidentiality agreements that prevent them from disclosing their conflicts of interest in this work.". If authors are unsure whether conflicts of interest exist, please refer to the "Conflicts of Interest" of *Chemical Synthesis* Editorial Policies for a full explanation.

2.3.3.6 Ethical Approval and Consent to Participate

Research involving human subjects, human material or human data must be performed in accordance with the Declaration of Helsinki and approved by an appropriate ethics committee. An informed consent to participate in the study should also be obtained from participants, or their parents or legal guardians for children under 16. A statement detailing the name of the ethics committee (including the reference number where appropriate) and the informed consent obtained must appear in the manuscripts reporting such research.

Studies involving animals and cell lines must include a statement on ethical approval. More information is available at Editorial Policies.

If the manuscript does not involve such issue, please state "Not applicable." in this section.

2.3.3.7 Consent for Publication

Manuscripts containing individual details, images or videos, must obtain consent for publication from that person, or in the case of children, their parents or legal guardians. If the person has died, consent for publication must be obtained from the next of kin of the participant. Manuscripts must include a statement that a written informed consent for publication was obtained. Authors do not have to submit such content accompanying the manuscript. However, these documents must be available if requested. If the manuscript does not involve this issue, state "Not applicable." in this section.

2.3.3.8 Copyright

Authors retain copyright of their works through a Creative Commons Attribution 4.0 International License that clearly states how readers can copy, distribute, and use their attributed research, free of charge. A declaration "© The Author(s)

2022." will be added to each article. Authors are required to sign License to Publish before formal publication.

2.3.3.9 References

References should be numbered in order of appearance at the end of manuscripts. In the text, reference numbers should be placed in square brackets and the corresponding references are cited thereafter. If the number of authors is less than or equal to six, we require to list all authors' names. If the number of authors is more than six, only the first three authors' names are required to be listed in the references, other authors' names should be omitted and replaced with "et al.". Abbreviations of the journals should be provided on the basis of Index Medicus. Information from manuscripts accepted but not published should be cited in the text as "Unpublished material" with written permission from the source.

References should be described as follows, depending on the types of works:

Types	Examples
Journal articles by individual authors	Weaver DL, Ashikaga T, Krag DN, et al. Effect of occult metastases on survival in node-negative breast cancer. *N Engl J Med* 2011;364:412-21. [PMID: 21247310 DOI: 10.1056/NEJMoa1008108]
Organization as author	Diabetes Prevention Program Research Group. Hypertension, insulin, and proinsulin in participants with impaired glucose tolerance. *Hypertension* 2002;40:679-86. [PMID: 12411462]
Both personal authors and organization as author	Vallancien G, Emberton M, Harving N, van Moorselaar RJ; Alf-One Study Group. Sexual dysfunction in 1,274 European men suffering from lower urinary tract symptoms. *J Urol* 2003;169:2257-61. [PMID: 12771764 DOI: 10.1097/01.ju.0000067940.76090.73]
Journal articles not in English	Zhang X, Xiong H, Ji TY, Zhang YH, Wang Y. Case report of anti-N-methyl-D-aspartate receptor encephalitis in child. *J Appl Clin Pediatr* 2012;27:1903-7. (in Chinese)
Journal articles ahead of print	Odibo AO. Falling stillbirth and neonatal mortality rates in twin gestation: not a reason for complacency. BJOG 2018; Epub ahead of print [PMID: 30461178 DOI: 10.1111/1471-0528.15541]
Books	Sherlock S, Dooley J. Diseases of the liver and billiary system. 9th ed. Oxford: Blackwell Sci Pub; 1993. pp. 258-96.
Book chapters	Meltzer PS, Kallioniemi A, Trent JM. Chromosome alterations in human solid tumors. In: Vogelstein B, Kinzler KW, editors. The genetic basis of human cancer. New York: McGraw-Hill; 2002. pp. 93-113.
Online resource	FDA News Release. FDA approval brings first gene therapy to the United States. Available from: https://www.fda.gov/NewsEvents/Newsroom/PressAnnouncements/ucm574058.htm. [Last accessed on 30 Oct 2017]
Conference proceedings	Harnden P, Joffe JK, Jones WG, editors. Germ cell tumours V. Proceedings of the 5th Germ Cell Tumour Conference; 2001 Sep 13-15; Leeds, UK. New York: Springer; 2002.
Conference paper	Christensen S, Oppacher F. An analysis of Koza's computational effort statistic for genetic programming. In: Foster JA, Lutton E, Miller J, Ryan C, Tettamanzi AG, editors. Genetic programming. EuroGP 2002: Proceedings of the 5th European Conference on Genetic Programming; 2002 Apr 3-5; Kinsdale, Ireland. Berlin: Springer; 2002. pp. 182-91.
Unpublished material	Tian D, Araki H, Stahl E, Bergelson J, Kreitman M. Signature of balancing selection in Arabidopsis. *Proc Natl Acad Sci U S A*. Forthcoming 2002.

For other types of references, please refer to U.S. National Library of Medicine.
The journal also recommends that authors prepare references with a bibliography software package, such as EndNote to avoid typing mistakes and duplicated references.

2.3.3.10 Supplementary Materials

Additional data and information can be uploaded as Supplementary Materials to accompany the manuscripts. The supplementary materials will also be available to the referees as part of the peer-review process. Any file format is acceptable, such as data sheet (word, excel, csv, cdx, fasta, pdf or zip files), presentation (PowerPoint, pdf or zip files), image (cdx, eps, jpeg, pdf, png or tiff), table (word, excel, csv or pdf), audio (mp3, wav or wma) or video (avi, divx, flv, mov, mp4, mpeg, mpg or wmv). All information should be clearly presented. Supplementary materials should be cited in the main text in numeric order (e.g., Supplementary Figure 1, Supplementary Figure 2, Supplementary Table 1, Supplementary Table 2, etc.). The style of supplementary figures or tables complies with the same requirements on figures or tables in main text. Videos and audios should be prepared in English, and limited to a size of 500 MB or a duration of 3 minutes.

2.4 Manuscript Format

2.4.1 File Format

Manuscript files can be in DOC and DOCX formats and should not be locked or protected.

2.4.2 Length

There are no restrictions on paper length, number of figures, or amount of supporting documents. Authors are encouraged to present and discuss their findings concisely.

2.4.3 Language

Manuscripts must be written in English.

2.4.4 Multimedia Files

The journal supports manuscripts with multimedia files. The requirements are listed as follows:
Videos or audio files are only acceptable in English. The presentation and introduction should be easy to understand. The frames should be clear, and the speech speed should be moderate.
A brief overview of the video or audio files should be given in the manuscript text.
The video or audio files should be limited to a size of up to 500 MB.
Please use professional software to produce high-quality video files, to facilitate acceptance and publication along with the submitted article. Upload the videos in mp4, wmv, or rm format (preferably mp4) and audio files in mp3 or wav format.

2.4.5 Figures

Figures should be cited in numeric order (e.g., Figure 1, Figure 2) and placed after the paragraph where it is first cited;
Figures can be submitted in format of tiff, psd, AI or jpeg, with resolution of 300-600 dpi;
Figure caption is placed under the Figure;
Diagrams with describing words (including, flow chart, coordinate diagram, bar chart, line chart, and scatter diagram, *etc.*) should be editable in word, excel or powerpoint format. Non-English information should be avoided;
Labels, numbers, letters, arrows, and symbols in figure should be clear, of uniform size, and contrast with the background;
Symbols, arrows, numbers, or letters used to identify parts of the illustrations must be identified and explained in the legend;
Internal scale (magnification) should be explained and the staining method in photomicrographs should be identified;
All non-standard abbreviations should be explained in the legend;
Permission for use of copyrighted materials from other sources, including re-published, adapted, modified, or partial figures and images from the internet, must be obtained. It is authors' responsibility to acquire the licenses, to follow any citation instruction requested by third-party rights holders, and cover any supplementary charges.

2.4.6 Tables

Tables should be cited in numeric order and placed after the paragraph where it is first cited;
The table caption should be placed above the table and labeled sequentially (e.g., Table 1, Table 2);
Tables should be provided in editable form like DOC or DOCX format (picture is not allowed);
Abbreviations and symbols used in table should be explained in footnote;
Explanatory matter should also be placed in footnotes;
Permission for use of copyrighted materials from other sources, including re-published, adapted, modified, or partial tables from the internet, must be obtained. It is authors' responsibility to acquire the licenses, to follow any citation instruction requested by third-party rights holders, and cover any supplementary charges.

2.4.7 Abbreviations

Abbreviations should be defined upon first appearance in the abstract, main text, and in figure or table captions and used consistently thereafter. Non-standard abbreviations are not allowed unless they appear at least three times in the text. Commonly-used abbreviations, such as DNA, RNA, ATP, *etc*., can be used directly without definition. Abbreviations in titles and keywords should be avoided, except for the ones which are widely used.

2.4.8 Italics

General italic words like *vs*., *et al., etc*., *in vivo*, *in vitro*; *t* test, *F* test, *U* test; related coefficient as *r*, sample number as *n*, and probability as *P*; names of genses; names of bacteria and biology species in Latin.

2.4.9 Units

SI Units should be used. Imperial, US customary and other units should be converted to SI units whenever possible. There is a space between the number and the unit (i.e., 23 mL). Hour, minute, second should be written as h, min, s.

2.4.10 Numbers

Numbers appearing at the beginning of sentences should be expressed in English. When there are two or more numbers in a paragraph, they should be expressed as Arabic numerals; when there is only one number in a paragraph, number < 10 should be expressed in English and number > 10 should be expressed as Arabic numerals. 12345678 should be written as 12,345,678.

2.4.11 Equations

Equations should be editable and not appear in a picture format. Authors are advised to use either the Microsoft Equation Editor or the MathType for display and inline equations.

2.5 Submission Link

Submit an article via https://oaemesas.com/login?JournalId=cs.

www.oaepublish.com

Chemical Synthesis
(*CS*)
Los Angeles Office
245 E Main Street ste122, Alhambra,
CA 91801, USA
E-mail: editorialoffice@chesynjournal.com
Website: www.chesynjournal.com